



HAL
open science

Intraplate strain localization due to olivine viscous anisotropy in the lithospheric mantle

Lucan Mameri Calcagno de Oliveira

► **To cite this version:**

Lucan Mameri Calcagno de Oliveira. Intraplate strain localization due to olivine viscous anisotropy in the lithospheric mantle. Other. Université Montpellier, 2020. English. NNT : 2020MONTG008 . tel-03136979v2

HAL Id: tel-03136979

<https://theses.hal.science/tel-03136979v2>

Submitted on 10 Feb 2021

HAL is a multi-disciplinary open access archive for the deposit and dissemination of scientific research documents, whether they are published or not. The documents may come from teaching and research institutions in France or abroad, or from public or private research centers.

L'archive ouverte pluridisciplinaire **HAL**, est destinée au dépôt et à la diffusion de documents scientifiques de niveau recherche, publiés ou non, émanant des établissements d'enseignement et de recherche français ou étrangers, des laboratoires publics ou privés.

THESIS FOR THE DEGREE OF DOCTOR OF PHILOSOPHY AT THE UNIVERSITY OF MONTPELLIER

In Earth Science

GAIA Doctoral School

Research unit Géosciences Montpellier – UMR 5243

Intraplate strain localization due to olivine viscous anisotropy in the lithospheric mantle

Presented by Lucan MAMERI

The 28th February 2020

Under the supervision of Andréa TOMMASI
and Javier Signorelli

In the presence of the thesis jury composed of

Dr. Fanny GAREL, Maître de Conférences, Université de Montpellier

Dr. Riad HASSANI, Professeur, Université Côte d'Azur

Dr. Olivier CASTELNAU, Directeur de Recherche, CNRS, ENS Arts et Métiers

Dr. Boris KAUS, Full Professor, JG University Mainz

Dr. Anne Davaille, Directeur de Recherche, CNRS, Université Paris-Sud

Dr. Javier Signorelli, Professor, CONICET, Universidade Nacional de Rosário

Dr. Andréa TOMMASI, Directeur de Recherche, CNRS, Université de Montpellier

Examiner

Invited

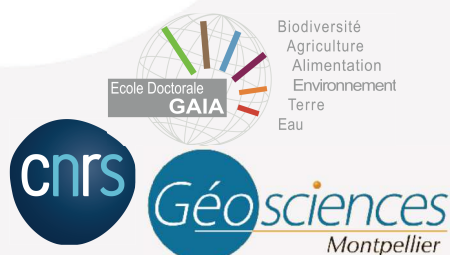
Reviewer

Reviewer

Examiner (President)

Co-supervisor

Supervisor



UNIVERSITÉ
DE MONTPELLIER



THÈSE POUR OBTENIR LE GRADE DE DOCTEUR DE L'UNIVERSITÉ DE MONTPELLIER

En Sciences de la Terre

École doctorale GAIA

Unité de recherche Géosciences Montpellier – UMR 5243

Localisation de la déformation intraplaque due à l'anisotropie visqueuse de l'olivine dans le manteau lithosphérique

Présentée par **Lucan MAMERI**

Le 28 février 2020

Sous la direction de **Andréa TOMMASI**
et **Javier SIGNORELLI**

Devant le jury composé de

Dr. Fanny GAREL, Maître de Conférences, Université de Montpellier

Dr. Riad HASSANI, Professeur, Université Côte d'Azur

Dr. Olivier CASTELNAU, Directeur de Recherche, CNRS, ENS Arts et Métiers

Dr. Boris KAUS, Full Professor, JG University Mainz

Dr. Anne Davaille, Directeur de Recherche, CNRS, Université Paris-Sud

Dr. Javier SIGNORELLI, Professor, CONICET, Universidade Nacional de Rosario

Dr. Andréa TOMMASI, Directeur de Recherche, CNRS, Université de Montpellier

Examinatrice

Invité

Rapporteur

Rapporteur

Examinatrice (Président)

Co-encadrant

Directrice



UNIVERSITÉ
DE MONTPELLIER



We must have perseverance and above all confidence in ourselves. We must believe that we are gifted for something and that this thing must be attained.

Marie Skłodowska-Curie

Aos meus Pais, Avós, e Sobrinhos

ACKNOWLEDGEMENTS

First, all my thanks to my mother, Giovana, for all the love and affection. Thanks my father, Lêlê (Nilzileno), for supporting me to chase my dreams.

Gratitude to my grandmother, Linda. I was able to overcome the 'logistic' problems and follow my scientific career because of her help.

A big thanks to my sister, Rebeca, and to her adorable kids, João and Bernardo. These little guys motivate me to keep fighting for a better tomorrow, and bring me hope.

I am grateful that Sonia became part of my story in the last 3 years. Without her, things would be so difficult.

A massive big-up to Andréa, Javier & Riad, for guiding me along the rigorous path of science and providing the foundations for my quantitative thinking in geoscience. Thanks for all discussions, corrections and advices.

Andréa THANKS for this PhD opportunity, for believing I could go through it, and also for bringing me closer to home with the great Brazilian dinners.

Merci for the colleagues from the *Manteau et Interfaces* Group, Catherine, Sylvie, José, Françoise, Emilien, Marco, for the diverse discussions and for pushing me to keep doing my best. Notably Alain, for the friendly insightful discussions.

I would also like to *thank* Alida and Manuel for the hours we have accumulated chatting after work, enjoying life outdoors. Huge thanks also for my mate Luiz Pereira. The time spent with you guys has renewed my energies to keep the work flowing.

Obrigado to Professor Del'Rey, who introduced me to structural geology when I was a 2nd year undergraduate student at the *Universidade de Brasília*, Brazil. You are a continuous source of inspiration.

My gratitude to Hélène, Anne, Bernadette, Sylvie, Renaud for saving me of all that boring (sorry..) administration tasks.

And finally, I would like to thank the jury of the present thesis for accepting to evaluate my thesis research and to exchange ideas. I'm glad you're part of this cycle that it's coming to an end...

ABSTRACT

The generation of earth-like plates implies efficient strain localization in the lithosphere for long times-spans. In this thesis, I quantified the contribution of viscous anisotropy due to crystal preferred orientations (CPO) of olivine in the lithospheric mantle on strain localization at the plate-scale. First, I performed numerical experiments using polycrystal plasticity models (e.g., VPSC) to evaluate the magnitude and controlling parameters of olivine-induced viscous anisotropy at the rock-scale and compared their predictions to experimental data to validate the model results. Then, a parameterization based on these models has been developed and implemented in a 3D finite-element geodynamical code to study structural reactivation and deformation regime associated with fossil lithospheric shear zones. The aim is to investigate the role of intrinsic (olivine CPO) viscous anisotropy on the development old lithospheric shear zones and its possible relation with the onset of linear seismicity in intraplate settings.

The results show that activation of 2nd mechanisms at the rock scale greatly contributes to reducing the magnitude of viscous anisotropy in mantle rocks, resulting in maximum contrast of <6 in stress (for a constant strain rate). Imposed boundary conditions regulate the CPO-induced viscous anisotropy at both rock- and plate scale, mainly due to the 3D (out-of-plane) strain and stress components that develops. The presence of olivine CPO in the lithospheric mantle lead to strong directional dependence of the strain localization within the mantle shear zone, which, if well oriented to be reactivated, induces strain localization in the entire lithosphere. Deformation regime in the crust follows the one in the mantle. The mechanical feedbacks between both rheological layers, which are affect by the isotropic (composition) and anisotropic (CPO) parts, greatly affect strain localization in continental plates.

RÉSUMÉ ÉTENDU (en Français)

La génération de plaques tectoniques implique une localisation efficace de la déformation dans la lithosphère sur de longues périodes géologiques. Dans cette thèse, j'ai quantifié la contribution de l'anisotropie visqueuse due aux Orientations Préférentielles du Réseau (OPR ou texture) cristallin de l'olivine dans le manteau lithosphérique sur la déformation continentale à l'échelle de la plaque. Tout d'abord, j'ai réalisé des expériences numériques en utilisant des modèles de plasticité polycristalline (e.g., ViscoPlastic Self-Consistent – VPSC - models) pour évaluer la magnitude et les paramètres de contrôle de l'anisotropie visqueuse induite par OPR d'olivine, et j'ai comparé les prédictions de modèles aux données expérimentales pour valider les résultats du modèle VPSC. Ensuite, une paramétrisation de l'anisotropie visqueuse a été développée et implémentée dans un code géodynamique 3D à éléments-finis pour étudier la réactivation structurale et le régime de déformation associé aux zones de cisaillement lithosphériques fossiles. L'objectif est d'étudier le rôle de l'anisotropie visqueuse intrinsèque à l'échelle de la roche (i.e., OPR d'olivine) sur le développement des anciennes zones de cisaillement et sa relation avec la sismicité linéaire dans les domaines continentaux intraplaques et la formation de nouvelles limites de plaque.

Les résultats montrent que l'activation de mécanismes secondaires à l'échelle de la roche contribue considérablement à réduire la magnitude de l'anisotropie visqueuse dans les principales roches du manteau, les péridotites, ce qui se traduit par un contraste maximal d'un facteur 6 en contrainte pour un taux de déformation constant (viscosité anisotrope entre cisaillement simple suivi par extension normale). Les conditions aux limites, que dans le cas anisotrope représentent le degré de liberté de la déformation cisailant induite par la texture, régulent l'anisotropie visqueuse à l'échelle de la roche et de la plaque, principalement en raison des développements à composantes 3-D de contrainte et de déformation. La présence d'OPR d'olivine dans le manteau lithosphérique produit une dépendance non négligeable de la localisation de la déformation en fonction du champ de contrainte, qui, s'il est bien orienté, peut produire une localisation de la déformation dans toute la lithosphère. Le régime de déformation dans la croûte suit celui du manteau. Les interactions mécaniques entre ces deux couches rhéologiques, qui sont en fonction des parties isotropes (compositions) et anisotropes (OPRs) de la lithosphère, affectent considérablement la localisation des déformations dans les plaques continentales.

Chapitre 1 - L'introduction générale du sujet d'étude.

Les tectoniques sont constituées de vastes segments relativement rigides séparés par des frontières étroites et mécaniquement faibles (**Kreemer et al., 2003**). Un élément clé des plaques tectoniques est donc cette localisation de la déformation dans des zones de cisaillement qui se déforment à plusieurs ordres de magnitude plus rapide que le milieu externe (**Bercovici et al., 2000, Tackley, 2000**). C'est une caractéristique unique de la dynamique de la Terre. La partie la plus profonde et la plus chaude des plaques - le manteau lithosphérique - est composé de péridotites, une roche riche (>60%) en olivine. Ainsi, les propriétés mécaniques du manteau lithosphérique dépendent fortement des propriétés mécaniques de l'olivine. Une caractéristique remarquable des cristaux d'olivines est leurs fortes anisotropies visqueuses, autrement dit, la variation de la viscosité en fonction de la direction dans laquelle elle est mesurée. Dans des roches (i.e., agrégats de cristaux), l'anisotropie mécanique se produit lorsque les cristaux d'olivines développent une OPR au cours de la déformation plastique (**Nicolas, A., & Christensen, 1987**).

L'anisotropie sismique à grande échelle associée aux structures régionales, constitue également une évidence de texture d'olivine (fossile ou active) dans le manteau lithosphérique (**Vauchez et al., 2012**). L'hypothèse de base dans cette thèse est que l'anisotropie mécanique produite par l'OPR d'olivine fossile dans ces zones mantellique peut conduire à une sismicité linéaire intraplaque ou l'apparition de nouvelles limites de plaques (**Knoll et al., 2009, Tommasi et al., 2009**). Ici, je m'intéresse aux effets de l'anisotropie mécanique produite par la fabrique d'olivine sur la déformation des domaines continentaux intraplaques. Quelle est l'amplitude et les paramètres déterminants de l'anisotropie mécanique induite par l'OPR à l'échelle de la roche? Et à l'échelle de la plaque? L'anisotropie mécanique de l'olivine dans le manteau lithosphérique peut-elle localiser la déformation dans la croûte et modifier la déformation dans l'ensemble de la lithosphère? Quel est le rôle de l'OPR d'olivine sur l'héritage structural de la lithosphère? La présence de l'OPR fossile dans le manteau lithosphérique explique-t-elle la sismicité linéaire associée à d'anciennes zones de cisaillement mantelliques intraplaques? Quelles sont les différences fondamentales en anisotropie visqueuse associée à des zones de cisaillement mantellique avec des OPR formées dans des cinématiques passées distinctes? Ce sont là quelques questions clés qui seront abordées dans cette thèse.

Chapitre 2 – Les concepts fondamentaux.

Ce chapitre résume brièvement les connaissances actuelles en matière d'anisotropie visqueuse des cristaux d'olivines, des polycristaux et ses

effets sur la déformation des plaques tectoniques. Des concepts de base comme la mécanique du continu et la théorie de la plasticité polycristalline, qui sont fondamentaux pour comprendre la recherche présentée dans cette thèse, sont aussi revisités de façon brève. Je termine le chapitre en rappelant, chronologiquement, les expériences numériques qui ont exploré l'effet de l'anisotropie mécanique dans le contexte de la déformation du manteau lithosphérique ou géodynamique.

Chapitre 3 - Prédiction de l'anisotropie visqueuse des polycristaux d'olivines.

Ce chapitre fait partie d'un article publié dans la revue *Physics of the Earth and Planetary Interiors (PEPI)*. Dans le cadre de cette thèse, les implications de l'anisotropie visqueuse induite par l'OPR sur la déformation intraplaque sont étudiées en utilisant une approche de paramétrage basé sur les prédictions des simulations viscoplastiques auto-cohérentes (VPSC). Pour ce faire, il est nécessaire de tester d'abord si le modèle VPSC peut simuler correctement l'anisotropie visqueuse mesurée lors de la déformation des agrégats d'olivines en laboratoire, puis d'évaluer la magnitude possible de l'anisotropie produite par l'olivine OPR dans les péridotites en condition du manteau lithosphérique, et aussi les paramètres de contrôle à cette échelle (i.e., roche). Ces questions sont abordées dans ce chapitre.

Les polycristaux d'olivines déformés expérimentalement en torsion puis en tension normale au plan de cisaillement précédent ont des contraintes de tension en facteur <2 supérieures à celles de la torsion (**Hansen et al., 2012**). Ici, nous comparons aux données expérimentales les réponses viscoplastiques des polycristaux d'olivines prédites par les approches *Tangent* et *Second-Order* du modèle viscoplastique auto cohérent du VPSC, et aussi par les modèles basés sur l'équilibre des contraintes (*Lower Bound*). Ces modèles de plasticité polycristalline, dans lesquels seul le glissement de dislocation est considéré comme prenant en compte la déformation, reproduisent qualitativement l'anisotropie viscoplastique observée en laboratoire, mais surestiment son intensité pour les roches à forte texture. Le modèle *Lower Bound* se rapproche davantage des résultats de laboratoire, ce qui suggère que l'écart entre les expériences de laboratoire et numériques provient des modèles imposant la compatibilité des déformations dans les polycristaux d'olivines qui ne peuvent se déformer que par fluage de dislocation.

Les données expérimentales sont tout de même bien reproduites par le modèle VPSC *Second-Order* modifié pour permettre la contribution des mécanismes de déformation isotrope supplémentaires. Ces résultats

corroborent le fait que d'autres processus, en plus du glissement de dislocation, contribuent de manière significative à la déformation viscoplastique dans des conditions de laboratoire, réduisant ainsi la magnitude de l'anisotropie mécanique mesurée. Dans la nature, des tailles de grains plus grossières des péridotites entraînent probablement une activité réduite de ces processus de déformations supplémentaires. Nous proposons donc que les modèles VPSC *Second-Order*, standards et modifiés pour accommoder déformation isotrope, fournissent une bonne prédiction de la gamme possible de l'anisotropie viscoplastique induite par la texture d'olivine dans les domaines du manteau lithosphérique.

J'ai aussi comparé la prédiction VPSC avec les expériences de laboratoire de **Hansen et al. (2016)**, qui consistaient en un cisaillement orienté normalement à l'extension précédente qui a formé l'OPR d'olivine. Cela consiste à appliquer une cinématique de déformation opposée à celle des expériences rapportées dans la section précédente (de **Hansen et al., 2012**), ce qui résulte à des textures et des géométries de charge considérablement différentes par rapport à l'OPR. En accord avec les résultats précédents, les modèles VPSC *Second-Order* sous-estiment l'anisotropie visqueuse des agrégats d'olivines qui ont une faible OPR. Cependant, ces résultats ne peuvent être expliqués en utilisant la même philosophie de modélisation que celle de **Mameri et al. (2019)**, dans laquelle la plus faible anisotropie mécanique mesurée en laboratoire était expliquée en termes d'activation d'un processus de déformation isotrope en plus du fluage de dislocation dû à la taille des grains réduite des échantillons de laboratoire.

Pour compléter l'étude sur les paramètres de contrôle de l'anisotropie visqueuse induite par les OPR d'olivine à l'échelle de la roche, des simulations VPSC ont été effectuées pour différentes OPR, les plus communes sont à haute température, dominées par le glissement [100]. Elles ont été créées numériquement sous différentes déformations finies (i.e., intensité de texture) et différents régimes de déformation (i.e., symétrie d'OPR). Les résultats montrent que de fortes variations de magnitude d'anisotropie sont prédites en fonction de l'intensité de l'OPR, alors qu'une variation relativement faible est prédite pour différentes symétries (orthorhombique, axial-[100] et -[010]) mais avec l'intensité équivalente. Le *pattern* de l'anisotropie par rapport à la géométrie de la charge dépend de la sollicitation mécanique (cisaillement simple, extension...). Ce *pattern* peut être modifié par les conditions aux limites imposées. Par conséquent, en dehors de l'activation des processus de

déformations secondaires, l'anisotropie visqueuse induite par l'OPR dans les polycristaux d'olivines se déformant à haute température est contrôlée - au premier ordre - par l'intensité de l'OPR, les conditions aux limites imposées et la symétrie de l'OPR.

Chapitre 4 - Paramétrage de l'anisotropie visqueuse prédite par VPSC et son implémentation dans le code géodynamique ADELI3D.

Ce chapitre fait partie d'un article soumis au *Journal of Theoretical, Computational and Applied Mechanics (JTCAM)*. Nous décrivons le formalisme mathématique et l'implémentation d'une paramétrisation efficace de l'anisotropie visqueuse des matériaux orthorhombiques produits par des OPR qui peuvent être intégrées dans des codes de géodynamique ou des sciences des matériaux. Ici, l'approche a été appliquée pour caractériser l'anisotropie visqueuse du principal constituant du manteau lithosphérique de la terre, l'olivine. Le paramétrage est basé sur le critère de plasticité anisotrope de **Hill (1948)**. Les coefficients qui décrivent le tenseur anisotrope du matériel sont calibrés en se basant sur des tests numériques effectués à l'aide du modèle VPSC. La paramétrisation a été implémentée dans un code éléments finis thermo-mécanique 3D développé pour modéliser les écoulements géodynamiques, combinant des comportements élastiques, visqueux isotropiques et anisotropiques non-linéaires. L'implémentation a été validée par comparaison avec les résultats de la solution analytique et du modèle VPSC pour le cisaillement simple et la compression axiale d'un matériau anisotrope homogène. Une application permettant d'examiner l'effet de l'anisotropie visqueuse induite par l'OPR sur la réactivation des zones de cisaillement du manteau intraplaque met en évidence des couplages mécaniques entre la localisation de la déformation contrôlée par les variations d'orientation et d'intensité d'OPR d'olivine dans le manteau lithosphérique et le comportement mécanique de la croûte élasto-visco-plastique sus-jacente. Le temps de calcul n'augmente que d'un facteur 2-3 par rapport à la rhéologie viscoélastique isotrope classique de Maxwell.

Chapitre 5 - Modélisation de l'anisotropie visqueuse dans les zones de décrochement fossilisées de la lithosphère.

Ce chapitre fait partie d'un article publié dans *Geophysical Journal International (GJI)*. Nous proposons que la localisation de la déformation à l'intérieur des plaques tectoniques, telles que les ceintures linéaires de sismicité à l'intérieur des continents, peut résulter de variations spatiales de l'anisotropie visqueuse produite par la texture d'olivine héritée des épisodes de déformation antérieurs du manteau lithosphérique. Pour quantifier cet effet, nous modélisons

la déformation d'une plaque constituée d'une zone de cisaillement fossile dans le manteau à différentes orientations par rapport à un raccourcissement imposé, mais sans hétérogénéité initiale dans la croûte. La zone de cisaillement fossile est caractérisée par une orientation et une intensité différente de l'OPR d'olivine par rapport au manteau environnant, qui est isotrope dans la plupart des simulations.

L'anisotropie de la viscosité produite par l'OPR, qui reste fixe tout au long des simulations, est décrite par la fonction d'anisotrope de Hill paramétrée sur la base de modèles viscoplastiques auto-cohérents (VPSC). Les résultats indiquent que les variations latérales de l'OPR, ainsi de l'anisotropie visqueuse, dans le manteau lithosphérique affectent la distribution de la déformation dans l'ensemble de la lithosphère, i.e., croûte et manteau. La réactivation de la zone de cisaillement fossile du manteau et la localisation de la déformation dans la croûte au-dessus de celui-ci se produisent pour une compression horizontale à 35-55° par rapport à la zone de cisaillement verticale du manteau, avec un maximum à 45°. La localisation de la déformation dépend (i) du contraste de l'anisotropie visqueuse et, par conséquent, de l'orientation et de l'intensité de la CPO dans les domaines du manteau lithosphérique, (ii) des conditions aux limites, i.e. comment la plaque accommode la déformation 3D (hors du plan) induite par la texture d'olivine, et (iii) des *feedbacks* entre la déformation ductile du manteau et de la croûte. Pour une intense OPR d'olivine, lorsque les conditions aux limites n'entravent pas le cisaillement parallèle à la zone de cisaillement du manteau, les taux de déformation à l'intérieur de celle-ci sont jusqu'à un facteur 30 plus élevé que dans un manteau adjacent isotrope, ou jusqu'à un facteur 200 plus élevés lorsque le manteau adjacent est aussi anisotrope. Ce qui se traduit par des taux de déformation jusqu'à un facteur 10 ou jusqu'à facteur un100 plus élevés dans la croûte au-dessus de la zone de cisaillement fossile, respectivement.

L'affaiblissement par réduction de la friction dans les failles de la croûte augmente la localisation de la déformation dans toute la colonne lithosphérique. Les contrastes de contraintes élevés entre le manteau lithosphérique et la croûte ductile entraînent un couplage moins efficace, avec une localisation forte dans le manteau et la croûte inférieure, mais faible dans la croûte supérieure fragile. La diminution du contraste de contrainte entre le manteau et la croûte améliore le couplage mécanique plus efficace et produit une distribution plus homogène de la déformation en fonction de la profondeur, ainsi qu'une évolution de la localisation de la déformation en fonction du temps. La comparaison des

données sur l'anisotropie sismique, les contraintes régionales et les mécanismes focaux dans des zones de cisaillement intraplaque, comme New Madrid - USA et Armoricaire - France, avec les prévisions de nos modèles corroborent le fait que l'OPR d'olivine préservée dans les zones de cisaillement lithosphérique fossile pourrait être la clé du développement de telles structures.

Chapitre 6 - Comparaison de l'anisotropie visqueuse induite par la OPR d'olivine dans les zones de cisaillement lithosphériques fossiles avec des différentes cinématiques passées.

L'analyse de la déformation des massifs de péridotites ainsi que les données géophysiques suggèrent la présence de zones de cisaillement décrochantes et en extension (ou en compression) dans le manteau lithosphérique (revue dans **Vaucher et al., 2012**). Dans ce chapitre, j'ai effectué des simulations de plasticité viscoplastique (SO-VPSC) et d'éléments finis-3D thermomécanique (ADELI-anis) pour caractériser les différences fondamentales de la réactivation structurale anisotrope produites par l'OPR qui se développe dans ces zones de cisaillement mantelliques. J'ai comparé leurs réponses mécaniques pour différentes orientations du *strike* et *dip* du plan de cisaillement fossile par rapport à la déformation appliquée, en utilisant des conditions aux limites et OPR équivalents. L'objectif est d'établir les caractéristiques du premier ordre de la localisation et du régime de déformation induite par l'anisotropie d'olivine dans des zones de cisaillement lithosphérique décrochantes et extensives (ou compressives).

Des différences significatives peuvent apparaître dans le comportement mécanique des zones de cisaillement du manteau lithosphérique anisotrope en fonction de l'orientation et direction du plan de cisaillement fossile par rapport à la nouvelle déformation imposée. Les zones de cisaillement fossiles formées en extension horizontale ont le potentiel de localiser la nouvelle déformation imposée dans une plus vaste gamme d'orientation de sollicitation mécanique par rapport aux zones de cisaillement mantellique de type *strike-slip*; cependant, pour le cas plus faible (c'est-à-dire à 45°), la localisation de la déformation dans ces dernières est plus efficace. La localisation de la déformation dans la zone de cisaillement fossile est plus efficace lorsque la nouvelle déformation est en extension, car dans ce cas, les forces gravitationnelles s'ajoutent aux forces tectoniques. Si les *strike* et *dip* d'une zone de cisaillement fossile s'écartent de la géométrie de charge optimale, il est peu probable que la localisation de la déformation se produise. La réactivation d'une zone de cisaillement en extension est moins sensible à l'angle d'inclinaison du plan de cisaillement fossile. La relation d'orientation entre zone de cisaillement fossile (et ainsi OPR

d'olivine) et la déformation imposée affecte le degré d'épaississement (ou d'amincissement) de la lithosphère pendant une nouvelle compression (ou extension) imposée. La présence d'une zone de cisaillement fossile dans le manteau lithosphérique à pendage modéré et une linéation d'étirement parallèle à la concentration maximale d'axes [100] (et ainsi de la direction d'extension ou compression) pourrait favoriser un épaississement (ou amincissement). Ces résultats sont encore l'objet d'une enquête plus approfondie.

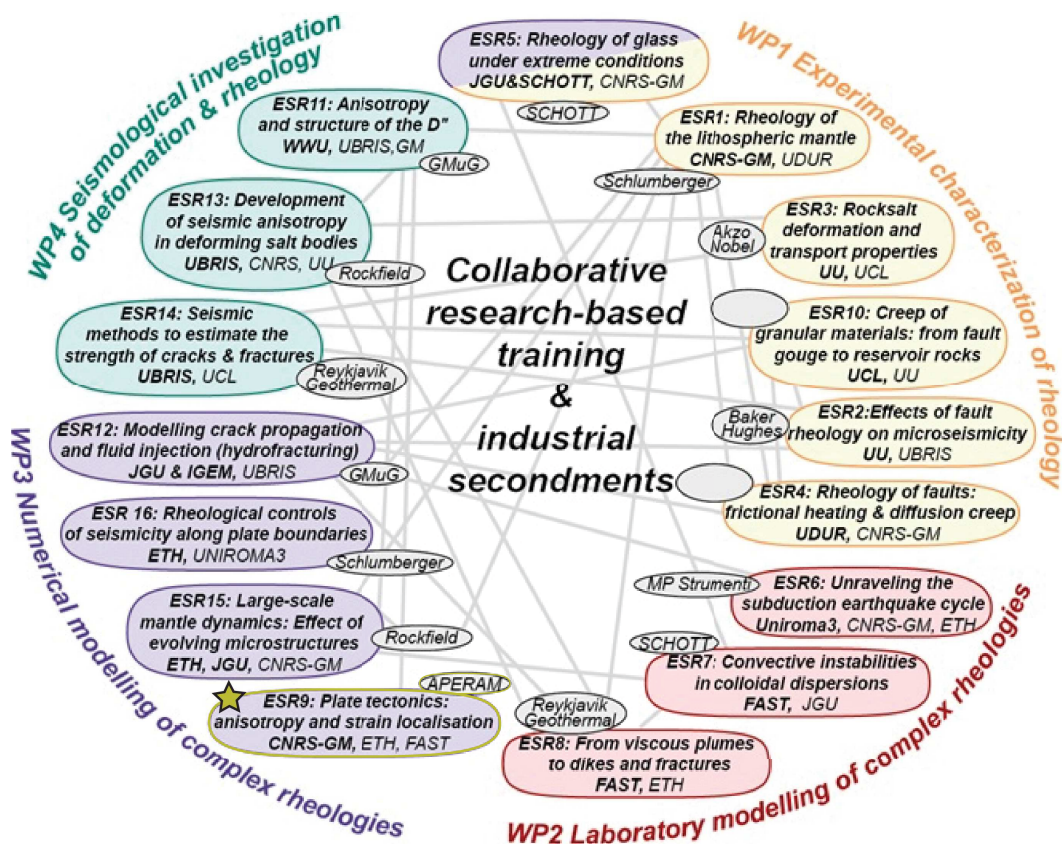
Ces prédictions peuvent apporter une lumière sur les rares évidences de réactivation structurale des zones de cisaillement du manteau par chevauchement (**Bastow et al., 2007**) par rapport aux évidences relativement nombreuses de réactivation des zones de cisaillement décrochantes (**Vauchez et al., 1998, 2003, Tommasi et Vauchez, 2001, Storti et al., 2003**). De plus, des variations dans les relations d'orientation pourraient expliquer, en partie, la distribution spatiale discontinue des zones de cisaillement réactivées, même si les données d'anisotropie sismique semblent indiquer la continuité de la fabrique du manteau pour de longues distances. Dans l'est des États-Unis et au Canada, par exemple, la sismicité linéaire s'est répartie dans une série de zones de cisaillement relativement discrètes (<100 km), malgré la présence à grande échelle (>500 km) d'OPR d'olivine fossile cohérente et continue dans toute la région. Les prévisions présentées dans ce chapitre peuvent également contribuer à la réflexion sur l'effet de la fabrique d'olivine sur le taux d'exhumation de roches du manteau dans des failles lithosphérique.

Chapitre 7 - Conclusions, limitations et perspectives futures.

Dans ce chapitre, les résultats de mes recherches et quelques questions ouvertes sont mises en évidence. Les limites de l'étude sont présentées, et les perspectives d'avenir pour le sujet sont discutées. L'objectif est de contextualiser les découvertes de cette thèse doctorale et de proposer des lignes de recherche dans l'étude de l'anisotropie viscoplastique dans les roches et de ses conséquences pour la déformation à grande échelle (géodynamique). Cette recherche a des implications sur (i) le contraste maximal du taux de déformation induit par l'anisotropie visqueuse de l'olivine, (ii) les facteurs de contrôle de l'anisotropie et de la localisation de la déformation, (iii) ainsi que sur l'importance de l'olivine fossilisée dans le manteau pour la mémoire structurale des plaques tectoniques et (iv) sur la réactivation structurale des zones de cisaillement du manteau, comme par exemple la sismicité linéaire intraplaque.

THESIS CONTEXT

This thesis is part of the European project *Complex Rheologies in Earth and industrial Processes (CREEP)*. The CREEP is a platform for career development of young scientists funded by the Innovative Training Network (ITN) EU-H2020 Marie Skłodowska-Curie actions. The network focuses on rheology of geological and industrial materials by means of numerical and laboratory experiments. The research in the present thesis was design to investigate intrinsic anisotropy of olivine at the rock- and plate-scale numerically, as part of the workpackage ‘Numerical modelling of complex rheologies’.



Workpackages and the respective research projects comprising the CREEP network. The yellow star indicates the subject of the PhD research presented in this thesis.

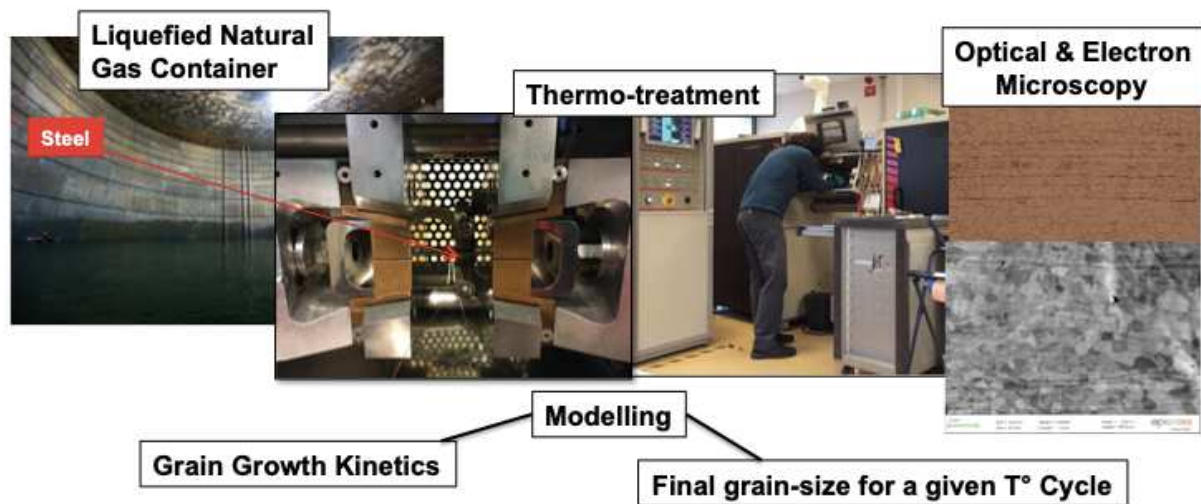


Horizon 2020 - Marie Skłodowska-Curie Actions
 Innovative Training Network (ITN)
 Complex Rheologies in Earth dynamics and industrial Processes

The CREEP project received funding from the European Union's Horizon 2020 research and innovation program under the Marie Skłodowska-Curie grant agreement No. 642029.

In the scope of this thesis project, I had enrolled in an industrial internship in collaboration with APERAM-Isbergues, France, in collaboration with Dr-Eng. Francis Chassagne and Dr-Eng. Jessica Delacroix , in order to work on recrystallization of a given steel manufactured for Liquefied Natural Gas Container (LNGC).

A internal scientific-technical document was produced on the matter, *Modelling grain growth in Imm-thick cooled rolled NM20*, which reports thermal treatment in a metal alloy used in the LNGC. The goal was to parameterize the kinetics of grain growth using the acquired experimental data and applies this data in a grain growth model. The approach allowed obtaining a predicted grain size of the alloy for given thermal cycle imposed during the manufacturing processes. This research subject was not directly related to the topic of thesis, and therefore the study will not be included in present thesis.



I acknowledged here the importance of this internship for my scientific growing during my thesis. By doing more than 60 experiments (for the first time in a systematic manner), I came across the ‘human’ aspect of the laboratory-experimental work. After this project in APERAM, I became more enthusiastic and confident to follow a post-doc position on experimental rock-deformation.



TABLE OF CONTENTS

ACKNOWLEDGEMENTS	7
ABSTRACT	9
RÉSUMÉ ÉTENDU (EN FRANÇAIS)	11
THESIS CONTEXT	19
CHAPTER I	25
1 INTRODUCTION	26
1.1 WHY STUDY OLIVINE VISCOUS ANISOTROPY IN THE LITHOSPHERIC MANTLE?	26
1.2 HOW OLIVINE MECHANICAL ANISOTROPY IS STUDY IN THIS THESIS?	30
1.3 OBJECTIVES AND WORK HYPOTHESIS	31
1.4 ORGANISATION OF THE THESIS	32
CHAPTER II	35
2 INTRODUCTION	36
2.1 OLIVINE MECHANICAL ANISOTROPY: FROM CRYSTAL TO PLATE	36
2.1.1 ANISOTROPIC RHEOLOGY OF THE SINGLE CRYSTAL	36
2.1.2 ANISOTROPIC RHEOLOGY OF THE POLYCRYSTAL	38
2.1.3 ANISOTROPY IN THE LITHOSPHERIC MANTLE	40
2.2 MODELLING FUNDAMENTALS	41
2.2.1 CONTINUUM MECHANICS BASICS	41
2.2.2 RHEOLOGY AND FLOW LAWS	47
2.3 MODELLING OLIVINE POLYCRYSTALLINE PLASTICITY	52
2.4 VISCOUS ANISOTROPY IN GEODYNAMICS	55
CHAPTER III	67
3 MODELLING CPO-INDUCED VISCOPLASTIC ANISOTROPY IN OLIVINE-RICH ROCKS	68
3.1 <i>ARTICLE #1</i>	68
3.1.1 INTRODUCTION	70
3.1.2 METHODS	71
3.1.3 RESULTS	75
3.1.4 DISCUSSION	82
3.1.5 CONCLUSIONS	84
3.1.6 SUPPLEMENTARY MATERIAL OF THE ARTICLE #1	89
3.2 COMPARISON BETWEEN NUMERICAL AND EXPERIMENTAL DATA	97
3.2.1 INTRODUCTION	97
3.2.2 METHODS	97
3.2.3 RESULTS	98
3.2.4 DISCUSSIONS	100
3.3 VISCOPLASTIC ANISOTROPY OF COMMON OLIVINE CPOS	102
3.3.1 METHOD	102
3.3.2 RESULTS	103
3.3.3 DISCUSSION AND CONCLUSIONS	106

CHAPTER IV **111**

4 PARAMETERIZATION OF CPO-INDUCED VISCOUS ANISOTROPY WITH APPLICATION FOR MODELLING LITHOSPHERIC DEFORMATION **112**

4.1	GENERAL INTRODUCTION	112
4.2	ARTICLE #2	112
4.2.1	INTRODUCTION	113
4.2.2	PARAMETERIZING TEXTURE-INDUCED VISCOUS ANISOTROPY	115
4.2.2.1	THERMO-MECHANICAL CODE	115
4.2.2.2	MAXWELL VISCOELASTICITY	116
4.2.2.3	HILL (1948) ORTHOTROPIC YIELD CRITERION	117
4.2.2.4	NUMERICAL INTEGRATION	118
4.2.2.5	VALIDATION OF THE IMPLEMENTED HILL-BASED PARAMETERIZATION	120
4.2.3	DETERMINING THE HILL COEFFICIENTS USING THE VPSC MODEL	122
4.2.3.1	POLYCRYSTAL EQUIPOTENCIAL SURFACE	124
4.2.3.2	MODEL VALIDATION	129
4.2.4	APPLICATION: OLIVINE VISCOUS ANISOTROPY IN MANTLE SHEAR ZONES	131
4.2.5	COMPUTATIONAL COST	133
4.2.6	CONCLUSION	134
4.3	SUPPLEMENTARY VALIDATION	136

CHAPTER V **143**

5 STRAIN LOCALIZATION IN INTRAPLATE LITHOSPHERIC STRIKE-SLIP SHEAR ZONES DUE TO CPO-INDUCED VISCOUS ANISOTROPY IN THE MANTLE **144**

5.1	GENERAL INTRODUCTION (ARTICLE #3)	144
5.2.1	INTRODUCTION	145
5.2.2	NUMERICAL MODELLING	147
5.2.3	GEODYNAMICAL MODEL SETUP	151
	GEOMETRY AND BOUNDARY CONDITIONS	151
	MATERIAL BEHAVIOUR AND OLIVINE CPO	153
5.3	RESULTS	154
5.3.1	IMPACT OF THE MANTLE SHEAR ZONE ORIENTATION AND CPO INTENSITY	154
5.3.2	INFLUENCE OF IMPOSING DIFFERENT LATERAL BOUNDARY CONDITIONS	157
5.3.3	ANISOTROPY VERSUS ISOTROPIC VISCOUS WEAKENING	159
5.3.4	INTERACTIONS BETWEEN STRAIN LOCALIZATION IN THE MANTLE AND CRUST	163
5.3.5	MECHANICAL COUPLING BETWEEN THE DUCTILE CRUST AND UPPER MANTLE	165
5.4	DISCUSSION	169
5.5	CONCLUSIONS	175
	ACKNOWLEDGMENTS	177
5.6	SUPPLEMENTARY MATERIAL OF THE ARTICLE #3	177
5.6	APPENDIX MATERIAL OF THE CHAPTER	180

CHAPTER VI	193
<hr/>	
6 COMPARING CPO-INDUCED VISCOUS ANISOTROPY IN FOSSIL LITHOSPHERIC SHEAR ZONES WITH DIFFERENT PAST KINEMATICS	194
<hr/>	
6.1 INTRODUCTION	194
6.2 GEODYNAMICAL MODEL SETUP	195
6.3 RESULTS	196
6.4 DISCUSSION AND CONCLUSIONS	204
CHAPTER VII	209
<hr/>	
7 CONCLUSIONS, LIMITATIONS OF THE STUDY, AND FUTURE PERSPECTIVES	210
<hr/>	
7.1. OVERALL CONCLUSIONS	210
7.1.1 CONCLUSIONS 1: MAXIMUM STRAIN-RATE CONTRAST INDUCED BY OLIVINE VISCOUS ANISOTROPY	210
7.1.2 CONCLUSIONS 2: MAIN FACTORS MODERATING OLIVINE VISCOUS ANISOTROPY AND THE RESULTING STRAIN LOCALIZATION	210
7.1.3 CONCLUSIONS 3: STRUCTURAL REACTIVATION DUE TO OLIVINE VISCOUS ANISOTROPY IN MANTLE SHEAR ZONES	212
7.1.4 CONCLUSIONS 4: STRUCTURAL MEMORY OF PLATE TECTONICS: THE IMPORTANCE OF OLIVINE VISCOUS ANISOTROPY FOSSILIZED IN THE MANTLE	212
7.2 MAIN LIMITATIONS	214
7.3 SOME OPEN QUESTIONS AND FUTURE DIRECTIONS	215
ABSTRACT	222
<hr/>	

CHAPTER I

GENERAL INTRODUCTION

*The mind seemed to grow
giddy by looking so far into
the abyss of time.*

Sir James Hall

1 Introduction

1.1 Why study olivine viscous anisotropy in the lithospheric mantle?

Tectonic plates are the uppermost expression of mantle convection (Coltice et al., 2017). They consist of large and relatively rigid segments separated by narrow and weak boundaries (Kreemer et al. 2003). A key element of earth-like plates therefore is the localization of the deformation in rapid creeping shear zones (Bercovici et al. 2000, Tackley, 2000) (Figure 1.1). This is a unique feature of Earth dynamics. Despite this, why and how the strain is localized in otherwise stable continental plates remains enigmatic. The deepest and hottest part of the plates - the lithospheric mantle - is composed of peridotites, an olivine rich-rock. Thus, the mechanical properties of the lithospheric mantle depend on the mechanical properties of olivine.

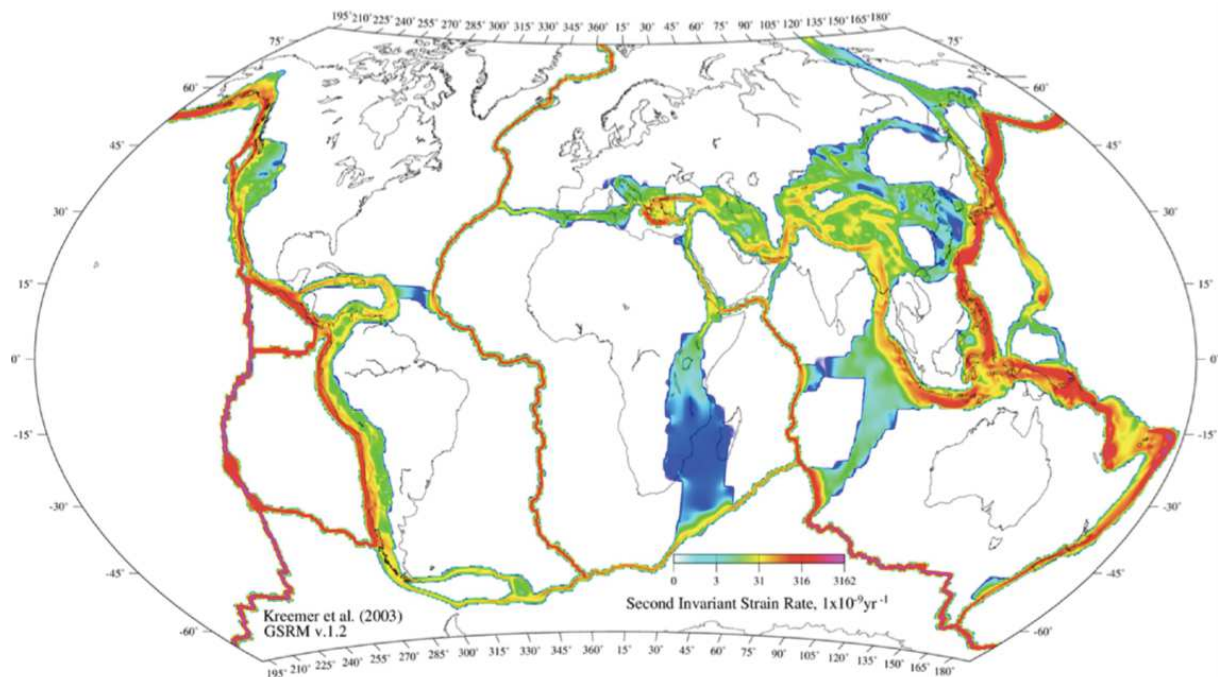


Figure 1.1: Global strain rate map derived mainly from geodetic data. Rigid plates in white separated by coloured rapid deforming boundaries (adapted from Kreemer et al., 2003).

A remarkable feature of olivine crystals is its high anisotropy of viscous properties, that is, the variation of the viscosity as a function of direction in which it is measured, in this chapter called mechanical anisotropy. Heterogeneity of mechanical (anisotropic) properties is a major property of the lithosphere controlling plates-scale strain localization (review in Tommasi et al., 2015). The basic principals of mechanical anisotropy can be easily

understood by considering a box containing two springs with different elastic constant (i.e. strength), coupled to a central mobile ring that can move under an external force F and thus deform both springs (**Figure 1.2.** based on lecture by **A. Tommasi**). Two outcomes can be outlined from this *thought experiment*: (1) the magnitude of the force required to equally displace the ring varies depending on the direction of the applied force; (2) to apply an oblique displacement relative to the axis connecting the springs, the force has to be applied in a different direction from the target obliquity. These effects scale with the relative strength of the springs, which might change if the springs setup change, for instance, if the spring 1 lies perpendicular to the spring 2.

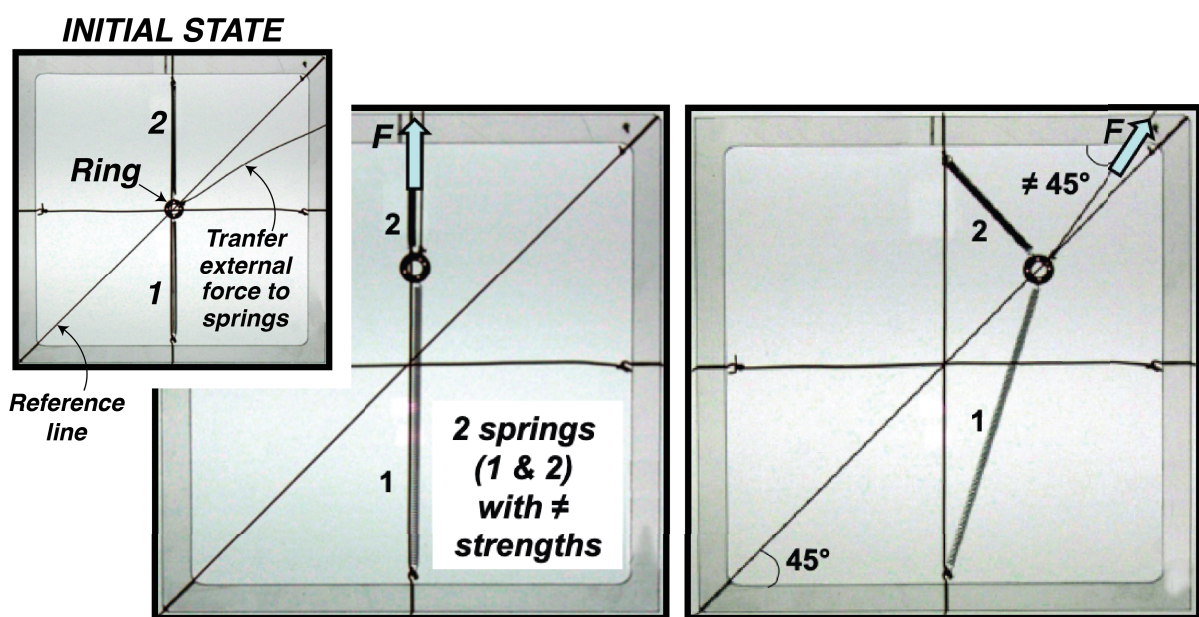


Figure 1.2: Thought experiment: concept of mechanical (elastic) anisotropy illustrated with springs (1 and 2) with different strengths. **(Left)** In order to impose the same amount of displacement, the force F applied in the direction of the spring 2 is different from F in the direction of the spring 1. **(Right)** To displace the ring at 45° to the horizontal direction F must be applied at an angle different of 45° .

In mantle rocks (as in others polycrystals), mechanical anisotropy might occur when preferred orientation olivine crystals (CPO) are developed during plastic deformation (Nicolas, A., & Christensen, 1987, Hansen et al., 2012). The anisotropy at this scale depend primarily on the CPO symmetry and intensity (Knoll et al., 2009), which may vary as a function of dominant slip system (relative strength and number), finite strain, and the interplay between diffusion and dislocation creep to accommodate strain in the polycrystal.

At larger-scale, an important constraint for sustaining the plate-tectonic mode of mantle convection is that it requires lithospheric softening mechanisms that may act over

relatively long periods of time. A good candidate therefore is the fossil mantle fabric in continents. Once olivine CPO is formed, it might be modified by subsequent deformation events but not destroyed, as indicated by laboratory (Boneh et al., 2015) and natural observations (Falus et al., 2011 Michibayashi, & Mainprice, 2004). This is corroborated by the widespread coherent seismic anisotropy far from active plate boundaries (**Figure 1.3**), which is interpreted in most of the cases as froze-in past mantle deformation (**Mainprice et al., 2007**). Thus, large-scale lateral variations in fossilised olivine CPO in the lithospheric mantle might contribute to the long-term strain localization required for maintaining global tectonics.

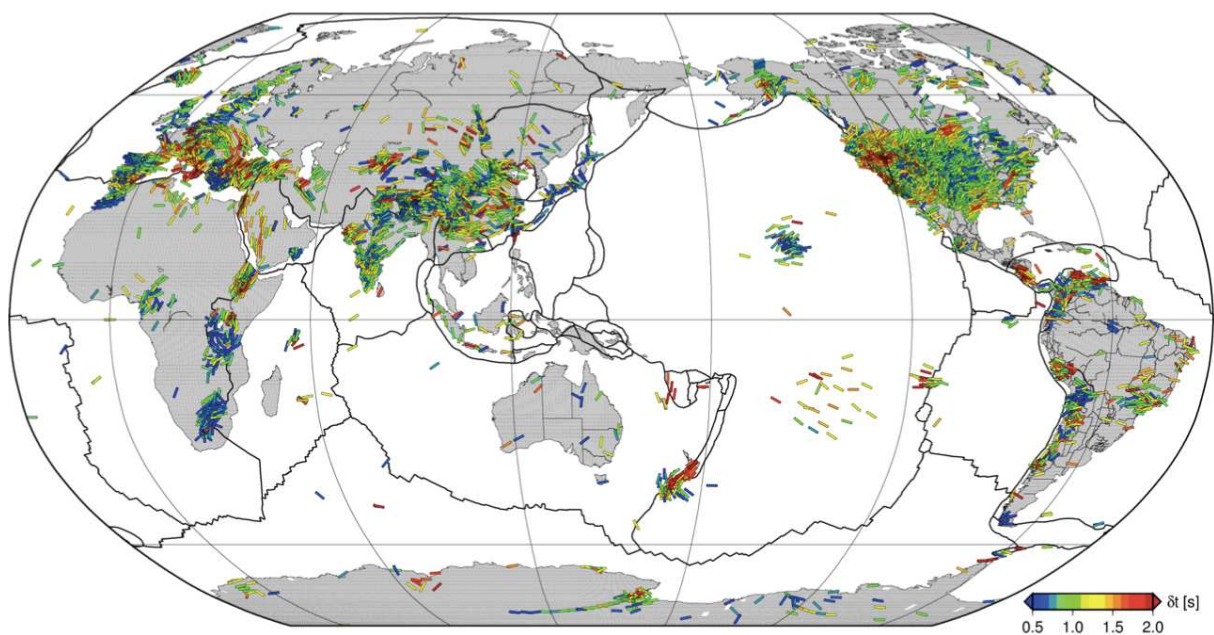


Figure 1.3: Seismic anisotropy database available online at <http://www.gm.univ-montp2.fr/splitting/DB/>. SKS splitting waves map with most of the delay time ≥ 1 s. The splitting is interpreted as mainly controlled by olivine anisotropy in the mantle (**Mainprice, 2007**) (source: <http://www-udc.ig.utexas.edu/external/becker/sksdata>).

Coherent seismic anisotropy associated with large-scale deformed regions comprise complementary evidence, together for instance with Moho offsets imaged by seismic reflectors (**Wittlinger et al. 2004**), for the presence of deep shear zones down to lithospheric mantle (**Vaucher et al., 1997, 1998, 2005**). Mechanical anisotropy produced by fossil olivine CPO in these mantle shear zones may result in linear seismicity in otherwise stable continents or, in the onset of new plate boundaries subparallel to old mantle fabric (**Knoll et al., 2009, Tommasi et al., 2009**), as corroborated by the remarkable correlation between mantle and crustal deformation in old fault systems worldwide (**Figure 1.4**).

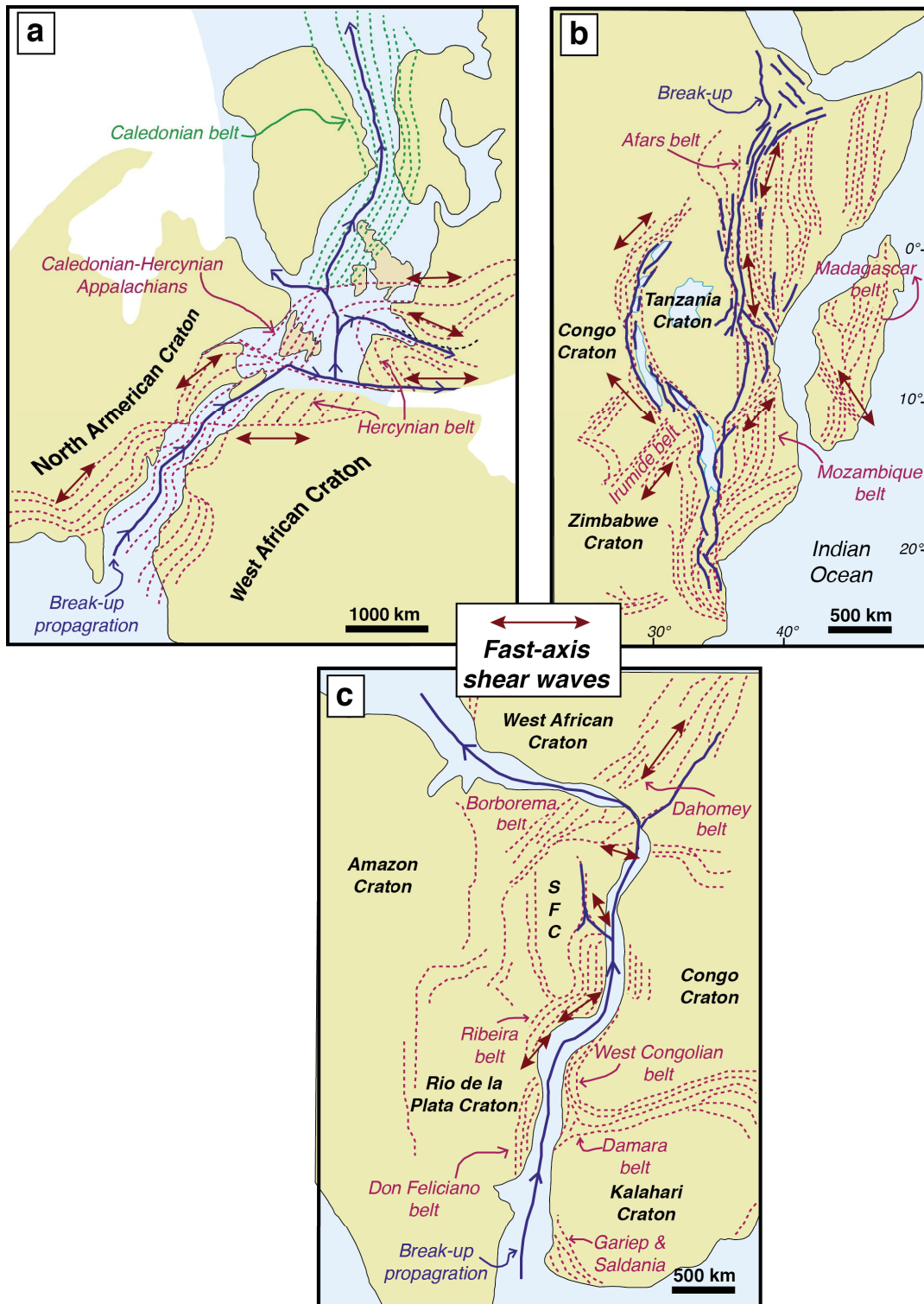


Figure 1.4: a) Reconstruction of the opening of the Central and North Atlantic oceans (adapted from **Tommasi and Vauchez, 2015**). b) Ongoing break-up of Eastern African Rift (adapted from **Vauchez et al., 2005**). c) Reconstruction of the opening of the South Atlantic Ocean (adapted from **Tommasi and Vauchez, 2001**). SFC stands for San Francisco Craton. The red two-sided arrows show the fast-axis direction of shear waves from the SKS splitting database (source: <http://splitting.gm.univ-montp2.fr/DB/>), which commonly follows the trend of reactivated lithospheric shear zones.

In this thesis, I am interested in the effects of mechanical anisotropy produced by the fossilized olivine fabric on deformation far from active plate boundaries (i.e. intraplate domains).

Some of the key questions that will be addressed are:

- Which is the magnitude and governing parameters of CPO-induced mechanical anisotropy at the rock- and plate scale?
- Can olivine mechanical anisotropy in the mantle localize deformation in the crust, and modify the deformation pattern in the entire lithosphere?
- What is the role of olivine CPO on the long-lived structural memory of the lithospheric mantle?
- Does the presence of fossilized olivine CPO explain the onset of linear seismicity associated with old, intraplate strike-slip mantle shear zones?
- What are the fundamental differences in CPO-induced structural reactivation of fossil mantle shear zones formed in distinct past kinematics?

1.2 How olivine mechanical anisotropy is studied in this thesis?

Modelling the effects of mechanical anisotropy in the deformation of the lithosphere is a multiscale problem (**Figure 1.5**). The approach requires quantifying the possible range of CPO-induced mechanical anisotropy in olivine-rich rocks, and its controlling parameters relying on experiments on single crystal (**Bai et al., 1991; Durham & Goetze, 1977**). The feedback between dislocation creep and other deformation processes needs to be accounted to modulate the CPO (symmetry and intensity), and consequently, of the resulting mechanical anisotropy. This was examined by performing viscoplastic self-consistent (VPSC) simulations modified to account for isotropic processes (**Detrez et al. 2015**). The approach is presented in the chapter 3.

In order to explore the effect of the presence of olivine CPO fossilized in the lithospheric mantle and the associated crust response, as well as their mechanical interactions, the resulting mechanical anisotropy needs to be implemented in a geodynamical model. This is fundamentally a three-dimensional problem, since the full viscosity tensor of olivine might induce non-parallelism between the principal stress and strain components, which can be challenging in terms of computational cost. In this thesis, we aimed to isolate the effect of olivine CPO on intraplate deformation, therefore, we do not explicitly account for the effects of grain size reduction or transient thermal states, but our models

predictions can be used to make inferences on the role of these processes for long-term strain localization.

The novelty of this thesis is that the large-scale problem was tackled by describing the mechanical anisotropy of olivine CPO through parameterized equations (Hill, 1948), calibrated based on second-order VPSC simulations (Lebensohn et al., 2011), which has the advantage of accounting for the response of olivine polycrystals relying on rigorous physical bases and at relatively fast computation time.

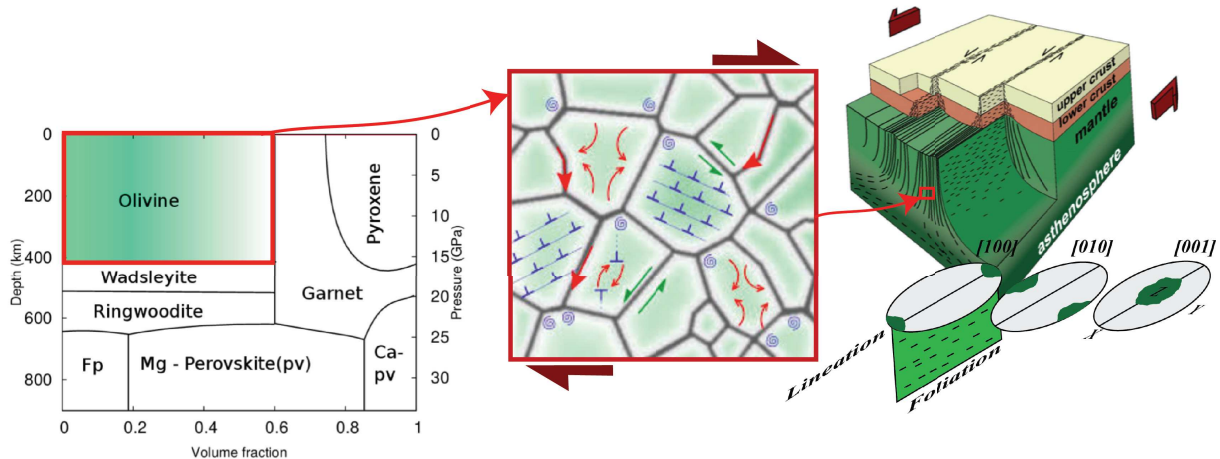


Figure 1.5: The approach consists of accounting for (1) the intrinsic mechanical anisotropy of olivine crystal in polycrystals plasticity models in order to calculate the CPO-induced mechanical anisotropy at the rock-scale, while considering implicitly the effect of intra- and intercrystalline mechanism to rock bulk viscosity (2). The resulting mechanical behavior is parameterized in a geodynamic model to study the effects on (3) lithospheric shear zones

1.3 Objectives and work hypothesis

The aim of this thesis is threefold: better understanding of CPO-induced mechanical anisotropy in olivine-rich rocks (1), and of its consequences for the mechanical behavior of textured lithospheric shear zones in continental tectonic environments (2); the development of a physics-based (3) parameterized description of mechanical anisotropy derived from viscoplastic self-consistent (VPSC) models, which can be incorporated into geodynamical and material science codes.

The central hypothesis of the thesis:

- ✓ Fossilized crystallographic preferred orientation of olivine in the lithospheric mantle, formed during past tectonic events, controls the location, orientation, and style of strain localization in intraplate settings.

For the first time this hypothesis is tested by performing 3D geodynamical numerical experiments that take into account the feedbacks between CPO-induced mechanical anisotropy anisotropic in the mantle and the resulting deformation in the crust.

1.4 Organisation of the thesis

The present thesis is divided in seven chapters. **Chapter One** comprise the present introduction. **Chapter Two** summarize the current knowledge on olivine-produce mechanical anisotropy, from the crystal to the plate, and some fundaments concepts on continuous mechanics. **Chapter Three** present a comparison of polycrystal plasticity models against laboratory experiments and also a non-published comparisons and a parametric study using VPSC simulations. Part of this study is presented in the form an article, published in the journal *Physics of the Earth and Planetary Interiors*. **Chapter Four** details the methods used to parameterize the CPO-induced viscous anisotropy together with the validation of the numerical routines implemented in the geodynamical finite-element model. Part of this chapter was submitted to the *Journal of Theoretical, Computational and Applied Mechanics*. I co-authored the work. **Chapter Five** investigates the implications of CPO-induced mechanical anisotropy in fossilized strike-slip mantle shear zones for strain localization and patterns in the lithosphere. This work is accepted - *in press* - in the journal *Geophysical Journal International*. Some non-published materials (Appendix figures) are also presented. **Chapter Six** report the anisotropic response of mantle shear zones with different past kinematics (fossil extensional and strike-slip CPOs) to a new extensional or compression deformation event at different orientaion of strike and dip of the fossil shear zone. The results are part of an manuscript being further improved to be submitted to a scientific journal. **Chapter Seven** summarize the main conclusions and limitations of the models, discuss some open questions and give some future perspectives.

REFERENCES

Bai, Q., Mackwell, S.L., Kohlstedt D.L., 1991, High-temperature creep of olivine single crystals.1. Mechanical results for buffered samples, *Journal of Geophysical Research*, 96, 2441-2463.

Bercovici, D., Ricard, Y., & Richards, M. A. (2000). The relation between mantle dynamics

and plate tectonics: A primer. Geophysical Monograph-American Geophysical Union, 121, 5-46.

Coltice, N., G erault, M., & Ulvrova, M. (2017). A mantle convection perspective on global tectonics. *Earth-science reviews*, 165, 120-150.

Detrez, F., O. Castelnau, P. Cordier, S. Merkel, and P. Raterron (2015), Effective viscoplastic behavior of polycrystalline aggregates lacking four independent slip systems inferred from homogenization methods. application to olivine, *J. Mech. Phys. Solids*, 83, 199–220, doi:10.1016/j.jmps.2015.05.022

Durham, W.B., Goetze, C., 1977, Plastic flow of single crystals of olivine 1. Mechanical data, *Journal of Geophysical Research*, 82, 5737 - 5753.

Hansen, L. N., Zimmerman, M. E., & Kohlstedt, D. L. (2012). Laboratory measurements of the viscous anisotropy of olivine aggregates. *Nature*, 492(7429), 415.

Hassani, R., 1994. Mod elisation num erique de la d eformation des syst emes g eologiques, Ph.D thesis, Universit e de Montpellier II, Montpellier, p. 130

Kreemer, C., Holt, W. E., & Haines, A. J. (2003). An integrated global model of present-day plate motions and plate boundary deformation. *Geophysical Journal International*, 154(1), 8-34.

Lebensohn, R.A., Ponte Casta neda, P., Brenner, R., Castelnau, O., 2011. Full-field vs. homogenization methods to predict microstructure-property relations for poly-crystalline materials. In: *Computational Methods for Microstructure-Property Relationships*. Springer, New York, pp. 393–441.

Michibayashi, K., & Mainprice, D. (2004). The role of pre-existing mechanical anisotropy on shear zone development within oceanic mantle lithosphere: an example from the Oman ophiolite. *Journal of Petrology*, 45(2), 405-414.

Nicolas, A., & Christensen, N. I. (1987). Formation of anisotropy in upper mantle peridotites. A review. *Composition, structure and dynamics of the lithosphere-asthenosphere system*, 16, 111-123.

Tackley, P. J. (2000). The quest for self-consistent generation of plate tectonics in mantle convection models. *Geophysical Monograph-American Geophysical Union*, 121, 47-72.

Tommasi, A., & Vauchez, A. (2015). Heterogeneity and anisotropy in the lithospheric mantle. *Tectonophysics*, 661, 11-37.

Wittlinger, G., Vergne, J., Tapponnier, P., Farra, V., Poupinet, G., Jiang, M., ... & Paul, A. (2004). Teleseismic imaging of subducting lithosphere and Moho offsets beneath western Tibet. *Earth and Planetary Science Letters*, 221(1-4), 117-130

W ustefeld, A. and Bokelmann, G. H. R. and Barruol, G. and Montagner, J. P.: Identifying global seismic anisotropy patterns by correlating shear-wave splitting and surface-wave data, *Phys. Earth Planet. Int.*, 176, 198-212, 2009.

CHAPTER II

AN (BRIEF) OVERVIEW OF OLIVINE VISCOUS ANISOTROPY

*If I look at me from a distance, I'm a dot.
If I look at me up too close, I'm but a blur.
If I look at me from within, I'm chaos in order.
If I look within from the outside, I'm order in chaos.
If I just stop looking, I'm who I want to be.
A fluid.*

Unknown author

2 Introduction

This chapter briefly summarize the current knowledge in the matter of viscoplastic anisotropic of olivine crystals, polycrystals and of tectonic plates. Basic concepts of continuum mechanics and polycrystal plasticity theory that are fundamental to understand the present thesis research is revisited. I finish by recalling, chronologically, numerical experiments that explored the effect of mechanical anisotropy in the context of geodynamics.

2.1 Olivine mechanical anisotropy: from crystal to plate

2.1.1 Anisotropic rheology of the single crystal

Plastic deformation of olivine, and consequently its mechanical anisotropy, depends primarily on the crystallo-chemistry of the crystal. Most of naturally occurring olivine crystals comprise a complete solid solution between an Mg-rich end-member, called Fosterite (Mg_2SiO_4), and a Fe-rich end-member, called Fayalite (Fe_2SiO_4). The olivine structure is part of the family of the nesosilicates, meaning that the tetrahedrons sites of anions $[\text{SiO}_4]^{4-}$ are not directly connected to each other. Instead; they are linked to to interstitial divalent cations (Mg^{2+} and Fe^{2+}) placed in two distinct octahedral sites (M1 and M2, respectively, in **Figure 2.1**). The strength of the bond Si-O is significantly higher than the (Mg, Fr)-O bond due to the covalent nature of the first and the ionic nature of the former (**Bragg and Brown, 1926. Deer et al. 1997**)

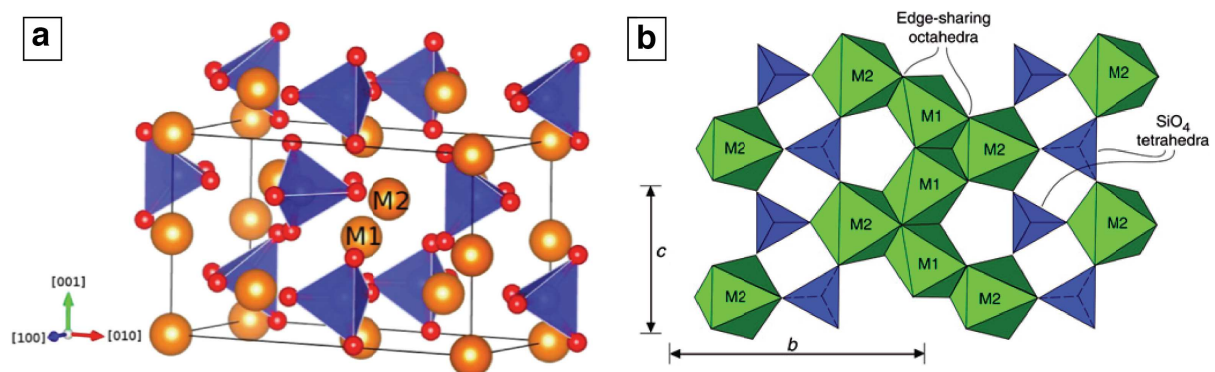


Figure 2.1: a) Structure of olivine crystal showing the M1 and M2 sites relative to the silicon tetrahedron in blue. b) Representative elementary arrangement of olivine octahedral and tetrahedral sites.

. The crystal structure however is not perfectly arranged. Point and line lattice defects work together to allow the crystal to deform plastically. Point defects allow transport of matter, while motion of dislocations, a crucial line defect, promotes coherent slip of lattice domains in specific directions. Dislocations are characterized by a direction of dislocation line and a Burgers vector, which describes the magnitude and direction of slip. Slip occurs after reaching a critical stress on planes containing the highest density of atoms. Hence, intracrystalline plasticity is primarily dependent on the spatial arrangement of the crystal lattice.

Olivine crystal crystallizes in the orthorhombic symmetry with a hexagonal close-packed (**hcp**) array of oxygen ions (**Birle et al., 1968**). This results in a lack of slip plane and directions (i.e. slip systems) available to ensure arbitrary plastic strain (**Von Mises, 1928**). Olivine deformation is restricted to $[100]$ and $[001]$ directions only (**Poirier, 1975**), which have profound consequences for the anisotropy of physical properties of olivine crystals (and of aggregates and tectonic plates).

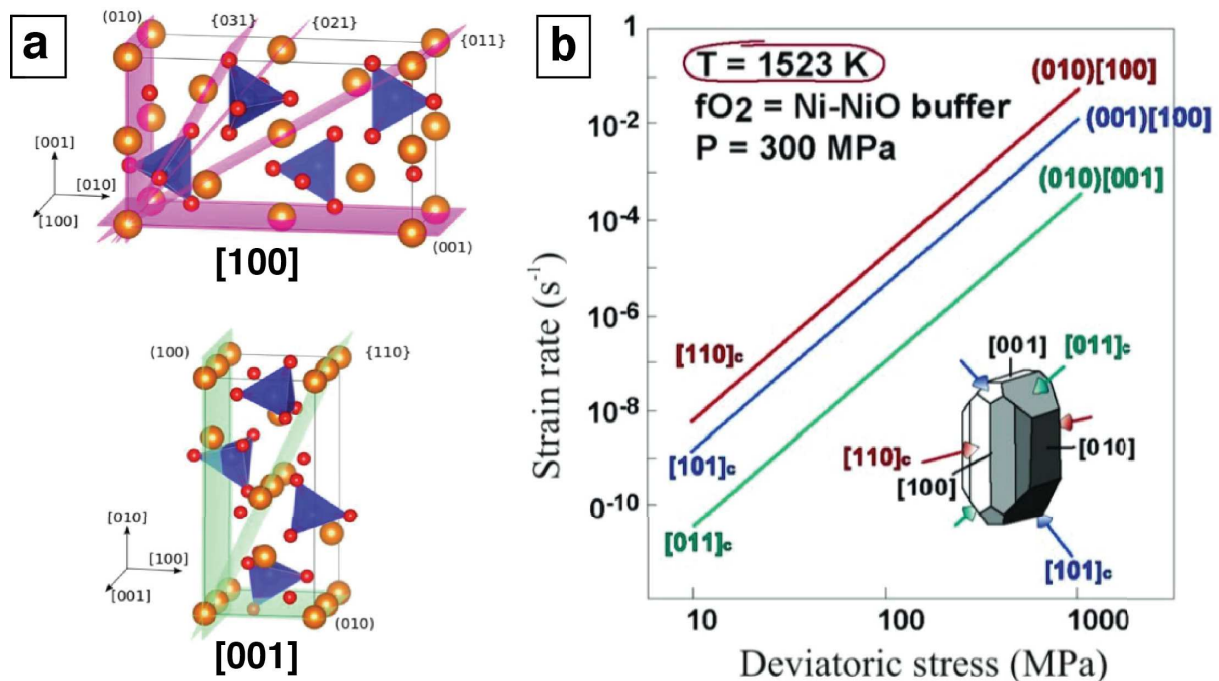


Figure 2.2: **a)** Common slip systems available for plastic deformation of olivine. $[100]$ and $[001]$ -axes in **a** are two dominant slip directions in olivine. **b)** Laboratory deformation indicates that at high temperature and moderate pressure the main activated slip systems are $(010)[100]$, $(001)[100]$ and $(010)[001]$. At these experimental conditions, slip on the $[100]$ of olivine might be a factor of 100 times faster than in the $[001]$ direction.

The work by **Durham and Goetze, (1977)** and **Bai et al. 1991** showed olivine might display >100 times contrast in strain rate depending on the direction of the applied stress (**Figure 2.2 and 2.3**). **Durham and Goetze, (1977)** showed indeed that the dominant slip planes vary as function of temperature and differential stress, which may shift from dominant glide [100] at high temperature and low stresses to dominant glide [001] when temperature is low and differential stresses are high.

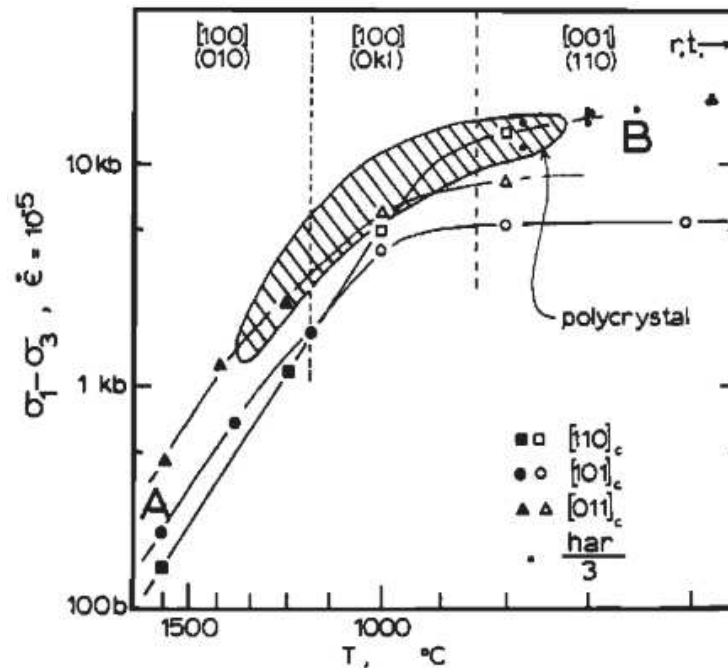


Figure 2.3: Variation of the dominant slip systems as a function of temperature and differential stresses. Glide in olivine is significantly mechanical anisotropic (different strength of slip systems) for the whole range of variable space temperature (**Durham and Goetze, 1977**)

2.1.2 Anisotropic rheology of the polycrystal

During plastic deformation of olivine, grain rotation in only 3 dominant slip systems may produce sharp Crystallographic Preferred Orientations (CPO) (**Carter and Ave'Lallemant, 1970. Chopra and Paterson, 1981**). CPO is characterized by the alignment of the crystal at a stable position relative to the imposed stress; CPO development transfer crystal anisotropy (or a portion of it) to the rock-scale, and larger. Due to the limit number of available slip systems, diffusion- and grain boundary-related deformation mechanism must assist dislocation creep, modifying the olivine CPO, and consequently the anisotropic rheology associated to it.

For instance, it has been argued that the activation of other deformation processes in addition to intracrystalline glide might explain the (1) relative fast steady-state CPO intensity and reorientation during simple shear deformation (**Signorelli and Tommasi, 2015**), (2) the formation of axial-olivine CPOs (**Warren et al., 2008**), and (3) the CPO weakening during static (**Boneh et al., 2017**) and dynamic recrystallization (**Falus et al., 2011**). Moreover, CPO evolves differently depending on the deformation history. Transient CPO symmetries and intensities can be formed as a function of the preexisting CPO and deformation regime (**Boneh and Skemer, 2014. Boneh et al. 2014, 2015**), which further complicates revealing past deformation events.

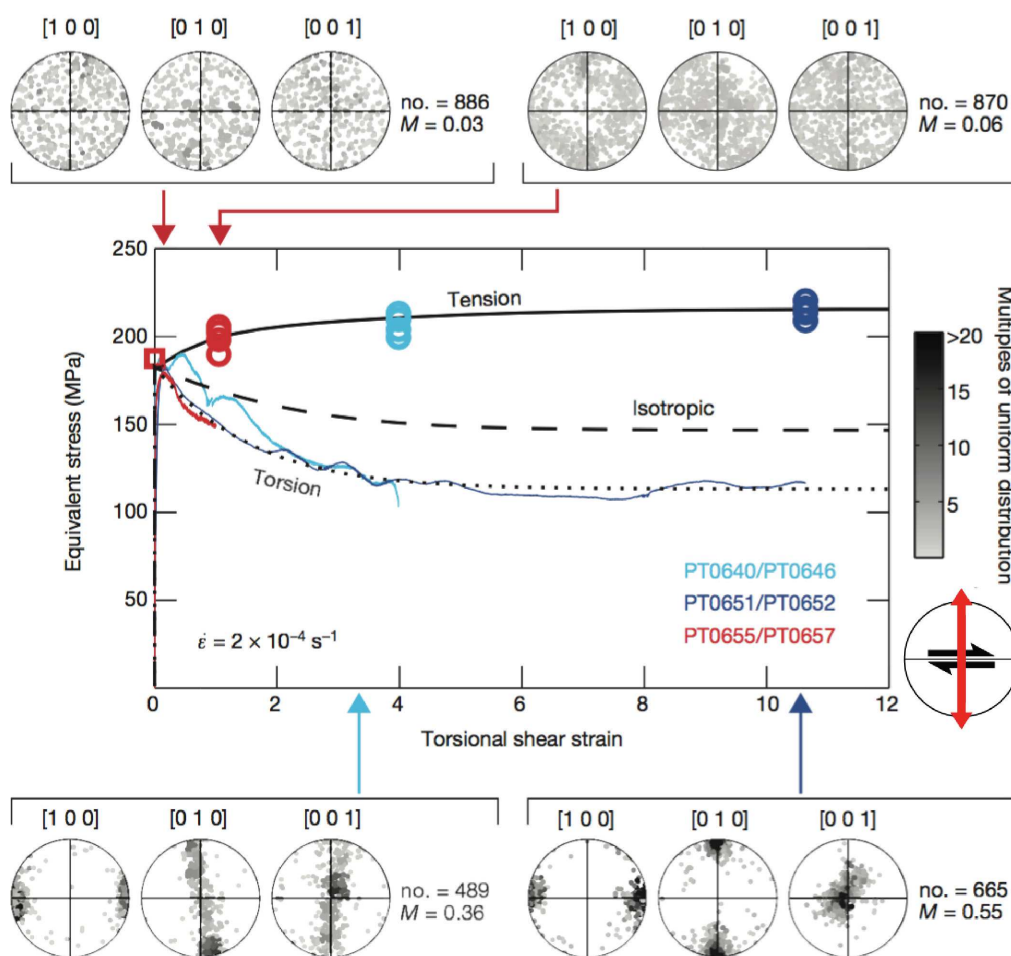


Figure 2.4: Laboratory experiments on mechanical (viscous) anisotropy of olivine aggregates by **Hansen et al. 2012**, which an olivine CPO created in torsion was further deformed in torsion and tensional deformation. The loading-geometry relative to the olivine CPO is shown in the bottom right.

On the basis of laboratory experiments, **Hansen et al., 2012b** showed that torsion parallel to a previous torsional deformation, which formed the initial olivine CPO, display <2

lower equivalent stresses (for a constant strain rate) than tension perpendicular to the shear plane (**Figure 2.4**). At the conditions the experiments were performed (high temperature, moderate pressures and very fine [μm] grain sizes), the plastic deformation was interpreted to be mediated by a combination of dislocation creep and grain boundary-related processes (**Hansen et al., 2012a**). The measured viscous anisotropy in laboratory experiments is influenced by the activation of these additional deformation processes, which reduced the magnitude of the anisotropy in more than a factor of 3 times compared to viscous anisotropy produced only by dislocation creep (**Mameri et al., 2019**, *article presented in chapter 3*).

In another series of laboratory experiments, **Hansen et al., 2016** investigated the viscous anisotropy rising from olivine CPO deformed in axial extension followed by torsion perpendicular to the previous deformation. As in **Hansen et al., 2012a** stresses did not surpass a factor of 2 times (at constant strain-rate) despite the considerably different olivine CPO symmetry, intensity and deformation history. Both sets of experiments will be further explored in a comparison against viscoplastic plasticity models, presented in the chapter that follows (Chapter 3).

2.1.3 Anisotropy in the lithospheric mantle

Olivine is not only viscous but also elastic anisotropic (**Liu et al., 2005**), as evidenced by polarized seismic waves in the upper mantle (**Silver and Chan, 1991. Savage, 1999 Karato et al., 2008. Lev, 2009**). Both present and past mantle deformation can be constrain from the difference in arrival times between the polarized shear waves (δt : *delay time*) and from the azimuth of the fast polarized direction (ϕ), which can be used to estimate the thickness of the anisotropic medium, and the orientation of the anisotropic structure, respectively. The delay time beneath continents is of tern $\geq 1\text{s}$ (**Wüstefeld et al., 2009**), which is commonly interpreted as anisotropy at mantle depth. Delay times $< 0.5\text{s}$ are interpreted as crustal signal (**Silver et al., 1999**).

During plastic deformation of the mantle by shear, the [100] and [010] axes of the olivine CPO align respectively parallel and perpendicular to shear plane. The faster axis of propagation in olivine crystals is the [100] (**Mainprice, et al., 2000**), hence, the CPO, as well as the foliation and lineation directions in the mantle, can be inferred from the anisotropic of seismic waves. This is a central assumption in the present thesis. I use seismic anisotropy measurements to infer the first-order orientation of the mantle fabric associated with lithospheric shear zones (**Figure 2.5**).

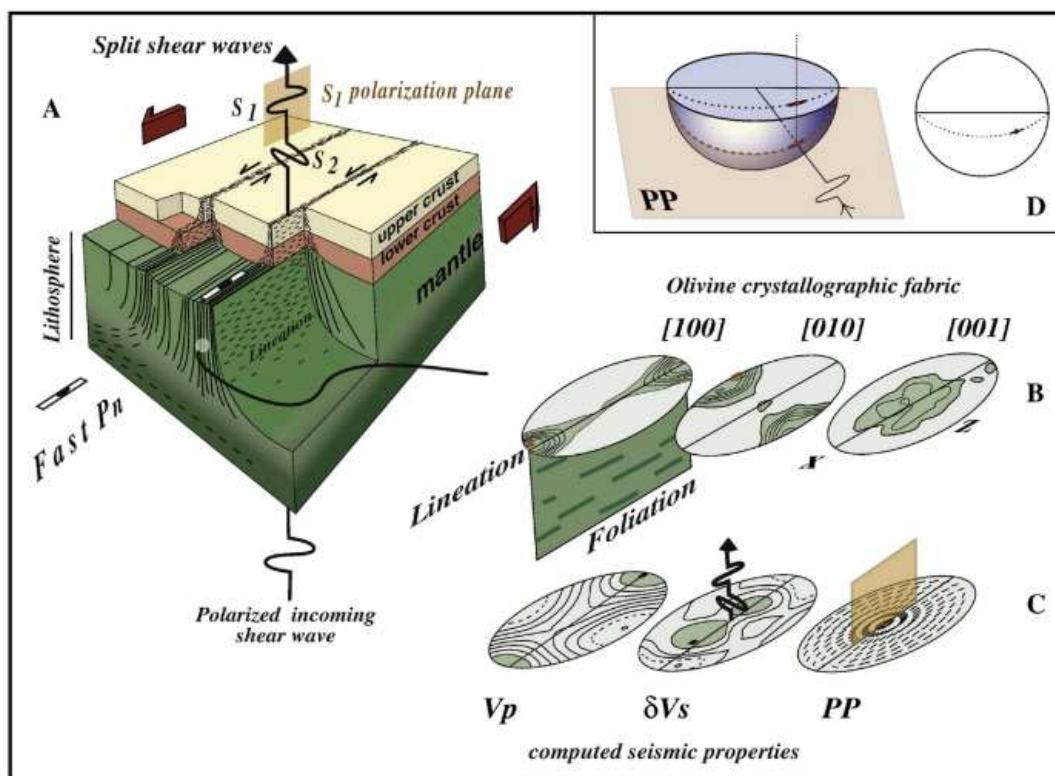


Figure 2.5: Schematic representation shear wave splitting in a strike-slip shear zone (A) and the associated orthorhombic olivine CPO (B). The seismic properties are show in (C). V_p shows the highest P-wave velocity. The δV_s the contrast between fast and slow split S-waves. The PP the orientation of the fast S-wave polarization plane (from **Vauchez et al, 2012**).

Mantle xenoliths and exposed mantle rocks in peridotites massifs suggest that the presence of olivine CPO is common in the lithospheric mantle (**Ismail and Mainprice, 1998**). Therefore, the lithospheric mantle is very unlikely to be mechanical isotropic, as usually take for granted. Large-scale lateral variations in seismic anisotropy patterns corroborate this hypothesis, and further suggest that the anisotropy in the lithosphere mechanical is not homogeneously distributed either (review in **Tommasi and Vauchez, 2015**).

2.2 Modelling fundamentals

2.2.1 Continuum mechanics basics

The following mathematical formalism on continuum mechanics are mainly based on the books *Numerical Geodynamic Modelling* by Gerya, T. (2009), *Geodynamics* by Turcotte and Schubert (1982), and *Introduction to Tectonophysics* by Rey, P. (2018).

Plastic (rock) deformation can be approximated as a continuum process. This means that the material fills completely the space and that the material behavior can be described by continuous equations rather than discrete ones, once the field variables might vary at every space-point the continuous body. Together with scalars quantities, vectors and (higher) tensors quantities are important field variables in continuum/fluid mechanics, and they comprise the ‘keystones’ in quantitative/modelling geo-mechanics. Stress, strain and strain-rate are second-rank tensor, classically defined as:

Stress

Stress can be defined as force per unit area, in which the stress *is* directly proportional to the applied force and inversely proportional to the area in which the force is exerted. Consider an infinitesimal cube inside a body under an applied net force (**Figure 2.6**).

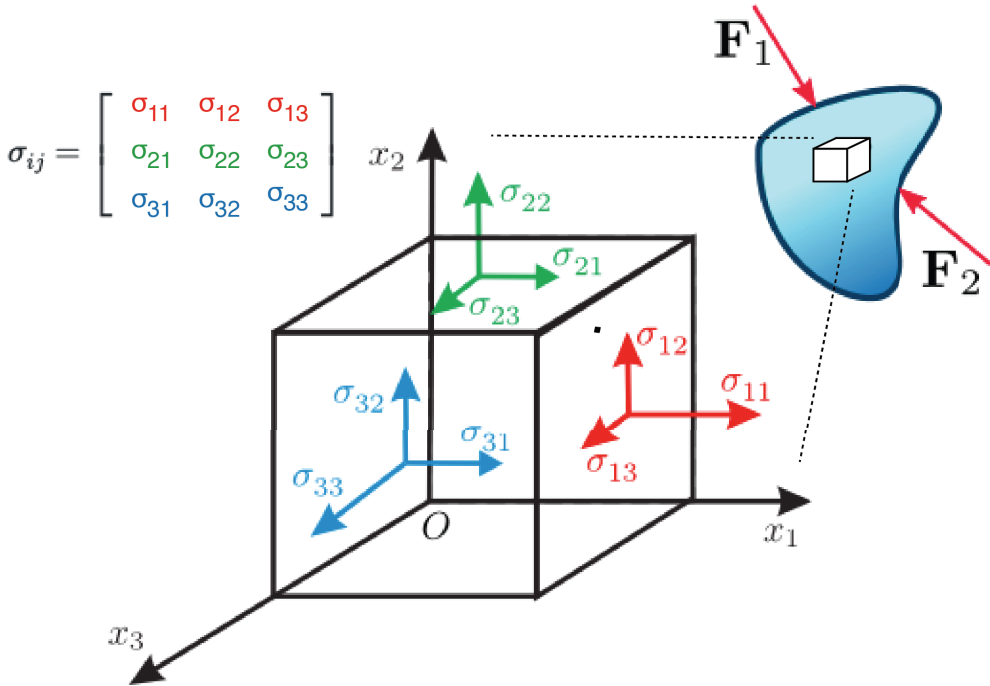


Figure 2.6: Normal and shear stress components of the stress tensor σ_{ij} acting in an infinitesimal cube submitted to external forces.

The force can be decomposed in components acting perpendicular to the surface (normal stress, $\sigma_{11}, \sigma_{22}, \sigma_{33}$) and those components acting parallel to the surface (shear stress. $\sigma_{12}, \sigma_{21}, \sigma_{13}, \sigma_{31}, \sigma_{23}, \sigma_{32}$). In 3D, this can be written in the form of a stress tensor, comprising nine components defined as a 3×3 matrix that characterize the state of stress in a given point. The stress components need to counteract each other to maintain equilibrium force

balance, then $\sigma_{12} = \sigma_{21}, \sigma_{13} = \sigma_{31}$ and $\sigma_{23} = \sigma_{32}$, resulting in six independent stress components.

In rock deformation, we are often interested in the deviation of stresses (i.e. deviatoric stress σ'_{ij}) relative to a mean stress state (i.e. hydrostatic stress P), which can be written as:

$$\sigma'_{ij} = \sigma_{ij} + P\delta_{ij}$$

where δ_{ij} (Kronecker delta) = 1 when $i=j$ and $\delta_{ij} = 0$ when $i \neq j$, i and j are coordinate indices in the 3D space (x, y, z), and P is the hydrostatic pressure as a function of depth (y) and density $\rho(y)$, defined as:

$$P(y) = P_0 + g \int_0^y \rho(y) dy$$

where P_0 is the pressure at the earth surface and g the acceleration of gravity.

The sum of the diagonal deviatoric stresses comprises the first invariant of the stress tensor (i.e. trace of stress tensor). The second invariant of the deviatoric stress tensor give the local stress deviation in the continuous rock relative to the lithostatic stress state, as follow:

$$\sigma_{II} = \sqrt{\frac{1}{2} \sigma'_{ij}{}^2}$$

where i and j indexes stands for summation over the stress components.

Cauchy law of stress tensor

Since the stress tensor is symmetric $\sigma_{ij} = \sigma_{ji}$, given the stress components σ_{ij} and the normal unit vector ($n = n_i e_i$) in an arbitrary plane, the traction (i.e. force) vector ($t^{(n)} = t_i e_i$) acting on that plane can be determined using the Cauchy's law in the form:

$$t_i = \sigma_{ij} n_j$$

where i and j indexes stands for summation over the stress components. The Cauchy's law can be illustrated graphically using a tetrahedron representation, where just the positive stress components are shown (**Figure 2.7**).

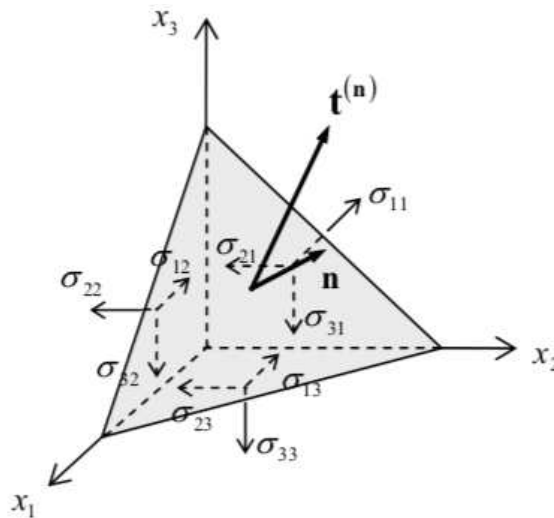


Figure 2.7: Cauchy's tetrahedron. The traction vector acting on a plane can be determined by giving the stresses tensor and the normal to the plane.

Strain

Stress result in deformation. The amount of changing in the distance separating elements in the body during deformation is represented by the dimensionless quantity called *Strain*. Strain describes the deformation of the body by means of relative displacement, which can be perpendicular to the face where stress was applied (normal strain) or parallel to it (shear strain).

Consider a rectangle with initial length L in which an applied deformation change the initial length in a given amount ΔL (**Figure 2.8**). The normal and shear strain can be defined in 1D as ϵ :

$$\epsilon = \frac{\Delta L}{L}$$

In the case the shear strain is expressed as the angular relation between the lines before and after the deformation, strain is defined as:

$$\gamma = \tan\phi$$

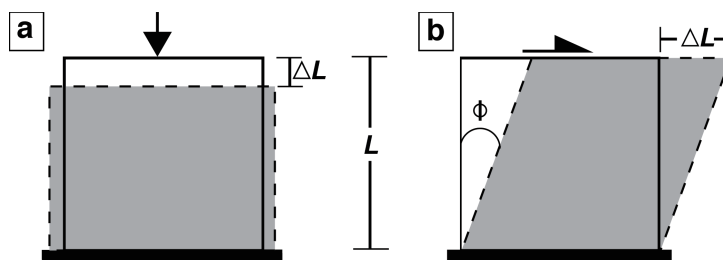


Figure 2.8: Sketch of **a)** axial and **b)** shear strain of a square deformed by ΔL .

Likewise the stress tensor, the strain tensor for incremental deformation is defined in 3D by nine components, comprising three normal strains components ($\epsilon_{xx}, \epsilon_{yy}, \epsilon_{zz}$) and six shear strain components ($\epsilon_{xy}, \epsilon_{yx}, \epsilon_{xz}, \epsilon_{zx}, \epsilon_{yz}, \epsilon_{zy}$). These components are defined in terms of the gradient of displacement field u in the three principal directions x, y and z relative to the original position:

$$\epsilon_{xx} = \frac{\partial u_x}{\partial x}, \quad \epsilon_{yy} = \frac{\partial u_y}{\partial y}, \quad \epsilon_{zz} = \frac{\partial u_z}{\partial z}.$$

$$\epsilon_{xy} = \epsilon_{yx} = \frac{1}{2} \left(\frac{\partial u_x}{\partial y} + \frac{\partial u_y}{\partial x} \right), \quad \epsilon_{xz} = \epsilon_{zx} = \frac{1}{2} \left(\frac{\partial u_x}{\partial z} + \frac{\partial u_z}{\partial x} \right), \quad \epsilon_{yz} = \epsilon_{zy} = \frac{1}{2} \left(\frac{\partial u_z}{\partial y} + \frac{\partial u_y}{\partial z} \right)$$

The strain is calculated by integrating the deformation over the entire deformation history.

Strain rate

The change in displacement field (strain tensor) over time is given by the strain rate tensor ($\dot{\epsilon}$), that is, the rate in change in the distance separating elements in the body. The strain rate tensor is defined in 3D by the nine components of time derivative of the gradients of the velocity field v , also separated on normal ($\dot{\epsilon}_{xx}, \dot{\epsilon}_{yy}, \dot{\epsilon}_{zz}$) and shear components ($\dot{\epsilon}_{xy}, \dot{\epsilon}_{yx}, \dot{\epsilon}_{xz}, \dot{\epsilon}_{zx}, \dot{\epsilon}_{yz}, \dot{\epsilon}_{zy}$):

$$\dot{\epsilon}_{xx} = \frac{\partial v_x}{\partial x}; \quad \dot{\epsilon}_{yy} = \frac{\partial v_y}{\partial y}; \quad \dot{\epsilon}_{zz} = \frac{\partial v_z}{\partial z};$$

$$\dot{\epsilon}_{xy} = \frac{1}{2} \left(\frac{\partial v_x}{\partial y} + \frac{\partial v_y}{\partial x} \right) = \dot{\epsilon}_{yx}; \quad \dot{\epsilon}_{xz} = \frac{1}{2} \left(\frac{\partial v_x}{\partial z} + \frac{\partial v_z}{\partial x} \right) = \dot{\epsilon}_{zx}; \quad \dot{\epsilon}_{yz} = \frac{1}{2} \left(\frac{\partial v_z}{\partial y} + \frac{\partial v_y}{\partial z} \right) = \dot{\epsilon}_{zy}$$

The strain rate is given as inverse of time (s^{-1}), and describes the local change in deformation state at each incremental time, therefore, it is related to an infinitesimal deformation rather than a finite one. Strain rate can be obtained by subtracting the non-diagonal components (i.e. rotation rate) of the velocity gradient v .

The first invariant of strain rate tensor define the isotropic part of this quantity, which represent the rate in change of volume. The second-invariant is the shear strain-rate, given as:

$$\dot{\epsilon}_{II} = \sqrt{\frac{1}{2} \dot{\epsilon}'_{ij}{}^2}$$

where i and j indexes stands for summation over the strain rate components.

Viscosity

The viscosity relates the shear strain-rate ($\frac{\partial v}{\partial x}$) to the applied shear stress (τ), thus it has the dimension (Pa.s). It characterizes the resistance to flow of the body. In the form of the newton's second law ($F = m \frac{\partial v}{\partial t}$), and considering an incompressible and isotropic fluid, it can be written as:

$$\tau = \eta \frac{\partial v}{\partial x}$$

If $\eta = 1$, the relation of shear stress and the rate of shear strain is linear, and the fluid is called Newtonian). The implemented anisotropic viscosity induced by olivine fabric in the present thesis is described by a fourth-rank tensor (η_{ijkl}), and in most of the simulations characterize a non-Newtonian fluid flow ($\eta \neq 1$).

Finite Element Modelling and Lagrangian Framework

The geodynamical code ADELI use a Finite-Element Method (FEM) to discretize the studied domain into nodes in which the numerical solution of partial differential equation can be interpolated over the parameters space. In our approach, we used four-node tetrahedral elements (i.e. 3D mesh), where temperature, velocity and displacement field are calculated in each node. Given the partial derivatives of the velocity and displacement field, the strain, strain rate, and stress tensors, is defined in each finite-element of the tetrahedron.

ADELI use a Lagrangian scheme to solve the continuity equations, which implies in advection of the elements of the mesh with the field variables. A material point is always related to the same (Lagrangian) point independent of time; in this case one might define a 'fluid' reference frame. This formulation can be written mathematically in the form:

$$\frac{D\rho}{Dt} + \rho \operatorname{div}(\vec{v}) = 0$$

where $\frac{D}{Dt}$ is the Lagrangian time derivative, ρ is the local density, \vec{v} is the local velocity and $\text{div}(\vec{v})$ is a scalar function defined in 3D as follows:

$$\text{div}(\vec{v}) = \frac{\partial v_x}{\partial x} + \frac{\partial v_y}{\partial y} + \frac{\partial v_z}{\partial z}$$

This expression characterizes the direction of the material with flow relative to the Lagrangian points, being divergent, convergent or neutral vector or scalar field (**Figure 2.9**). If the flow is diverging (a) there is a net flow out of the volume element, and if it is converging (b) the net flow goes into the volume element.

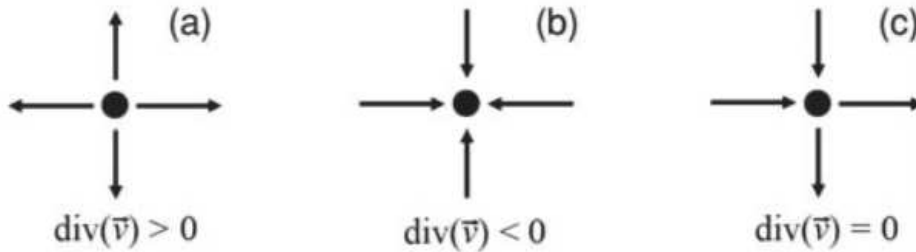


Figure 2.9: Types of divergence field around a point

In the geodynamic code ADELI the fluid is considered incompressible, meaning that the time derivative of density is equal to zero, in other words, the density (i.e. volume) does not change over time. In this case, the divergence of the velocity field is neutral, $\text{div}(\vec{v}) = 0$

2.2.2 Rheology and flow laws

The lithospheric strength in its coldest part is supported predominantly by elastic-brittle strength, whereas in the hotter lower crust and mantle the lithospheric strength is supported mostly by elastic-viscous strength (review in **Burov, 2011**). Thus, a widely accepted model of lithosphere strength profile comprises an upper crust with increasing brittle strength as a function of depth (i.e. pressure) that changes to thermally activated creep at the lower crust and upper mantle (**Figure 2.10a**). The strength profile depends on the details of each tectonic setting, such as thermal structure, rock composition, and fluid-pore pressure. In this thesis the deformation of both the mantle and the crust was modelled, which implies considering visco-elasto-plastic rheologies (**Figure 2.10b**).

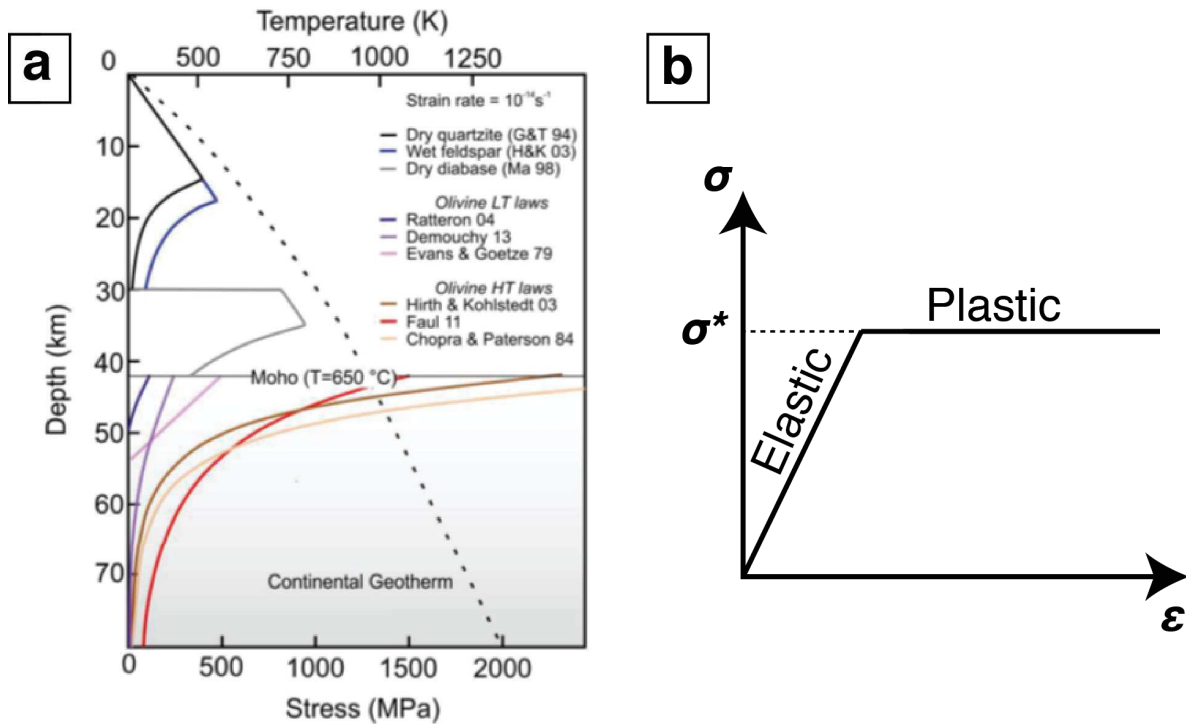


Figure 2.10: **a)** Strength envelope for a lithosphere deforming at constant strain-rate of 10^{-14} s^{-1} . The dashed grey line indicates the continental geotherm, with Moho temperature at 650°C . The solid lines show brittle and viscous strength of crust and mantle. **b)** Sketch of flow curve in the stress and strain space. Below the yield stress (σ^*) the rock behaves elastically and above it plastically.

We are interested mainly in large deformation responsible for the long-term localized plastic strain in lithospheric shear zones, far beyond the elastic domain. In order to model these constitutive relations, a yield criterion must be defined, which characterise the critical stress (σ^*) in which the rock might deform permanently (i.e. beyond the elastic behavior), either by breaking or creeping (**Figure 2.10b**).

Yield Criteria

Consider a yield surface in the stress space in its classical sense, i.e., from elastic to plastic behavior. Three types of yield criterion were explored in our models: one pressure-dependent ascribed to the upper crust, called **Drucker-Prager (1962)** criterion, and two pressure-independent, an isotropic called **Von Mises (1913)** criterion ascribed to the lower and upper mantle, and the **Hill (1948)** criterion that characterize the anisotropic yield criterion in the lithospheric mantle when olivine fabric is present. The mathematical formulation of the yield criterion is:

$$f(\sigma, \alpha) = 0$$

where σ contains the six independent components of the stress tensor, and α represent the material parameters. In our approach, the parameterization of the anisotropic viscosity is performed *via* the parameter space α , which in the Hill yield criterion is represented by six coefficients. The yield criteria and the method to calibrate the Hill's parameters will be described in detail in the chapter 4.

A general mathematical description of the yielding problem is represented by a function f in the form:

$$\begin{cases} f < 0, \text{elastic} \\ f = 0, \text{plastic} \\ f > 0, \text{inadmissible} \end{cases}$$

This yield function can be defined graphically by a surface in the stress space. The actual state of stress of the rock is given by a point either inside (i.e. elastic) or on the yield surface (i.e. plastic), where the boundary $f = 0$ define the permissible stress limit (**Figure 2.11**):

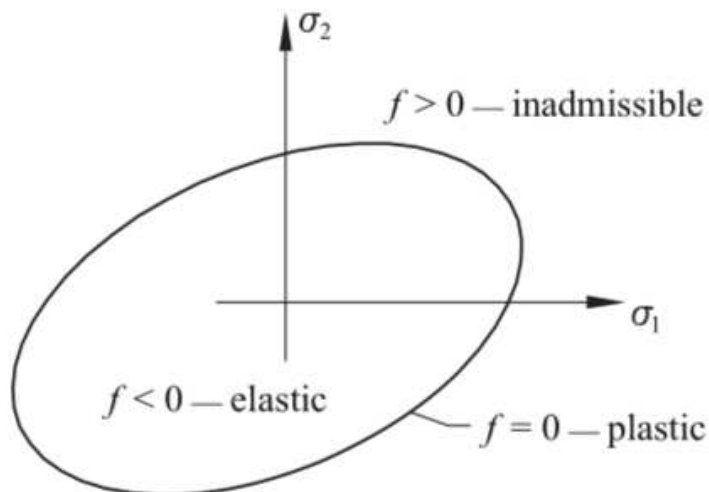


Figure 2.11: General plastic yield surface.

Elastic (isotropic) deformation

The elastic behavior occurs as soon as the stress is applied to the rock, which then recovers its original shape when stress is relaxed. The analogue of this behavior is a spring. As the stress σ increases the elastic strain ϵ increases linearly proportional to the elastic moduli E (i.e. the slope of the curve in the stress strain space).

$$\sigma = E \epsilon$$

where ϵ is $\frac{\Delta L}{L}$, as previously defined. In 3D it can be written in the general tensorial form in two parts, a volumetric ϵ_{kk} and a deviatoric strain tensor ϵ_{ij} that are related directly to the magnitude of the applied deformation:

$$\sigma_{ij} = \lambda \delta_{ij} \epsilon_{kk} + 2\mu \epsilon_{ij}$$

where λ and μ are elastic constants, the bulk and shear modulus, respectively, and depends on the material properties and deformation conditions (T and P).

Plastic (brittle) isotropic deformation

Once plastic yield is reached irreversible deformation occurs. The brittle Drucker-Prager criterion that is used in the geodynamic code ADELI is a smooth version of the sharp yield surface defined by the Mohr-Coulomb criterion:

$$\tau = \sigma \tan(\phi) + c,$$

expressed in the form of a linear relation between normal (σ) and shear stresses (τ). Failure occurs after that the cohesion c and the internal frictional angle ϕ of the material is overcome.

The larger the normal stress, which depends on lithostatic pressure, the more shear stresses the rock can sustain (**Figure 2.12**). For relatively small shear stress the rock strength increase with the normal stress and is slightly dependent of the characteristic roughness of the failure surface. For high shear stresses, the rate of increase in rock-strength decreases and becomes independent of rock type (**Byerlee, 1978**).

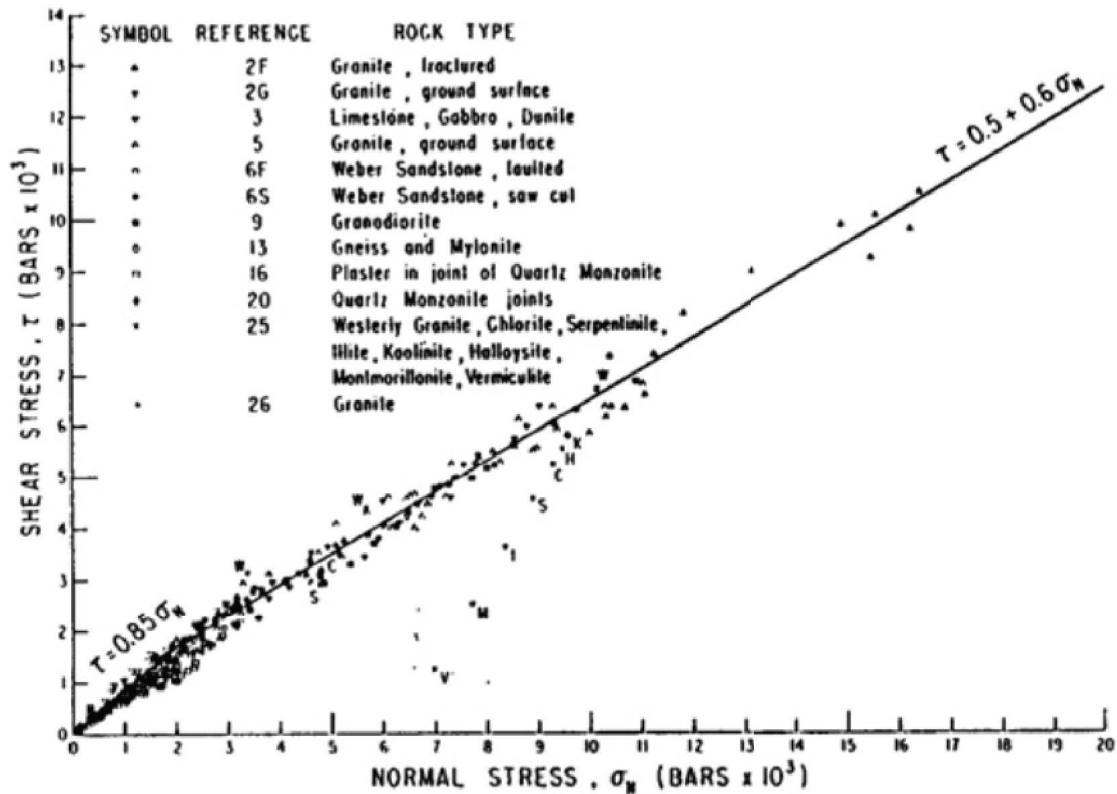


Figure 2.12: Shear and normal stress for a variety of rock-types (after Byerlee, 1978).

Plastic (Viscous) isotropic deformation

If cohesion in the material is maintained, the rock may deform irreversibly by flowing without failure. At long time scale the lithosphere deforms by viscous creep, which depends on many factors such as rock type, grain size, temperature, strain rate, fluid content... The simpler viscous behavior is the Newtonian fluid mode, which relates linearly the shear stress σ_{xy} and the shear strain rate $\dot{\epsilon}_{xy}$ through a material constant proportional to the viscosity η .

$$\sigma_{xy} = 2 \eta \dot{\epsilon}_{xy}$$

The mechanical properties of the lower crust and upper mantle can be approximated as a Non-Newtonian viscous fluid through a constitutive law calibrated relying on experimental rock-deformation deforming by most by dislocation creep. This is modelled in ADELI using a power-law relationship, so called due to dependence of strain-rate on the stress raised to the power n , which leads to an apparent viscosity that is neither constant nor linear. In terms of strain-rate $\dot{\epsilon}_d$ as a function of deviatoric stress σ_d , the viscous power-law relation is:

$$\dot{\epsilon}_d = A (\sigma_d)^n \exp\left(-\frac{Q}{RT}\right)$$

where A is a material constant ($\text{Pa}^{-n} \text{s}^{-1}$), n is the dimensionless stress exponent defining the sensitivity of strain rate on the differential stress, Q is the energy barrier of the creep mechanism, also called activation energy (J.mol^{-1}), R is the Boltzmann constant ($\text{J.mol}^{-1} \text{K}^{-1}$), and T is temperature (K). In the case that the controlling mechanism is Diffusion creep, n is equal to 1 and a grain-size dependent variable must be added to the equation.

This relation indicates that the flow is thermally activated and that temperature and differential stress play a fundamental role on the rate of the viscous flow. For a constant stress, an increase in temperature either increases the strain rate or decrease the stress required to produce a given strain rate.

2.3 Modelling olivine polycrystalline plasticity

There are two classes of widely used approaches to models plasticity of aggregates (review in **Lebensohn et al., 2011**): Full-field and Mean-field models. The Mean field models are based on statistics of the microstructure in which the exact shape and position of a grain in relation to neighbouring grains is unknown. The Full-filled approach, such as Finite Element Method or the Fast Fourier Transforms - FFT (**Lebensohn, 2001**), requires to explicitly defining the microstructure, leading to more accurate calculation but also requires considerably more time of computation, which have implications for the size of the investigated microstructures. In this thesis, the Mean-field models were use to relate olivine CPO to its anisotropic (mechanical) properties. In the next paragraphs, I will focus on this class of models (mean-field), revising chronologically the classical papers that establish the bases for their development. I do not intend to exhaustively revise the physics behind polycrystal plasticity models. Instead, the fundamentals improvements of the mean-field approach until the second-order self-consistent approach we use. Some new developments and capabilities of polycrystal plasticity simulation can be found in (Pokharel et al., 2014, and references there in)

The pioneer work by **Sachs (1928)** and **Taylor (1938)** has established the bases for Mean-field models. Their models, called lower- and upper-bound models, respectively, allowed calculating the effective behaviour of the polycrystal without taking into account the interactions between grains. In the lower-bound the grains are subjected to the same stress

that the polycrystal, whereas in the upper-bound the grains are subjected to the same plastic strain that the polycrystal. The lower-bound model is suitable for materials with few slip systems because under uniform stress only grains well oriented to deform are expected to accommodate strain. This might result in underestimation of the effective behavior of the high symmetry materials. On the other hand, the upper bound is well adapted to materials with abundant available slip systems because under uniform strain all grains, despite their orientation, will be forced to accommodate the same amount of strain. This approach might result in unrealistic high effective stress if the material has low symmetry (high anisotropy).

Based on the Eshelby's inclusion theory (**Eshelby, 1957**) the self-consistent scheme was introduced in the Kröner and Budiansky-Wu models (**Kröner, 1961, Budiansky and Wu, 1962**) to account for grain interaction with a Homogenous Equivalent Medium (HEM), leading to intermediate mechanical behavior compared to the lower- and upper-bound approaches. A linearization scheme of the constitutive relations is required to approximate the non-linear solution of the grain. The properties of the polycrystal (i.e. HEM) are determined by considering the average properties of the single crystal and of the polycrystal, related by inclusion-matrix interaction tensor $\tilde{\mathcal{M}}$. Solving the equilibrium equation for the ellipsoidal inclusion (strain rate $\dot{\epsilon}$ and stress s) embedded in an effective medium (strain rate \dot{E} and stress S) leads to an (interaction) equation in the form:

$$\dot{\epsilon} - \dot{E} = -\tilde{\mathcal{M}} : (s - S)$$

where $\tilde{\mathcal{M}}$ is characterized by a term, $\tilde{\mathcal{B}}$, depending on the inclusion geometry and matrix rheology, a compliance tensor \mathcal{M} , and an interaction term n_{eff} , written as:

$$\tilde{\mathcal{M}} = n_{eff}(I - \tilde{\mathcal{B}})^{-1} : \tilde{\mathcal{B}} : -\mathcal{M}$$

The difference of the strain rate in the grain relative to the polycrystal average strain rate is given by the interaction term n_{eff} . When $n_{eff} = 0$, the crystal strain rate is the same of the average one independent of stress (Taylor model). When $n_{eff} = \infty$, the stress difference in the grain relative to the polycrystal average is zero (Sachs model).

The first self-consistent models accounted only for elastic deformation, therefore, it were applicable for small deformation. **Hill (1965)** extended this approach by accounting for an elastic-plastic coupling using the concept of constraint tensor, a fourth rank tensor. Hill considered the HEM as an anisotropic medium that depended on elastic plastic stiffness of the

single crystal and on the geometrical features of the ellipsoidal inclusion. **Hutchinson (1976)** proposed an extension of these models by considering a small, incremental, effective viscoplastic behaviour using a *secant* linearization procedure ($n_{eff} = 1$) to account for the non-linear the constitutive relation of the polycrystal.

Molinari et al. (1978) proposed a non-incremental approach based on a *tangent* (TGT) linearization procedure ($n_{eff} = n$) that led to a softer grain-matrix interaction and allow considering large deformations. **Lebensohn and Tome (1993)** generalized this formulation to account for low symmetry materials, such as ice (**Castelnau et al., 1996, 1997**) and olivine (**Tommasi et al., 1999, 2000**). Intermediate behavior can be obtained by considering an *affine* linearization procedure (**Masson et al., 2000. Castelnau et al., 2008b**), which has n_{eff} between the *secant* and *tangent* (**Figure 2.13**).

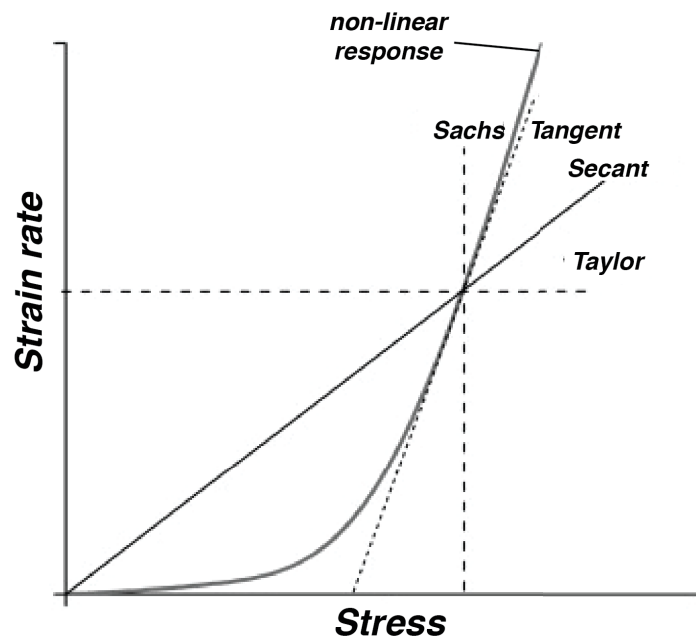


Figure 2.13: Linearization procedures in the stress strain rate space

The self-consistent predictions were significantly improved by the so-called *second-order* approximation. This approach account for average field fluctuations inside the grains (**Ponte Castañeda, 2002**), and allow better predictions of the effective stress and strain rate of the polycrystal, notably for those that are formed by highly anisotropic crystals, such as olivine. **Castelnau et al. (2008)** has shown that the mechanical response of olivine polycrystals calculated with the *second-order* viscoplastic self-consistent model (SO-VPSC), display similar results compared to more sophisticated solutions given by Full-field

simulations (**Figure 2.14**). In the present thesis, I use SO-VPSC to sample the viscoplastic yield-stress space of olivine polycrystals and parameterize their anisotropy to be used in a geodynamical model.

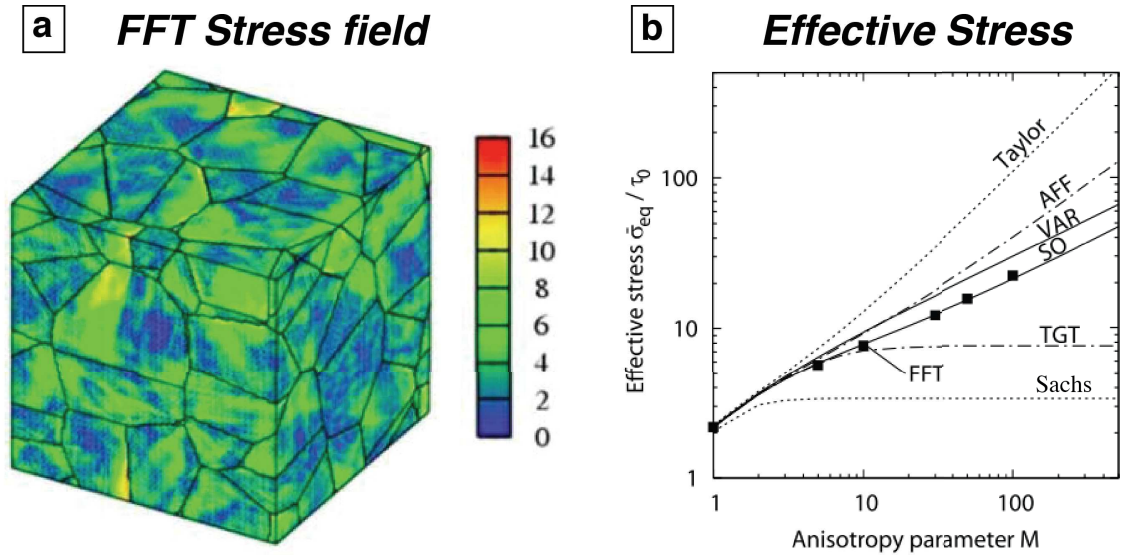


Figure 2.14: **a)** Stress field calculate by Fast Fourier Transform (FFT) in olivine polycrystal **b)** Comparison between FFT-based solutions and several mean-field approaches (SO: second-order linearization. AFF: affine linearization. TGT: tangent linearization) for different values of plastic anisotropic parameters M (adapted from **Castelnau et al., 2008**). FFT and SO-VPSC show remarkably similar responses.

Signorelli and Tommasi, (2015) extended the TGT-VPSC to account for dynamic recrystallization by subgrain rotation in olivine aggregates and simulate the fast steady-state olivine CPO evolution and weakening of the aggregate at relatively low shear strains. This work used a recrystallization criterion based on the internal energy and strain threshold. In this thesis, we developed an alternative approach to relax strain compatibility in the polycrystal using the most recent SO-VPSC formulation (presented in the next chapter in the form of a published article. The results obtained are comparable to those by **Signorelli and Tommasi, (2015)** with considerably less computation cost. Our new routine was used to constrain the magnitude and governing parameters of olivine viscoplastic anisotropy.

2.4 Viscous anisotropy in geodynamics

The first studies on mechanical anisotropy in the context of geodynamics used simplistic parameterizations of the anisotropy to investigate its consequences on mantle

convection. **Richter and Daly (1978)** and **Saito and Abe (1984)** derived analytical solutions to study length-scale of convection in an anisotropic viscous fluid by considering a constant horizontal layer with shear flow easier than normal flow. These authors, without explicitly defining the physical mechanism generating the anisotropy, found that the presence of a mechanical anisotropy layer affect the wavelength of the convection cell.

Honda (1986) and **Christensen (1987)**, as in the previous work cited, also used a hexagonal anisotropy characterized by constant contrast in shear and normal viscosity (transverse isotropic). They included 2D stress-strain rate relationships to investigate the anisotropic mantle convection. **Honda (1986)** considered anisotropy from partial melt zones and used a fixed anisotropy in the spatial coordinated. **Christensen (1987)** accounted for anisotropy rising from compositional layering and crystal alignment, which anisotropy carried out by the convective flow. These studies suggested that the presence of anisotropy layer affect the style of thermal convection.

Schmeling (1987) investigated the feedbacks between mantle convection and glacial rebound flow and found that the superposition of non-Newtonian fluids give rise to apparent anisotropic viscosity, which indeed influence the orientation of small-scale convection cells under a moving plate. The interaction of anisotropic flow and glacial rebound was also investigated by **Christensen (1987)** and **Han and Wahr (1997)**, in which the latter has extended previous works to consider transverse isotropic viscous-elasticity and spherical geometry (3D). These works suggested that viscous anisotropy do modified the geoid response, flow geometry and the relaxation time during post-glacial rebound. By considering a fourth-rank anisotropic viscosity tensor applied to the cubic symmetry of Ringwoodite crystals, **Pouilloux et al. (2007)** corroborate previous studies and suggest that viscous anisotropy may induce even more significant modification on mantle convection style and post-glacial rebound than predicted the previously.

Hearn et al. (1997) relying on higher thermal diffusivity and lower shear viscosity produced by crystal preferred orientations aligned with the flow direction, developed a model for cooling and deformation of the oceanic upper mantle. The study showed that viscous anisotropy might also affect the thermal structure of the oceanic lithosphere. **Lev and Hager (2011)** using a 2D finite element model (FEM) investigate the relation between transverse isotropic viscosity induced by crystal alignment in the mantle and the resulting thermal structure of subduction zones. By tracking the evolution of crystal preferred orientations (CPO) in the mantle wedge as a function of strain and considering viscosity as a temperature

dependent parameter, this work found that anisotropic viscosity change the thermal structure of subduction zones.

Using 2D-FEM with transverse isotropy viscosity defined as a scalar, such as in their work in 2011, and also through analytical solutions, **Lev and Hager (2008)** studied the role of viscous anisotropy in density instabilities and showed that viscous anisotropy modified the spatial and temporal distributions of dropping instabilities. Recently, **Perry-Houts and Karlstrom (2018)** re-examined this problem and confirmed these results, further suggesting a non-trivial relation between viscous anisotropy and the rate at which the gravitational instability develop.

Using a FEM approach, **Becker and Kawakatsu (2011)** performed 2D and 3D calculation to study the role of anisotropic viscosity in an asthenospheric flow driven by a distant downward plate. Viscous anisotropy was defined using a transverse isotropic symmetry characterized by the ratio of the asthenosphere and background viscosity tensors. This work concluded that viscous anisotropy affect the instantaneous flow, but that the trade-off between isotropic and anisotropic viscosity variations may hinder the effect of anisotropic viscosity.

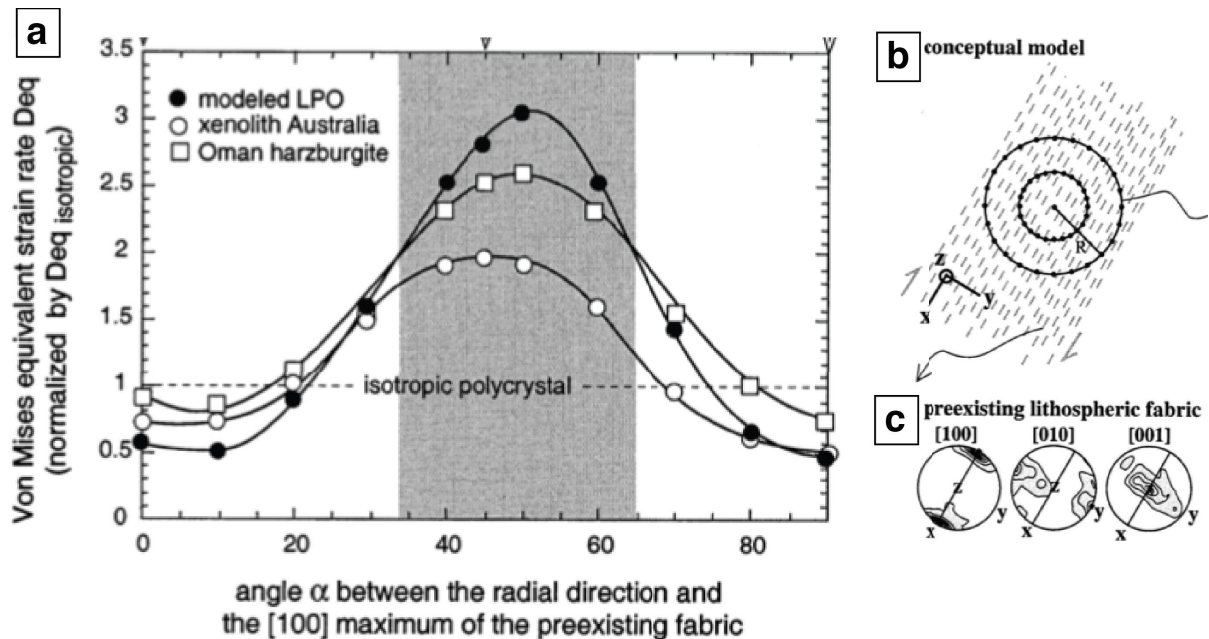


Figure 2.15. a) Normalized strain rate as a function of the orientation of the tensional stress relative to the [100]-axis maximum of the preexisting LPO. b) Conceptual anisotropic model showing the plume radius (black circle) and c) the pre-existing olivine CPO coherent with fossil strike-slip shear zones (adapted from **Tommasi and Vauchez, 2001**).

Castelnau et al. (2008) investigated a corner-flow scenario, where significant feedbacks between flow pattern and viscous anisotropy are expected to occur due to rapid change of rock texture. Viscoplastic self-consistent (VPSC) simulations and upper bound models of olivine crystallographic preferred orientations and flow stresses were coupled with a 2D flow modes. Their model indicated that viscous anisotropy influence the pattern of flow and the magnitude of flow stress in plate boundaries. **Tommasi and Vauchez (2001)** used polycrystal plasticity models to calculate the instantaneous elastic stresses of natural and numerical olivine CPOs typical of strike-slip shear zones for different orientations-relations between stresses and CPO. Although they calculated stresses expected to develop above an upwelling mantle plume (axis-symmetrical), their predictions are also valid for two-dimensional tensional stress field expected from plate tectonics-related forces. The models suggested that strain localization in textured shear zone depend on the orientation of the applied stress relative to the shear zone fabric; shear zone is most likely to be reactivated when stresses are oblique stresses. The reactivation of the textured domain is controlled by parallel-strike deformation regime (**Figure 2.15**). Their findings have implications for the understating of the systematic continental rifting parallel to ancient collisional belts.

Knoll et al. (2009) and **Tommasi et al. (2009)** explicitly coupled VPSC models to a finite-element code to study viscous anisotropy due to the presence of coherent olivine fabric in plates. The first considered the deformation of a homogenous anisotropic plate and the second the deformation of a heterogeneous anisotropic plate containing a strike-slip shear zone (**Figure 2.16**). These models, which accounted for the full viscosity tensor of olivine (3D) and also for its evolution with time/strain (evolving CPO), concluded that the presence of olivine CPO in a homogenous plate leads to non-parallelism between stress and strain-rate eigenvectors and to strain localization in an heterogeneous plate that is strongly dependent on the orientation of the olivine CPO relative to the direction of the mechanical solicitation. Moreover, **Tommasi et al. (2009)** showed that CPO-induced reactivation of the shear zone modified the associated toroidal flow.

The effects of mechanical anisotropy due the development of foliation and CPO on the evolution of shear zone and porphyroblast in the rock and was investigated recently by **Griera et al. (2013)**, **DeRiese et al. (2019)** and **Han et al. (2019)**. They used a full-filed approach to model viscoplastic yielding of the polycrystal; therefore I will briefly comment an important outcome. The authors found that fabric development and mechanical anisotropy affect the vortices of rotating minerals and the magnitude of strain localization in shear bands.

The authors highlighted that intrinsic mechanical anisotropy has no characteristic length-scale, and therefore, must also influence large-scale structures.

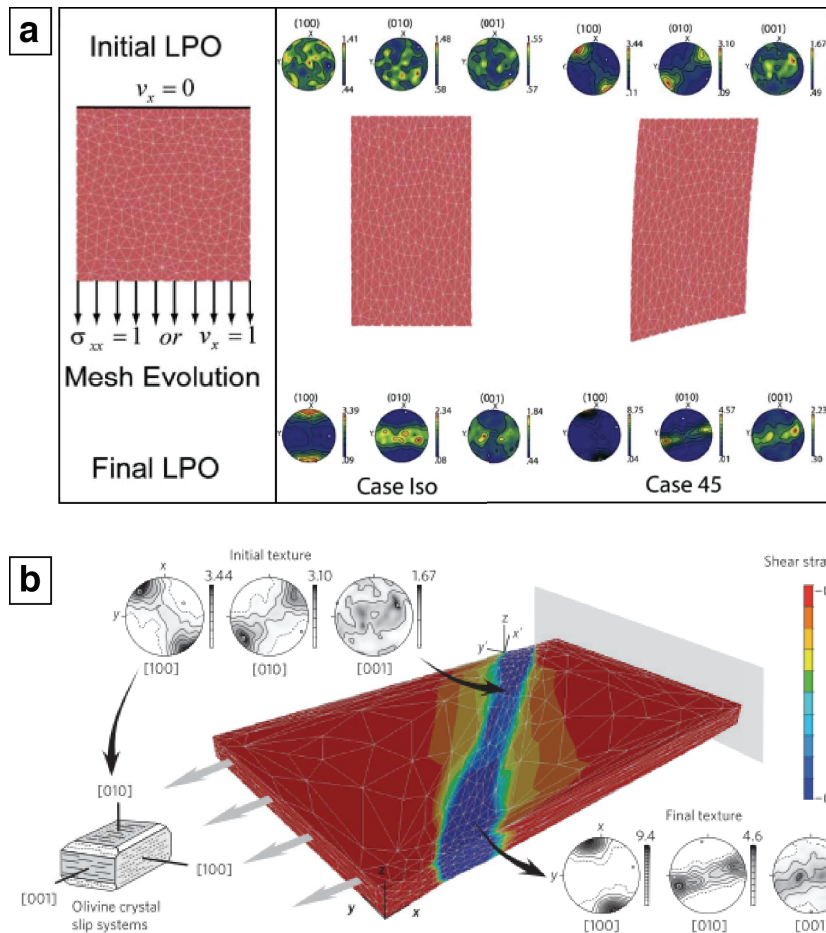


Figure 2.16. a) Plate deformation and evolution of olivine CPO in models where a homogeneous plate with different initial CPO (random: Case Isotropic. and Case 45°: Anisotropic) is submitted to a constant extensional stress. b) 3D model setup and shear-strain distribution in a model with an ‘inherited shear zone’ at 45° of the imposed extension direction. The initial (top left) and final (bottom right) olivine CPO are shown (adapted from Knoll et al. 2009 and Tommasi et al. 2009).

The recent work by Király et al. (2020) investigated the effect of olivine viscous anisotropy in the asthenosphere for the change in plate kinematics and structural reactivation. They used the pseudo-Taylor approximation described in Hansen et al 2016 and derived from olivine polycrystal deformed in extension and simple shear, in order to estimate the stress tensor for a given strain rate in the slip systems. A constitutive power-law relation was used to link the 3D strain-stress state in the aggregate with olivine CPO to the fluidity (viscous rheology). The study found that the magnitude of shearing and the deformation components in the asthenosphere depends significantly on the olivine CPO that is developed. They

deduced that the contrast in viscosity due to the evolution of viscous anisotropy in the asthenosphere could favour (or hinder) the onset of lithospheric scale structures.

REFERENCES

Bai, Q., Mackwell, S. J., & Kohlstedt, D. L. (1991). High-temperature creep of olivine single crystals 1. Mechanical results for buffered samples. *Journal of Geophysical Research: Solid Earth*, 96(B2), 2441-2463.

Becker, T.W., Kawakatsu, H., 2011. On the role of anisotropic viscosity for plate- scale flow. *Geophys. Res. Lett.* 38 (17), L17307. <http://dx.doi.org/10.1029/2011GL048584>.

Birle, J. D., Gibbs, G. V., Moore, P. B., & Smith, J. V. (1968). Crystal structures of natural olivines. *American Mineralogist: Journal of Earth and Planetary Materials*, 53(5-6), 807-824.

Boneh, Y., & Skemer, P. (2014). The effect of deformation history on the evolution of olivine CPO. *Earth and Planetary Science Letters*, 406, 213-222.

Boneh, Y., Morales, L. F., Kaminski, E., & Skemer, P. (2015). Modeling olivine CPO evolution with complex deformation histories: Implications for the interpretation of seismic anisotropy in the mantle. *Geochemistry, Geophysics, Geosystems*, 16(10), 3436-3455.

Boudier, F., 1978. Structure and petrology of the Lanzo massif (Piedmont Alps). *Geological Society of America Bulletin* 89, 1574–1591.

Boudier, F., Coleman, R.G., 1981. Cross section through the peridotite in the Samail Ophiolite, Southeastern Oman Mountains. *Journal of Geophysical Research* 86, 2573–2592.

Bragg, W. L., and G. B. Brown (1926), Die struktur des Olivins, *Zeit. Krist.*, 63, 538.

Budiansky, B. and Wu, T.T. (1962). Theoretical Prediction of Plastic Strains of Polycrystals. *Proc. 4th Congr. Appl. Mech.*, 1175.

Burov, E. B. (2011). Rheology and strength of the lithosphere. *Marine and Petroleum Geology*, 28(8), 1402-1443.

Byerlee, J. (1978). Friction of rocks. In *Rock friction and earthquake prediction* (pp. 615-626). Birkhäuser, Basel.

Carter, N. L., and H. G. Ave'Lallemant (1970), High temperature flow of dunite and peridotite, *Geol. Soc. Am. Bull.*, 81, 2181–2202

Chopra, P.N., Paterson, M.S., 1981. The experimental deformation of dunite. *Tectonophysics* 78, 453–473.

Christensen, U.R., 1987. Some geodynamical effects of anisotropic viscosity. *Geophys. J.*

R. Astron. Soc. 91 (3), 711–736. <http://dx.doi.org/10.1111/j.1365-246X.1987.tb01666.x>.

DeRiese, T., Evans, L., Gomez-Rivas, E., Griera, A., Lebensohn, R. A., Llorens, M. G., ... & Bons, P. D. (2019). Shear localisation in anisotropic, non-linear viscous materials that develop a CPO: A numerical study. *Journal of Structural Geology*, 124, 81-90.

Deer, W.A., Howie, R.A., Zussmann, J., 1997. Rock forming minerals: Orthosilicates. Vol. 1A. Geological Society of London, London, p.187.

Durham, W. B., & Goetze, C. (1977). Plastic flow of oriented single crystals of olivine: 1. Mechanical data. *Journal of geophysical Research*, 82(36), 5737-5753.

Eshelby, J. (1957). The determination of the elastic field of an ellipsoidal inclusion, and related problems., *Proceedings of the Royal Society of London Series a-Mathematical and Physical Sciences*, A241, 376-396.

Falus, G., Tommasi, A., & Soustelle, V. (2011). The effect of dynamic recrystallization on olivine crystal preferred orientations in mantle xenoliths deformed under varied stress conditions. *Journal of Structural Geology*, 33(11), 1528-1540.

Gibert, B., Seipold, U., Tommasi, A., Mainprice, D., 2003. Upper mantle thermal diffusivity: pressure- and temperature dependences and anisotropy. *J. Geophys. Res.* 108, 2359. <http://dx.doi.org/10.1029/2002JB002108>.

Griera, A., Llorens, M.G., Gomez-Rivas, E., Bons, P.D., Jessell, M.W., Evans, L.A., Lebensohn, R., 2013. Numerical modelling of porphyroclast and porphyroblast rotation in anisotropic rocks. *Tectonophysics* 587, 4–29.

Han, D., Wahr, J., 1997. An analysis of anisotropic mantle viscosity, and its possible effects on post-glacial rebound. *Phys. Earth Planet. Inter.* 102 (1), 33–50. [http://dx.doi.org/10.1016/S0031-9201\(96\)03268-2](http://dx.doi.org/10.1016/S0031-9201(96)03268-2)

Hansen, L. N., Warren, J. M., Zimmerman, M. E., & Kohlstedt, D. L. (2016). Viscous anisotropy of textured olivine aggregates, Part 1: Measurement of the magnitude and evolution of anisotropy. *Earth and Planetary Science Letters*, 445, 92-103.

Hansen, L. N., Zimmerman, M. E., & Kohlstedt, D. L. (2012a). The influence of microstructure on deformation of olivine in the grain-boundary sliding regime. *Journal of Geophysical Research: Solid Earth*, 117(B9).

Hansen, L. N., Zimmerman, M. E., & Kohlstedt, D. L. (2012b). Laboratory measurements of the viscous anisotropy of olivine aggregates. *Nature*, 492(7429), 415.

Hearn, E.H., Humphreys, E.D., Chai, M., Brown, J.M., 1997. Effect of anisotropy on oceanic upper mantle temperatures, structure, and dynamics. *J. Geophys. Res., Solid Earth*

102 (B6), 11943–11956. <http://dx.doi.org/10.1029/97JB00506>

Hill, R., 1965. Continuum micro-mechanics of elastoplastic polycrystals. *J. Mech. Phys. Solids* 13, 89.

Honda, S. (1986). Strong anisotropic flow in a finely layered asthenosphere. *Geophysical Research Letters*, 13(13), 1454-1457.

Hutchinson, J. W. (1976), Bounds and self-consistent estimates for creep of polycrystalline materials, *Proceedings of the Royal Society of London Series a-Mathematical and Physical Sciences*, A348, 101

Introduction to Tectonophysics, book, Patrice Rey.

Ismail, W. B., & Mainprice, D. (1998). An olivine fabric database: an overview of upper mantle fabrics and seismic anisotropy. *Tectonophysics*, 296(1-2), 145-157.

Kaczmarek, M.-A., Tommasi, A., 2011. Anatomy of an extensional shear zone in the mantle (Lanzo massif, Italy). *Geochemistry, Geophysics, Geosystems* Q0AG06,

Karato, S. I., Jung, H., Katayama, I., & Skemer, P. (2008). Geodynamic significance of seismic anisotropy of the upper mantle: new insights from laboratory studies. *Annu. Rev. Earth Planet. Sci.*, 36, 59-95.

Karato, S. I., Paterson, M. S., & FitzGerald, J. D. (1986). Rheology of synthetic olivine aggregates: influence of grain size and water. *Journal of Geophysical Research: Solid Earth*, 91(B8), 8151-8176.

Király, Á., Conrad, C. P., & Hansen, L. N. (2020). Evolving viscous anisotropy in the upper mantle and its geodynamic implications. *Geochemistry, Geophysics, Geosystems*, e2020GC009159.

Knoll, M., Tommasi, A., Logé, R.E., Signorelli, J.W., 2009. A multiscale approach to model the anisotropic deformation of lithospheric plates. *Geochem. Geophys. Geosyst.* 10, Q08009. <http://dx.doi.org/10.1029/2009GC002423>. Kohlstedt,

Kröner, E. (1961). Zur Plastischen Verformung des Vielkristalls. *Acta metall.* 9, 155.

Lebensohn, R. A., Castañeda, P. P., Brenner, R., & Castelnau, O. (2011). Full-field vs. homogenization methods to predict microstructure–property relations for polycrystalline materials. In *Computational Methods for Microstructure-Property Relationships* (pp. 393-441). Springer, Boston, MA.

Lebensohn, R.A., 2001. N-site modeling of a 3-d viscoplastic polycrystal using fast fourier transform. *Acta Mater.* 49, 2723–2737.

Lev, E. (2009). Elastic and viscous anisotropy in Earth's mantle: observations and

implications (Doctoral dissertation, Massachusetts Institute of Technology).

Lev, E., Hager, B.H., 2008. Rayleigh–Taylor instabilities with anisotropic lithospheric viscosity. *Geophys. J. Int.* 173 (3), 806–814. <http://dx.doi.org/10.1111/j.1365-246X.2008.03731.x>.

Lev, E., Hager, B.H., 2011. Anisotropic viscosity changes subduction zone thermal structure. *Geochem. Geophys. Geosyst.* 12 (4). Mei,

Liu, W., Kung, J., & Li, B. (2005). Elasticity of San Carlos olivine to 8 GPa and 1073 K. *Geophysical Research Letters*, 32(16).

Mainprice, D., Barruol, G., & Ismail, W. B. (2000). The seismic anisotropy of the Earth's mantle: from single crystal to polycrystal.

Masson, R., Bornert, M., Suquet, P., & Zaoui, A. (2000). An affine formulation for the prediction of the effective properties of nonlinear composites and polycrystals. *Journal of the Mechanics and Physics of Solids*, 48(6-7), 1203-1227.

Mercier, J. C., & Nicolas, A. (1975). Textures and fabrics of upper-mantle peridotites as illustrated by xenoliths from basalts. *Journal of Petrology*, 16(1), 454-487.

Molinari, A., Canova, G. R., & Ahzi, S. (1987). A self consistent approach of the large deformation polycrystal viscoplasticity. *Acta Metallurgica*, 35(12), 2983-2994.

Nicolas, A. (1986). Structure and petrology of peridotites: clues to their geodynamic environment. *Reviews of Geophysics*, 24(4), 875-895.

Perry-Houts, J., & Karlstrom, L. (2018). Anisotropic viscosity and time-evolving lithospheric instabilities due to aligned igneous intrusions. *Geophysical Journal International*, 216(2), 794-802.

Pokharel, R., Lind, J., Kanjarla, A. K., Lebensohn, R. A., Li, S. F., Kenesei, P., ... & Rollett, A. D. (2014). Polycrystal plasticity: comparison between grain-scale observations of deformation and simulations. *Annu. Rev. Condens. Matter Phys.*, 5(1), 317-346.

Pouilloux, L., Kaminski, E., & Labrosse, S. (2007). Anisotropic rheology of a cubic medium and implications for geological materials. *Geophysical Journal International*, 170(2), 876-885.

Ran, H., de Riese, T., Llorens, M. G., Finch, M. A., Evans, L. A., Gomez-Rivas, E., ... & Bons, P. D. (2019). Time for anisotropy: The significance of mechanical anisotropy for the development of deformation structures. *Journal of Structural Geology*, 125, 41-47.

Richter, F. M. & Daly, S. F., 1978. Convection models having a multiplicity of large horizontal scales, *J. geophys. Res.*, 83,495 I -4956,

- Sachs, G. (1928). Zur Ableitung einer Fließbedingung, *Z. Ver. Deut. Ing.*, 72(8), 734-736.
- Saito, M. & Abe, Y., 1984. Consequences of anisotropic viscosity in the Earth's mantle, *Zisin*. 37, 237-245 (in Japanese with English abstract).
- Schmeling, H. (1987). On the interaction between small-and large-scale convection and postglacial rebound flow in a power-law mantle. *Earth and planetary science letters*, 84(2-3), 254-262.
- Signorelli, J., & Tommasi, A. (2015). Modeling the effect of subgrain rotation recrystallization on the evolution of olivine crystal preferred orientations in simple shear. *Earth and Planetary Science Letters*, 430, 356-366.
- Silver, P., Mainprice, D., Ismail, W., Tommasi, A., & Barruol, G. (1999). Mantle structural geology from seismic anisotropy.
- Silver, P.G., 1996. Seismic anisotropy beneath the continents: probing the depths of geology. *Annu. Rev. Earth Planet. Sci.* 24, 385–432.
- Silver, P.G., Chan, W.W., 1991. Shear wave splitting and subcontinental mantle deformation.
- Taylor, G. I. (1938). Plastic strain in metals, *J. Inst. Metals*, 62, 307-324.
- Titus, S.J., Medaris, L.G., Wang, H.F., Tikoff, B., 2007. Continuation of the San Andreas Fault system into the upper mantle: evidence from spinel peridotite xenoliths in the Coyote Lake basalt, central California. *Tectonophysics* 429, 1–20.
- Tommasi, A., & Vauchez, A. (2001). Continental rifting parallel to ancient collisional belts: an effect of the mechanical anisotropy of the lithospheric mantle. *Earth and Planetary Science Letters*, 185(1-2), 199-210.
- Tommasi, A., & Vauchez, A. (2015). Heterogeneity and anisotropy in the lithospheric mantle. *Tectonophysics*, 661, 11-37.
- Tommasi, A., Gibert, B., Seipold, U., Mainprice, D., 2001. Anisotropy of thermal diffusivity in the upper mantle. *Nature* 411, 783–787. Tommasi,
- Tommasi, A., Knoll, M., Vauchez, A., Signorelli, J.W., Thoraval, C., Logé, R., 2009. Structural reactivation in plate tectonics controlled by olivine crystal anisotropy. *Nat. Geosci.* 2 (6), 423–427. <http://dx.doi.org/10.1038/ngeo528>.
- Van der Wal, D., Vissers, R.L.M., 1996. Structural petrology of the Ronda peridotite, SW Spain: deformation history. *Journal of Petrology* 37, 23–43.
- Vauchez, A., Barruol, G., & Tommasi, A. (1997). Why do continents break-up parallel to ancient orogenic belts?. *Terra Nova*, 9(2), 62-66.

Vaucher, A., Dineur, F., & Rudnick, R. (2005). Microstructure, texture and seismic anisotropy of the lithospheric mantle above a mantle plume: insights from the Labait volcano xenoliths (Tanzania). *Earth and Planetary Science Letters*, 232(3-4), 295-314.

Vaucher, A., Tommasi, A., & Mainprice, D. (2012). Faults (shear zones) in the Earth's mantle. *Tectonophysics*, 558, 1-27.

Vaucher, A., Tommasi, A., Barruol, G., 1998. Rheological heterogeneity, mechanical anisotropy, and tectonics of the continental lithosphere. *Tectonophysics* 296, 61–86.

Warren, J. M., & Hirth, G. (2006). Grain size sensitive deformation mechanisms in naturally deformed peridotites. *Earth and Planetary Science Letters*, 248(1-2), 438-450.

Wüstefeld, A., Bokelmann, G., Barruol, G., & Montagner, J. P. (2009). Identifying global seismic anisotropy patterns by correlating shear-wave splitting and surface-wave data. *Physics of the Earth and Planetary Interiors*, 176(3-4), 198-212.

CHAPTER III

PREDICTING VISCOUS ANISOTROPY OF TEXTURED OLIVINE POLYCRYSTALS

*No one believes the results of the computational modeler
except the modeler, for only he understands the premises.*

*No one doubts the experimentalist's results except the
experimentalist, for only he knows his mistakes.*

Unknown author

3 Modelling CPO-induced viscoplastic anisotropy in olivine-rich rocks

In this thesis, the implications of CPO-induced viscous anisotropy on intraplate deformation are investigated using a parameterization approach based on the predictions of viscoplastic self-consistent simulations (VPSC). For doing so, it is necessary first to test whether the VPSC model can simulate viscous anisotropy measured in laboratory experiments, then, evaluate the possible magnitude of anisotropy produced by olivine CPO in mantle peridotites, and the controlling parameters at this (rock)-scale. In this chapter, these issues are tackled.

Part of the results, a comparison with laboratory experiments by Hansen et al., 2012, was published in the journal *Physics of Earth and Planetary Interiors (PEPI)* and is presented in section “Article #1”, together with the published “Supplementary Material”. After the article section it is also reported and discussed non-published VPSC simulations where I compared the model predictions against laboratory experiments by Hansen et al., 2016. Moreover, I also performed a parametric study exploring the effects of CPO symmetry, intensity and boundary conditions for typical (numerical) olivine CPOs and for simple shear, axial extension/compression on the predicted viscous anisotropy.

3.1 Article #1



ELSEVIER

Physics of the Earth and Planetary
Interiors

Volume 286, January 2019, Pages 69-80



Predicting viscoplastic anisotropy in the upper mantle: a comparison between experiments and polycrystal plasticity models

Lucan Mameri ^a  , Andréa Tommasi ^a  , Javier Signorelli ^b, Lars N. Hansen ^c

[Show more](#) 

<https://doi.org/10.1016/j.pepi.2018.11.002> [Get rights and content](#)

ABSTRACT

Viscoplastic deformation of mantle rocks produces crystal preferred orientations (CPO or texture) of olivine and, by consequence, an anisotropic mechanical response for subsequent deformation events. Olivine polycrystals deformed experimentally in torsion and then in extension normal to the previous shear plane have extensional strengths <2 times higher than the torsional ones. Implementation of this viscoplastic anisotropy in geodynamic codes depends nevertheless on the predictions of polycrystal plasticity models, since the full range of orientation relations between applied stresses and the broad range of texture types observed in upper mantle rocks may only be tested numerically. Here, we compare instantaneous viscoplastic responses of olivine polycrystals predicted by tangent and second-order viscoplastic self-consistent (VPSC) and stress equilibrium-based models to experimental data. These polycrystal plasticity models, in which only dislocation glide is considered to accommodate strain, reproduce qualitatively the viscoplastic anisotropy observed in the laboratory, but overestimate its magnitude for rocks with strong textures. The lower bound model better approaches the laboratory results, suggesting that the discrepancy between laboratory and numerical experiments arises from the models forcing strain compatibility in olivine polycrystals that can only deform by dislocation creep. The experimental data is indeed well reproduced by the second-order VPSC model modified to include additional isotropic deformation mechanisms, which accommodate the deformation components that cannot be produced by dislocation glide but do not produce plastic spin. These results corroborate that other processes in addition to dislocation glide contribute significantly to viscoplastic deformation under laboratory conditions, reducing the magnitude of anisotropy. In nature, coarser grain sizes probably result in lower activity of these additional deformation processes. We therefore propose that standard and modified second-order VPSC models provide a good prediction of the possible range of texture-induced viscoplastic anisotropy in upper mantle domains deforming by dislocation creep.

Keywords: olivine; crystal preferred orientation; mechanical anisotropy; dislocation creep. mantle deformation; rheology

3.1.1 Introduction

The lithospheric mantle is predominantly composed of olivine, a mineral that displays highly anisotropic elastic and viscoplastic mechanical behavior (**Kumazawa and Anderson, 1969. Bai et al., 1991**). Upper mantle deformation by viscoplastic processes produces crystallographic preferred orientation (CPO or texture) of olivine (**Nicolas and Christensen, 1987**). These CPO result in anisotropic behavior at the scale of the rock (cm- to m-scale) and larger, as indicated by observations of coherent seismic anisotropy patterns correlated with the tectonic fabric of continental plates at the scale of hundreds of km (cf. review in **Tommasi and Vauchez, 2015**). Large-scale olivine CPO in the upper mantle has therefore been proposed as a source of structural memory in the upper mantle, leading to strain localization along shear zones formed during previous tectonic events (**Vauchez et al., 1998. Tommasi and Vauchez, 2001**).

The consequences of upper mantle viscoplastic anisotropy on the deformation of both the plates and convective mantle have been analyzed in a variety of numerical models. Many of these models used a simplified description of this anisotropy by imposing a constant difference between 'shear' and 'normal' viscosities and reorienting the viscosity tensor in response to flow based on a director vector approach (e.g., **Honda, 1986. Christensen, 1987. Lev and Hager, 2008, 2011**). These models, which tested normal to shear viscosity ratios of 10–100, concluded that viscous anisotropy does change mantle flow patterns by stabilizing the boundary layers and enhancing strain localization. Most recent models have coupled polycrystal plasticity simulations into finite-element models. this allows the follow-up of the evolution of the orientation and intensity of the full viscosity tensor (e.g., **Chastel et al., 1993. Knoll et al., 2009. Tommasi et al., 2009. Castelnau et al., 2009. Blackman et al., 2017**). These more sophisticated models support the early conclusions on the role of viscous anisotropy on the stability of convection (**Chastel et al., 1993**), and corroborate that the olivine CPO formed during preexisting deformation episodes and

subsequently frozen into the lithospheric mantle may explain the reactivation of ancient continental-scale structures to form new plate boundaries (**Knoll et al., 2009. Tommasi et al., 2009**) and change the mantle flow pattern beneath spreading ridges (**Castelnau et al., 2009, Blackman et al., 2017**). However, at the time most of those calculations were carried out, no experimental data existed for corroborating the predictions of the polycrystal plasticity models.

Recently, laboratory experiments demonstrated that olivine aggregates with textures formed in torsion are ~2 times weaker for further deformation in torsion than for extension perpendicular to the previous shear plane (**Hansen et al., 2012a**). These experiments provided the first quantitative data for validating the predictions of viscoplastic anisotropy in olivine-rich rocks by polycrystal plasticity models. This validation is important because the use of geodynamical models to study the effects of an anisotropic rheology on Earth dynamics depends directly on our ability to predict the anisotropy of viscoplastic behavior associated with any combination of CPO and loading geometry. Only polycrystal plasticity models can test in a physically consistent way the full range of orientation relations between applied stresses and the broad range of texture types observed in upper-mantle rocks.

In this work, we test how well different polycrystal plasticity models simulate the viscoplastic anisotropy of olivine polycrystals measured in the laboratory by calculating the instantaneous mechanical response in simple shear and axial extension for polycrystals with the same CPO as the experimental samples and comparing these predictions to (1) the final stresses measured in the torsion experiments that produced the CPO and (2) to the peak stresses measured in axial extension experiments subsequent to torsion. The comparison between the polycrystal plasticity models and the experimental data allows us to quantify the contribution of other processes to the deformation of olivine polycrystals under laboratory conditions and propose modeling approaches that predict the possible range of

texture-induced viscoplastic anisotropy in upper mantle domains deforming by dislocation creep.

3.1.2 Methods

Modeling viscoplastic behavior and texture evolution

We tested the capability of different polycrystal plasticity models to predict the viscoplastic behavior of textured olivine-rich rocks at high temperature and moderate pressure by simulating the torsion and extension tests of **Hansen et al. (2012a)**. **Hansen et al. (2016a)** presents complementary results (extension followed by torsion), but a heterogeneous distribution of strain in the initial extension experiments resulted in large variability among textures and stresses. For testing the different polycrystal plasticity models, we require higher precision data. Therefore in the present study,

we focus solely on simulating experiments from **Hansen et al. (2012a)** in which torsion was followed by extension. To do so, we calculated the instantaneous mechanical response of four olivine polycrystals that have precisely the same CPO as those measured in the experimental samples. We also applied the same loading geometries as in the experiments: simple shear parallel to the previous shear deformation that created the texture or axial extension parallel to the previous torsional axis (**Figure 3.1**). The employed models are viscoplastic and include no elasticity. This simplification is justified by full-field simulations of polycrystalline materials performed in the elasto-viscoplastic regime that demonstrate that the viscoplastic behavior controls the mechanical response of the polycrystal even at very small strains ($< 1\%$, **Lebensohn et al., 2012**).

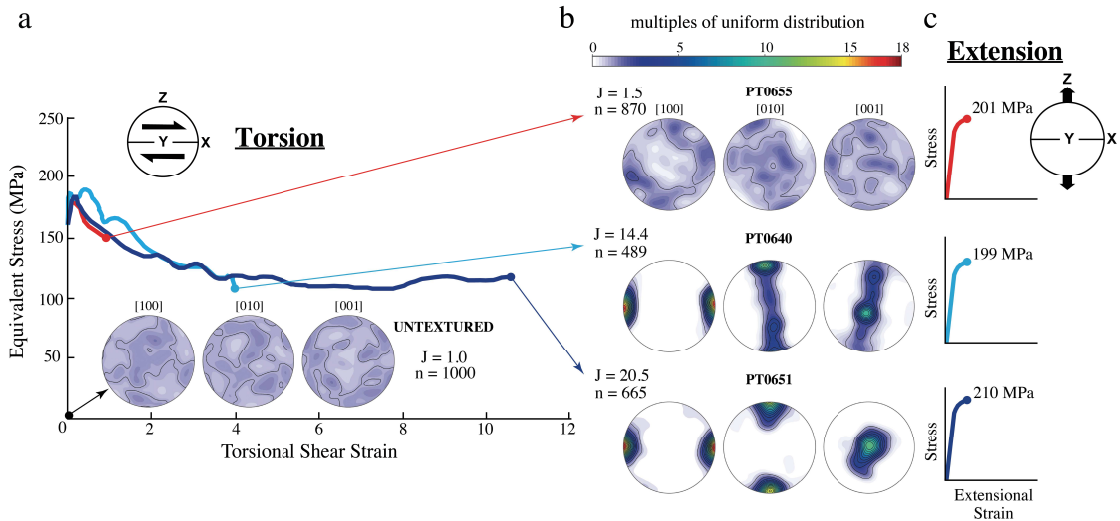


Figure 3.1. (a) Stress-strain curves for torsion experiments by **Hansen et al. (2012a)**. (b) CPO produced by the torsion experiments and used as initial textures in the extension experiments and in the polycrystal plasticity models. (c) Stress-strain curves for extension experiments by **Hansen et al. (2012a)**. Instantaneous stresses predicted by the models in simple shear and extension are compared to (a) final stresses in torsion and (c) peak stresses in extension, respectively. The stresses in extension are averaged values normalized to a constant strain-rate of $2 \times 10^{-4} \text{ s}^{-1}$. The number of grains in each CPO is indicated by the value n , and the CPO intensity by the value J (J -index). Pole figures are contoured as multiples of uniform distribution. the same contour range limits are applied to all pole figures for easy evaluation of variations in CPO strength.

The viscoplastic mechanical response of the olivine polycrystals to the imposed extensional or simple shear deformation has been modeled using three polycrystal plasticity

models: the uniform stress (lower bound) approach (**Sachs, 1928**, **Chastel et al., 1993**), the tangent VPSC model (**Lebensohn and Tomé, 1993**), and the more recent second-order

formulation of the VPSC model (**Ponte Castañeda, 2002. Lebensohn et al., 2011**). The three approaches differ in the way the crystal interactions are modeled. The lower bound assumes constant stress in all grains and disregards strain compatibility. In the VPSC approach, each grain is represented as a viscoplastic inclusion embedded in and interacting with a homogeneous viscoplastic medium that represents the average polycrystal behavior. Stress equilibrium and strain compatibility at the aggregate scale are obtained by approximating the macroscopic strain rate and stress to the average of strain rate and stress at the grain scale, respectively. The second-order (SO)- and tangent (TGT)-VPSC models differ in how the non-linear behavior of the material is estimated. Both formulations are based on the same linearization scheme, which considers heterogeneous stress and strain rate within the polycrystal. However, only the second-order formulation accounts for intragranular strain rate fluctuations to predict the effective polycrystal behavior (**Ponte Castañeda, 2002. Lebensohn et al., 2011**).

In all three approaches, individual crystals deform only by dislocation glide on a finite number of slip systems, which are a function of the crystal structure. The relative strength of these slip systems, that is, the critical resolved shear stress (CRSS) needed to activate dislocation glide on each system, depends on the temperature, pressure, and stress. For technical reasons, the experiments of **Hansen et al. (2012a)** were performed using olivine crystals enriched in iron (Fo50) relative to typical mantle olivines (Fo90), for which mechanical data are not available for creep of single crystals. In the present study, we use CRSSs (**Table 3.1**) derived from deformation of natural olivine single crystals (Fo90) at high temperatures and low pressure (Bai et al., 1991). The choice of these CRSSs, although arbitrary, is justified by the analysis of the CPO produced in the torsion experiments of **Hansen et al. (2012a)**, which is consistent with the dominant activation of the (010)[100] slip system. We also examined the effect of setting equal the values of CRSS for the (001)[100] and (010)[100] slip systems, as used

in previous VPSC models studying olivine CPO evolution at high temperature and low pressure (e.g., **Tommasi et al., 2000**), and we observed negligible variations in terms of mechanical behavior compared to the present model setup. Laboratory experiments and atomistic modeling suggest nevertheless a change in the relative resistance between the different slip systems, favouring glide of dislocations with [001] Burgers vectors relative to those with [100] Burgers vectors at high pressure (e.g., **Durinck et al., 2007. Raterron et al., 2007**). Comparison of the seismic anisotropy predicted by polycrystal plasticity models with high and low pressure CRSS sets with seismic anisotropy observations suggests that the CRSS data used in the present study are representative of deformation in the upper 200–250 km of the mantle (**Mainprice et al., 2005**).

Table 3.1

Slip systems parameters used in the VPSC simulations.^a

Slip Systems	Critical Resolved Shear Stress ^b	Stress exponent
(0 1 0)[1 0 0]	1	3
(0 0 1)[1 0 0]	1.5	3
(0 1 0)[0 0 1]	2	3
(1 0 0)[0 0 1]	3	3
(0 1 1)[1 0 0]	4	3
(1 1 0)[0 0 1]	6	3
(1 1 1)<1 1 0> ^c	β	3
(1 1 1)<0 1 1> ^c	β	3
(1 1 1)<1 0 1> ^c	β	3

^a Lower bound simulations only consider the first four slip systems.

^b Dimensional values; normalized by the flow stress of the (0 1 0)[1 0 0] slip system.

^c Dummy slip systems, which represent additional strain accommodation processes and do not contribute to plastic spin.

The shear strain rate in each slip system is proportional to the resolved shear stress on the slip plane in the slip direction normalized to the CRSS of the slip system raised to the power n . The iron-rich olivine polycrystals display a stress exponent n of 4.1, whereas typical mantle olivine has lower n values (e.g., 3.5, Bai et al., 1991). We tested n equal to 3 or 4 and observed little difference in terms of magnitude of anisotropy (cf. supplementary material, **Figure S3.1**). In the following we focus on the results for $n = 3$ in order to agree with most laboratory and previous numerical experiments on olivine polycrystals, which usually find stress exponent $n = 3 \pm 0.5$.

A major challenge in modeling viscoplastic anisotropy of a rock (i.e., an aggregate of crystals with different orientations) is that traditional polycrystal plasticity models only account for deformation accommodated by dislocation glide. Since olivine has fewer than 4 independent slip systems, deformation processes other than glide are required to ensure strain compatibility. To simulate the contribution of these other processes, **Detrez et al. (2015)** modified the SO-VPSC model by adding an isotropic deformation process. In the present study we build on this already validated development. To close the yield surface and simulate the contribution of isotropic deformation processes to plastic deformation, we add three fictitious pyramidal slip systems in the VPSC models: $\{111\} \langle 110 \rangle$, $\{111\} \langle 011 \rangle$ and $\{111\} \langle 101 \rangle$, here referred as dummy slip systems. These slip systems were defined such that they may accommodate any imposed plastic strain, but do not contribute to plastic spin. They mimic therefore isotropic strain accommodation mechanisms, which do not contribute to CPO evolution. The contribution of the dummy systems to the total viscoplastic deformation is varied by changing their CRSS by a factor β (**Table 3.1**). Thus, the present implementation differs from previous VPSC model applied to olivine polycrystals, referred thereafter as ‘standard’ VPSC model, since in the latter the dummy slip systems contributed to plastic spin and were not allowed to accommodate $> 5\%$ (therefore contributing only in a minor way to the CPO evolution) by using β values ≥ 50 (e.g., **Wenk et al., 1991. Tommasi et al., 2000. Castelnau et al., 2009**).

Hardening is not considered in the present models since in most high-temperature (1200°C) deformation experiments on olivine aggregates, in the absence of significant microstructural changes, steady-state mechanical behavior is achieved after relatively small strains (e.g., **Chopra and Paterson, 1984. Hansen et al., 2012b. Thieme et al., 2018**). In the present models, diffusive processes are therefore implicitly accounted for in two ways: via their contribution to avoid hardening by dislocation entanglements and via the activation of the

dummy slip systems. Indeed, although we do not model any specific additional process, but solely their contribution to strain accommodation in the olivine polycrystal, most possible additional processes, such as recrystallization, grain boundary migration or sliding, involve diffusion.

Model setup

Two series of tests were run to simulate the stresses measured in the laboratory: (1) simple shear parallel to a previous shearing deformation that produced the olivine CPO, that is, shearing in the X direction and in a plane normal to the Z direction. (2) axial extension normal to the previous shear plane, parallel to the Z direction (**Figure 3.1**). Lower bound simulations were run under kinematic boundary conditions by imposing all components of the velocity gradient tensor L (s^{-1}). For easy comparison between simple shear (ss) and axial extension (ext) simulations, L is defined with the condition that the norm of the strain rate tensor in both cases equals 1 (cf. supplementary material):

$$L_{ss} = \begin{bmatrix} 0 & 1.4 & 0 \\ 0 & 0 & 0 \\ 0 & 0 & 0 \end{bmatrix}; L_{ext} = \begin{bmatrix} -0.4 & 0 & 0 \\ 0 & 0.8 & 0 \\ 0 & 0 & -0.4 \end{bmatrix};$$

In the VPSC simulations, mixed boundary conditions were enforced because they better mimic the actual conditions in laboratory experiments: imposed torsion on the plane normal to the piston axis or imposed axial extension and homogeneous stress in the plane normal to the piston axis.

$$L_{ss} = \begin{bmatrix} * & 1.4 & 0 \\ 0 & 0 & 0 \\ 0 & 0 & * \end{bmatrix}; L_{ext} = \begin{bmatrix} * & 0 & 0 \\ 0 & 0.8 & 0 \\ 0 & 0 & * \end{bmatrix}; \sigma_{ss,ext} = \begin{bmatrix} -0.5 & * & * \\ * & * & * \\ * & * & -0.5 \end{bmatrix};$$

* = not imposed

We also ran VPSC simulations using fully kinematic boundary conditions. Differences between stresses predicted by TGT or SO-VPSC simulations using either kinematic or mixed boundary conditions are low ($< 10\%$, cf. supplementary material, **Figure S3.2**),

by consequence we focus on the results for mixed boundary conditions.

The models are run for a single deformation step of 1% Von Mises equivalent strain and the mechanical behavior is analyzed before actualization of the texture, in other words, we calculated the instantaneous mechanical response of the olivine polycrystals. The stresses predicted by the viscoplastic models in simple shear and in axial extension were compared to final stresses measured in the torsion experiments and to peak stresses in the extensional ones, respectively (**Figure 3.1**). For internal consistency, stresses measured in the laboratory were normalized for a homogeneous Von Mises equivalent strain rate of $2 \times 10^{-4} \text{s}^{-1}$

(**Table 3.2**; the normalization procedure is presented in the Supplementary Material). Stresses calculated in the models are normalized by the strength of the easiest slip system, (010)[100]. In addition, for comparing the viscoplastic anisotropy observed in the laboratory to the one predicted by the different numerical models, Von Mises equivalent stresses for simple shear and axial extension were normalized by the Von Mises equivalent stress of the isotropic aggregate in each data set (experiments or different modeling approaches).

Table 3.2

Model predictions and laboratory measurements.

Instantaneous stresses predicted by the models and final (simple shear) and peak (extension) stresses measured in the experiments					Instantaneous stresses [*] predicted by SO-VPSC models for different β values					
Mechanical Solicitation	Initial texture	SO-VPSC [†] $\beta = 50$	TGT-VPSC [†] $\beta = 50$	Lower Bound [†]	Laboratory Data [†] (MPa)	$\beta = 10$	5	3	2	1
Simple Shear	UNTEXTURED	16.77	9.64	3.94	–	8.33	6.03	4.56	3.53	2.10
	PT0655	14.86	8.57	3.59	148.23	7.54	5.56	4.29	3.39	2.09
	PT0640	8.43	5.87	2.86	118.47	4.82	3.82	3.18	2.73	1.95
	PT0651	7.58	5.19	2.57	109.43	4.38	3.48	2.92	2.50	1.78
Extension	UNTEXTURED	16.72	10.05	3.89	168.00	8.27	5.97	4.52	3.50	2.08
	PT0655	18.00	11.20	3.94	201.24	8.64	6.12	4.56	3.50	2.06
	PT0640	28.04	20.82	6.00	199.44	12.31	8.03	5.53	3.98	2.14
	PT0651	37.13	33.32	5.69	209.85	14.88	9.08	6.00	4.22	2.23

^{*} Von Mises equivalent stress normalized by the strength of the (010)[100] slip system.

[†] Von Mises equivalent stress recalculated for a homogeneous strain rate of $2 \times 10^{-4} \text{s}^{-1}$; extension values are average ones.

The effect of the texture on the viscoplastic mechanical behavior was tested using four different initial CPOs: an untextured and three olivine CPOs measured at the end of the torsional tests by **Hansen et al. (2012a)**, performed at high temperature and moderate pressure conditions (**Figure 3.1**). These initial textures are representative of common CPO symmetries observed in natural and experimental samples deformed in simple shear and cover the entire range of CPO intensities measured in peridotite massifs and mantle xenoliths (**Tommasi and Vauchez, 2015**). In the models, grains are initially spherical. The untextured polycrystal is made of 1000 grains. The CPO intensity is characterized by the J-index, which is the integral of the squared orientation distribution function (ODF), quantified using the

MTEX toolbox based on an ODF calculated using a “de la Vallée Poussin” kernel with a half width of 10° (**Mainprice et al., 2014**). Sample PT0655, which was initially deformed to a shear strain of 1, is represented by a texture composed of 870 grains. This texture is very weak (J-index of 1.5). It is characterized by a subtle double maximum of [100] at low and high angles to the shear direction and by a dispersed girdle of [010] at high angle to the maximum finite elongation with a weak maximum normal to the foliation. Samples PT0640 and PT0651, which underwent initial shear strains of 4 and 10, are represented by textures composed of 489 and 665 grains, respectively. Both have very strong olivine CPOs (J-index of 14.5 and 20.5, respectively) and are characterized by alignment of the [100] maximum with the shear direction and of the

[010] maximum normal to the shear plane. However, the textures differ by the distribution of the [010] axes, which forms a girdle normal to the shear direction (X) in PT640 and a point maximum normal to the shear plane (XY plane) in PT655 (**Figure 3.1**).

To verify if the modified SO-VPSC approach used in this work is capable of reproducing the CPO evolution recorded in simple shear deformation, we run simple shear tests up to shear strains of 20 for an initially untextured olivine polycrystal composed of 1000 grains. The simulations were conducted applying the same slip system parameters and (mixed) boundary conditions used to model the viscoplastic mechanical behavior.

This study focuses on the SO-VPSC predictions because they have been shown to better reproduce the solutions of full-field simulations (**Castelnaud et al., 2008**). The predictions of the TGT-VPSC model are nevertheless presented for continuity with previous work (e.g., **Wenk et al., 2009**, **Tommasi et al., 1999, 2000**).

3.1.3 Results

Mechanical behavior

Figure 3.2a presents a comparison between the stresses normalized to the strength of the untextured polycrystal predicted by the different viscoplastic models (colored markers) at standard conditions (CRSS of the dummy slip systems in TGT and SO-VPSC models, $\beta = 50$) and the experimental measurements (black circles), as a function of the intensity of the initial CPO. Both laboratory and numerical experiments show that textured olivine polycrystals deformed in simple shear parallel to the preexisting fabric (empty markers) are weaker than the untextured aggregate, whereas those deformed in axial extension normal to the preexisting fabric (filled markers) are harder. There is a positive correlation between CPO intensity and magnitude of viscoplastic anisotropy, defined as the ratio between the Von Mises equivalent stresses in extension and in simple shear tests, but the relationship is not linear (**Figure 3.2b**).

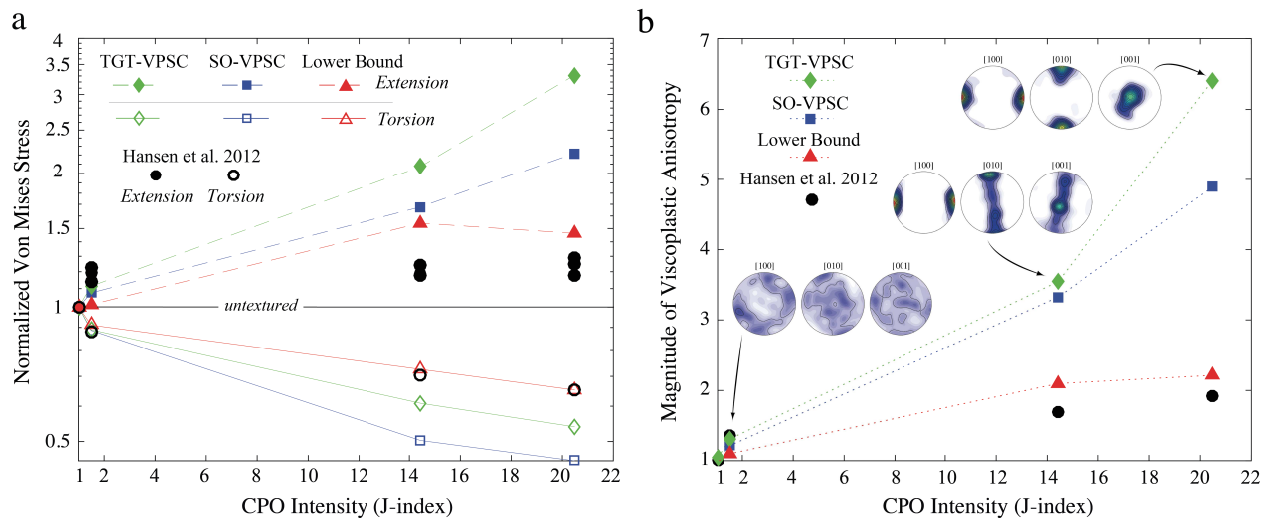


Figure 3.2. (a) Instantaneous normalized Von Mises equivalent stresses (relative to behavior of an isotropic polycrystal) and (b) magnitude of viscoplastic anisotropy (ratio between Von Mises equivalent stresses in extension and simple shear) for lower bound and VPSC simulations (colored symbols), in which the CRSS of the dummy slip systems (β) is set to 50 for the three initial olivine CPO (recalled in **Figure 3.2b** and presented as a function of the CPO intensity – J-index). Black circles indicate stresses measured in the laboratory experiments. The empty markers present the results for simple shear parallel to the [100] maximum in a plane normal to the [010] maximum of the initial CPO. The filled markers present the results for axial extension parallel to the [010] maximum of the initial CPO. For calculating the magnitude of anisotropy the stresses in extension were averaged. for the color legend and labels of the pole figures, as well as loading geometries, refer to **Figure 3.1**.

In simple shear, the lower bound and TGT-VPSC models predict normalized stresses in reasonable agreement with the experimental data, but SO-VPSC simulations predict lower normalized stresses. In axial extension, the models overestimate the strength of the olivine polycrystals relative to the experimental measurements, except for the sample PT0655, which despite a very weak CPO, displays a stronger anisotropy than the one predicted by the models. The predictions of the lower bound approach are the closest to the experimental data and the TGT-VPSC models are the farthest.

The discrepancy between numerical and laboratory experiments, which increases with increasing intensity of the CPO, results therefore from overprediction of the strength of olivine polycrystals deformed numerically in extension. In this loading geometry, most crystals are in hard orientations relative to extension axis, that is, low resolved shear stresses are expected on the three main slip systems of olivine: (010)[100], (001)[100] and (010)[001]. By consequence, high stresses are required to deform the polycrystal by dislocation creep.

The lower bound model, which only enforces stress equilibrium and not strain compatibility, predicts the lowest polycrystal strengths for all textures and loading geometries. The better fit of the experimental data by the lower bound approach points to the major role of enforcing strain compatibility in modeling the mechanical behavior of olivine polycrystals. Further analysis of the stresses predicted by the different models (**Figure 3.3.** and **Table 3.2**) corroborates this point. The SO-VPSC, which most strictly enforces strain compatibility and better fits full-field polycrystal plasticity simulations (**Castelnau et al., 2006**), predicts the highest stress values for both simple shear and extension.

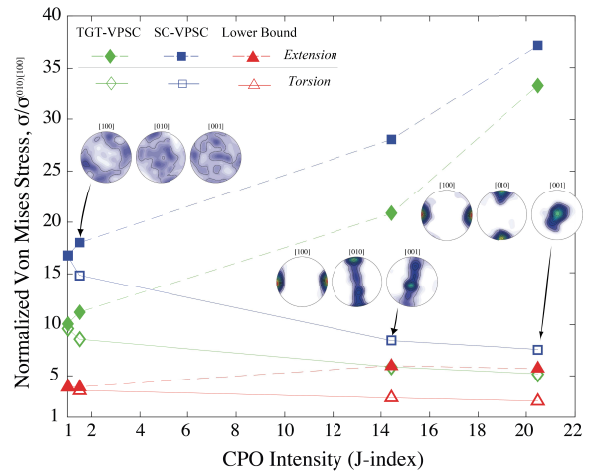


Figure 3.3. Instantaneous Von Mises equivalent stresses (normalized to the strength of the easy (010)[100] slip system) predicted by different polycrystal plasticity models as a function of the initial CPO intensity for simple shear (empty markers) and axial extension (filled markers). The strength of the dummy slip systems (β) is set to 50. Pole figures show the CPO measured at the end of the torsion experiments (**Hansen et al., 2012a**), which are used as the initial CPO in the models. for the color legend and labels of the pole figures, as well as loading geometries, refer to **Figure 3.1**.

The high stresses predicted in axial extension by the SO-VPSC model for the strongly textured polycrystals PT0640 and PT0651 result from low activities of the (010)[100] and (001)[100] slip systems, which have the lowest CRSSs (**Figure 3.4**). For these textures, resolved shear stresses on these two slip systems are low in most crystals (i.e., extension is applied parallel to the maximum concentration of [010] axes and normal to the maximum concentrations of [100] and [001] axes). To accommodate the imposed extensional deformation, the very hard ($\beta = 50$) dummy slip systems have to be activated in many crystals. Even though these systems contribute to $< 5\%$ of the total deformation (**Figure 3.4**), this moderate amount of activation still requires high stresses. The (010)[001] slip system, which has intermediate CRSS values, contributes significantly to the total deformation ($\sim 55\%$) in axial extension. In most crystals, resolved shear

stresses on the (010)[001] slip system are also low, but the high stresses attained in the extensional deformation allow their activation.

In contrast, by imposing simple shear parallel to the maximum concentration of [100] olivine axes in a plane parallel to the maximum concentration of (010) planes in the strongly textured polycrystals PT0640 and PT0651, we obtain maximum resolved shear stresses on the easy slip system (010)[100], which accommodates > 50% of the deformation. In both simple shear and axial extension, the activity of the (010)[100] slip system is higher in the more strongly textured polycrystal (PT0651) than in the polycrystal with a CPO of intermediate strength. A closer analysis of the slip system activities highlights nevertheless some subtle differences between predictions for samples PT0640 and PT0651 (**Figure 3.4**). This variation may be explained by differences in the symmetry of the CPO between the two polycrystals. PT0640 (J-index of 14.1) has a girdle distribution of [010] and [001], which allows in axial extension for high resolved shear stresses on (010)[001] in a larger number of crystals relative to PT0651 (J-index of 20), which has point distributions of the three main axes.

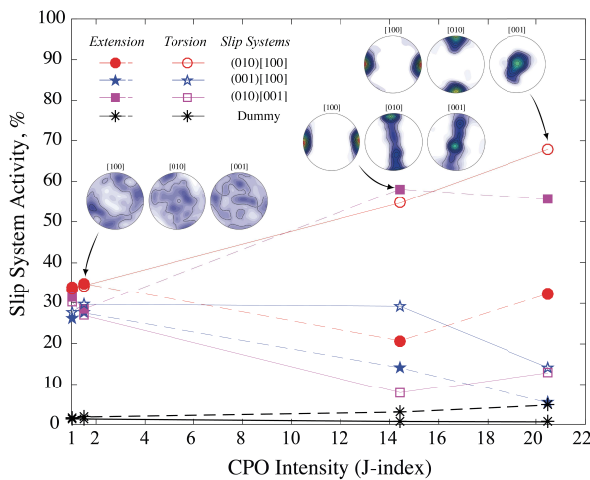


Figure 3.4. Slip system activity predicted by the SO-VPSC model for simple shear (empty markers) and axial extension (filled markers). The sum of the activity of the three dummy systems, that is, the total contribution of the strain accommodation processes, is shown as black asterisks. Strength of the dummy slip systems (β) is set to 50 in these simulations. The activity of (100)[001], (011) [100], and (110)[100]

slip systems, which accommodate less than 1% of viscoplastic deformation, are not represented. Pole figures show the CPO measured at the end of the torsion experiments (Hansen et al., 2012a), for which the instantaneous viscoplastic response are calculated. for the color legend and labels of the pole figures, as well as loading geometries, refer to **Figure 3.1**.

The observed discrepancy between laboratory results and model predictions advocates in favor of a significant contribution of others processes in addition to dislocation glide during deformation of olivine aggregates at laboratory conditions. This contribution appears to be particularly important if most crystals in the aggregate are unfavorably oriented to deform by dislocation glide on the easy slip systems, such as the present extensional tests on the strongly textured polycrystals. To evaluate if an increase of the contribution of isotropic deformation processes allows reproducing the stresses measured experimentally, the CRSS of the dummy slip systems was systematically decreased. The results are presented in the following section.

Strain accommodation by additional isotropic deformation processes

We tested the effect of increasing the contribution of isotropic deformation processes on the aggregate strength by decreasing the CRSS of the dummy slip systems ($\beta = 10, 5, 3, 2, 1$) in the SO-VPSC simulations. These dummy systems represent any additional process that allows olivine crystals to deform even if oriented in a manner that results in very low resolved shear stresses on the three main slip systems: (010)[100], (001)[100], and (010)[001]. The stress predictions in simple shear and axial extension as a function of CPO intensity for different β values are shown in **Figure 3.5** and in **Table 3.2**.

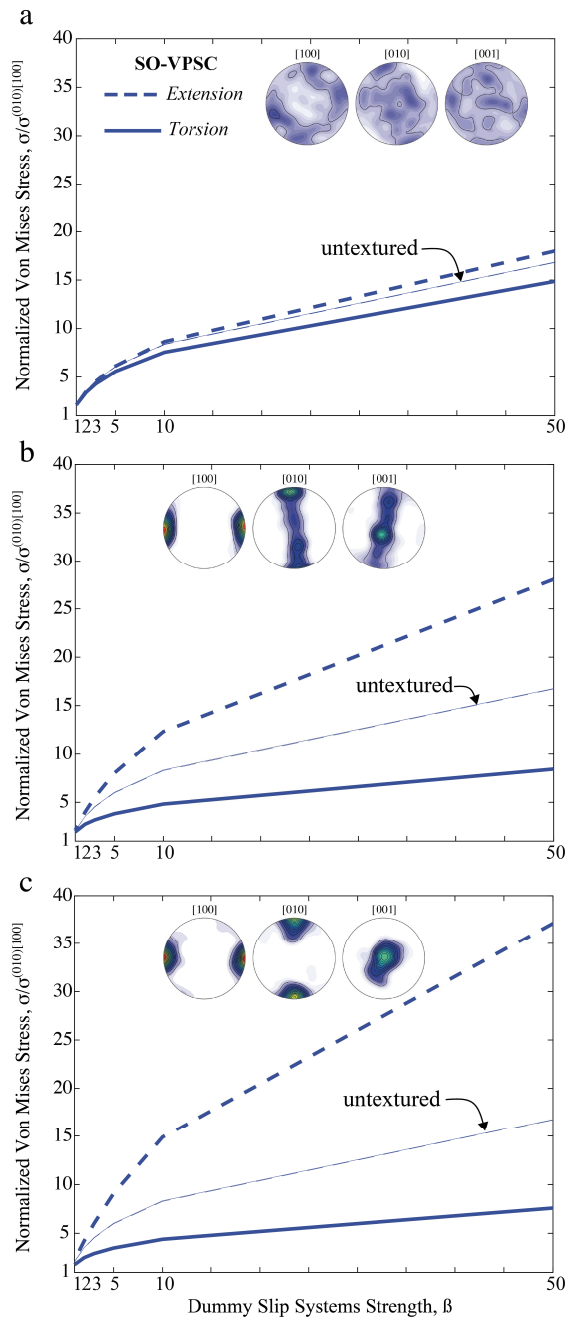


Figure 3.5. Effect of the critical resolved shear stress (CRSS) of the dummy slip systems (β) on the Von Mises equivalent stress (normalized to the strength of the easy (010)[100] slip system) predicted by the SO-VPSC model for simple shear (thick solid lines) and axial extension (thick dashed lines) using the three CPOs: (a) PT0655, (b) PT0640, and (c) PT0651, created in the torsion experiments (Hansen et al., 2012a). For reference, the mechanical behavior of an untextured polycrystal (isotropic) is displayed by a thin dashed (axial extension) or solid (simple shear) lines in all three figures. For the color legend of the pole figures and loading geometries, refer to **Figure 3.1**.

A decrease in β results in a non-linear decrease in the polycrystal strength for all textures and both loading geometries (**Figure 3.5a–c**). The rate of decrease varies as a function of CPO intensity and of loading geometry. The weakly textured aggregate deforms at similar stresses in both loading geometries (i.e., very weak anisotropic behavior) even at high values of β . In contrast, for the strongly textured aggregate (**Figure 3.5b,c**), decreasing β leads to distinct behaviours for the two loading geometries: the reduction in the polycrystal strength is more marked in the axial extension test than in the simple shear simulations. It results therefore in reduction of the magnitude of anisotropy with decreasing β (**Figure 3.6a**). The modified SO-VPSC simulation in which the dummy systems (that allow for isotropic deformation) are 3 times harder to activate than the (010)[100] and (001)[100] easy slip systems ($\beta=3$) better reproduces the mechanical behavior measured in the laboratory, except for the sample with the weakest CPO (PT0655), for which all models underestimate the magnitude of anisotropy (**Figure 3.6a,b**). Differences in mechanical predictions between TGT- and SO-VPSC models are only observed for $\beta > 10$ (cf. supplementary material, **Figure S3.3**).

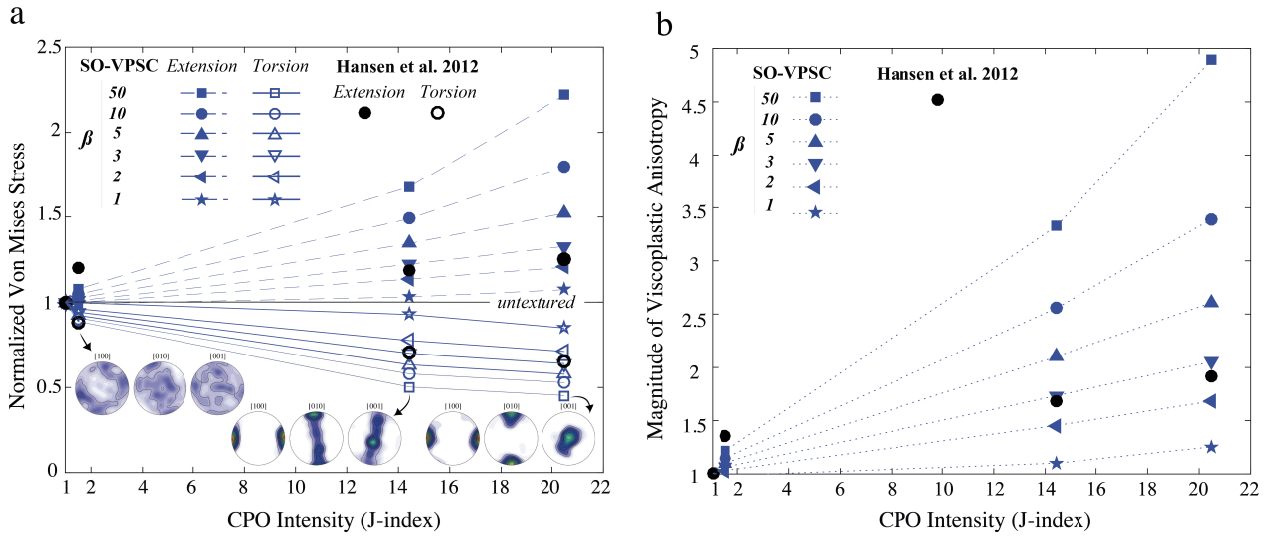


Figure 3.6. (a) Instantaneous Von Mises equivalent stresses normalized by the behavior of an isotropic polycrystal and (b) magnitude of the viscoplastic anisotropy predicted by SO-VPSC simulations with CRSS of the dummy systems (β) between 50 and 1 for the three experimental olivine CPO as a function of increasing CPO intensity (J-index). Empty markers show results for simple shear parallel to the [100] maximum in a plane normal to the [010] maximum of the preexisting CPO and filled markers indicate the results for axial extension parallel to the [010] maximum of the preexisting CPO. The experimental data is represented by the black circles. for the color legend of the pole figures and loading geometries, refer to **Figure 3.1**.

The change in mechanical behavior with decreasing β may be explained by variations in the relative activities of the actual olivine slip systems and of the dummy ones, which represent additional deformation processes activated to ensure strain compatibility constraints (**Figure 3.7**). In the VPSC model with $\beta = 50$, the three main slip systems (010)[100], (001)[100], and (010)[001] account for at least 95% of the viscoplastic deformation in axial extension and 99% of the deformation in simple shear. As β decreases, the activity of the dummy slip systems increases at the expense of the activity of the actual ones. In an untextured aggregate (**Figure 3.7a**), reduction of β from 50 to 10 results in an increase of the activity of the dummy slip systems from < 1% to ~11%, for both simple shear and axial extension. For $\beta = 5$, their activity increases to ~30%. A further decrease in β to 3 or 2, which is the range of values that better agrees with the mechanical data measured in the laboratory, leads to activities of the dummy slip systems of ~45% or ~60%, respectively. For $\beta = 1$, > 80% of the deformation is accommodated by the dummy slip systems. These high activities of the

relaxation mechanism, which is represented in the present study by the dummy slip systems, are similar to those previously observed by **Detrez et al. (2015)**.

The presence of an olivine CPO results in different relative slip system activities in axial extension and simple shear (**Figure 7b–d**). This difference increases with increasing CPO intensity, because in a strongly textured aggregate, a larger proportion of the crystals will be either well or poorly oriented to accommodate the imposed deformation. The three olivine aggregates used in the present simulations have textures in which most crystals are well oriented to accommodate the imposed simple shear, but poorly oriented to accommodate the imposed axial extension. For β equal to 5 or 3, the isotropic mechanism in simple shear respectively accommodates ~25% or ~40% (PT0655), ~15% or ~25% (PT0640), and ~10% or ~20% (PT0651) of the total viscoplastic deformation, whereas in axial extension it accommodates ~30% or ~50% (PT0655), ~50% or ~70% (PT0640), and ~60% or ~75% (PT0651), (**Figure 3.7b–d**).

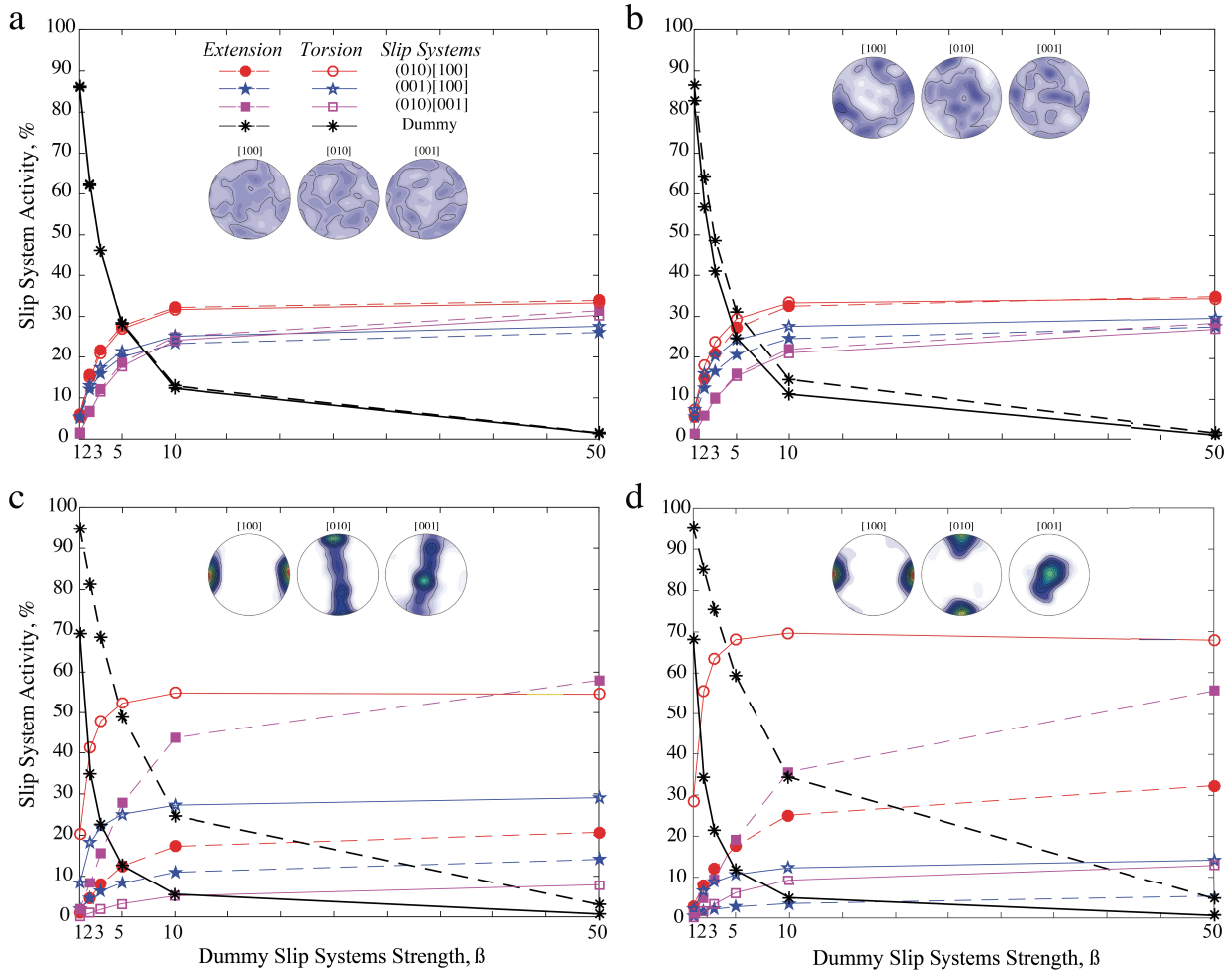


Figure 3.7. Effect of the dummy slip system strength (β) on the activity of the slip systems predicted by SO-VPSC models for the polycrystals: **(a)** untextured, **(b)** PT0655, **(c)** PT0640, and **(d)** PT0651. Empty markers represent simple shear simulations and filled markers axial extension simulations. The activity of the (100)[001], (011)[100], and (110)[100] slips systems, which accommodate less than 1% of viscoplastic deformation, is not shown. The sum of the activity of the three dummy systems, that is, the total contribution of the strain accommodation processes, is shown as black asterisks. for the color legend of the pole figures and loading geometries, refer to **Fig. 3.1**.

It is noteworthy that for $\beta \leq 5$, the dummy slip systems remain active even if most crystals in the aggregates are well oriented to deform by dislocation glide on the easy (010)[100] and (010)[001] slip systems, such as when simple shear is applied on the strongly textured aggregates (PT0640 and PT0651). Their isotropic character may explain this behavior. there is always at least one system among the 12 systems that compose the three dummy slip modes on which the resolved shear stresses are high.

Olivine CPO evolution

To test if the modified SO-VPSC model that better fits the viscoplastic anisotropy measured in the experiments can also reproduce the texture evolution in simple shear, we compare the CPO evolution predicted in simulations with different CRSSs for the dummy slip systems ($\beta=50, 5, \text{ or } 3$) to CPO data for olivine polycrystals deformed experimentally in simple shear at high temperature conditions (Zhang and Karato, 1995. Bystricky et al., 2000. Demouchy et al., 2012. Hansen et al., 2012a,b,c, 2014). **Figure 3.8** displays the

evolution of the CPO intensity characterized by the J-index and the angle between the maximum eigenvector of the [100] axis distribution and the shear direction as a function of the shear strain. Note that the CPO evolution of the olivine aggregates presented by **Hansen et al. (2012a)**, for which the mechanical responses were simulated in the present study, is also included in **Figure 3.8**. In this figure, we also compare the CPO evolution predicted by the present modified SO-VPSC model to those of a VPSC model modified to account for dynamic recrystallization by subgrain rotation in olivine aggregates (CDRX-TG-VPSC, for details on the model cf. **Signorelli and Tommasi, 2015**). The CRSSs in this previous model are slightly different from those used in the present study, but the relative strengths between slip systems are maintained. Thus, we do not expect significant differences in CPO evolution. Pole figures displaying the evolution of the olivine CPO in the SO-VPSC model with $\beta = 50, 5, \text{ or } 3$

are shown in the Supplementary material (**Figure S3.5**).

The SO-VPSC simulations in which the strength of the dummy slip systems (β) is equal to 50 show a rotation of the [100] axes towards the shear direction that closely follows the rotation of the finite strain ellipsoid, poorly reproducing the experimental data. A decrease in β leads to faster rotation of [100] maximum towards the shear direction, which better reproduces the CPO reorientation trend observed in the experiments. However, for low strengths of the dummy slip systems ($\beta \leq 3$), that is, when the additional deformation process are very active, and at high shear strains (≥ 5), the CPO evolution departs from a continuous trend: the maximum concentration of [100] oscillates between 0° and 10° from the shear direction (**Figure 3.8**). Models with $\beta = 5$ also exhibit a similar behavior, but the oscillations start at higher shear strains (~ 10) and are smaller ($\geq 5^\circ$).

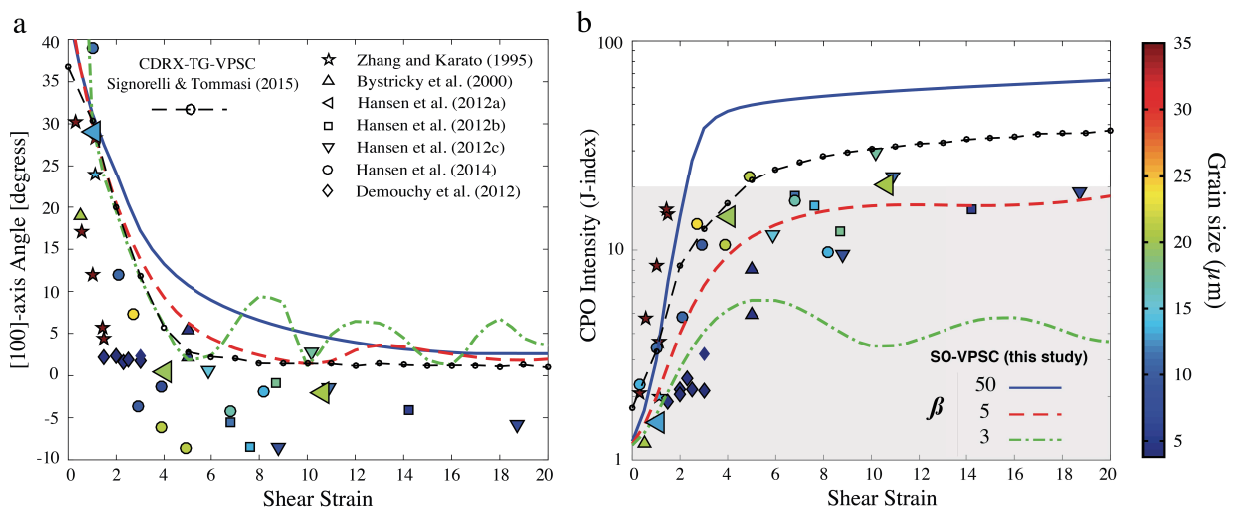


Figure 3.8. CPO evolution as a function of increasing shear strain predicted by SO-VPSC simulations with different dummy slip system strengths (β). a) CPO orientation defined by the angle between shear direction and the maximum eigenvector of the [100]-axis orientation distribution. b) CPO intensity evolution characterized by the J-index. Experimental data from **Zhang and Karato (1995)**, **Bystricky et al. (2000)**, **Demouchy et al. (2012)**, and **Hansen et al. (2012a,b,c,2014)** are displayed for comparison. The CPO evolution of the olivine aggregates in **Hansen et al. (2012a)**, in which the viscoplastic response were simulated in the present study, is highlighted as larger left-pointing triangles. The color gradient in the experimental data symbols indicate the average grain sizes. The predictions of the CDRX-TG-VPSC model by **Signorelli and Tommasi (2015)**, which simulates recrystallization by subgrain rotation, are shown by the dotted-dashed line. The pale gray rectangle in (b) indicates the range of J-index measured in > 600 natural samples (**Tommasi and Vauchez, 2015**).

Analysis of the evolution of the CPO intensity shows that the decrease in the strength

of the dummy slip systems results in stabilization of the CPO at lower J-index values

(**Figure 3.8b**). This observation highlights the essential role of additional processes, such as diffusion or dynamic recrystallization, on the evolution of the CPO intensity. CPO intensities measured in the high shear strain experiments are significantly overestimated for VPSC simulations with $\beta=50$ and underestimated for VPSC simulations with $\beta=3$, but they are well reproduced by models with $\beta = 5$. As for the CPO orientation, periodic oscillation of the CPO intensity is observed for shear strains ≥ 5 for $\beta = 3$ (**Figure 3.8**). In **Figure 3.8**, the experimental data is colored as a function of the average grain size. CPO intensity saturates at lower values in the finer grain size aggregates, being better fitted by models with low β values. This observation provides indication that the additional deformation process might be grain-size sensitive.

In conclusion, the modified SO-VPSC model with $\beta = 5$ better reproduces the CPO evolution in simple shear or torsion experiments than standard SO-VPSC simulations in which most of the deformation is accommodated by dislocation glide on the actual olivine slip systems ($\beta = 50$). CPO evolution in the modified SO-VPSC model with $\beta = 5$ is similar, though less stable at shear strains ≥ 10 , to the one predicted by the VPSC model modified to account for dynamic recrystallization by subgrain rotation (CDRX-TG-VPSC model. **Signorelli and Tommasi, 2015**). The modified SO-VPSC model with $\beta = 3$, which better reproduces the viscoplastic anisotropy measured in the experiments, predicts well the evolution of the CPO orientation observed in simple shear or torsion experiments up to shear strains of ~ 5 , but it underestimates the CPO strength and diverges from the experimental data at higher shear strains.

3.1.4 Discussion

Viscoplastic anisotropy under laboratory conditions

All polycrystal plasticity models analyzed in the present study reproduce qualitatively the mechanical results of **Hansen et**

al. (2012a): simple shear in a direction parallel to the [100] maximum on a plane normal to the [010] maximum requires lower stresses than axial extension parallel to the [010] maximum (**Figure 3.2a**). This behavior may be explained by simple geometrical considerations. In simple shear, re-solved shear stresses on the easy slip systems, (010)[100] and (001) [100], are high for most olivine crystals composing the aggregate, whereas if axial extension is imposed parallel to the [010] maximum resolved shear stresses are very low on these easy slip systems for most crystals.

Despite the qualitatively coherent results, the polycrystal plasticity models overestimate the magnitude of viscoplastic anisotropy relative to laboratory experiments for polycrystals with a well-developed CPO (**Figure 2b**). Based on the better agreement between the lower bound model predictions and the experimental data, we infer that the discrepancy between numerical models and experiments arises from imposing strain compatibility in a system that does not have enough degrees of freedom (< 4 independent slip systems). In the experiments, other strain accommodation mechanisms are active (recrystallization, grain boundary sliding or migration, diffusional mass transfer, climb, formation of kinks...). Some of these processes are isotropic, others are not. The fact that the viscous anisotropy measured in the laboratory is lower than the one predicted by VPSC simulations in which most of the deformation is accommodated by dislocation glide ($\beta = 50$) implies nevertheless that these additional processes play an important role in strain accommodation in the experiments. To test this hypothesis, we reduced the critical resolved shear stress of the dummy slip systems, which simulate the contribution of isotropic deformation processes to strain accommodation in the VPSC simulations. For strongly textured aggregates, models in which the strength of the dummy slip systems is 3 times higher than the strength of the easiest (010)[100] slip system in olivine do reproduce the magnitude of anisotropy measured in the laboratory experiments (**Figure 3.6**). In these models, the dummy systems contribute more to the total deformation when the polycrystal is in

hard orientation than when it is in a soft one (**Figure 3.7**), decreasing the magnitude of anisotropy. The present results are consistent with the previous analysis by **Hansen et al. (2016b)**, in which the mechanical data from the experiments simulated here together with other experiments on olivine aggregates were fitted by a pseudo-Taylor model that relaxed the strain compatibility constraint.

The SO-VPSC model modified to account for additional isotropic deformation processes, which produce plastic strain but no plastic spin, also better reproduces the CPO evolution measured in torsion experiments for $\beta = 5$ compared to predictions of the ‘standard’ VPSC model ($\beta = 50$). Higher contribution of the isotropic processes, which is associated with low β values, results in faster rotation of [100] maximum relative to shear plane and in slower evolution of the CPO intensity (**Figure 3.8**). These simulations reveal a CPO evolution in simple shear similar to the one predicted by the VPSC model modified to account for dynamic recrystallization by subgrain rotation, in which the strain compatibility was relaxed within subgrains (**Signorelli and Tommasi, 2015**). Both models therefore hint at the essential role of additional processes, which accommodate strain components that cannot be produced by dislocation glide in the deformation of olivine polycrystals. The modified VPSC model presented here therefore represents an acceptable alternative to predict olivine CPO evolution in simple shear, with a significantly lower calculation cost than VPSC models explicitly incorporating recrystallization.

The modified SO-VPSC simulations with $\beta = 3$, which better fit the viscoplastic anisotropy measured in the experiments, predict correctly the texture evolution observed in simple shear experiments up to shear strains of 5, but diverge from the experimental data by displaying an oscillatory behavior at higher shear strains. This oscillation is consistent with the fact that ellipsoidal inclusions embedded in a deformable media do not have any stable position in simple shear, but rotate continuously (**Jeffery, 1922**). Indeed, low β values result in a low strength of the equivalent homogeneous medium that represents the polycrystal in VPSC.

This interpretation is corroborated by the analysis of the SO-VPSC model in which the critical (maximum) aspect ratio of the crystals is changed. Higher critical aspect ratios result in higher oscillations of the CPO orientation (cf. supplementary material, **Figure S3.4**).

Comparison of the VPSC predictions to the experimental data suggests that although isotropic, the additional strain accommodation processes are associated with a non-linear mechanical behavior. The study of **Detrez et al. (2015)**, which first introduced additional isotropic deformation processes into the VPSC model, showed that significant activation of a Newtonian isotropic process resulted in a significant decrease of the apparent stress exponent of the polycrystal relative to the stress exponent associated with dislocation creep. The present study suggests that the mechanical data of **Hansen et al. (2012a)** are better reproduced by simulations in which the isotropic mechanisms accommodate a substantial proportion of the total viscoplastic deformation ($\geq 20\%$ in simple shear and $\geq 50\%$ in axial extension). Such a significant contribution from the isotropic processes would surely decrease the stress exponent if these processes were Newtonian. Yet, stress exponents measured in torsional experiments at high finite strains on polycrystals comprised by olivine F_{050} ($n = 4.1$, **Hansen et al., 2012b**) and F_{090} ($n = 3.3$, **Bystricky et al., 2000**) are high. We therefore suggest that the additional strain accommodation processes are probably non-Newtonian.

Viscoplastic anisotropy under upper mantle conditions

In the present simulations, we do not model specific additional deformation processes, but analyze their effect on the viscoplastic mechanical behavior of the textured rock (polycrystal) by modeling their contribution to strain accommodation. In other words, we calculate how the operation of these processes reduces the geometrical hardening. However, to extrapolate the conclusions of our analysis to the upper mantle, assumptions must be made about the nature of these processes. Increased amounts

of strain from diffusive mass transfer or sliding on grain boundaries relative to strain from dislocation glide are favoured by smaller grain sizes. This grain-size dependence has been clearly imaged *in situ* by the difference in strain distribution in deformation experiments on halite aggregates with different grain sizes (**Bourcier et al., 2013**). Thus, these grain-size sensitive processes are potentially more active in experiments that use fine-grained olivine polycrystals (5–20 μm) than during deformation of coarse-grained peridotites in the upper mantle. Indeed, strain rates measured during axial compression experiments on fine-grained (< 10 μm) olivine aggregates were up to 4.6 times higher than strain rates predicted by a lower bound model for the same textures and loading conditions, but no enhancement in strain rate relative to the models was observed for experiments on aggregates with coarser (> 100 μm) grain sizes (**Tielke et al., 2016**). In the present study, grain-size sensitivity of the additional processes is suggested by the comparison of the evolution of the CPO intensity in simple shear predicted by the modified SO-VPSC model and the CPO intensity measured experimentally (**Figure 3.8b**): the observations on the finest-grained aggregates are better fitted by models with lower β values, in which the dummy slip systems representing these additional processes are more active. One should note that the present results do not imply that grain-size sensitive processes are isotropic – these processes might be anisotropic in the presence of a shape-preferred orientation (**Wheeler, 2010**). The present work solely indicates that the additional processes operating in the experiments allow avoiding strain compatibility problems arising from the viscoplastic anisotropy of the olivine crystal by accommodating strain components that cannot be achieved by the activation of the easy slip systems in olivine.

The partitioning of deformation among different processes (dislocation glide, diffusive mass transfer, grain-boundary sliding, and others) depends on temperature, stress, and chemical environment, but all other conditions being similar, an increase in grain size should favor dislocation glide. Olivine grain sizes in

naturally deformed upper mantle rocks are typically plurimillimetric. Finer-grained peridotites are limited to shear zones (< 1 km wide) localized in the shallow parts of the lithospheric mantle and, even within these shear zones, in the absence of synkinematic reactions, olivine grain sizes are most often > 100 μm (cf. **Tommasi and Vauchez, 2015. Vauchez et al., 2012**). Thus, although strain rates and stresses are lower than in the experiments, one may expect a greater contribution of dislocation glide to plastic deformation in most of the upper mantle. If that is the case, our results suggest that the viscoplastic anisotropy of the upper mantle might be higher than the one measured in the experiments and better represented by the VPSC simulations in which the contribution of the dummy slip systems is reduced ($\beta > 10$).

By consequence, previous studies that coupled the standard VPSC model to finite element simulations, such as **Knoll et al. (2009), Tommasi et al. (2009), and Blackman et al. (2017)**, have estimated the maximum effect of olivine viscoplastic anisotropy on the reactivation of preexisting plate-scale structures for creating new plate boundaries (**Tommasi et al., 2009**) and on the flow and seismic anisotropy patterns beneath oceanic plates (**Blackman et al., 2017**). On the other hand, the ratios of 10–100 between normal and shear viscosity used in convection models by **Christensen (1987), Lev and Hager (2008, 2011), and Becker and Kawakatsu (2011)** moderately to strongly overestimate viscous anisotropy associated with strain-induced CPO in the upper mantle. Indeed, the CPO-induced viscoplastic anisotropy in olivine-rich rocks predicted by standard SO-VPSC models does not surpass a factor 6.

3.1.5 Conclusions

The viscoplastic anisotropy of olivine polycrystals deformed in simple shear and axial extension was modeled using three polycrystal plasticity models: the uniform stress (lower bound) approach and the tangent and second-order VPSC models, which was modified to account for variable contribution of other deformation processes in addition to

dislocation glide. The instantaneous mechanical responses predicted in the various simulations were compared to stresses measured in laboratory experiments for similar textures, loading geometries, and boundary conditions.

Laboratory data and numerical experiments suggest that the intensity of the viscoplastic anisotropy depends non-linearly on the CPO intensity. It increases faster for weak to moderate CPO intensities than at high CPO strengths. VPSC simulations in which strain is essentially accommodated by dislocation glide ($\beta = 50$) slightly underestimate the strength of the strongly textured aggregates relative to the strengths measured experimentally in torsion, but strongly overestimates the strength relatively to the experimental data in axial extension. This leads to overprediction of the viscoplastic anisotropy. Lower bound simulations, in which strain compatibility constraints are relaxed, better fit the experimental data. This suggests that in the laboratory experiments additional deformation processes operate, allowing the accommodation of the strain components that cannot be achieved by the activation of the easy slip systems in olivine.

The experimental data for the strongly textured aggregates is indeed well reproduced by the SO-VPSC model that includes dummy slip systems simulating additional isotropic strain accommodation processes without producing grain rotation. The best fit to the experimentally measured viscoplastic anisotropy is obtained for simulations in which the CRSS of the dummy systems is 3 times higher than the CRSS of the easiest slip system in olivine, (010)[100]. In these models, the dummy slip systems accommodate up to 50% of the viscoplastic deformation in axial extension and up to 20% of the deformation in simple shear. This modified SO-VPSC model also better reproduces the texture evolution measured in torsion experiments than the standard VPSC model. However, the best fit is obtained for simulations with lower activity of additional isotropic processes ($\beta = 5$). Simulations with $\beta = 3$ underestimate the CPO strength relatively to the experimental data and do not evolve into a stable orientation at high shear strains.

The present work implies that the

viscoplastic anisotropy associated with deformation by dislocation creep in the upper mantle may be decreased by the operation of additional strain accommodation processes. If we assume that in most of the upper mantle the contribution of deformation processes such as grain boundary sliding or diffusive mass transfer is lower than in the experiments due to larger grain sizes, the viscoplastic anisotropy should be well predicted by the standard SO-VPSC model. In high-stress shear zones in the shallow part of the lithospheric mantle, in which grain sizes are small, the viscoplastic anisotropy is probably reduced and better predicted by the modified SO-VPSC model. The standard ($\beta = 50$) and modified ($\beta = 3-5$) SO-VPSC models therefore reflect the possible range of texture-induced viscoplastic anisotropy in the upper mantle, that is, the viscous anisotropy relevant to domains of the upper mantle deforming dominantly by dislocation creep. The present simulations, which use CRSS for the olivine slip systems derived from high temperature low pressure single crystal experiments, provide good predictions of anisotropic viscous deformation for the upper 200–250 km of the mantle. Different CRSS derived from high-pressure experiments should be used for deeper parts of the upper mantle.

Acknowledgments

We thank Ricardo Lebensohn and Carlos Tomé for making the code VPSC7c, which includes most of the last developments in viscoplastic self-consistent modeling, freely available. We also gratefully acknowledge Alain Vauchez, Sylvie Demouchy, Catherine Thoraval for discussions and Manuel Thieme and Sonia Ouadahi for comments on the figures. Anonymous reviewers are thanked for insightful comments. This project received funding from the European Union's Horizon 2020 research and innovation program under the Marie Skłodowska-Curie grant agreement No. 642029 (ITN-CREEP) and from the CNRS (France) and CONICET (Argentina) under the *Project International de Cooperation Scientifique* MicroTex (No. 067785).

REFERENCES

- Bai, Q., Mackwell, S.J., Kohlstedt, D.L., 1991. High-temperature creep of olivine single crystals 1. Mechanical results for buffered samples. *J. Geophys. Res.* 96, 2441–2460. <https://doi.org/10.1029/90JB01723>.
- Becker, T.W., Kawakatsu, H., 2011. On the role of anisotropic viscosity for plate-scale flow. *Geophys. Res. Lett.* 38, 1–5. <https://doi.org/10.1029/2011GL048584>.
- Blackman, D.K., Boyce, D.E., Castelnau, O., Dawson, P.R., Laske, G., 2017. Effects of crystal preferred orientation on upper-mantle flow near plate boundaries: rheologic feedbacks and seismic anisotropy. *Geophys. J. Int.* 210 (3), 1481–1493. <https://doi.org/10.1093/gji/ggx251>.
- Bourcier, M., Bornert, M., Dimanov, A., Héripré, E., Raphanel, J.L., 2013. Multiscale experimental investigation of crystal plasticity and grain boundary sliding in synthetic halite using digital image correlation. *J. Geophys. Res. Solid Earth* 118, 511–526. <https://doi.org/10.1002/jgrb.50065>.
- Bystricky, M., Kunze, K., Burlini, L., Burg, J.P., 2000. High shear strain of olivine aggregates: rheological and seismic consequences. *Science* 290, 1564–1567. <https://doi.org/10.1126/science.290.5496.1564>.
- Castelnau, O., Brenner, R., Lebensohn, R.A., 2006. The effect of strain heterogeneity on the work hardening of polycrystals predicted by mean-field approaches. *Acta Mater.* 54, 2745–2756. <https://doi.org/10.1016/j.actamat.2006.02.014>.
- Castelnau, O., Blackman, D.K., Lebensohn, R.A., Castañeda, P.P., 2008. Micromechanical modeling of the viscoplastic behavior of olivine. *J. Geophys. Res. Solid Earth* 113, 1–18. <https://doi.org/10.1029/2007JB005444>.
- Castelnau, O., Blackman, D.K., Becker, T.W., 2009. Numerical simulations of texture development and associated rheological anisotropy in regions of complex mantle flow. *Geophys. Res. Lett.* 36, 1–6. <https://doi.org/10.1029/2009GL038027>.
- Chastel, Y.B., Dawson, P.R., Wenk, H.-R., Bennett, K., 1993. Anisotropic convection with implications for the upper mantle. *J. Geophys. Res.* 98, 17757–17771. <https://doi.org/10.1029/93JB01161>.
- Chopra, P.N., Paterson, M.S., 1984. The role of water in the deformation of dunite. *J. Geophys. Res.* 89, 7861–7876. <https://doi.org/10.1029/JB089iB09p07861>.
- Christensen, U., 1987. Some geodynamical effects of anisotropic viscosity. *Geophys. J. R. Astr. Soc.* 91, 711–736. <https://doi.org/10.1111/j.1365-246X.1987.tb01666.x>.
- Demouchy, S., Tommasi, A., Barou, F., Mainprice, D., Cordier, P., 2012. Deformation of olivine in torsion under hydrous conditions. *Phys. Earth Planet. Inter.* 202–203, 56–70. <https://doi.org/10.1016/j.pepi.2012.05.001>.
- Detrez, F., Castelnau, O., Cordier, P., Merkel, S., Raterron, P., 2015. Effective viscoplastic behavior of polycrystalline aggregates lacking four independent slip systems inferred from homogenization methods. application to olivine. *J. Mech. Phys. Solids* 83, 199–220. <https://doi.org/10.1016/j.jmps.2015.05.022>.
- Durinck, J., Carrez, P., Cordier, P., 2007. Application of the Peierls-Nabarro model to dislocations in forsterite. *Eur. J. Mineral.* 19, 631–639. <https://doi.org/10.1127/0935-1221/2007/0019-1757>.
- Hansen, L.N., Zimmerman, M.E., Kohlstedt, D.L., 2012a. Laboratory measurements of the viscous anisotropy of olivine aggregates. *Nature* 492, 415–418. <https://doi.org/10.1038/nature11671>.
- Hansen, L.N., Zimmerman, M.E., Kohlstedt, D.L., 2012b. The influence of microstructure on deformation of olivine in the grain-boundary sliding regime. *J. Geophys. Res.* 117, 1–17. <https://doi.org/10.1029/2012JB009305>.
- Hansen, L.N., Zimmerman, M.E., Dillman, A.M., Kohlstedt, D.L., 2012c. Strain localization in olivine aggregates at high temperature: a laboratory comparison of constant-strain-rate and constant-stress boundary conditions. *Earth Planet. Sci. Lett.* 333–334, 134–145. <https://doi.org/10.1016/j.epsl.2012.04.016>.
- Hansen, L.N., Zhao, Y.H., Zimmerman, M.E., Kohlstedt, D.L., 2014. Protracted fabric evolution in olivine: implications for the relationship among strain, crystallographic fabric, and seismic anisotropy. *Earth Planet. Sci. Lett.* 387, 157–168. <https://doi.org/10.1016/j.epsl.2013.11.009>.
- Hansen, L.N., Warren, J.M., Zimmerman, M.E., Kohlstedt, D.L., 2016a. Viscous anisotropy of textured olivine aggregates, Part 1: measurement of

the magnitude and evolution of anisotropy. *Earth Planet. Sci. Lett.* 445, 92–103.
<https://doi.org/10.1016/j.epsl.2016.04.008>.

Hansen, L.N., Conrad, C.P., Boneh, Y., Skemer, P., Warren, J.M., Kohlstedt, D.L., 2016b. Viscous anisotropy of textured olivine aggregates: 2. Micromechanical model. *J. Geophys. Res. Solid Earth* 121, 7137–7160.
<https://doi.org/10.1002/2016JB013240>.

Honda, S., 1986. Strong anisotropic flow in a finely layered asthenosphere. *Geophys. Res. Lett.* 13, 1454–1457. <https://doi.org/10.1029/GL013i013p01454>.

Jeffery, G.B., 1922. The motion of ellipsoidal particles immersed in a viscous fluid. *Proc. Royal Soc. A* 102. <https://doi.org/10.1098/rspa.1922.0078>.

Knoll, M., Tommasi, A., Logé, R.E., Signorelli, J.W., 2009. A multiscale approach to model the anisotropic deformation of lithospheric plates. *Geochem. Geophys. Geosyst.* 10, 1–18.
<https://doi.org/10.1029/2009GC002423>.

Kumazawa, M., Anderson, O.L., 1969. Elastic moduli, pressure derivatives, and temperature derivatives of single-crystal olivine and single-crystal forsterite. *J. Geophys. Res.* 74, 5961–5972.
<https://doi.org/10.1029/JB074i025p05961>.

Lebensohn, R.A., Tomé, C.N., 1993. A self-consistent anisotropic approach for the simulation of plastic deformation and texture development of polycrystals: application to zirconium alloys. *Acta Metall. Mater.* 41, 2611–2624.
[https://doi.org/10.1016/0956-7151\(93\)90130-K](https://doi.org/10.1016/0956-7151(93)90130-K).

Lebensohn, R.A., Ponte Castañeda, P., Brenner, R., Castelnau, O., 2011. Full-field vs. homogenization methods to predict microstructure-property relations for polycrystalline materials. In: *Computational Methods for Microstructure-Property Relationships*. Springer, New York, pp. 393–441.

Lebensohn, R.A., Kanjarla, A.K., Eisenlohr, P., 2012. An elasto-viscoplastic formulation based on fast Fourier transforms for the prediction of micromechanical fields in polycrystalline materials. *Int. J. Plast.* 32–33, 59–69. <https://doi.org/10.1016/j.ijplas.2011.12.005>.

Lev, E., Hager, B.H., 2008. Rayleigh-Taylor instabilities with anisotropic lithospheric viscosity. *Geophys. J. Int.* 173, 806–814.
<https://doi.org/10.1111/j.1365-246X.2008.03731.x>.

Lev, E., Hager, B.H., 2011. Anisotropic viscosity changes subduction zone thermal structure. *Geochem. Geophys. Geosyst.* 12, 1–9. <https://doi.org/10.1029/2010GC003382>.

Mainprice, D., Bachmann, F., Hielcher, R., Schaeben, H., 2014. Descriptive tools for the analysis of texture projects with large datasets using MTEX—Strength, symmetry and components. In: Faulkner, D.R., Mariani, E., Mecklenburgh, J. (Eds.), *Rock Deformation from Field, Experiments and Theory: A Volume in Honour of Ernie Rutter*, Spec. Publ. Geol. Soc., London, U. K., pp. 409
<http://dx.doi.org/10.1144/SP409.8>.

Nicolas, A., Christensen, N.I., 1987. Formation of anisotropy in upper mantle peridotites: a review, in *Composition, Structure and Dynamics of the Lithosphere–Asthenosphere System*. *Am. Geophys. Union Geo-Dyn. Monogr. Ser.*, vol. 16, pp. 111–123.
<https://doi.org/10.1029/GD016>.

Ponte Castañeda, P., 2002. Second-order homogenization estimates for nonlinear composites incorporating field fluctuations: I—theory. *J. Mech. Phys. Solids* 50, 737–757.
[https://doi.org/10.1016/S0022-5096\(01\)00099-0](https://doi.org/10.1016/S0022-5096(01)00099-0).

Raterron, P., Chen, J., Li, L., Weidner, D., Cordier, P., 2007. Pressure-induced slip-system transition in forsterite: single-crystal rheological properties at mantle pressure and temperature. *Am. Mineral.* 92, 1436–1445. <https://doi.org/10.2138/am.2007.2474>.

Sachs, G., 1928. Zur Ableitung einer Fließbedingung. *Z. Ver. Dtsch. Ing.* 72, 734–736.

Signorelli, J., Tommasi, A., 2015. Modeling the effect of subgrain rotation recrystallization on the evolution of olivine crystal preferred orientations in simple shear. *Earth Planet. Sci. Lett.* 430, 356–366.
<https://doi.org/10.1016/j.epsl.2015.08.018>.

Thieme, M., Demouchy, S., Mainprice, D., Barou, F., Cordier, P., 2018. Stress evolution and associated microstructure during transient creep of olivine at 1000–1200 °C. *Phys. Earth Planet. Inter.* 278, 34–46.
<https://doi.org/10.1016/j.pepi.2018.03.002>.

Tielke, J.A., Hansen, L.N., Tasaka, M., Meyers, C., Zimmerman, M.E., Kohlstedt, D.L., 2016. Observations of grain size sensitive power law creep of olivine aggregates over a large range of lattice-preferred orientation strength. *J. Geophys. Res.* 121, 506–516. <https://doi.org/10.1002/2015JB012302>.

Tommasi, A., Mainprice, D., Canova, G., Chastel, Y., 2000. Viscoplastic self-consistent and equilibrium-based modeling of olivine lattice preferred orientations: implications for the upper mantle seismic anisotropy. *J. Geophys. Res.* 105, 7893–7908. <https://doi.org/10.1029/1999JB900411>.

Tommasi, A., Vauchez, A., 2001. Continental rifting parallel to ancient collisional belts: an effect of the mechanical anisotropy of the lithospheric mantle. *Earth Planet. Sci. Lett.* 185, 199–210. [https://doi.org/10.1016/S0012-821X\(00\)00350-2](https://doi.org/10.1016/S0012-821X(00)00350-2).

Tommasi, A., Knoll, M., Vauchez, A., Signorelli, J.W., Thoraval, C., Logé, R., 2009. Structural reactivation in plate tectonics controlled by olivine crystal anisotropy. *Nat. Geosci.* 2, 423–427. <https://doi.org/10.1038/ngeo528>.

Tommasi, A., Vauchez, A., 2015. Heterogeneity and anisotropy in the lithospheric mantle. *Tectonophysics* 661, 11–37. <https://doi.org/10.1016/j.tecto.2015.07.026>.

Tommasi, A., Tiko, B., Vauchez, A., 1999. Upper mantle tectonics: Three-dimensional deformation, olivine crystallographic fabrics and seismic properties. *Earth Planet. Sci. Lett.* 168, 173–186. [https://doi.org/10.1016/S0012-821X\(99\)00046-1](https://doi.org/10.1016/S0012-821X(99)00046-1).

Vauchez, A., Tommasi, A., Mainprice, D., 2012. Faults (shear zones) in the Earth's mantle. *Tectonophysics* 558–559, 1–27. <https://doi.org/10.1016/j.tecto.2012.06.006>.

Vauchez, A., Tommasi, A., Barruol, G., 1998. Rheological heterogeneity, mechanical anisotropy and deformation of the continental lithosphere. *Tectonophysics* 296, 61–86. [https://doi.org/10.1016/S0040-1951\(98\)00137-1](https://doi.org/10.1016/S0040-1951(98)00137-1).

Wenk, H.R., Bennett, K., Canova, G.R.A., Molinari, 1991. Modelling plastic deformation of peridotite with the self-consistent theory. *J. Geophys. Res.* 96, 8337–8349. <https://doi.org/10.1029/91JB00117>.

Wenk, H.R., Armann, M., Burlini, L., Kunze, K., Bortolotti, M., 2009. Large strain shearing of halite: experimental and theoretical evidence for dynamic texture changes. *Earth Planet. Sci. Lett.* 280, 205–210. <https://doi.org/10.1016/j.epsl.2009.01.036>.

Wheeler, J., 2010. Anisotropic rheology during grain boundary diffusion creep and its relation to grain rotation, grain boundary sliding and superplasticity. *Philos. Mag.* 37–41.

<https://doi.org/10.1080/14786431003636097>.

Zhang, S., Karato, S.I., 1995. Lattice preferred orientation of olivine aggregates deformed in simple shear. *Nature*. <https://doi.org/10.1038/375774a0>.

3.1.6 Supplementary material of the article #1

The supplementary material comprises:

(1) a presentation of the methods used to define the components of the velocity gradient tensor in extension and simple shear, to calculate the Von Mises equivalent stresses and strain rates, and to normalize the experimental data in torsion and axial extension to a constant value of the norm of the strain rate.

(2) a comparison between TGT- and SO-VPSC predictions for different boundary conditions (mixed vs. kinematic. **Figure S3.1**) and stress exponent n values (Fig. S3.2).

(3) a comparison of the effect of varying the strength of the dummy slip systems (β) on the mechanical behavior of the aggregate predicted by TGT- and SO-VPSC models (**Figure S3.3**).

(4) a comparison of the effect of varying the critical (maximum) aspect ratio of olivine for SO-VPSC models with the strength of the dummy slip systems (β) equals to 50 and 3 (**Figure S3.4**).

(5) a presentation of the pole figures showing the CPO evolution with increasing shear strain (γ) as a function of the strength of the dummy slip systems in modified SO-VPSC models (**Figure S3.5**).

Methods

Norm of the strain-rate tensor in simple shear and axial extension

For comparison between simulations in simple shear and axial extension we imposed that the norm of the overall strain rate tensor¹ in both cases equals 1.

1

The average first-order moment of the equivalent stress and strain rate was used. The SO-VPSC formulation allow to express the this quantities using the second-order moment of the equivalent stress and strain rate as the average of the corresponding magnitudes at the grain level, defined as $\sigma_{eq}^{(g)} = \sqrt{\frac{3}{2} \sigma_{ij}^{(g)} \sigma_{ij}^{(g)}}$ and $\dot{\epsilon}_{eq}^{(g)} = \sqrt{\frac{2}{3} \dot{\epsilon}_{ij}^{(g)} \dot{\epsilon}_{ij}^{(g)}}$. However, these expressions are only valid for linear and isotropic cases (see VPSC7c Manual for further details).

$$\|\dot{\epsilon}\|^2 = \dot{\epsilon}_{ij}\dot{\epsilon}_{ij} = 1$$

In axial extension 22, the velocity gradient tensor is thus defined as:

$$L_{\text{ext}} = \dot{\epsilon}_{\text{ext}} = \begin{bmatrix} -a & 0 & 0 \\ 0 & 2a & 0 \\ 0 & 0 & -a \end{bmatrix}$$

with a :

$$a = 1/\sqrt{6}$$

In simple shear 12 the velocity gradient tensor is defined as:

$$L_{\text{ss}} = \begin{bmatrix} 0 & 2a & 0 \\ 0 & 0 & 0 \\ 0 & 0 & 0 \end{bmatrix} \cdot \dot{\epsilon}_{\text{ss}} = \begin{bmatrix} 0 & a & 0 \\ a & 0 & 0 \\ 0 & 0 & 0 \end{bmatrix}$$

with a :

$$a = 1/\sqrt{2}$$

Von Mises equivalent strain rate and stress¹

Von Mises equivalent strain rate ($\dot{\epsilon}_{\text{eq}}$) and stress (σ_{eq}) are scalar quantities. Their product results in the same viscoplastic work rate (\dot{w}) as the dot product of the deviatoric stress and strain rate tensors:

$$\dot{w} = \sigma'_{ij} \dot{\epsilon}_{ij} = \sigma_{\text{eq}} \dot{\epsilon}_{\text{eq}}$$

The equivalent stress in the Von Mises sense is defined as:

$$\sigma_{\text{eq}}^{\text{vm}} = \sqrt{\frac{3}{2} \sigma'_{ij} \sigma'_{ij}}$$

The Von Mises equivalent strain rate is calculated by enforcing the work conjugate condition:

$$\dot{\epsilon}_{eq} = \frac{\dot{w}}{\sigma_{eq}}$$

Normalization of experimental data to a constant value of the norm of the strain rate tensor for comparison between torsion and axial extension mechanical data

The stresses measured in the laboratory by **Hansen et al. (2012a)** were normalized to a constant Von Mises equivalent strain rate ($\dot{\epsilon}_{eq}$) of 2×10^{-4} following the general constitutive relation:

$$\dot{\epsilon}_{eq} = A (\sigma_{eq})^n$$

in which σ_{eq} is the Von Mises equivalent stress, A is a material constant, and n the stress exponent, which in the experiments is equal to 4.1. The Von Mises equivalent stress is thus recalculated (σ_{eq}^*) for $\dot{\epsilon}_{eq} = 2 \times 10^{-4} \text{ s}^{-1}$ according to:

$$\sigma_{eq}^* = \left(\frac{2 \times 10^{-4}}{\dot{\epsilon}_{eq} / \sigma_{eq}^{4.1}} \right)^{1/4.1}$$

Supplementary Figures

The supplementary figures were already discussed in the context of the published article #1, therefore, it will only be presented with a short legend description.

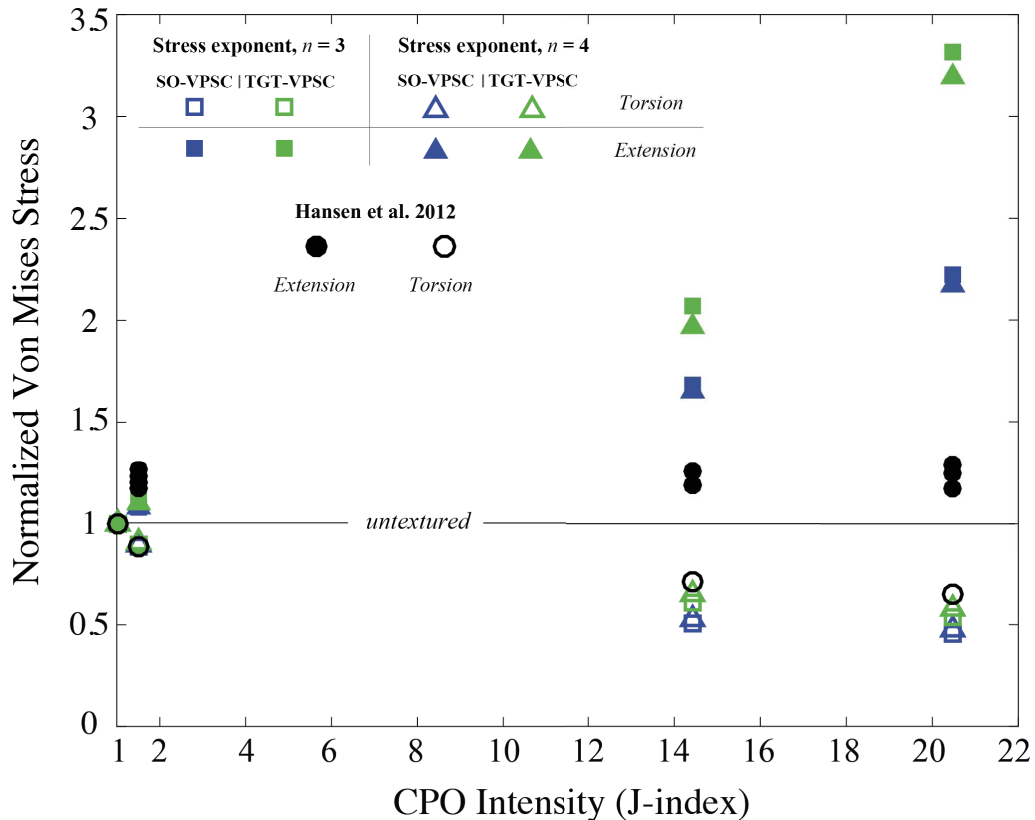


Figure S3.1: Effect on the Von Mises equivalent stresses (normalized to the behavior of an isotropic polycrystal) of varying the stress exponent (n) between 3 and 4 for SO- and TGT-VPSC models in simple shear and axial extension. Empty and filled black circles indicate the laboratory data (Hansen et al. 2012a) and empty and filled color markers represent model predictions.

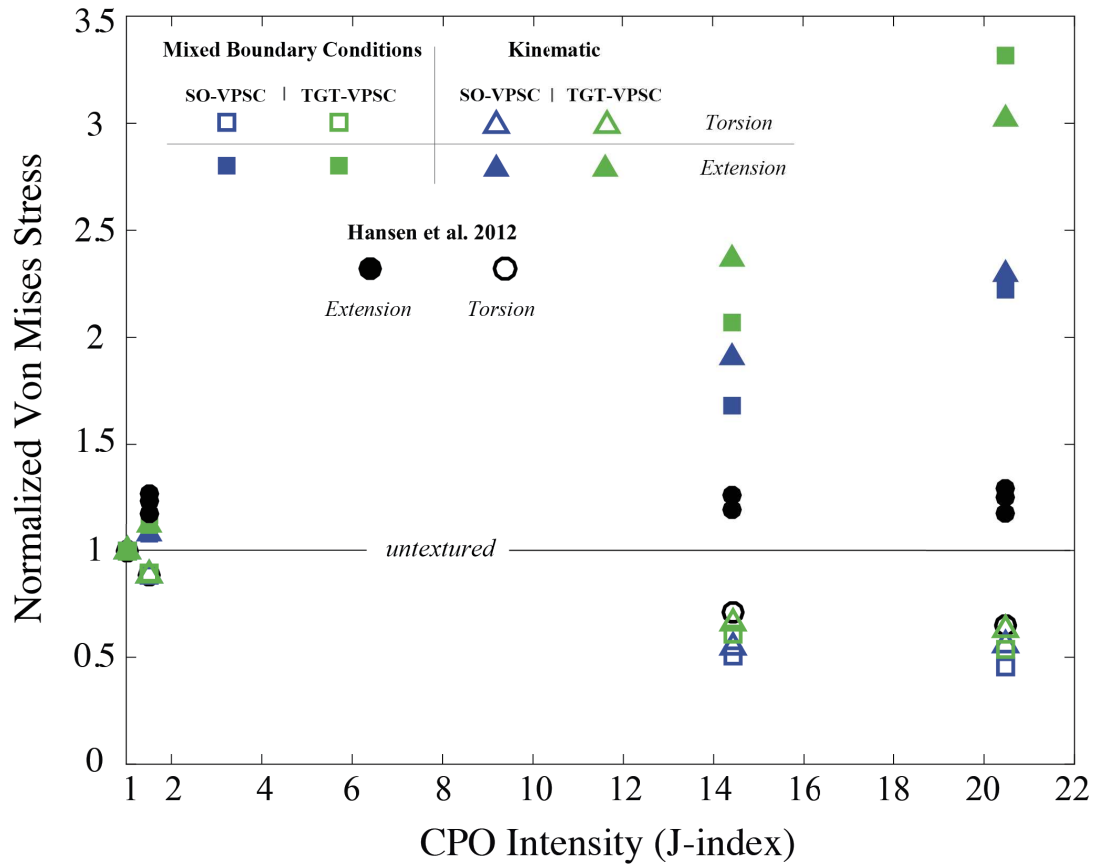


Figure S3.2: Effect on the Von Mises equivalent stresses (normalized to the behavior of the isotropic olivine polycrystal) of changing boundary conditions (fully kinematic or mixed) for SO- and TGT-VPSC simulations in simple shear (empty markers) and axial extension (filled markers) solicitations. Empty and filled black circles indicate the laboratory data (**Hansen et al. 2012a**), and the colour markers represent the model predictions.

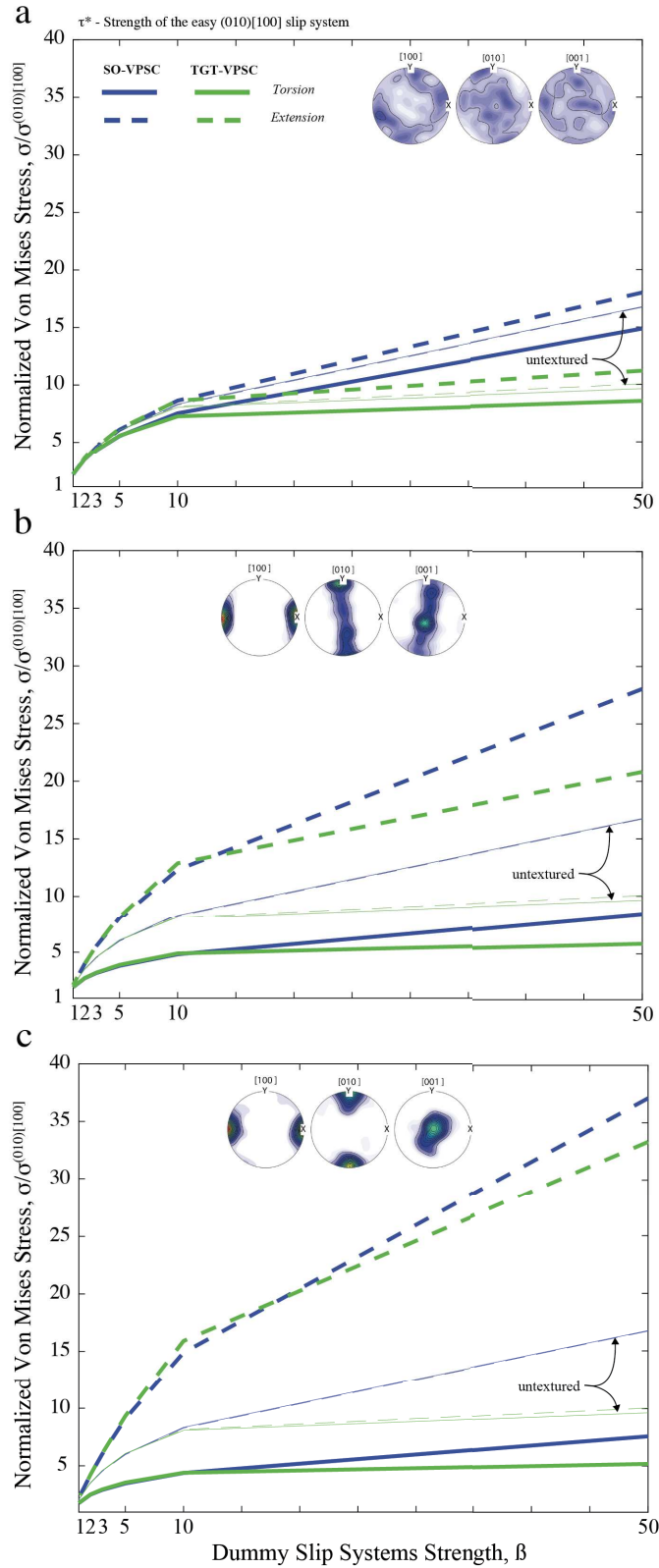


Figure S3.3: Effect on the Von Mises equivalent stresses (normalized by the strength of the easy (010)[100] slip system) of varying the dummy slip systems strength (β) on the stresses predicted by the SO- and TGT- VPSC models in simple shear (thick solid lines) and axial extension (thick dashed lines). **a)** PT0655, **b)** PT0640 and **c)** PT0651.

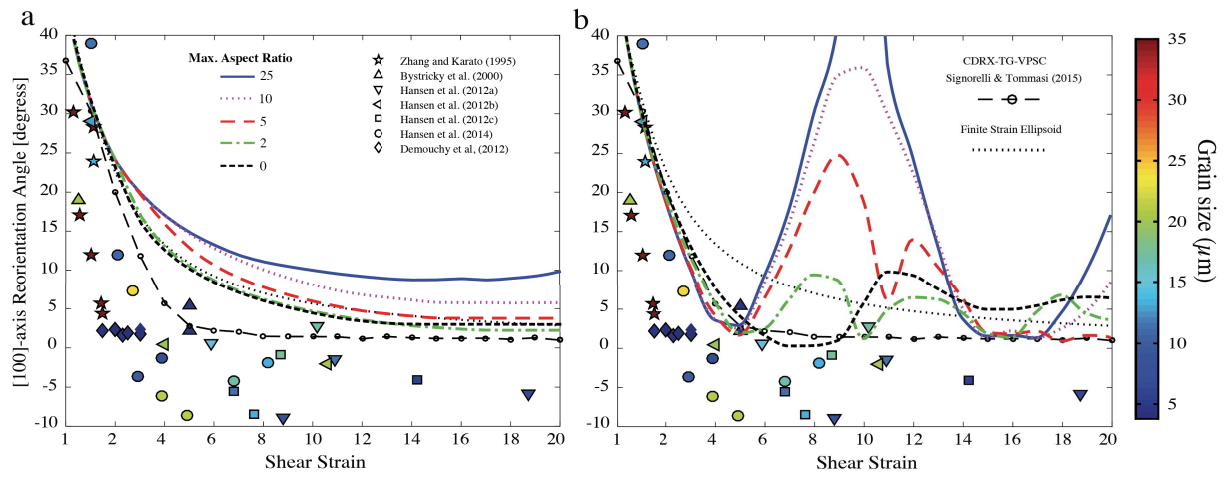


Figure S3.4: Effect of varying the maximum aspect ratio (25, 10, 5, 2, 0) of olivine on the CPO reorientation predicted by SO-VPSC simulations with the strengths of dummy slip systems (β) equals to **a)** 50 and **b)** 3. For details refers to figure 8 of the article.

3.2 Comparison between numerical and experimental data of olivine polycrystal deformed in extension followed by torsion

3.2.1 Introduction

In this section I compared the VPSC prediction with laboratory experiments by **Hansen et al., 2016**, which consisted of torsional solicitation with shear plane oriented normal to a previous extension that formed the initial olivine CPO. This consists in the opposite deformation kinematics applied in the experiments reported in previous section, which result in considerably different textures and loading-geometries.

3.2.2 Methods

The numerical experiments here presented follows the same methodology and model setup presented in the supplementary material of **Mameri et al., 2019**. The instantaneous viscoplastic response of the olivine polycrystals was calculated using the SO- and TGT-VPSC and Lower bound models with the norm of the overall strain rate tensor in extension and simple shear equals to 1. The VPSC models does not account for the effect of isotropic mechanism, then, the strength of the pyramidal slip system is (β) 50 times higher than the ‘easy’ slip system (‘standard’ VPSC models). Exactly the same olivine CPO measured in the laboratory experiments by **Hansen et al., 2016** was used in the numerical experiments, as well as equivalent loading-geometries and boundary conditions. The stresses obtained numerically in extension and simple shear were compared, to the final extension and initial torsional stresses measured in laboratory, respectively.

Simulations were ran for both kinematic and mixed boundary conditions (B.C), but no significant difference in the mechanical response is observed between both B.C, then for sake of simplicity, only the results for the kinematic B.C are shown. The slips systems available, the critical resolved shear stresses (CRSS), and the stress exponents are similar to those in the previous comparison (with the **Hansen, et al., 2012**), with a slight difference in the CRSS of the (001)[100], which in the present comparison was set to 1 instead of the value of 1.5. The influence of grain size on the measured aggregate strength at laboratory conditions was tested by recalculating the final stresses at the end of the extension to the initial grain-sizes following the relation, $\sigma_{\text{new}} = \left(\frac{\dot{\epsilon}_1 \times d^p}{A} \right)^{1/n}$, where n is the stress exponent ($n = 4.1$), d the initial grain-size, p the grain-size exponent ($p = 0.73$), A is material constant and $\dot{\epsilon}_1$ the

strain-rate measured in laboratory.

3.2.3 Results

Comparison between instantaneous stresses predicted by models (coloured markers) and the stresses measured experimentally (black circles) as a function of the CPO intensity is shown in the **Figure 3.9** (normalized to the strength of the random polycrystal τ^{iso}). The models are able to qualitatively reproduce the aggregate behavior measured in the laboratory experiments, that is, final stresses in extension (sub-perpendicular to [010]-girdle of CPO) are weaker than simple shear normal to it (sub-parallel to [010]-girdle of CPO). However, stresses measured in laboratory are underestimated in all simulations, which display stresses closer to the isotropic response, notably in torsional deformation.

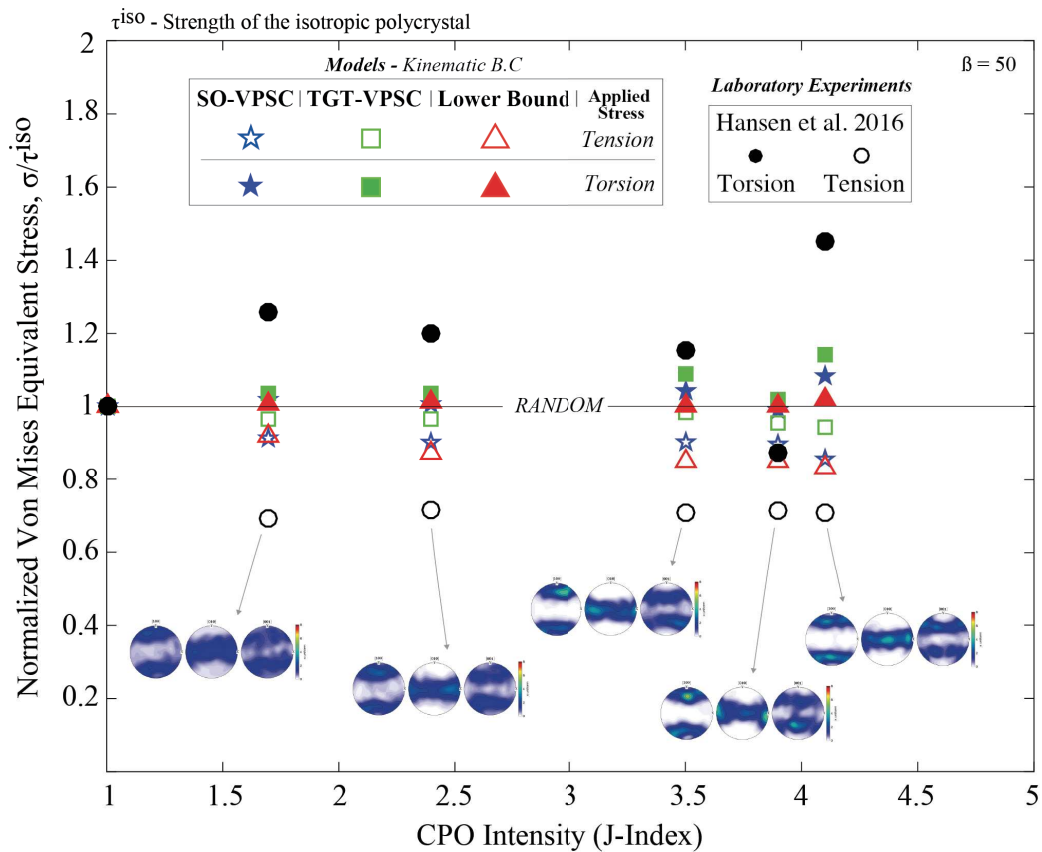


Figure 3.9: Von Mises equivalent stresses (normalized to the behavior of a random texture polycrystal) as a function of the olivine CPO intensity for laboratory and numerical experiments. Empty markers represent axial extension parallel to the [100] maximum. Filled markers represent simple shear in a plane parallel to the [010] girdle, in a direction perpendicular to the [100] maximum of the preexisting CPO.

The magnitude of mechanical anisotropy was calculated using the ratio between

simple shear and extension stresses as a function of CPO intensity (**Figure 3.10**). In the laboratory experiments, simple shear flow stresses are a factor 2 to 1.25 times higher than extensional stresses (filled black circles). The numerical experiments (filled coloured markers), for most of the simulations, predict anisotropy below the minimum value measured in the laboratory. A weak positive correlation between CPO intensity and anisotropy is predicted in the models, while in the laboratory experiments this trend is not observed. The stresses measured in the laboratory for final grain sizes (grain size indicated next to the filled black circle) when recalculated for initial grain sizes ($27\mu\text{m}$, red empty circles) better approach the anisotropy predicted by the models, but the discrepancy between numerical and laboratory experiments remain considerable.

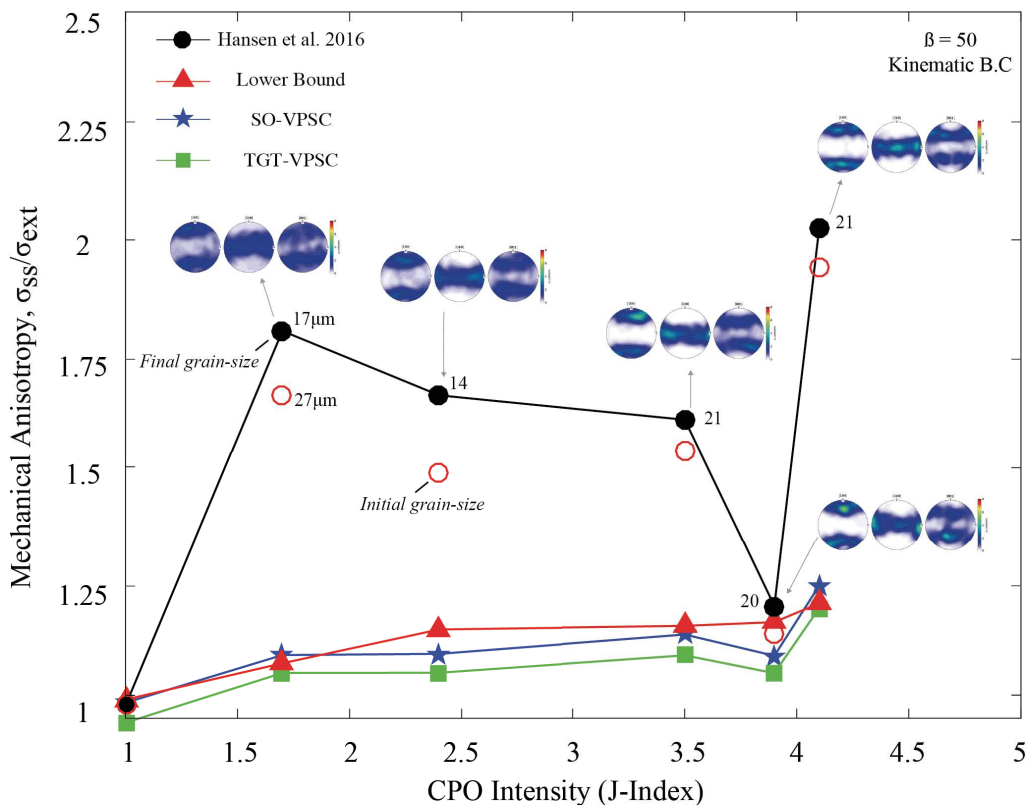


Figure 3.10: Magnitude of mechanical anisotropy (ratio between Von Mises equivalent stresses in extension and torsion) predicted by numerical models and measured by laboratory experiments as a function of CPO intensity.

The slip system activity (in %) as a function of the CPO intensity was calculated for the SO-VPSC model (**Figure 3.11**). The lower stresses predicted in extensional perpendicular to the [010]-girdle of the preexisting olivine CPO results from higher activities of the easy (001)[100] slip system (CRSS=1), which it is increased from 30% in the isotropic polycrystal

to 60% in the aggregates with the higher intensity of CPO (J-index ≈ 4). The (010)[001] slip system (CRSS=2) accommodates from 30% to 10% of the total viscoplastic deformation in extension. The higher stresses in simple shear compared to the extension result from lower resolved shear stresses on the easy (010)[100] slip system in most of crystals, which accommodated <40% of deformation. This occurs because of the [100] maximum of olivine is orientated at high angles to the imposed shear plane. The activation of the hard (010)[001] slip system in simple shear is not negligible, being roughly constant around $\sim 30\%$.

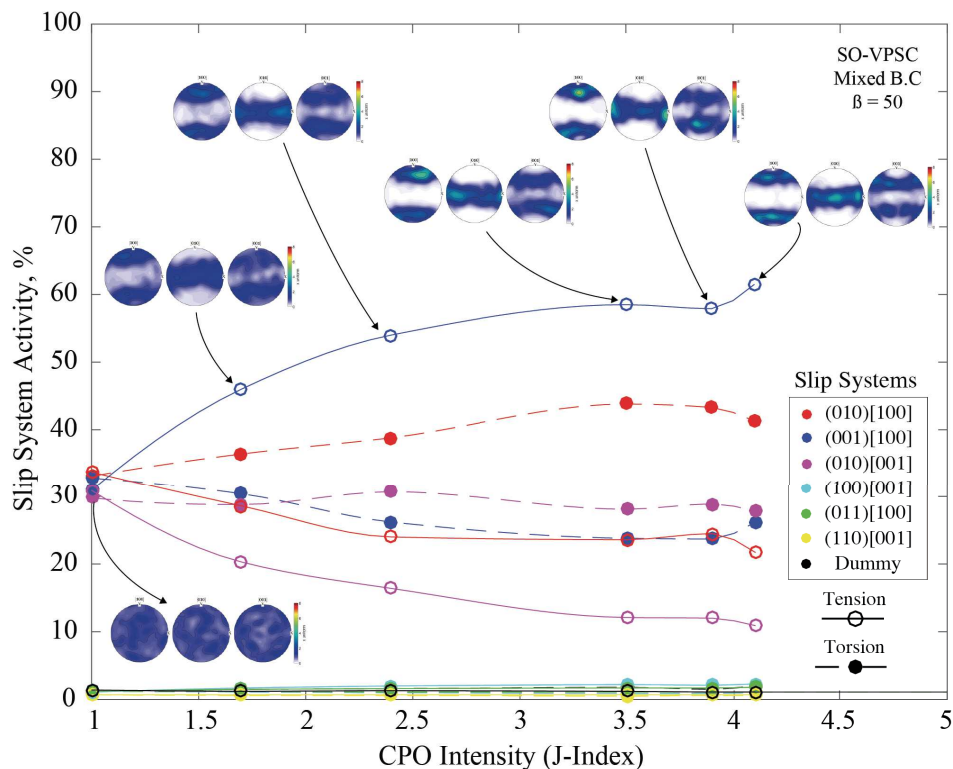


Figure 3.11: Slip systems activation predicted by SO-VPSC model for simple shear (filled markers linked by dashed lines) and axial extension (empty markers linked by solid lines). The sum of the activity of the three ‘dummy’ systems is shown by the black circles.

3.2.4 Discussions

The qualitative agreement between the VPSC (robust dislocation-based microphysical model) and laboratory experiments, together with the CPO evolution coherent [100]-glide-dominated deformation suggest that dislocation creep accommodates a significant portion of the polycrystal deformation at laboratory conditions. In agreement with Hansen et al. (2012) and Mameri et al. (2019), the models underestimate the viscous anisotropy of olivine aggregates that have weak CPO. However, these results cannot be explained employing the same modelling philosophy in Mameri et al. (2019), in which the lower mechanical

anisotropy measured in the laboratory was explained in terms of the activation of an isotropic deformation processes in addition to dislocation creep.

VPSC simulations accounts for intracrystalline glide in a very robust physical basis (glide + recovery allowing to fully avoid hardening), which dislocation creep in olivine result from glide in a very limited number of slip (shear) directions in 3 dominant slip system with significant difference in relative strengths. But, to fit the data published by **Hansen et al. (2016)**, one needs to consider a deformation process that is more mechanical anisotropic than dislocation creep. In the light of the result presented in **Mameri et al., 2019**, this deformation process (if it exist) has to decrease the magnitude of the anisotropy at high finite strain (strong CPO), and decrease it at low finite strain (weak CPOs). Once the experiments conditions are very similar, it is unlikely that the activated deformation processes are significantly different between both experiments. Moreover, the contribution of this additional deformation process must vary weakly with CPO intensity, since despite the large range of CPO intensity (J-index = 1,5 – 21), the mechanical anisotropy measured in the laboratory experiments lied below a factor 2.

Hansen et al. (2016b) fitted the mechanical behavior in the experiments using a pseudo-Taylor model. This approach approximates the strain rate tensor in the grain to the strain rate tensor in the polycrystal deforming in only three (common) slip systems of olivine. Slip systems available and their strengths are comparable to the ones in ours models, but the (010)[001] system is 4 times harder than the easy (010)[100], instead of 2 times. In their model the strain misfit between the grain and polycrystal, resulting from the lack of slip systems to accommodate arbitrary plastic deformation, is partially neglected, This corresponds to consider that there exists another deformation process that accommodates the strain incompatibility without contributing to the strength of the aggregate. In our SO-VPSC calculations however strain compatibility is respected at the aggregate scale. The additional isotropic process that was added (ensuring that compatibility respected) does contribute to the calculation of the mechanical behavior of the aggregate.

In our view there are no general principles of polycrystalline plasticity that explain both laboratory results in the same microphysical framework. The existence of a secondary deformation processes in olivine polycrystal deformed at laboratory conditions that gather all the features described above is unknown. The existence of this process at geological conditions is even more uncertain. But, it is worthy to mention that very little is known about anisotropy of grain boundary properties (**Wheeler, 2010. review in Marquardt and Faul,**

2018), for instance, the importance of contrast in sliding velocities for the polycrystal anisotropy. Yet, is unlikely that these mechanisms are more anisotropic than shear in specific directions of just a few available slip system that have different strength, such as during dislocation creep in olivine at high temperature.

3.3 Viscoplastic anisotropy associated with fossil (common) olivine CPOs in the lithospheric mantle

For completeness of the study on the controlling parameters of CPO-induced viscous anisotropy at the rock-scale, VPSC simulations were run for different olivine CPOs created numerically under different finite strains (CPO intensity) and deformation regimes (CPO symmetries). These CPOs were deformed in simple shear, axial extension and compression at different orientations relative to the preexisting orthorhombic, axial-[100] and -[010] olivine CPOs (from 0° to 90°, at every 15°. Either mixed or kinematic boundary conditions were imposed. The CPOs symmetries and intensities that were used in this parametric studies are representative of most olivine CPOs measured (>80%) in peridotites massif and xenoliths collected in different tectonic settings worldwide (Tommasi and Vauchez, 2015).

3.3.1 Method

The numerical experiments follow the same methodology presented in previous sections. The instantaneous viscoplastic responses of the olivine polycrystals were predicted (i.e. no CPO evolution). For comparison between simulations in simple shear and axial extension the norm of the strain rate tensor in both cases equals 1. The dummy slip systems, have strength 50 times higher than the easy slip system (standard VPSC model). The relative strength of slips systems available are the same used in the comparison with Hansen et al., 2016, that is, it has glide in the [100] ‘easy’ direction two times higher than glide in the [001] ‘hard’ direction. The parameters used in the simulations are presented in the **Table 3.1**.

In the analyses that follow, only the response of the second-order (SO-) VPSC is explored. The choice for this linearization scheme, which control grain- polycrystal interactions in the simulations, is based on two conclusions. First, as recall in the chapter 2 (Figure 2.14), the response of SO-VPSC closely follows the prediction of full-field simulations of olivine polycrystal deformation (Lebensohn et al., 2007; Castelnau et al., 2009). Second, our tests using strong olivine CPOs (formed up to $\gamma > 10$ in torsion experiments) indicated that the viscoplastic behavior depends on the linearization. The widely

used tangent VPSC predictions might display a non-convex yield surface in stress-space when the CPO strength is high (**Figure 3.12**), whereas SO-VPSC did not. The convexity ensures (material) numerical stability in the polycrystal simulations (Drucke, 1964). This is also in agreement with previous tangent VPSC simulations used to predict olivine CPO evolution (Hansen et al., 2016), which showed that at relatively high shear strains ($\gamma > 5$) tangent VPSC generates numerical instabilities on the orientation of the eigenvectors.

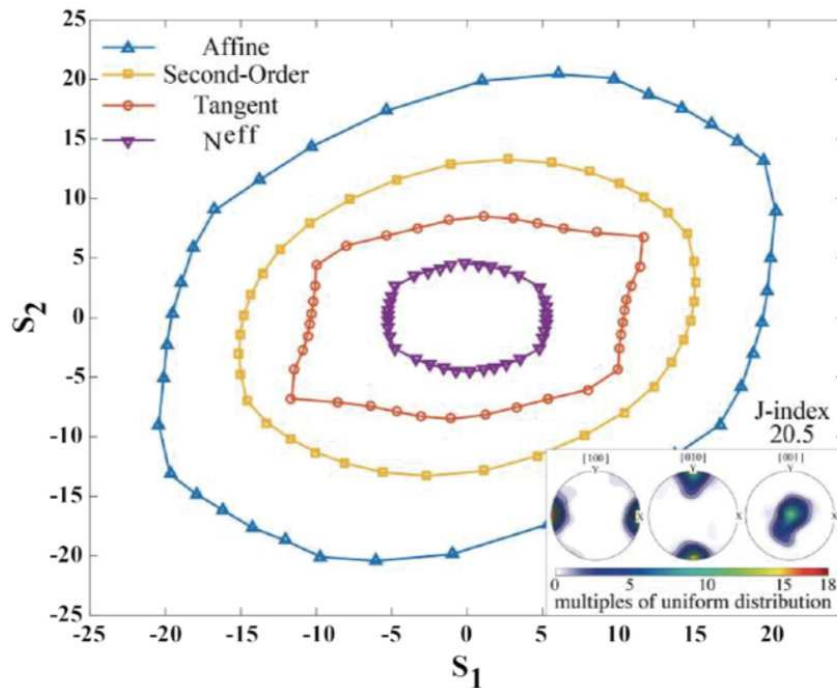


Figure 3.12: Two-dimensional projection (S_1 - S_2) of the viscoplastic equipotential yield surface predicted by VPSC models employing the same olivine CPO but different linearization schemes.

3.3.2 Results

For a given boundary conditions, the mechanical responses of all polycrystals display comparable pattern as a function of the orientation of the mechanical sollicitation (**Figure 3.13**). In extension, when the XY plane is oriented sub-perpendicular or sub-parallel to the imposed sollicitation the polycrystals is harder than the isotropic behavior ($\sigma = 1$). At highly obliquity (i.e. $\approx 45^\circ$) to the extensional the mechanical behavior is weaker than the isotropic behavior, because high shear stresses (RSS) are resolved onto the easy (010)[100] or (010)[001] slip systems of most crystals, while low RSS are resolved onto the hard (010)[001] slip system. In simple shear sollicitation, the opposite behavior is predicted in terms of the orientation of the hard and soft loading-geometries as a function of the sollicitation

orientation. Stresses weaker than the isotropic behavior is predicted for applied mechanical solicitations sub-parallel or sub-perpendicular to the plane XY. Whereas highly oblique solicitation display normalized stresses higher than the isotropic polycrystal. The maximum contrast in viscous anisotropy (ratio between high and lower normalized stress) does not surpass a factor 10.

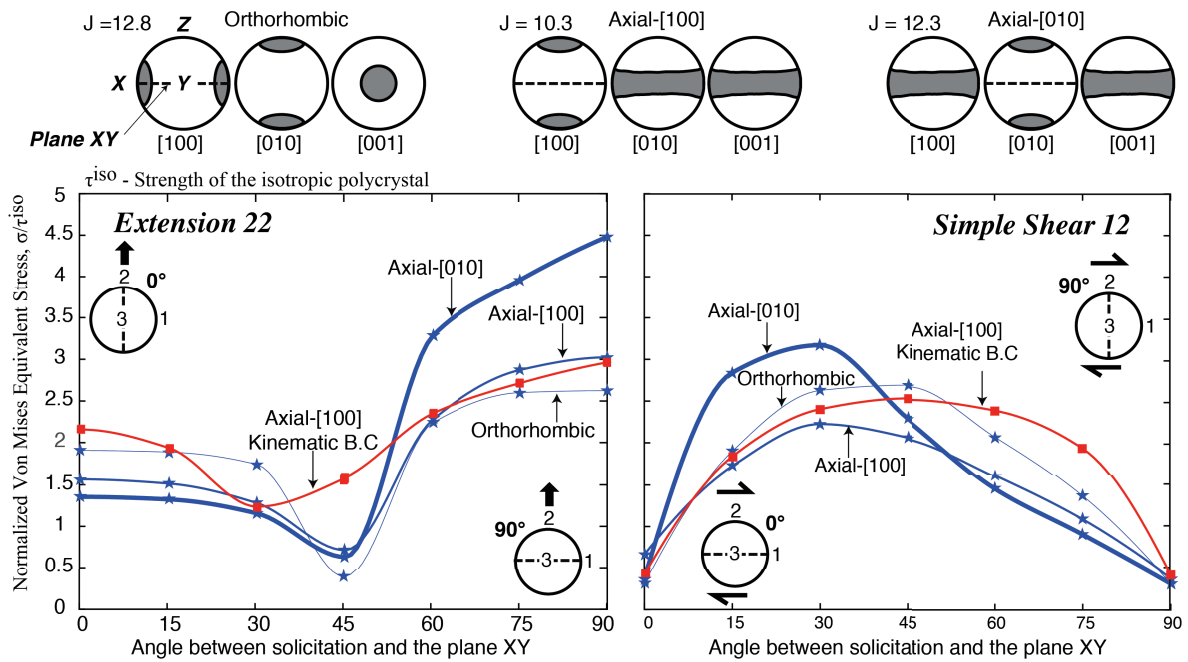


Figure 3.13: Von Mises equivalent stress (normalized to the isotropic behavior) as a function of the angle between the imposed extension 22 (left) and simple shear 12 (right) for orthorhombic and axial olivine CPOs. Mixed boundary condition (B.C) in blue and kinematic B.C in red.

The asymmetry in mechanical behavior relative to complementary loading-geometry (i.e. 30° differs from 60°) is a direct consequence of the feedbacks between the single-crystal anisotropy and imposed boundary conditions. The latter may affect the stress pattern and the magnitude of the anisotropy, because the crystal cannot freely deform and expresses its anisotropy controlled mainly by glide on the 100 direction. For extension deformation, by imposing kinematic boundary conditions (red curve), which is strict boundary conditions, the softer loading-geometry might be shifted if CPO girdle is presented. In the case of the orthorhombic symmetry, imposing kinematic condition hardens the aggregate deforming at the softer loading-geometry without affecting the anisotropy pattern relative to the loading-geometry. For simple shear numerical experiments, imposing kinematic boundary conditions result in more monotonous stress pattern; the mechanical response of the three CPOs tested is symmetrical relative to complementary loading geometries (e.g. 30° - 60°, or 15°-75°).

In both extensional and simple shear solicitations, the imposed boundary conditions affect the aggregate behavior notably when ‘out-of plane’ components are produced, which is likely to occur at oblique loading-geometries. This is corroborated by the invariant response of the polycrystal deformed in the 0° and 90° loading-geometries.

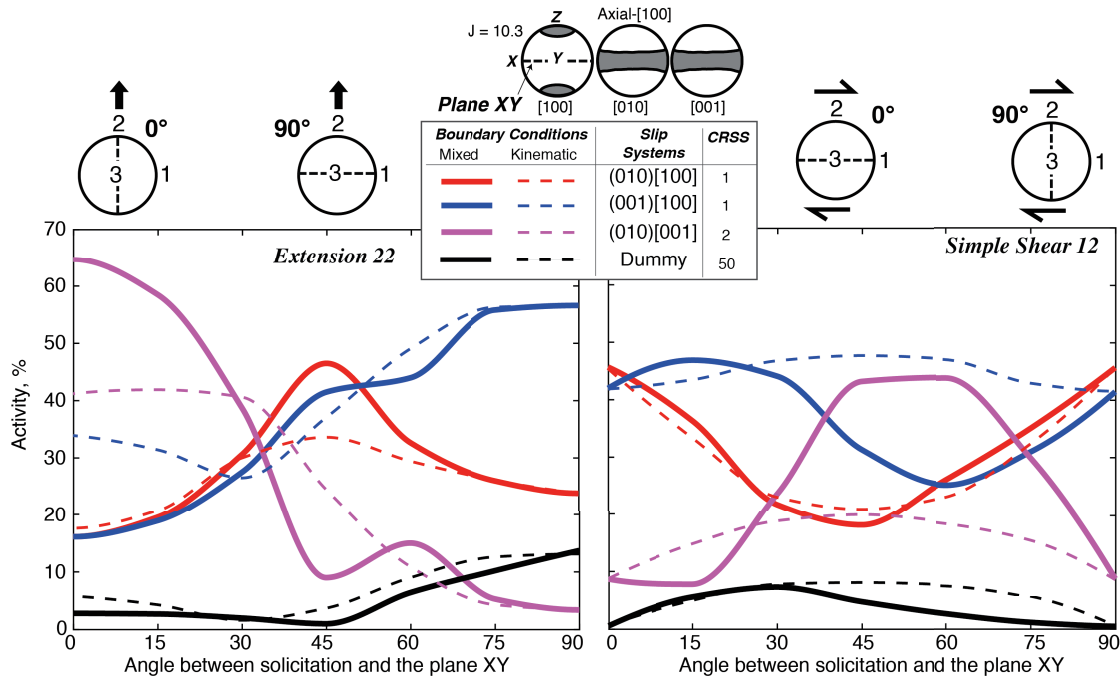


Figure 3.14: Axial-[100] olivine CPO. Activity (%) of the main slip systems (coloured lines) and the dummy slip system (black line) as a function of the angle between the imposed extension 22 (left) and simple shear 12 (right) for both kinematic and mixed boundary conditions.

The effect of the imposed boundary conditions on the slip system activation was investigated using the axial-[100] CPO. For extensional deformation between 90° and 60° to the plane XY, most of the deformation is accommodated by the easy slip system (010)[001] (>40%), and the dummy slip system is moderately activated ($\approx 10\% - 8\%$, $\beta = 50$). Whereas between 30° and 0°, the hard (010)[001] slip system accommodate most of the deformation (>40%), and the dummy slip system is not considerably activated (only 5%; **Figure 3.14**). At around 45° loading-geometry, the activation of both dummy and the hard slip system is considered low (<10%), while most of the deformation is accommodate by both the easy slip systems. By imposing kinematic boundary conditions, the pattern of activation is ‘smoothed’ (**Figure 3.13**). In simple shear, the ‘smoothing effect’ on the pattern of activation is even more obvious. The stringent boundary conditions affect notably orientations between 45° and 90°. In simple shear and extensional deformation tests, the activation of the easy

(010)[100] slip system is little affected by the imposed boundary conditions, while the harder ones can be significantly modified.

The effect of the CPO intensity on the viscous anisotropy was verified by performing SO-VPSC simulations at mixed boundary conditions using the same CPOs symmetries but with variable CPO intensities (**Figure 3.15**). Thus, the polycrystals were deformed in simple shear parallel to the plane XY and extension perpendicular it at a given loading-geometry and only CPO intensity is varied. Simple shear parallel to the plane XY is systematically weaker than extension perpendicular to it independent of the CPO symmetry. The magnitude of the viscous anisotropy significantly increases with increasing CPO intensity. A change in CPO intensity in two times (from about ≈ 6 to ≈ 12 ; J-index) results in a non-linear increase in mechanical anisotropy. The axial [100]- and [010] CPOs tends to display more non-linear increase in viscoplastic anisotropy as a function of the change in CPO intensity than the orthorhombic CPO. This prediction is also corroborated by the more asymmetrical behavior of the axial CPO relative to the loading-geometry in the **Figure 3.13** and **3.14**.

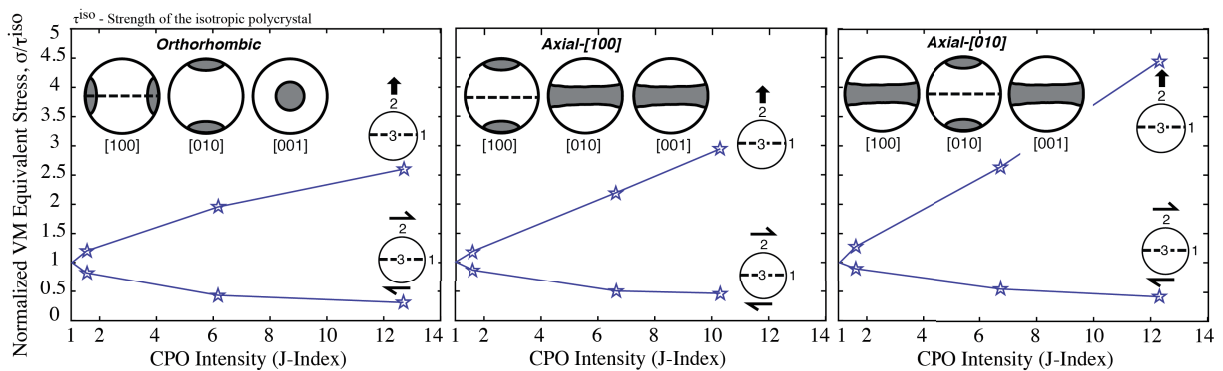


Figure 3.15: Von Mises equivalent stress (normalized to the isotropic behavior) as a function of the CPO intensity for the different olivine CPOs deformed in extension 22 (above the isotropic reference line, stress equals 1) and simple shear 12 (below the isotropic line). All the models shown were run at mixed boundary conditions.

3.3.3 Discussion and Conclusions

Strong variations of the magnitude of anisotropy is predicted as a function of the CPO intensity, whereas relatively little variation is predicted for different CPOs symmetries with similar intensities. The pattern of the anisotropy relative to the loading-geometry depends on the mechanical solicitation (simple shear, extension...), which might be slightly modified by the imposed boundary conditions. The pattern of the anisotropy is insensible to CPO intensity, and is weakly dependent of the CPO symmetry. Hence, apart from the activation of secondary

deformation processes, CPO-induced viscoplastic anisotropy in olivine polycrystals deforming at high temperature is controlled at the first-order by: the CPO intensity, imposed boundary conditions and CPO symmetry.

The slip system strength depends on temperature, pressure, water content and stress (cf. Karato et al., 2008. Bernard et al., 2019). Laboratory experiments by Katawama and Karato, 2006, has suggested that in the presence of water in olivine deforming at relatively high stresses and pressure conditions, a decrease in temperature favour intracrystalline slip dominated by the (010)[001] slip system (B-type). High-pressure experiments suggest that in the lower part of the upper mantle dislocation creep operates dominantly by slip in the [001] direction (Mainprice et al., 2005. Durinck et al. 2005: Ratteron et al., 2012). High concentrations of hydrous point defects may induce bimodal olivine CPO and transition from (010)[100]-dominated glide (A-type, orthorhombic CPO) to E- and C-type olivine CPO dominated by glide on (001)[100] and (100)[001] slips systems (Tasaka et al., 2016, Wallis et al., 2019). The results presented indicate that during high temperature deformation of olivine polycrystals, which [100]-glide is the dominant slip direction, the pattern of the viscous anisotropy is most likely little affected by changes in the CPO symmetry, as suggested by worldwide compilation of olivine CPOs (Tommasi & Vauchez 2015). The changes in symmetry are often partial dispersion of the olivine CPO, which might decrease the intensity of crystal alignments and consequently the magnitude of the viscous anisotropy.

REFERENCES

Bernard, R. E., Behr, W. M., Becker, T. W., & Young, D. J. (2019). Relationships between olivine CPO and deformation parameters in naturally deformed rocks and implications for mantle seismic anisotropy. *Geochemistry, Geophysics, Geosystems*.

Blackman, D. K., Boyce, D. E., Castelnau, O., Dawson, P. R., & Laske, G. (2017). Effects of crystal preferred orientation on upper-mantle flow near plate boundaries: rheologic feedbacks and seismic anisotropy. *Geophysical Journal International*, 210(3), 1481-1493.

Boneh, Y., Morales, L. F., Kaminski, E., & Skemer, P. (2015). Modeling olivine CPO evolution with complex deformation histories: Implications for the interpretation of seismic anisotropy in the mantle. *Geochemistry, Geophysics, Geosystems*, 16(10), 3436-3455.

Castelnau, O., Blackman, D. K., & Becker, T. W. (2009). Numerical simulations of texture development and associated rheological anisotropy in regions of complex mantle flow. *Geophysical Research Letters*, 36(12).

Durinck, J., Legris, A., & Cordier, P. (2005). Pressure sensitivity of olivine slip systems: first-principle calculations of generalised stacking faults. *Physics and Chemistry of Minerals*, 32(8-9), 646-654.

Drucker, D. On the postulate of stability of material in the mechanics of continua. *J Méc* 1964; 3: 235-249.

Falus, G., Tommasi, A., & Soustelle, V. (2011). The effect of dynamic recrystallization on olivine crystal preferred orientations in mantle xenoliths deformed under varied stress conditions. *Journal of Structural Geology*, 33(11), 1528-1540.

Hansen, L. N., Conrad, C. P., Boneh, Y., Skemer, P., Warren, J. M., & Kohlstedt, D. L. (2016). Viscous anisotropy of textured olivine aggregates: 2. Micromechanical model. *Journal of Geophysical Research: Solid Earth*, 121(10), 7137-7160.

Karato, S. I., Jung, H., Katayama, I., & Skemer, P. (2008). Geodynamic significance of seismic anisotropy of the upper mantle: new insights from laboratory studies. *Annu. Rev. Earth Planet. Sci.*, 36, 59-95.

Katayama, I., & Karato, S. I. (2006). Effect of temperature on the B-to C-type olivine fabric transition and implication for flow pattern in subduction zones. *Physics of the Earth and Planetary Interiors*, 157(1-2), 33-45.

Lebensohn, R. A., Tomé, C. N., & Castaneda, P. P. (2007). Self-consistent modelling of the mechanical behaviour of viscoplastic polycrystals incorporating intragranular field fluctuations. *Philosophical Magazine*, 87(28), 4287-4322.

Lev, E., & Hager, B. H. (2011). Anisotropic viscosity changes subduction zone thermal structure. *Geochemistry, Geophysics, Geosystems*, 12(4).

Mameri, L., Tommasi, A., Signorelli, J., & Hansen, L. N. (2019). Predicting viscoplastic anisotropy in the upper mantle: a comparison between experiments and polycrystal plasticity models. *Physics of the Earth and Planetary Interiors*, 286, 69-80.

Mainprice, D., Tommasi, A., Couvy, H., Cordier, P., & Frost, D. J. (2005). Pressure sensitivity of olivine slip systems and seismic anisotropy of Earth's upper mantle. *Nature*, 433(7027), 731.

Marquardt, K., & Faul, U. H. (2018). The structure and composition of olivine grain boundaries: 40 years of studies, status and current developments. *Physics and Chemistry of Minerals*, 45(2), 139-172.

Raterron, P., Girard, J., & Chen, J. (2012). Activities of olivine slip systems in the upper mantle. *Physics of the Earth and Planetary Interiors*, 200, 105-112.

Tasaka, M., Zimmerman, M. E., & Kohlstedt, D. L. (2016). Evolution of the rheological

and microstructural properties of olivine aggregates during dislocation creep under hydrous conditions. *Journal of Geophysical Research: Solid Earth*, 121(1), 92-113.

Signorelli, J., & Tommasi, A. (2015). Modeling the effect of subgrain rotation recrystallization on the evolution of olivine crystal preferred orientations in simple shear. *Earth and Planetary Science Letters*, 430, 356-366.

Tommasi, A., Mainprice, D., Canova, G. & Chastel, Y. Viscoplastic self-consistent and equilibrium-based modelling of olivine lattice preferred orientations. Implications for upper mantle seismic anisotropy. *J. Geophys. Res.* 105, 7893–7908 (2000).

Tommasi, A., Tikoff, B., & Vauchez, A. (1999). Upper mantle tectonics: three-dimensional deformation, olivine crystallographic fabrics and seismic properties. *Earth and Planetary Science Letters*, 168(1-2), 173-186.

Wallis, D., Hansen, L. N., Tasaka, M., Kumamoto, K. M., Parsons, A. J., Lloyd, G. E., ... & Wilkinson, A. J. (2019). The impact of water on slip system activity in olivine and the formation of bimodal crystallographic preferred orientations. *Earth and Planetary Science Letters*, 508, 51-61.

Wheeler, J. (2010). Anisotropic rheology during grain boundary diffusion creep and its relation to grain rotation, grain boundary sliding and superplasticity. *Philosophical Magazine*, 90(21), 2841-2864.

CHAPTER IV

PARAMETERIZATION OF THE ANISOTROPY PREDICTED BY VPSC MODELS AND ITS IMPLEMENTATION IN THE GEODYNAMICAL CODE ADELI3D

*The mathematical sciences particularly
exhibit order symmetry and limitations; and
these are the greatest forms of the beautiful.*

Aristotle

4 Parameterization of CPO-induced viscous anisotropy with application for modelling lithospheric deformation

4.1 General Introduction

Here is described the numerical methods developed to parameterize CPO-induced anisotropic response in olivine polycrystals. The approach to implement viscous anisotropy in the geodynamical code ADELI3D is detailed. The numerical routines are validated and the computational performance is tested. The conception of the parameterization and its implementation in ADELI3D started before the beginning of this thesis and were mainly performed by the first three authors. My contribution concerned mainly on developing post-processing codes for both VPSC and ADELI simulations and validates the new routines implemented in this latter.

4.2 Article #2

This chapter is part of an article submitted to the *Journal of Theoretical, Computational and Applied Mechanics* by Javier Signorelli, Riad Hassani, Andrea Tommasi and myself.

An effective parameterization of texture-induced viscous anisotropy in orthotropic materials with application for modeling geodynamical flows

Javier Signorelli^a, Riad Hassani^b, Andréa Tommasi^c, Lucan Mameri^c

^a *Instituto de Física de Rosario, CONICET & Universidad Nacional de Rosario, Argentina*

^b *Université Côte d'Azur, CNRS, Observatoire de la Côte d'Azur, IRD, Géoazur, France*

^c *Géosciences Montpellier – CNRS & Université de Montpellier, France*

ABSTRACT

In this article, we describe the mathematical formulation and the numerical implementation of an effective parametrization of the viscous anisotropy of orthorhombic materials produced by crystallographic preferred orientations (CPO or texture), which can be integrated into 3D geodynamic and materials science codes. Here, the approach is applied to characterize the texture-induced viscous anisotropy of olivine polycrystals, the main constituent of the Earth's upper mantle. The parameterization is based on the Hill (1948) orthotropic yield criterion. The coefficients of the Hill yield surface are calibrated based on numerical tests performed using the second order Viscoplastic Self-consistent (SO-VPSC) model. The parametrization was implemented in a 3D thermo-mechanical finite-element code developed to model large-scale geodynamical flows, in the form of a Maxwell rheology combining isotropic elastic and anisotropic non-linear viscous behaviors. The implementation was validated by comparison with results of the analytical solution and of the SO-VPSC model for simple shear and axial compression of a homogeneous anisotropic material. An application designed to examine the effect of texture-induced viscous anisotropy on the reactivation of mantle shear zones in continental plates highlights unexpected couplings between localized deformation controlled by variations in the orientation and intensity of the olivine texture in the mantle and the mechanical behavior of the elasto-viscoplastic overlying crust. Importantly, the computational time only increases by a factor 2-3 with respect to the classic isotropic Maxwell viscoelastic rheology.

4.2.1 Introduction

The greatest challenge in modeling the dynamics of the solid Earth is to reproduce the extremely heterogeneous deformation of the outer layer of the planet – the tectonic plates, which have thicknesses ranging from a few km at oceanic ridges to >200 km beneath some continental domains, in response to the continuous motion that animates the underlying convective mantle. Texture-induced viscous anisotropy is a key parameter in producing strain localization, since: (1) plates deform mostly by non-linear viscoplastic processes and (2) all major rock-forming minerals have low symmetries (hexagonal, trigonal, orthorhombic, monoclinic, or triclinic). They usually develop strong textures in response to deformation and therefore the rocks that compose the plates display a strongly anisotropy of their physical properties.

Olivine, which is the major constituent (60-80%) of the, in most cases, strongest section of the tectonic plates (50-90% of the total thickness of the plate), is orthorhombic. It displays a marked anisotropy of its thermal and mechanical properties (**Tommasi et al. 2001; Bai et al. 1991**). Geodynamical flows produce strong olivine textures, which are only significantly modified by further deformation (e.g., **Nicolas and Christensen 1987, Wenk et al. 1991, Tommasi et al. 2000**). Seismological measurements are able to detect the elastic anisotropy produced by these textures (e.g., **Hess 1969; Savage, 1999; Tommasi and Vauchez, 2015**). These data record patterns of active or old (fossilized) olivine textures, which are homogeneous at the scale of several tens to hundreds of km in the upper mantle. These textures produce viscoplastic anisotropy at large-scale (**Knoll et al. 2009; Hansen et al. 2012; Mameri et al. 2019**), which in turn modifies subsequent deformation. Texture-induced viscous anisotropy has been proposed, for instance, as a major feature of plate tectonics, explaining the reactivation of ancient structures, even at hundreds of thousands years of intervals (**Vauchez et al. 1997; Tommasi et al. 2001; Tommasi et al. 2009**). It has also been proposed to modify the convective patterns and the interactions between the plates and the convective mantle (**Castelnau et al. 2009; Lev et al. 2011; Blackman et al. 2017**). A precise description of the viscous anisotropy produced by olivine textures was achieved by explicitly coupling viscoplastic self-consistent calculations of polycrystal deformation into geodynamical flow models (**Knoll et al. 2009; Tommasi et al. 2009; Castelnau et al. 2009; Blackman et al. 2017**). However, this approach remains too time- and memory-consuming for widespread use.

Hierarchical multi-scale modelling provides a path for exchanging information between systems with different characteristic length scales. Several strategies may be defined (**Gawad et al, 2015**). Analytical yield functions are often preferred to polycrystal models for describing the anisotropy of materials in large-scale simulations due to their simplicity and numerical efficiency. However, definition of such functions for low-symmetry materials is not trivial. In the present work, we adopt the virtual-experiment strategy for exploring the viscosity tensor of a textured material composed of orthorhombic crystals. In this approach, a number of fine-scale simulations are performed to determine the parameters that characterize the phenomenological yield function implemented in the large-scale simulations. This strategy allows combining the accuracy of the description of the texture-induced viscous anisotropy of the fine-scale model and the numerical performance of the yield functions (**Plunkett et al. 2006**). Additionally, since simulations are able to calculate the material

response at any point of the loci-surface, the virtual-experiment strategy provides a method for identifying the parameters in the yield function for deformation modes that cannot be achieved in laboratory experiments.

In this article, we describe the mathematical formulation and the numerical implementation of a parametrization of the anisotropic viscoplastic rheology of olivine polycrystals in a 3D finite-element thermo-mechanical code (Adeli3D, **Hassani et al., 1997**). The parameterization is based on the Hill (1948) orthotropic yield criterion in which the coefficients that calibrated the Hill yield surface are based on numerical tests performed using the second order Viscoplastic Self-consistent (SO-VPSC) model. The aim is to provide a simplified Maxwell rheology model, combining isotropic elastic and anisotropic non-linear viscous behavior, that can be integrated into 3D geodynamic and materials science codes, allowing the physical description of a complex multi-scale system with reasonable computational times.

4.2.2 Parameterizing texture-induced viscous anisotropy in viscoelastic orthotropic materials

The framework presented in this section to parameterize the anisotropic rheology of an olivine polycrystal is based on the notion of hierarchical multi-scale modelling. It extends the classical viscoelastic Maxwell model to consider viscous anisotropy calibrated based on the Hill (1948) orthotropic yield criterion. The parameters describing the anisotropy are identified using fine-scale virtual experiments performed using viscoplastic self-consistent simulations of the deformation of an olivine polycrystal.

4.2.2.1 Thermo-mechanical code

We implement the viscous anisotropy parameterization in the 3D thermo-mechanical code Adeli3D (**Hassani et al., 1997**), which is optimized to model large-scale geodynamical flows, focusing on the deformation of the lithosphere, i.e. the semi-rigid plates that compose the outer layer of the Earth. The code is based on a Lagrangian finite-element discretization of the quasi-static mechanical behavior of the lithosphere, which solves the obtained non-linear equations using a dynamic relaxation method (**Cundall and Board, 1988**). The problem consists in finding the velocity field \mathbf{v} and the symmetric tensor $\boldsymbol{\sigma}$ satisfying

$$\begin{cases} \mathbf{div} \boldsymbol{\sigma} + \rho_l \mathbf{g} = \mathbf{0} \\ \frac{D\boldsymbol{\sigma}}{Dt} = \mathcal{M}(\boldsymbol{\sigma}, \mathbf{D}) \end{cases} \quad \text{in } \Omega, \quad (1)$$

where Ω is the physical domain, \mathbf{g} is the acceleration vector due to gravity, ρ_l is the lithosphere density and $\mathbf{D} = \frac{1}{2}(\nabla\mathbf{v} + \nabla\mathbf{v}^T)$. $\frac{D}{Dt}$ is an objective time derivative associated to the large strain formulation. Jaumann and Green-Naghdi are the most frequently used objective derivatives. They can be expressed using the same formulation:

$$\frac{D\boldsymbol{\sigma}}{Dt} = \dot{\boldsymbol{\sigma}} - \mathbf{W} \boldsymbol{\sigma} + \boldsymbol{\sigma} \mathbf{W}, \quad (2)$$

with $\mathbf{W} = \boldsymbol{\omega}$, for the Jaumann derivative

and $\mathbf{W} = \boldsymbol{\Omega}$, for the Green-Naghdi derivative

where $\omega_{ij} = \frac{1}{2} \left(\frac{\partial v_i}{\partial x_j} - \frac{\partial v_j}{\partial x_i} \right)$ is the material spin tensor (i.e., the screw part of the velocity gradient, $\frac{\partial v_i}{\partial x_j}$) and $\boldsymbol{\Omega} = \dot{\mathbf{R}} \mathbf{R}^T$ the rotation rate associated with the left polar decomposition of the deformation gradient \mathbf{F} ($\mathbf{F} = \mathbf{R}\mathbf{U}$). As generally in geodynamic simulations, we use the Jaumann corotational stress rate in our simulations.

The functional \mathcal{M} in Eq. (1) stands for a general hypoelastic constitutive law. In the present case, \mathcal{M} describes a Maxwell rheology combining isotropic elastic and anisotropic non-linear viscous behavior. The transition between the elastic and viscous regimes depends on the temperature and stress, which change the viscosity, and on the considered time-scale.

4.2.2.2 Maxwell viscoelasticity

The viscoelastic constitutive law combines the contributions of the elastic \mathbf{D}_e and the viscous \mathbf{D}_v strain-rates. The total strain-rate \mathbf{D} is defined as the sum of these two contributions:

$$\mathbf{D} = \mathbf{D}_e + \mathbf{D}_v \quad (3)$$

and the constitutive relationship is given by

$$\frac{D\boldsymbol{\sigma}}{Dt} = 2\mu (\mathbf{D} - \mathbf{D}_v) + \lambda \text{tr}(\mathbf{D} - \mathbf{D}_v) \mathbf{I} \quad (4)$$

with \mathbf{I} the second-order identity tensor, “tr” the trace operator, and μ and λ the Lamé moduli. The viscous strain-rate \mathbf{D}_v is given by the flow rule

$$\mathbf{D}_v = \frac{\partial \Phi}{\partial \boldsymbol{\sigma}} \quad (5)$$

where $\Phi(\boldsymbol{\sigma})$ is a viscous potential. A typical choice for this potential is the power-law equation:

$$\Phi(\boldsymbol{\sigma}) = \frac{2}{3} \frac{\gamma}{n+1} J^{n+1}(\boldsymbol{\sigma}), \quad (6)$$

where $J(\boldsymbol{\sigma})$ is the equivalent stress, $\gamma = \gamma_0 \exp(-Q/RT)$, n , Q and γ_0 are the experimentally-derived power-law exponent, activation energy in $\text{kJ mol}^{-1}\text{K}^{-1}$, fluidity in $\text{Pa}^{-n}\text{s}^{-1}$, respectively, R is the gas constant, and T is temperature in Kelvin. Using Eqs. (5) and (6), the viscous part of the total strain-rate can be expressed as:

$$\mathbf{D}_v = \frac{2}{3} \gamma J^n(\boldsymbol{\sigma}) \frac{\partial J(\boldsymbol{\sigma})}{\partial \boldsymbol{\sigma}}. \quad (7)$$

To describe an anisotropic viscous behavior, the yield condition, which was defined by the Von Mises yield function in the isotropic case, is here defined by the orthotropic yield function of **Hill (1948)**.

4.2.2.3 Hill (1948) orthotropic yield criterion

The Hill yield function, which builds on the Von Mises’ concept of plastic potential, defines a pressure-independent homogenous quadratic criterion. This form assumes that the reference axes are the principal axes of anisotropy of the material, which are orthogonal. The resulting yielding function takes the form:

$$J(\boldsymbol{\sigma}) =$$

$$\sqrt{F(\sigma_{11} - \sigma_{22})^2 + G(\sigma_{22} - \sigma_{33})^2 + H(\sigma_{33} - \sigma_{11})^2 + 2L\sigma_{12}^2 + 2M\sigma_{23}^2 + 2N\sigma_{31}^2} \quad (8)$$

To predict the viscous contribution of anisotropic materials under multiaxial stress conditions, $J(\boldsymbol{\sigma})$ is considered as the definition of the equivalent stress and Eq. (7) becomes:

$$\mathbf{D}_v = \gamma J^{n-1} \mathbf{A} : \mathbf{S} \quad (9)$$

where \mathbf{S} is the deviatoric part of $\boldsymbol{\sigma}$ and \mathbf{A} is a rank-4 tensor describing the material anisotropy, and stress dependency of J is omitted in order to simplify the notation. Using the Voigt notation, \mathbf{A} has the following matrix representation in the reference frame defined by the principal axes of anisotropy of the material:

$$\mathbf{A} = \frac{2}{3} \begin{bmatrix} F+H & -F & -H & 0 & 0 & 0 \\ -F & G+F & -G & 0 & 0 & 0 \\ -H & -G & H+G & 0 & 0 & 0 \\ 0 & 0 & 0 & L & 0 & 0 \\ 0 & 0 & 0 & 0 & M & 0 \\ 0 & 0 & 0 & 0 & 0 & N \end{bmatrix}, \quad (10)$$

where F, G, H, L, M, N are the Hill yield surface coefficients, which describe the anisotropy of the material. In the case of an isotropic aggregate,

$$F = G = H = \frac{1}{2}, \quad L = M = N = \frac{3}{2}, \quad (11)$$

and Eq. (8) reduces to the Von Mises yield function. With this particular choice of the potential, the viscous strain-rate is traceless and the Maxwell constitutive law takes the form:

$$\frac{D\boldsymbol{\sigma}}{Dt} = 2\mu \mathbf{D} + \lambda \text{tr}(\mathbf{D}) \mathbf{I} - 2\mu\gamma J^{n-1} \mathbf{A} : \mathbf{S}. \quad (12)$$

4.2.2.4 Numerical integration

It is convenient to split the constitutive law given in Eq. (4) in deviatoric and hydrostatic parts that can be integrated separately:

$$\dot{\mathbf{S}} + \mathbf{j}_\omega(\mathbf{S}) = 2\mu(\mathbf{D}' - \mathbf{D}'_v), \quad (13a)$$

$$\dot{p} = K \operatorname{tr}(\mathbf{D}) \quad (13b)$$

where \mathbf{D}' and $\mathbf{D}'_v (= \mathbf{D}_v)$ are the deviatoric parts of the total and viscous strain-rate tensors, respectively, and $\mathbf{j}_\omega(\mathbf{S}) = \mathbf{S}\boldsymbol{\omega} + (\mathbf{S}\boldsymbol{\omega})^T$ when the Jaumann derivative is used. Assuming \mathbf{D} and $\boldsymbol{\omega}$ constant in the time interval $[t, t + \Delta t]$ and using the Crank-Nicolson scheme, the stress at time station $t + \Delta t$ is sought as the solution of the non-linear equation:

$$\mathbf{S}^{t+\Delta t} = \mathbf{S}^t + 2\mu\Delta t \mathbf{D}' - \mu\Delta t \mathbf{D}'_v(\mathbf{S}^t) - \frac{\Delta t}{2} \mathbf{j}_\omega(\mathbf{S}^t) - \mu\Delta t \mathbf{D}'_v(\mathbf{S}^{t+\Delta t}) - \frac{\Delta t}{2} \mathbf{j}_\omega(\mathbf{S}^{t+\Delta t}) \quad (14a)$$

$$p^{t+\Delta t} = p^t + K \operatorname{tr}(\mathbf{D}) \quad (14b)$$

Eq. (14a) can be expressed as $\mathbf{r}(\mathbf{S}^{t+\Delta t}) = \mathbf{0}$, with

$$\mathbf{r}(\mathbf{S}) = \mathbf{S} + \mu\Delta t \mathbf{D}'_v(\mathbf{S}) + \frac{\Delta t}{2} \mathbf{j}_\omega(\mathbf{S}) - \tilde{\mathbf{S}}, \quad (15)$$

where $\tilde{\mathbf{S}}$ groups together the terms known at the beginning of the time interval (t):

$$\tilde{\mathbf{S}} = \mathbf{S}^t + 2\mu\Delta t \mathbf{D}' - \mu\Delta t \mathbf{D}'_v(\mathbf{S}^t) - \frac{\Delta t}{2} \mathbf{j}_\omega(\mathbf{S}^t). \quad (16)$$

Defining \mathcal{R} as the laboratory reference frame and $\hat{\mathcal{R}}$ the material reference frame, a second-order tensor $\hat{\mathbf{X}}$ defined in $\hat{\mathcal{R}}$ can be expressed in \mathcal{R} through a rotation matrix R_0 , which allows changing from the material to laboratory reference frame (i.e., from $\hat{\mathcal{R}}$ to \mathcal{R}):

$$\hat{\mathbf{X}} = R_0^T \mathbf{X} R_0 \quad (17)$$

Expressing Eqs. (15-16) in the material reference frame $\hat{\mathcal{R}}$, we obtain

$$\hat{\mathbf{r}}(\hat{\mathbf{S}}) = \hat{\mathbf{S}} + \mu\Delta t \hat{\mathbf{D}}'_v(\hat{\mathbf{S}}) + \frac{\Delta t}{2} \hat{\mathbf{j}}_\omega(\hat{\mathbf{S}}) - \hat{\tilde{\mathbf{S}}}, \quad (18)$$

$$\hat{\tilde{\mathbf{S}}} = \hat{\mathbf{S}}^t + 2\mu\Delta t \hat{\mathbf{D}}' - \mu \Delta t \hat{\mathbf{D}}'_v(\hat{\mathbf{S}}^t) - \frac{\Delta t}{2} \hat{\mathbf{j}}_\omega(\hat{\mathbf{S}}^t), \quad (19)$$

where $\hat{\mathbf{S}} = R_0^T \mathbf{S} R_0$ and $\hat{\mathbf{D}}' = R_0^T \mathbf{D}' R_0$. Newton's method is used to solve the non-linear system $\hat{\mathbf{r}}(\hat{\mathbf{S}}) = \mathbf{0}$ and the inverse rotation is applied to find the deviatoric stress at $t + \Delta t$ in the laboratory reference frame.

The numerical implementation in Adeli3D (hereinafter referred as Adeli3D-anis) of the procedure described in this section allows a parameterized description of the viscous anisotropy component of any orthotropic viscoelastic material. Before applying it to characterize the texture-induced viscous anisotropy of olivine polycrystals, we validated the implementation by comparison with semi-analytical solutions for simple settings.

4.2.2.5 Validation of the implemented Hill-based parameterization

The numerical integration technique associated with the anisotropic viscous parameterization presented in the previous section was first validated based on its ability to recover a semi-analytical solution for a shear test applied to a material with either a linear ($n = 1$) or a non-linear ($n = 3.6$) viscous rheology. Shear is imposed by a velocity field described in the laboratory reference frame \mathcal{R} (axes x, y, z) by $\mathbf{v}_{[\mathcal{R}]}(x, y, z) = (2ay, 0, 0)$, with $a > 0$. The material reference frame $\hat{\mathcal{R}}$ (anisotropy axes $x_1, x_2, x_3 = z$) is rotated from the laboratory reference frame \mathcal{R} by an angle θ (Figure 4.1a). The strain-rate, the corotational rotation rate and the deviatoric stress are expressed in $\hat{\mathcal{R}}$ as follows:

$$\hat{\mathbf{D}} = a \begin{bmatrix} \sin 2\theta & \cos 2\theta & 0 \\ \cos 2\theta & -\sin 2\theta & 0 \\ 0 & 0 & 0 \end{bmatrix}, \quad \hat{\boldsymbol{\omega}} = a \begin{bmatrix} 0 & 1 & 0 \\ -1 & 0 & 0 \\ 0 & 0 & 0 \end{bmatrix}, \quad \hat{\mathbf{S}} = \begin{bmatrix} \hat{s}_{11} & \hat{s}_{12} & 0 \\ \hat{s}_{12} & \hat{s}_{22} & 0 \\ 0 & 0 & -(\hat{s}_{11} + \hat{s}_{22}) \end{bmatrix} \#(20a)$$

and in \mathcal{R} the stress components are given by

$$\mathbf{S} = \mathbf{R}_0 \hat{\mathbf{S}} \mathbf{R}_0^T = \begin{bmatrix} \sigma_{xx} & \sigma_{xy} & 0 \\ \sigma_{xy} & \sigma_{yy} & 0 \\ 0 & 0 & -(\sigma_{xx} + \sigma_{yy}) \end{bmatrix} \#(20b)$$

with \mathbf{R}_0 the rotation matrix from $\hat{\mathcal{R}}$ to \mathcal{R} . In this simple case, from Eq. (13) and assuming zero initial stresses, the resulting differential system can be written as

$$\begin{cases} \dot{\mathbf{y}}(t) + \mathbf{C}_n(\mathbf{y}) \cdot \mathbf{y}(t) = \mathbf{b}, & 0 < t \leq t_f \\ \mathbf{y}(0) = \mathbf{0} \end{cases} \quad (21)$$

where $\mathbf{y} = (\hat{s}_{11}, \hat{s}_{22}, \hat{s}_{12})^T$, $\mathbf{b} = 2\mu a (\sin 2\theta, -\sin 2\theta, \cos 2\theta)^T$, and

$$\mathbf{C}_n(\mathbf{y}) = \begin{bmatrix} (F + 2H)\alpha_n(\mathbf{y}) & (H - F)\alpha_n(\mathbf{y}) & -2a \\ (G - F)\alpha_n(\mathbf{y}) & (F + 2G)\alpha_n(\mathbf{y}) & 2a \\ a & -a & L\alpha_n(\mathbf{y}) \end{bmatrix}, \quad (22)$$

with $\alpha_n(\mathbf{y}) = \frac{4}{3}\mu\gamma(F(y_1 - y_2)^2 + G(y_1 + 2y_2)^2 + H(2y_1 + y_2)^2 + 2Ly_3^2)^{(n-1)/2}$.

We can make the following remarks:

- 1) For the linear case ($n = 1$) the coefficients of \mathbf{C}_n are obviously constant and the solution of the system takes the form: $\mathbf{y} = (\mathbf{I} - e^{-t\mathbf{C}_1}) \cdot \mathbf{C}_1^{-1} \cdot \mathbf{b}$ while for the general non-linear case, only a numerical solution can be computed (for these validation tests, we used an ODE solver of Matlab).
- 2) The components 13, 23, 31 and 32 of \mathbf{C}_n (implying the magnitude of the velocity gradient a) come from the finite strain formalism (Jaumann derivative).
- 3) Unlike the isotropic case for which σ_{xx} and σ_{yy} are always opposite, an out-of-plane stress σ_{zz} exists whenever $H \neq G$.

Validation tests in Adeli3D-anis were run for a cube of 1 m^3 composed of 6 four-node tetrahedral finite-elements with homogenous isotropic and anisotropic material parameters (Figure 4.1b and 4.1c). Shear deformation was imposed by applying a constant tangential velocity parallel to the axis 1 on the face normal to axis 2 of the cube, while keeping the opposite face fixed and imposing null normal velocities to the two faces normal to axis 3 (Figure 4.4a). The isotropic material parameters are given in Table 4.1.

Table 4.1: Parameters describing the isotropic part of the rheology in all validation tests

	λ (GPa)	μ (GPa)	n	γ_0 ($\text{Pa}^{-n}\text{s}^{-1}$)	Q (kJ/mol)	T (K)
Test1	40	40	1	$0.5 \cdot 10^{-12}$	0	1423
Test2	40	40	3.6	$0.5 \cdot 10^{-18}$	500	1423

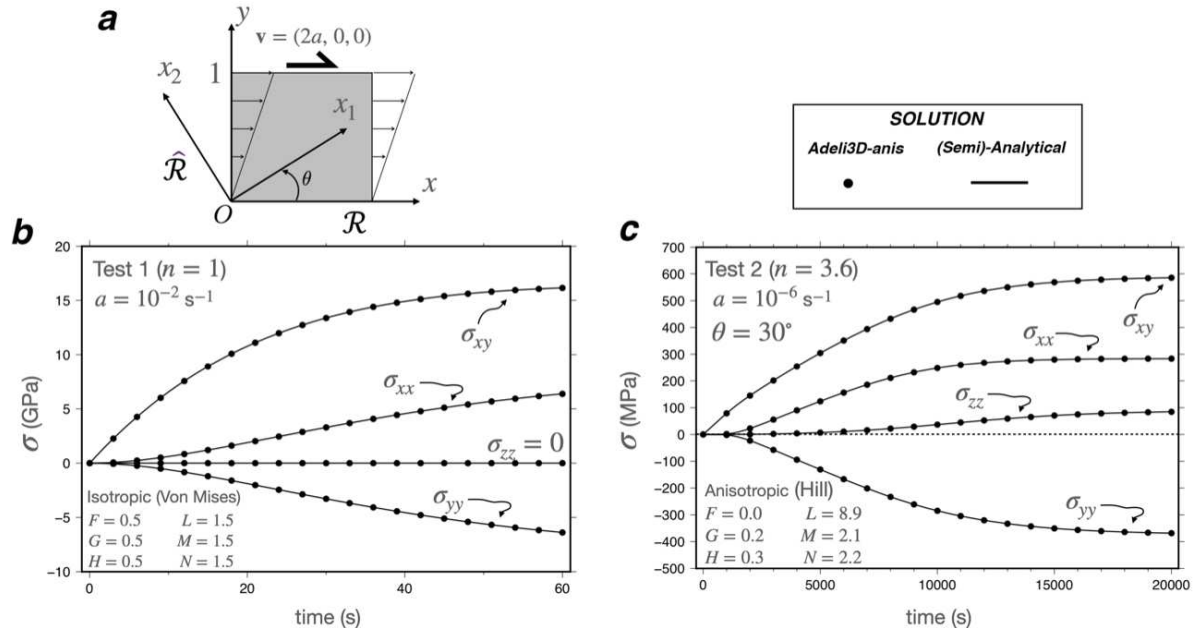


Figure 4.1: Simple shear tests for validating the implementation of the parameterization of the viscous anisotropy in large deformations for the general case of a misalignment $\theta = 30^\circ$ between the anisotropy axes ($\hat{\mathcal{R}}$) with respect to the laboratory axes (\mathcal{R}). Components of the stress tensor as a function of time for the semi-analytical solution and the Hill-based parameterization of the viscoplastic anisotropy implemented in Adeli3D-anis for (b) Newtonian isotropic ($n=1$) and (c) non-Newtonian ($n=3.6$) anisotropic case-studies. The Hill yield surface coefficients are defined in the material texture reference frame ($\hat{\mathcal{R}}$), which is orthotropic. They correspond to those of an isotropic and a strongly textured olivine polycrystal, determined following the approach described in section 2.3. Shear is imposed parallel to the maximum concentration of $[100]$ of the texture. a [s^{-1}] is a factor proportional to the norm of the imposed velocity gradient.

For both isotropic linear and anisotropic non-linear cases, the Adeli3D-anis and the semi-analytical solution are numerically identical (Figure 4.1b and 4.1c). In both cases, the imposed simple shear deformation is associated with a dominant σ_{xy} stress component, but the presence of a texture-induced anisotropy results in enhancement of this shear component relatively to the diagonal ones. As it is mentioned above anisotropy ($H \neq G$) induces a 3D stress field, where an out-of-plane stress σ_{zz} takes place (Figure 4.1c).

4.2.3 Determining the Hill coefficients for olivine polycrystals using the VPSC model

The constitutive relationship presented above includes the effects of anisotropy through the Hill coefficients. Normally in Materials Sciences, these coefficients are determined through a set of mechanical tests. However, such tests are often unfeasible for geological materials because viscous deformation is only attained experimentally at high

confining pressures, limiting the possible geometry of laboratory experiments. Thus, we calibrated the Hill coefficients, which describe the texture-induced viscous anisotropy of olivine polycrystals, based on VPSC polycrystal plasticity simulations.

Unlike the upper and lower bound models, the VPSC formulation allows each grain to deform according to its orientation and the strength of the interaction with its surroundings. Each grain is considered as an ellipsoidal inclusion surrounded by a homogeneous effective medium that has the average properties of the polycrystal. Several choices are possible for the linearized behavior at grain level. The secant (**Hill 1965; Hutchinson 1976**), affine (**Ponte Castañeda 1996; Masson et al. 2000**), and tangent approaches (**Molinari et al. 1987; Lebensohn and Tomé 1993**) are first-order approximations, which disregard higher-order statistical information inside the grains. However, for highly anisotropic materials displaying a strong contrast in mechanical behavior between differently oriented grains, such as olivine, the second order approximation (SO-VPSC), which takes into account average field fluctuations inside the grains (**Castañeda, 2002**), is a better choice (**Castelnau et al. 2008**). For completeness, a brief description of the theoretical framework of SO-VPSC is presented below.

The viscoplastic constitutive behavior is described by a rate-sensitive relation:

$$\mathbf{d}(\mathbf{x}) = \sum_s \mathbf{m}^s(\mathbf{x}) \dot{\gamma}^s(\mathbf{x}) = \dot{\gamma}_o \sum_s \mathbf{m}^s(\mathbf{x}) \left| \frac{\mathbf{m}^s(\mathbf{x}) : \mathbf{s}(\mathbf{x})}{\tau_c^s(\mathbf{x})} \right|^{\frac{1}{m}}, \quad (23)$$

where $\mathbf{m}^s = \frac{1}{2}(\mathbf{n}^s \otimes \mathbf{b}^s + \mathbf{b}^s \otimes \mathbf{n}^s)$ is defined as a symmetric tensor, with \mathbf{n}^s and \mathbf{b}^s the normal to the slip systems' glide plane and the Burgers' vector, respectively. $\dot{\gamma}^s$ represents the strain-rate accommodated by the slip system s . $\dot{\gamma}_o$ is a normalization factor, m is the inverse of the rate-sensitivity exponent and τ_c^s is the critical resolved shear stress of the slip system s . The tensors \mathbf{d} and \mathbf{s} are the local strain-rate and deviatoric stress, respectively. Linearizing Eq. (23), we obtain:

$$\mathbf{d}(\mathbf{x}) = \mathbf{l} : \mathbf{s}(\mathbf{x}) + \mathbf{d}^0, \quad (24a)$$

$$\mathbf{D} = \mathbf{L} : \mathbf{S} + \mathbf{D}^0, \quad (24b)$$

where \mathbf{l} , \mathbf{L} are the viscoplastic compliances, \mathbf{d}^0 , \mathbf{D}^0 are the back-extrapolated terms at the level of the grain and of the aggregate, respectively, and \mathbf{D} and \mathbf{S} are the macroscopic deviatoric strain-rate and stress tensors. The effective stress potential of the polycrystal

described by Eq. (24b) may be written in the form

$$U_T = \frac{1}{2} \mathbf{L} :: (\mathbf{S} \otimes \mathbf{S}) + \mathbf{D}^0 : \mathbf{S} + \frac{1}{2} G, \quad (25)$$

which expresses the effective potential U of the nonlinear viscoplastic polycrystal in terms of a linearly viscous aggregate with properties determined from variational principles. The last term in Eq. (25) is the power under zero applied stress. The average second-order moment of the stress field is a fourth-order tensor given by:

$$\langle \mathbf{s} \otimes \mathbf{s} \rangle = \frac{2}{c} \frac{\partial U_T}{\partial \mathbf{l}} = \frac{1}{c} \frac{\partial \mathbf{L}}{\partial \mathbf{l}} :: (\mathbf{S} \otimes \mathbf{S}) + \frac{1}{c} \frac{\partial \mathbf{D}^0}{\partial \mathbf{l}} : \mathbf{S} + \frac{1}{c} \frac{\partial G}{\partial \mathbf{l}}, \quad (26)$$

where c is the volume fraction of a given grain. From the average second-order moments of the stress, the associated second-order of the strain-rate can then be evaluated as:

$$\langle \mathbf{d} \otimes \mathbf{d} \rangle = (\mathbf{l} \otimes \mathbf{l}) :: \langle \mathbf{s} \otimes \mathbf{s} \rangle + \mathbf{d} \otimes \mathbf{d}^0 + \mathbf{d}^0 \otimes \mathbf{d} - \mathbf{d}^0 \otimes \mathbf{d}^0 \quad (27)$$

The average second-order moments of the stress field over each grain are obtained by calculating the derivatives in Eq. (26). The implementation of the second-order procedure in VPSC follows the work of **Liu and Ponte Castaneda (2004)** - for more details, see the VPSC7c manual (**Tomé and Lebensohn, 2012**).

4.2.3.1 Polycrystal Equipotential Surface

The anisotropy of a viscoplastic material can be described by comparing points that belong to the same reference equipotential surface. This requires probing the material in a given stress direction, while ensuring that the associated dissipation rate will be the same regardless of the chosen direction. This reference polycrystal equipotential surface (PES) is the locus of all stress states associated with a polycrystal with a given texture. In the present study, we use the SO-VPSC polycrystal plasticity model to estimate the PES.

The plastic potential is essentially a function of the stress that can be differentiated to derive the plastic strain-rate. This function $f(\mathbf{S})$ is defined by a constant plastic work rate, \dot{W}_0 , along the potential. The plastic work rate for an arbitrary macroscopic strain-rate, \mathbf{D}_0 , is defined as:

$$f(\mathbf{S}) = \mathbf{S} : \mathbf{D} = \mathbf{S}_0 : \mathbf{D}_0 = \dot{W}_0, \quad (28)$$

where \mathbf{S}_0 is the stress state corresponding to a given \mathbf{D}_0 (or inversely). This function defines a series of convex surfaces in the deviatoric stress space, which are equipotential surfaces when $f(\mathbf{S})$ is constant. As \mathbf{S} or \mathbf{D} is not known *a priori*, the obtained plastic potential rate can be different from \dot{W}_0 . In this case the stress point does not lie on the selected equipotential. The stress or strain-rate on the selected equipotential can be obtained based on **Hutchinson (1976)**, which showed that when the magnitude of the strain-rate is changed by a factor ζ , the stress response of the polycrystal becomes

$$\mathbf{S}(\zeta\mathbf{D}) = \zeta^n \mathbf{S}(\mathbf{D}) \quad (29)$$

As a consequence, the magnitude of \mathbf{S} or \mathbf{D} can be scaled as follows:

$$\mathbf{D}^* = \mathbf{D} \left(\frac{\dot{W}_0}{\dot{W}} \right)^{n/1+n}; \quad \mathbf{S}^* = \mathbf{S} \left(\frac{\dot{W}_0}{\dot{W}} \right)^{1/1+n} \quad (30a-b)$$

The standard VPSC code imposes the strain-rate vectors \mathbf{D} and calculates the associated stress \mathbf{S} for probing the material response. As mentioned above, both tensors can be renormalized to give the same dissipation rate for every point of the yield surface. The test direction in the strain-rate space is given by $n_{ij} = D_{ij}/\|\mathbf{D}\|$, where $\|\mathbf{D}\| = \sqrt{D_{ij}D_{ij}}$ defines the length of the strain-rate tensor \mathbf{D} . Thus, the strain-rate tensor can be characterized by a polar representation, which consists of a radius in strain-rate (deviatoric stress) space, $\|\mathbf{D}\|$, and a set of direction cosines (n_{ij}). In this representation $\|\mathbf{D}\|$ is an independent variable, whereas the nine values of n_{ij} are not. Since \mathbf{D} is a symmetric deviatoric second-order tensor, it is possible to represent the strain-rate tensor by a five-component unit vector using a second-order tensor with an orthonormal symmetric base $n_{ij} = n_\lambda b_{ij}^\lambda$, $\lambda = 1, \dots, 5$ (see Appendix). Using generalized spherical coordinates, the vector \mathbf{n} can be expressed as follows:

$$\begin{aligned} n_{(1)} &= \cos \theta_1 \sin \theta_2 \sin \theta_3 \sin \theta_4 \sin \theta_5 \\ n_{(2)} &= \cos \theta_2 \sin \theta_3 \sin \theta_4 \sin \theta_5 \\ n_{(3)} &= \cos \theta_3 \sin \theta_4 \sin \theta_5 \\ n_{(4)} &= \cos \theta_4 \sin \theta_5 \\ n_{(5)} &= \cos \theta_5 \end{aligned} \quad (31)$$

with $-\pi \leq \theta \leq \pi$ or $0 \leq \theta \leq \pi/2$ for centro or non-centro symmetric evaluation, respectively. As an example, if simulations are restricted to the $S_1 - S_2$ subspace, thus, $\theta_1 = 0, -\pi \leq \theta_2 \leq \pi, \theta_3 = \theta_4 = \theta_5 = \pi/2$, and Eq. (31) reduces to:

$$\begin{aligned}
 n_{(1)} &= \sin \theta_2 \\
 n_{(2)} &= \cos \theta_2 \\
 n_{(3)} &= 0 \\
 n_{(4)} &= 0 \\
 n_{(5)} &= 0
 \end{aligned} \tag{32}$$

with θ_2 scanned in steps of 1 degree and the probed strain-rate (deviatoric stress) tensor set to $\|\mathbf{D}\| = 1$. Here, we extend the original implementation of the PES calculation in the VPSC code (Tomé and Lebensohn; 2012 – VPSC7c manual) by allowing to choose whether the sampling points will be equispaced in strain-rate or in stress. The algorithm 1 presents how the PES can be evaluated.

Algorithm 1. Algorithm for evaluating the PESs assuming an equispaced strain-rate sampling.

Inputs: component i, j defining the subspace ($\lambda_i - \lambda_j$, Appendix), flag for sampling variable (strain-rate or stress), $\Delta\theta$ angular resolution, $\ \mathbf{a}_{probe}\ $ norm of the probe vector, reference plastic work rate \dot{W}_0	
Results: the associated mechanical state $(\mathbf{D}, \mathbf{S})_k, k = 1, \dots, N_{\Delta\theta}$	
for $\theta = 0$ to $\theta_{\max(\lambda)}$ every $\Delta\theta$ do	
$\mathbf{a}_{probe} = \ \mathbf{a}_{probe}\ \mathbf{n}(0, \dots, \theta_{\lambda_j}, \dots, 0)$	// calculates normalized vector in 5-d space. Only θ_{λ_j} is non null
If (sampling variable) then	
$\mathbf{D}_{probe} = \mathbf{a}_{probe}$	// equispaced strain-rate sampling
$\mathbf{S}_{response} \leftarrow \text{VPSC}(\mathbf{D}_{probe})$	// performs VPSC calculation
else	
$\mathbf{S}_{probe} = \mathbf{a}_{probe}$	// equispaced stress sampling
$\mathbf{D}_{response} \leftarrow \text{VPSC}(\mathbf{S}_{probe})$	// performs VPSC calculation
endif	
Eqs. (24a-b)	// mechanical states are normalized to the same reference plastic work rate
$\mathbf{D}^*_{probe/response} - \mathbf{S}^*_{response/probe}$	// store pairs (probe – response)
end	

As an example, we present in Figure 4.2 the $\{\pi\}$ - and shear projections of the PES for an olivine aggregate with a typical orthorhombic texture, described by 1000 orientations. Its orientation distribution function (ODF) and intensity (J-index) were quantified using the open-source MTEX toolbox (Mainprice et al., 2014). The olivine slip systems data (Table 4.2) are derived from experiments at high temperature and moderate pressure conditions (Bai et al. 1991). All curves are normalized by the work rate of an isotropic olivine polycrystal deformed under similar conditions (full symbols).

No appreciable differences are obtained either using a strain-rate or stress sampling for the calculation of the yield surfaces. Since only intracrystalline glide deformation modes are taken into account (no twinning), the predicted surfaces are centro-symmetric. The four equipotential surfaces are then fitted using a least-square method to obtain the six coefficients (F, G, H, L, M, N) that satisfy the anisotropic Hill yield function (Eq. 9). Table 4.3 presents the fitted coefficients for the orthorhombic texture showed in Figure 4.2.

Table 4.2: Slip systems parameters used in the SO-VPSC simulations

Slip Systems	Critical Resolved	
	Shear Stress #	Stress exponent
(010)[100]	1	3
(001)[100]	1	3
(010)[001]	2	3
(100)[001]	3	3
(011)[100]	4	3
(110)[001]	6	3
$\{111\}\langle 110 \rangle^a$	50	3
$\{111\}\langle 011 \rangle^a$	50	3
$\{111\}\langle 101 \rangle^a$	50	3

Adimensional values; normalized by flow stress of the (010)[100] slip system.

^a Slip systems not active in olivine, used for stabilizing the calculations, but accommodating $\ll 5\%$ strain in all simulations.

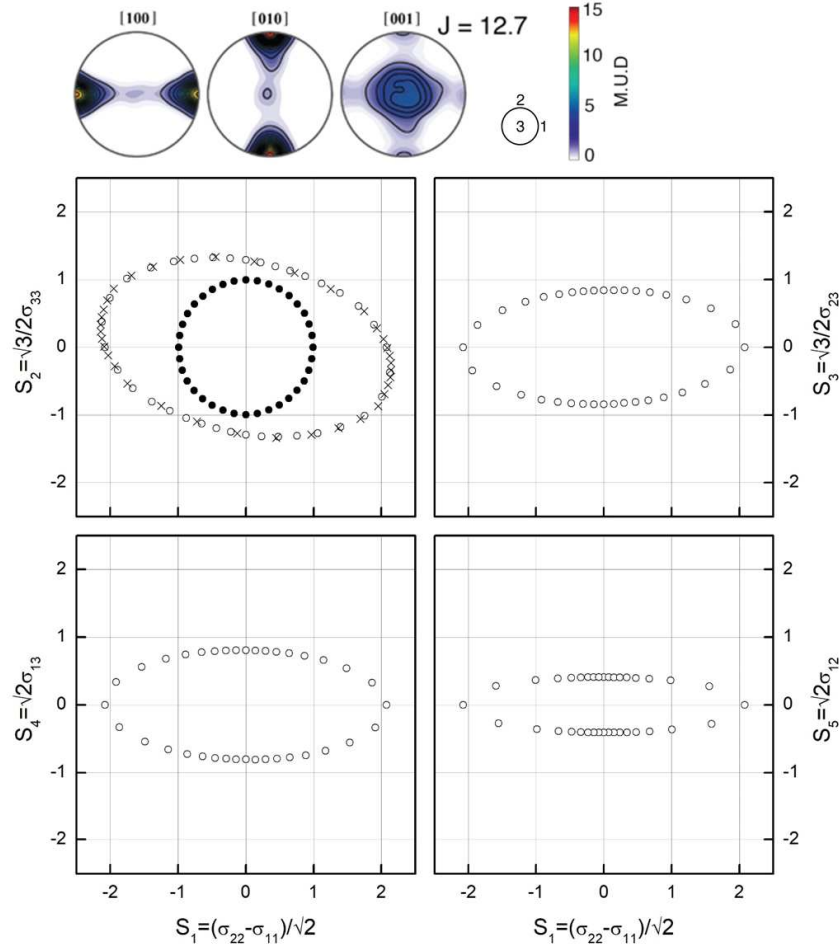


Figure 4.2: $\{\pi\}$ - and shear projections of the equipotential yield surface for a textured olivine polycrystal calculated using the SO-VPSC approach. Simulations were run using slip systems data compatible with high temperature and moderate pressure conditions (Table 4.2). The yield surface was sampled using 36 equispaced ($\Delta\theta = 15^\circ$) stress points (open circles). For comparison, the yield surface obtained using a strain-rate sampling is also displayed in the $\{\pi\}$ -projection (crosses). All loading conditions are normalized by the work rate displayed by an isotropic olivine polycrystal under similar conditions – the corresponding equipotential is displayed in the $\{\pi\}$ -projection as full circles. The insert on the top shows the olivine CPO used in the anisotropic calculations. The pole figure (contours in multiples of a uniform distribution) and the texture intensity (J-index) were processed using the open-source MTEX toolbox (Mainprice et al., 2014).

Table 4.3: Hill coefficients obtained by imposing strain-rate or stress for sampling the PES

Sampling variable	F	G	H	L	M	N
Strain-rate (err=0.034)	0.0220	0.2208	0.3769	8.6133	2.0777	2.3101
Stress (err=0.028)	0.0225	0.2275	0.3744	8.9183	2.1258	2.3016

4.2.3.2 Model validation

In this section, we compare Adeli3D-anis predictions with those obtained directly by SO-VPSC simulations for two simple case studies: simple shear or axial compression applied to a cube with a strong, but homogeneous olivine texture at various orientations relative to the mechanical solicitation. The slip systems data and the olivine texture used in both simulations are that reported in the previous section (Table 4.2 and Figure 4.2). Both models employ a large deformation formalism. The Hill constitutive material law is integrated in the material texture reference frame $\hat{\mathcal{R}}$ (i.e., Hill coefficients are defined in $\hat{\mathcal{R}}$).

Since texture evolution as a function of strain is not implemented in the finite-element simulations, Von Mises equivalent (VM) stresses $s_{eq} = \sqrt{\frac{3}{2}s_{ij}s_{ij}}$ predicted by the Adeli3D-anis at steady-state are compared with VM stresses predicted by the SO-VPSC at the end of a single deformation step, before reorientation of the texture. The VM stress in Adeli3D-anis is averaged over all (six) elements of the cube mesh. The orientation of the texture reference frame (XYZ) relative to the mechanical solicitation reference frame (123) is varied from 0° to 90° at 15° intervals. SO-VPSC simulations are adimensionalized: all stresses are normalized by the stress in the easiest (010)[100] slip system of olivine, whereas Adeli3D-anis produces absolute stresses that depend on the isotropic rheological parameters and on the imposed temperature. To compare the results of Adeli3D-anis and SO-VPSC models, the VM stresses for the textured polycrystal were therefore normalized by the VM of an olivine polycrystal with 1000 randomly oriented grains, which has an isotropic mechanical response.

Two sets of boundary conditions were considered in the axial extension tests. For the first set (BC1 in Figure 4.3a), extension was imposed in the Adeli3D-anis simulation by applying a constant velocity normal to the face normal to the axis 2 of the cube and keeping the opposite face fixed, one of the faces normal to the 1 and 3 axis is a symmetry plane (free slip conditions) and the other is free (free face). This correspond to mixed boundary conditions in SO-VPSC simulations, where an extensional velocity v_{22} is imposed, all shear velocity components are imposed null ($L_{i,j} = 0$), and equal non-null stresses σ_{11} and σ_{33} are imposed.

In the second set of boundary conditions (BC2 in Figure 4.4a), the two faces normal to the axis 1 are free in the Adeli3D-anis simulations. This corresponds to SO-VPSC simulations where the extensional velocity v_{22} , a null velocity to half of the shear components ($L_{12} = L_{13} = L_{23} = 0$), equal non null stresses σ_{11} and σ_{33} , and null shear stresses. The predicted

solutions for all loading-geometries are remarkably similar between the Adeli3D-anis and the SO-VPSC models for the two sets of boundary conditions (Figure 4.3b). The less stringent boundary conditions (BC2), i.e. allowing a rigid rotation, results in lower normalized VM stresses for all solicitations oblique to the texture reference frame, except at 45° (Figure 4.3b). In our case, due to the symmetry of the initial olivine texture, this rigid rotation may only occur around the extension axis.

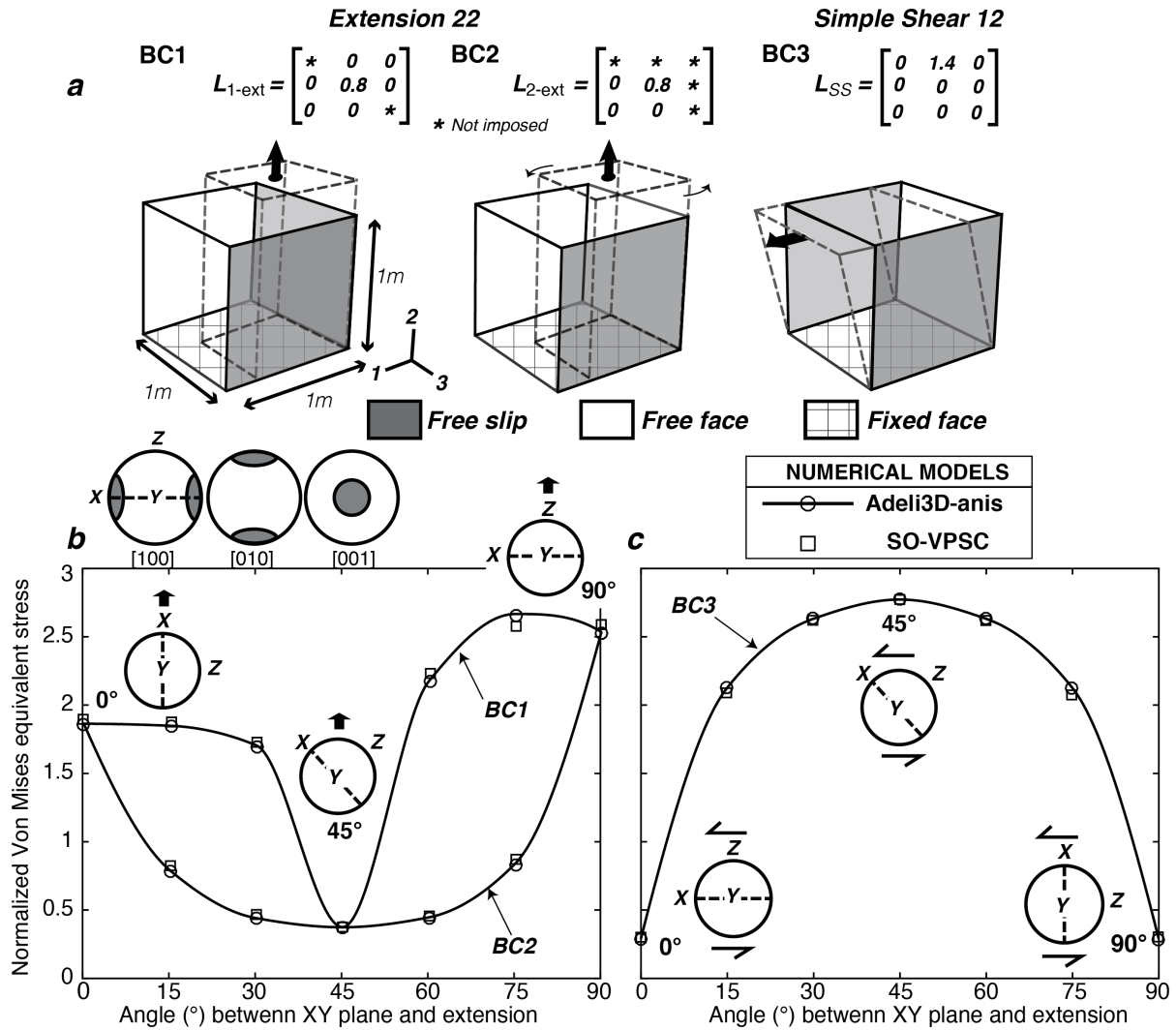


Figure 4.3: **a)** Imposed boundary conditions in Adeli3D-anis simulations and velocity gradient tensors (L) imposed in the corresponding SO-VPSC simulations: L_{ext} extension and L_{ss} simple shear. BC: boundary conditions. The symbol * indicates that the magnitude of the component is unknown and must be determined as a computational result. Comparison of the predictions of anisotropic ADELI3D and SO-VPSC simulations for **a)** axial extensional tests with two sets of boundary conditions (BC1 = two planes of symmetry and BC2 = a single plane of symmetry) and **b)** simple shear test (BC3). Parameters describing the isotropic part of the rheology are in Table 4.1.

Simple shear tests were performed by applying a constant tangential velocity parallel to the axis 1 on the face normal to axis 2, keeping the opposite face fixed, and imposing null normal velocities to the two faces normal to axis 3 (BC3 in Figure 4.3a). Equivalent boundary conditions are simulated in SO-VPSC by imposing a non-null component 12 and null values to all other components of the velocity gradient tensor. The stress variation as a function of the orientation of the imposed shear relative to the texture reference frame predicted by Adeli3D-anis and SO-VPSC models are also remarkably similar (Figure 4.3c).

4.2.4 Application: effect of texture-induced viscous anisotropy associated with fossil shear zones on the deformation of a continental plate

Viscoplastic deformation of mantle rocks in lithospheric-scale shear zones, i.e., narrow zones accommodating shear displacements between relatively undeformed domains of a tectonic plate, leads to development of olivine textures that may be preserved for very long time spans (hundreds of millions years, cf. **Tommasi and Vauchez 2015**). Anisotropic viscosity due to fossil olivine texture in mantle shear zones has been argued to trigger localized deformation in the plates when the mechanical solicitation is oblique to the trend of the shear zones, leading to the formation of new plate boundaries parallel to these ancient structures (**Vauchez et al. 1997**; **Tommasi et al. 2001**; **Tommasi et al. 2009**). However, previous simulations testing this effects, which directly coupled VPSC polycrystal plasticity models into the finite-element codes simulating the geodynamical flows, were too computationally demanding for full investigation of the interactions between texture-induced anisotropy and other strain localization processes active on Earth.

The parametrization presented here allows for a significant gain in both computation time and memory requirements, enabling to run 3D geodynamical models that explicitly consider the effect of texture-induced viscous anisotropy in the mantle on the plates' dynamics. Its first application in geodynamics, which focused on investigating the possible role of texture-induced viscous anisotropy in the mantle in producing enigmatic alignments of active seismicity in intraplate settings, corroborates the importance of texture-induced viscous anisotropy in controlling strain localization not only in the mantle, but also in the overlying crust. Most important, these simulations highlighted unexpected couplings between localized deformation controlled by variations in the orientation and intensity of olivine texture in the mantle and the deformation processes in the brittle (plastic) upper crust (Figure 4.4).

A detailed analysis of the geological aspects of the problem are presented in **Mameri et al. (2020)**. Parameters controlling the isotropic part of the mantle and crust rheologies are shown in Table 4.4.

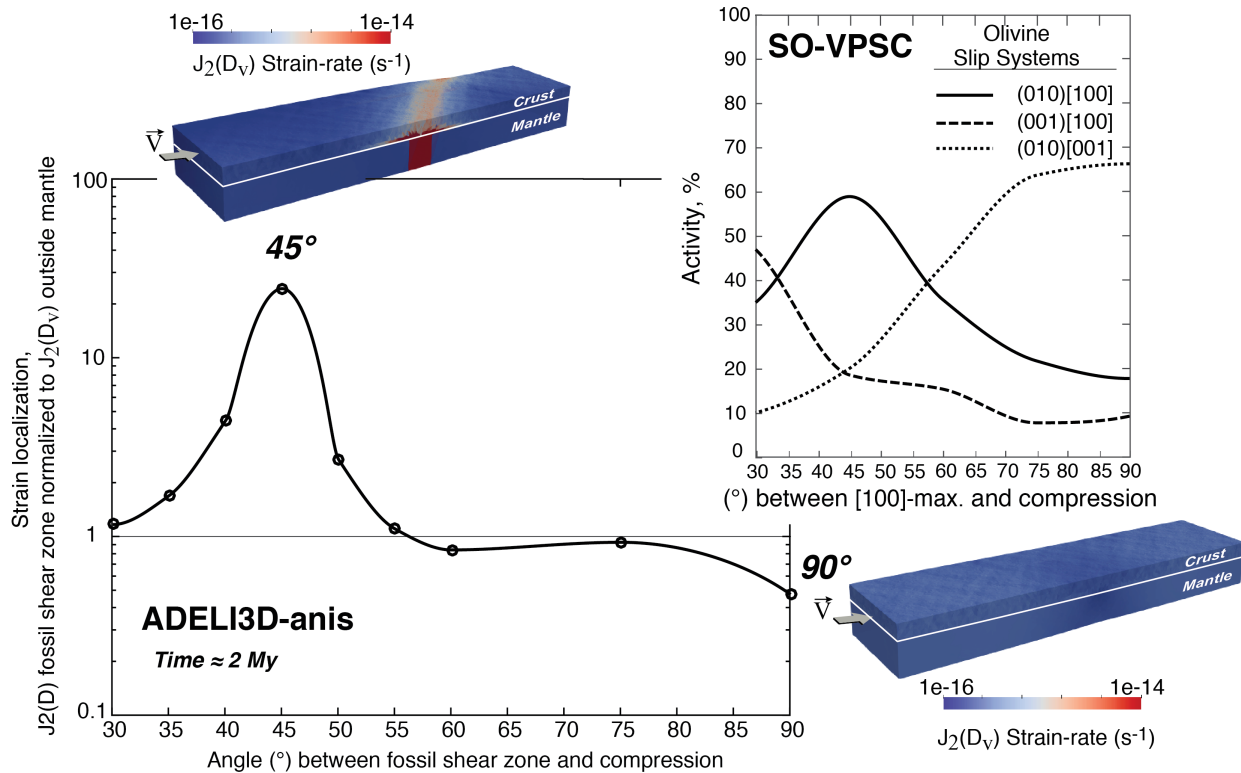


Figure 4.4 Strain localization quantified as the ratio between the average of second-invariant of the strain-rate within the fossil mantle shear zone and outside it for different orientations of the fossil shear zone relatively to the imposed shortening. The model represents a 1100 km long, 500 km wide, and 120 km thick continental plate containing a fossil shear zone marked by a change in the olivine texture in the lithospheric mantle. The olivine texture in the fossil shear zone is coherent with past strike-slip deformation (horizontal shear in a vertical plane, leading to a texture similar to the one presented in Fig. 4.2, with horizontal $[100]$ and $[010]$ maxima parallel and normal to the shear zone orientation, respectively). The surrounding mantle has a random texture. Strain localization is not symmetrical with respect to the orientation of the fossil shear zone relative to the imposed compression, reflecting correctly the fact that the CRSS of the easy $[100](010)$ system is lower than that of the hard $[001](010)$ system. Insert: Slip system activity predicted by the SO-VPSC approach as function of the orientation of the shortening relatively to the maximum concentration of $[100]$ -axes within the fossil shear zone plane. Strain localizes in the fossil shear zone when high shear stress are resolved onto the easy $[100](010)$ slip system of olivine within it.

Table 4.4: Isotropic material parameters used in the geodynamical simulations

	Wet quartzite^a	Wet dunite^b
Density (kg m^{-3}) ρ	2653	3300
Young modulus (GPa)	70	160
Poisson ratio	0.25	0.28
Fluidity ($\text{Pa}^{-n} \text{s}^{-1}$) γ_0	$1.63 \cdot 10^{-26}$	$3.98 \cdot 10^{-25}$
Activation Energy ($\text{kJmol}^{-1} \text{K}^{-1}$) Q	135	498
Stress exponent n	3.1	4.5
Angle of friction* ϕ	30	-
Cohesion (MPa) c	10	-

*frictional weakening is imposed, ϕ is set to 15° once crustal fault plasticity in the mesh element exceeds 1%.
References: ^aPaterson and Luan (1990) ^bChopra and Paterson (1984)

4.2.5 Computational cost

Figure 4.5 compares the cost associated with using the present anisotropic Maxwell rheology relatively to the classical isotropic formulation for simulations with increasing number of elements. Plane strain compression is imposed to a plate with homogeneous isotropic material parameters associated with random texture. Parameters controlling the isotropic part of the rheology are the same in the two simulations (Table 4.4).

Two difference tolerance values for convergence in the flow law integration were tested. Both isotropic and anisotropic calculation times increase almost linearly with the number of elements. Therefore, the ratio between the CPU times for Adeli3D-anis and Adeli3D does not depend significantly on the mesh size. It even decreases with increasing mesh size, stabilizing for fine meshes.

If more severe convergence tolerance criteria are imposed, the cost of the anisotropic rheology is slightly higher. In all cases, the proposed anisotropic parameterization induces an additional numerical effort < 3 times the computational cost of the isotropic rheology. It should be noted that this ratio may change slightly depending on the degree of anisotropy induced by the texture of the material.

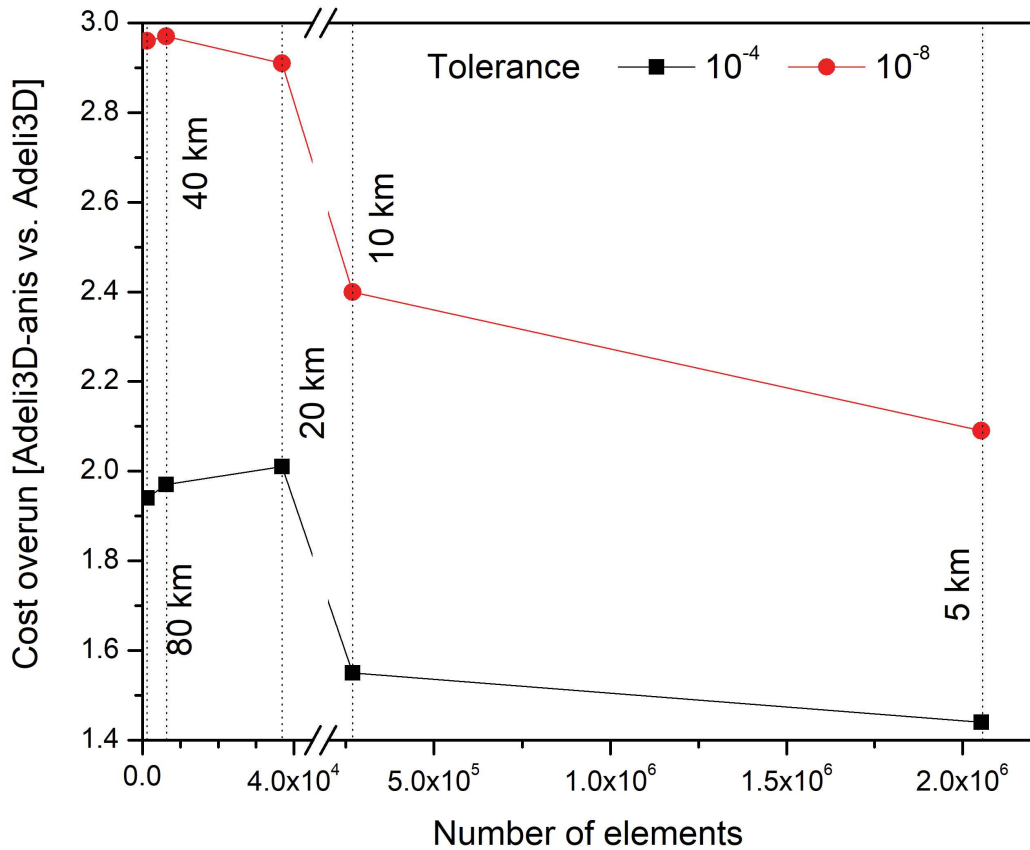


Figure 4.5: Evolution of the CPU time ratios between Adeli3D-anis / Adeli3D for increasingly finer mesh sizes, from 80km to 5km. The model domain has 1100 km long, 550 km wide, and 120 km thick. Simulations of Adeli3D-anis were performed using Hill yield surface coefficients for an isotropic texture ($F = G = H = \frac{1}{2}$, $L = M = N = \frac{3}{2}$).

4.2.6 Conclusion

We developed a relatively simple formulation for a Maxwell rheology combining an isotropic elastic and a texture-induced anisotropic non-linear viscous behavior, parameterized based on the Hill (1948) orthotropic yield criterion. The six Hill yield surface coefficients (F, G, H, L, M, N) are obtained by least-square fitting of four equipotential surfaces calculated using the SO-VPSC model. This formulation was implemented in the 3D thermo-mechanical code Adeli3D developed for modeling geodynamical flows. The numerical integration technique associated with the anisotropic viscous parameterization was validated by recovering the semi-analytical solution for a shear test either assuming a linear ($n=1$) or a non-linear ($n=3.6$) viscous rheology. Comparison of the predictions of Adeli3D-anis for simple shear and axial compression of a cube with a homogeneous olivine texture further validated the implementation. The computational effort only increases by a factor of 2-3 with

respect to the equivalent simulation with an isotropic Maxwell rheology. An example of the use of this parameterized viscous anisotropy is presented, allowing to quantify the effect of texture-induced viscous anisotropy in the mantle on the dynamics of tectonic plates. It predicts coupling between localized deformation controlled by variations in the orientation and intensity of olivine texture in the mantle and the strain distribution in the shallow crust. A current limitation for using of the present parameterization for modeling more complex geodynamical flows is our ability to take into account the evolution of the anisotropy induced by texture evolution, while retaining the computational efficiency. This is part of an ongoing study, where different strategies are evaluated.

Acknowledgments

We are grateful to Ricardo Lebensohn and Carlos Tomé for making the VPSC7c code freely available. This project received funding from the European Union's Horizon 2020 research and innovation program under the Marie Skłodowska-Curie grant agreement No. 642029 (ITN-CREEP), and from the CNRS (France) and CONICET (Argentina) under the Projet International de Cooperation Scientifique MicroTex (No. 067785).

Appendix

When dealing with incompressible media, it is convenient to explicitly decompose stress and strain-rate into deviatoric and hydrostatic components and to confine them to different subspaces, which may be decoupled for certain mechanical regimes. There are different ways of achieving such a decomposition. In the present calculations, we express the second-order tensorial quantities in an orthonormal basis of second-order symmetric tensors $\{\mathbf{b}^\lambda\}$, defined as:

$$\begin{aligned} \mathbf{b}^1 &= \frac{1}{\sqrt{2}} \begin{pmatrix} -1 & 0 & 0 \\ 0 & 1 & 0 \\ 0 & 0 & 0 \end{pmatrix}, \quad \mathbf{b}^2 = \frac{1}{\sqrt{6}} \begin{pmatrix} -1 & 0 & 0 \\ 0 & -1 & 0 \\ 0 & 0 & 2 \end{pmatrix}, \quad \mathbf{b}^3 = \frac{1}{\sqrt{2}} \begin{pmatrix} 0 & 0 & 0 \\ 0 & 0 & 1 \\ 0 & 1 & 0 \end{pmatrix} \\ \mathbf{b}^4 &= \frac{1}{\sqrt{2}} \begin{pmatrix} 0 & 0 & 1 \\ 0 & 0 & 0 \\ 1 & 0 & 0 \end{pmatrix}, \quad \mathbf{b}^5 = \frac{1}{\sqrt{2}} \begin{pmatrix} 0 & 1 & 0 \\ 1 & 0 & 0 \\ 0 & 0 & 0 \end{pmatrix}, \quad \mathbf{b}^6 = \frac{1}{\sqrt{3}} \begin{pmatrix} 1 & 0 & 0 \\ 0 & 1 & 0 \\ 0 & 0 & 1 \end{pmatrix} \end{aligned} \quad (\text{A.1})$$

The components of this basis have the property

$$b_{ij}^\lambda b_{ij}^{\lambda'} = \delta_{\lambda\lambda'}, \quad (\text{A.2})$$

and provide a unique ‘vector’ and ‘matrix’ representation of second- and fourth-order symmetric tensors, respectively. In the particular case of the stress tensor:

$$\sigma_{ij} = \sigma_\lambda b_{ij}^\lambda, \quad (\text{A.3})$$

where:

$$\sigma_\lambda = \sigma_{ij} b_{ij}^\lambda, \quad (\text{A.4})$$

The orthonormality of the basis guarantees that the six-dimensional strain-rate and stress vectors are work conjugate, i.e.

$$d_\lambda \sigma_\lambda = d_{ij} \sigma_{ij} \quad (\text{A.5})$$

The explicit form of the components σ_λ is:

$$(\sigma_1, \sigma_2, \sigma_3, \sigma_4, \sigma_5, \sigma_6) = \left(\frac{\sigma_{22} - \sigma_{11}}{\sqrt{2}}, \frac{2\sigma_{33} - \sigma_{11} - \sigma_{22}}{\sqrt{6}}, \sqrt{2}\sigma_{23}, \sqrt{2}\sigma_{13}, \sqrt{2}\sigma_{12}, \frac{\sigma_{11} + \sigma_{22} + \sigma_{33}}{\sqrt{3}} \right) \quad (\text{A.6})$$

and similarly for the components d_λ . It is clear that in this representation the first five components are deviatoric and the sixth is proportional to the hydrostatic component of the tensor. conversely, to convert back the vector to the second-order tensor:

$$\begin{pmatrix} \sigma_{11} & \sigma_{12} & \sigma_{13} \\ \text{sym} & \sigma_{22} & \sigma_{23} \\ & & \sigma_{33} \end{pmatrix} = \begin{pmatrix} -\frac{\sigma_1}{\sqrt{2}} - \frac{\sigma_2}{\sqrt{6}} + \frac{\sigma_6}{\sqrt{3}} & \sigma_5/\sqrt{2} & \sigma_4/\sqrt{2} \\ & \frac{\sigma_1}{\sqrt{2}} - \frac{\sigma_2}{\sqrt{6}} + \frac{\sigma_6}{\sqrt{3}} & \sigma_3/\sqrt{2} \\ \text{sym} & & \frac{2\sigma_2}{\sqrt{6}} + \frac{\sigma_6}{\sqrt{3}} \end{pmatrix} \quad (\text{A.7})$$

4.3 Supplementary Validation

Comparison between ADELI3D-anis and semi-analytical solutions in simple shear and axial extension applying formalism for small deformations and Hill parameters expresses in the laboratory reference frame

In this validation tests the corotational rotation rate $\widehat{S}\widehat{\omega} + (\widehat{S}\widehat{\omega})^T$ is neglected (small deformation formalism), which implies that $a = 0$ inside \mathbf{C}_n . In addition, the constitutive relation in ADELI3D-anis is integrated in the laboratory reference frame \mathcal{R} ($\theta = 0$), which require expressing the Hill parameters in this reference frame. The simple shear boundary conditions imposed to the cube in the ADELI3D-anis simulations are the same describe in the validation 1.

In axial extension, normal constant velocity is applied to one face and the opposite face is fixed (axis 2), whereas null normal velocities are applied to one of the faces in the

other two directions (one face in free-slip in both axis 1 and 3) (BC1 in **Figure S4.1**).

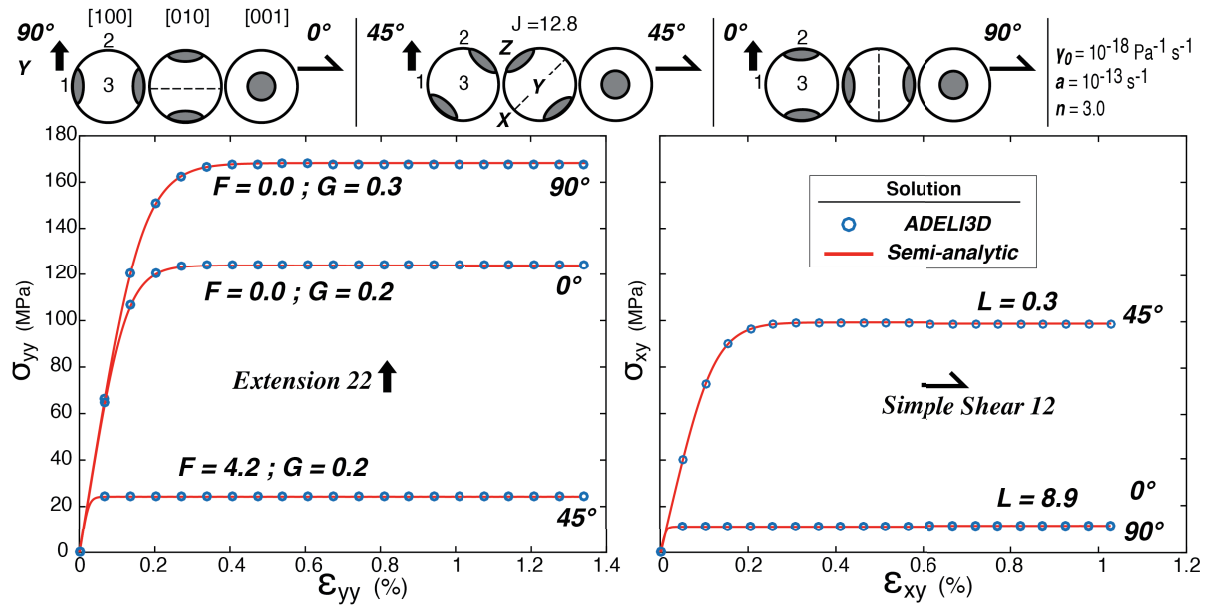


Figure S5.1: Principal components of the stress and strain tensor in simple shear and extension for the semi-analytical solution and the Hill-based parameterization of the viscoplastic anisotropy of olivine implemented in ADELI3D for a non-Newtonian study-case. The relevant Hill parameters for the given mechanical test are presented ($\theta = 0^\circ$). The constitutive relation is solved with the Hill parameters in this reference (laboratory) frame.

Deformation was applied at different orientations relative to the CPO reference frame (XYZ defined by the maximum concentrations of the [100], [010], and [001] olivine axes). The angle defines the orientation of the imposed extension or shear direction relative to XY plane of the CPO reference frame, that is, the plane normal to the [010] maximum (**Figure S4.1** above). For small deformation formalism in simple shear and axial extensional, and constitutive relation solved in the laboratory reference frame (Hill parameters in this reference frame), the ADELI3D-anis and semi-analytical solutions are identical for both anisotropic non-linear study-cases. Extensional deformation at 45° to the given XY plane is considerably weaker than extension at 0 and 90° to it. In simple shear deformation, the opposite behavior is predicted. In both simulations ϵ_{xy} and $\epsilon_{yy} < 1.5\%$.

REFERENCES

- Abramson, E. H., J. M. Brown, L. J. Slutsky, and J. Zaug (1997), The elastic constants of San Carlos olivine to 17 GPa, *J. Geophys. Res.*, 102, 12,253–12, 263.
- Bai, Q., S. J. Mackwell, and D. L. Kohlstedt (1991), High- temperature creep of olivine: Mechanical results for buffered samples, *J. Geophys. Res.*, 96, 2441–2463, doi:10.1029/90JB01723.
- Blackman, D. K., Boyce, D. E., Castelnau, O., Dawson, P. R., & Laske, G. (2017). Effects of crystal preferred orientation on upper-mantle flow near plate boundaries: rheologic feedbacks and seismic anisotropy. *Geophysical Journal International*, 210(3), 1481-1493.
- Castelnau, O., Blackman, D.K., Becker, T.W., 2009. Numerical simulations of texture development and associated rheological anisotropy in regions of complex mantle flow. *Geophys. Res. Lett.* 36, 1–6. <https://doi.org/10.1029/2009GL038027>
- Castelnau, O., Blackman, D.K., Lebensohn, R.A., Castañeda, P.P., 2008. Micromechanical modeling of the viscoplastic behavior of olivine. *J. Geophys. Res. Solid Earth* 113, 1–18. <https://doi.org/10.1029/2007JB005444>.
- Chopra, P. N., Paterson, M.S. 1984. The role of water in the deformation of dunite, *J. Geophys. Res.* 89, 7861–7876. <https://doi.org/10.1029/JB089iB09p07861>.
- Cundall, P. & Board, M. (1988). A microcomputer program for modeling large-strain plasticity problems. In Swoboda, C. (Ed.), *Numerical methods in geomechanics* (pp. 2102–2108). Rotterdam, the Netherlands: A. A.
- Gawad J., Banabic D., Van Bael A., Comsa D.S., Gologanu M., Eyckens P., Van Houtte P., Roose D., 2015, An evolving plane stress yield criterion based on crystal plasticity virtual experiments, *International Journal of Plasticity*, 75, 141-169
- Hansen, L.N., Zimmerman, M.E., Kohlstedt, D.L., 2012. Laboratory measurements of the viscous anisotropy of olivine aggregates. *Nature* 492, 415–418. <https://doi.org/10.1038/nature11671>
- Hassani, R., Jongmans, D., & Chéry, J. (1997). Study of plate deformation and stress in subduction processes using two-dimensional numerical models. *Journal of Geophysical Research: Solid Earth*, 102(B8), 17951-17965
- Hill, R., 1948. A theory of the yielding and plastic flow of anisotropic metals. *Proc. Roy. Soc. London* 193A, 281

- Hill, R., 1965. Continuum micro-mechanics of elastoplastic polycrystals. *J. Mech. Phys. Solids* 13, 89–101
- Hutchinson J., 1976. Bounds and self-consistent estimates for creep of polycrystalline materials. *Proceedings of the Royal Society of London A* 348, 101-121
- Knoll, M., Tommasi, A., Logé, R.E., Signorelli, J.W., 2009. A multiscale approach to model the anisotropic deformation of lithospheric plates. *Geochemistry, Geophys. Geosystems* 10, 1–18. <https://doi.org/10.1029/2009GC002423>
- Lebensohn, R.A., Ponte Castañeda, P., Brenner, R., Castelnau, O., 2011. Full-field vs. homogenization methods to predict microstructure-property relations for polycrystalline materials. In: *Computational Methods for Microstructure-Property Relationships*. Springer, New York, pp. 393–441.
- Lebensohn, R.A., Tomé, C.N., 1993. A self-consistent anisotropic approach for the simulation of plastic deformation and texture development of polycrystals: Application to zirconium alloys. *Acta Metall. Mater.* 41, 2611–2624. [https://doi.org/10.1016/0956-7151\(93\)90130-K](https://doi.org/10.1016/0956-7151(93)90130-K)
- Lev, E., Hager, B.H., 2011. Anisotropic viscosity changes subduction zone thermal structure. *Geochem. Geophys. Geosyst.* 12, 1–9. <https://doi.org/10.1029/2010GC003382>.
- Liu, Y., Castañeda, P.P., 2004. Second-order theory for the effective behavior and field fluctuations in viscoplastic polycrystals. *Journal of the Mechanics and Physics of Solids*, 52(2), 467-495.
- Mainprice, D., F. Bachmann, R. Hielcher, and H. Schaeben (2014). Descriptive tools for the analysis of texture projects with large datasets using MTEX—Strength, symmetry and components, in *Rock Deformation from Field, Experiments and Theory: A Volume in Honour of Ernie Rutter*, Spec. Publ., edited by D. R. Faulkner, E. Mariani, and J. Mecklenburgh, 409 pp., Geol. Soc., London, U. K., doi:10.1144/SP409.8.
- Mameri, L., Tommasi A., Signorelli, J., Hassani R. (2020), Olivine-induced viscous anisotropy in fossil strike-slip mantle shear zones and associated strain localization in the crust, *Geophysical Journal International*, in press
- Mameri, L., Tommasi, A., Signorelli, J., & Hansen, L. N. (2019). Predicting viscoplastic anisotropy in the upper mantle: a comparison between experiments and polycrystal plasticity models. *Physics of the Earth and Planetary Interiors*, 286, 69-80
- Masson, R., Bornert, M., Suquet, P., Zaoui, A., 2000. An affine formulation for the prediction

- of the effective properties of nonlinear composites and polycrystals. *Journal of the Mechanics and Physics of Solids* 48, 1203-1227.
- Molinari A., Canova G., Ahzi S., 1987. A self-consistent approach of the large deformation polycrystal viscoplasticity. *Acta Metallurgica et Materialia* 35, 2983-2994
- Nicolas, A., & Christensen, N. I. (1987). Formation of anisotropy in upper mantle peridotites- A review. Composition, structure and dynamics of the lithosphere–asthenosphere system, 16, 111-123
- Paterson, M.S., Luan, F.C., 1990. Quartzite rheology under geological conditions. In: Knipe, R.J., Rutter, E.H. (Eds.), *Deformation mechanisms, rheology and tectonics*. Geological Society Special Publication, pp. 299–307. Peacock
- Plunkett, B., Lebensohn, R.A., Cazacu, O., Barlat, F., Anisotropic yield function of hexagonal materials taking into account texture development and anisotropic hardening. *Acta Mater* 2006;54:4159–69. <https://doi.org/10.1016/j.actamat.2006.05.009>.
- Ponte Castañeda P., 1996. Exact second-order estimates for the effective mechanical properties of nonlinear composites. *Journal of the Mechanics and Physics of Solids* 44, 827-862
- Ponte Castañeda, P., 2002. Second-order homogenization estimates for nonlinear composites incorporating field fluctuations: I—theory. *J. Mech. Phys. Solids* 50, 737–757. [https://doi.org/10.1016/S0022-5096\(01\)00099-0](https://doi.org/10.1016/S0022-5096(01)00099-0)
- Professor Harry Hammond Hess. *Nature* 224, 393 (1969). <https://doi.org/10.1038/224393a0>
- Savage, M. K., 1999, Seismic anisotropy and mantle deformation: What have we learned from shear wave splitting?, *Reviews of Geophysics.*, v. 37(1), p. 65–106.
- Signorelli, J., Tommasi, A., 2015. Modeling the effect of subgrain rotation recrystallization on the evolution of olivine crystal preferred orientations in simple shear. *Earth Planet. Sci. Lett.* 430, 356–366. <https://doi.org/10.1016/j.epsl.2015.08.018>
- Tomé, C.N., Lebensohn, R.A., *Manual for VPSC7c*, Los Alamos National Laboratory, Los Alamos (2012), https://public.lanl.gov/lebenso/VPSC7c_manual.pdf
- Tommasi, A., Knoll, M., Vauchez, A., Signorelli, J.W., Thoraval, C., Logé, R., 2009. Structural reactivation in plate tectonics controlled by olivine crystal anisotropy. *Nat. Geosci.* 2, 423–427. <https://doi.org/10.1038/ngeo528>
- Tommasi, A., Mainprice, D., Canova, G., Chastel, Y., 2000. Viscoplastic self-consistent and equilibrium-based modeling of olivine lattice preferred orientations: Implications for the upper mantle seismic anisotropy. *J. Geophys. Res.* 105, 7893–7908.

<https://doi.org/10.1029/1999JB900411>

- Tommasi, A., Vauchez, A., 2001. Continental rifting parallel to ancient collisional belts: An effect of the mechanical anisotropy of the lithospheric mantle. *Earth Planet. Sci. Lett.* 185, 199–210. [https://doi.org/10.1016/S0012-821X\(00\)00350-2](https://doi.org/10.1016/S0012-821X(00)00350-2)
- Tommasi, A., Vauchez, A., 2015. Heterogeneity and anisotropy in the lithospheric mantle. *Tectonophysics* 661, 11–37. <https://doi.org/10.1016/j.tecto.2015.07.026>
- Vauchez, A., Barruol, G., Tommasi, A., 1997. Why do continents break up parallel to ancient orogenic belts? *Terra Nova*, 9(2), 63-66.
- Wenk, H.-R., Bennett, K., Canova, G.R., Molinari, a., 1991. Modelling plastic deformation of peridotite with the self-consistent theory. *J. Geophys. Res.* 96, 8337-8349. <https://doi.org/10.1029/91JB00117>

CHAPTER V

MODELLING VISCOUS ANISOTROPY IN FOSSILIZED LITHOSPHERIC STRIKE-SLIP SHEAR ZONES

*The purpose of models is not to fit the data,
but to sharpen the questions.*

Samuel Karlín

5 Strain localization in intraplate lithospheric strike-slip shear zones due to CPO-induced viscous anisotropy in the mantle

5.1 General Introduction

In this chapter, I explored the geodynamical implications of viscous anisotropy associated to a textured strike-slip mantle shear zone for the deformation of the mantle and crust far from active plate boundaries. The occurrence of linear seismicity (i.e. stress localization) in intraplate domains associated with old lithospheric shear zones is examined, and a conceptual model to explain these puzzling features of plate tectonics is proposed based on the model predictions presented here. In the next section the “Article #3” (§ 5.2) is presented, and in the following section (§ 5.3) its “Supplementary Material”.

Article #3

Most of the data presented in this chapter is part of an article published in the journal *Geophysical Journal International (GJI)*.

OXFORD
ACADEMIC

Geophysical Journal International

ACCEPTED MANUSCRIPT

Olivine-induced viscous anisotropy in fossil strike-slip mantle shear zones and associated strain localization in the crust

Lucan Mameri ✉, Andréa Tommasi, Javier Signorelli, Riad Hassani

Geophysical Journal International, ggaa400, <https://doi.org/10.1093/gji/ggaa400>

Published: 25 August 2020

Lucan Mameri^a, Andréa Tommasi^a, Javier Signorelli^b, Riad Hassani^c

^a *Géosciences Montpellier – CNRS & Université de Montpellier, France*

^b *Instituto de Física de Rosario, CONICET & Universidad Nacional de Rosario, Argentina*

^c *Géoazur, Observatoire de la Côte d’Azur, Université Côte d’Azur, France*

ABSTRACT

We propose that strain localization in plate interiors, such as linear belts of intraplate seismicity, may arise from spatial variations in viscous anisotropy produced by preferred orientation of olivine crystals (CPO or texture) inherited from previous deformation episodes in the lithospheric mantle. To quantify this effect, we model the deformation of a plate containing a fossil strike-slip mantle shear zone at different orientations relative to an imposed shortening, but no initial heterogeneity in the crust. The fossil shear zone is characterized by different orientation and intensity of the olivine CPO relatively to the surrounding mantle, which is isotropic in most simulations. The anisotropy in viscosity produced by the CPO, which remains fixed throughout the simulations, is described by an anisotropic (Hill) yield function parameterized based on second-order viscoplastic self-consistent (SO-VPSC) models. The results indicate that lateral variations in viscous anisotropy in the mantle affect the strain distribution in the entire lithosphere. Reactivation of the mantle shear zone and strain localization in the crust above it occur for compression at 35-55° to the mantle shear zone, with a maximum at 45°. The magnitude of strain localization depends on (i) the contrast in viscous anisotropy and, hence, on the CPO orientation and intensity in the mantle domains, (ii) the boundary conditions, and (iii) the feedbacks between mantle and crustal deformation. For a strong olivine CPO, when the boundary conditions do not hinder shear parallel to the fossil mantle shear zone, strain rates within it are up to 30 times higher than in an isotropic surrounding mantle or up to 200 times when the surrounding mantle is anisotropic, which results in strain rates up to 10 times or up to 100 times higher in the crust above the fossil shear zone. Frictional weakening in the crust faults increases strain localization in the entire lithospheric column. High strength contrasts between the mantle and the ductile crust result in less efficient coupling, with strong localization in the mantle and lower crust, but weak in the brittle upper crust. Decrease in the crust-mantle strength contrast enhances coupling and produces more homogenous strain distribution with depth, as well as a time-dependent evolution of strain localization, which reaches a peak and decreases before attaining steady-state. Comparison of seismic anisotropy, regional stress, and focal mechanism data in linear arrays of intraplate seismicity, like the New Madrid and South American seismic zones, to our models' predictions corroborates that olivine CPO preserved in fossil lithospheric-scale shear zones may be key for the development of such structures.

Keywords: Creep and deformation; Mantle processes; Intra-plate processes; Rheology: crust and lithosphere; Numerical modeling; Continental tectonics: strike-slip and transform;

5.2.1 Introduction

In intraplate domains, olivine crystallographic preferred orientations (CPO) formed during previous collisional or rifting events might be preserved for long time-spans. Directional dependence of the mantle viscosity due to olivine CPO fossilized in the lithospheric mantle, particularly that formed in large-scale strike-slip shear zones in

collisional belts, has been argued to influence the deformation of continental plates, producing structural reactivation of fossil mantle structures when subsequent stress fields generate high resolved shear stresses on them (**Tommasi and Vauchez 2001; Vauchez et al. 1997; Vauchez et al. 1998**).

The parallelism between the directions of fast shear-wave polarization, linear seismicity arrays, and inherited tectonic structures extending for several hundreds of kilometres in intraplate domains, as in the New Madrid (**Tuttle et al. 2002; Nyamwandha and Powell 2016**) and South Armorican seismic zones (**Judenherc 2000; Judenherc et al. 2003; Mazabraud et al. 2005a; Mazabraud et al. 2005b**), suggests a causal relation between CPO-induced viscous anisotropy in the lithospheric mantle and strain localization in the crust. However, there is a lack of studies addressing quantitatively the role of olivine viscous anisotropy on crustal deformation that could support this view. Here, we model the viscous anisotropy associated with fossil strike-slip mantle shear zones and the resulting strain localization in the entire continental lithosphere. The key questions are: (1) whether lateral variations in the (orientation and intensity of) olivine CPO within the mantle suffices to trigger strain localization in otherwise stable intraplate domains, and (2) which is the degree and pattern of strain localization in both the crust and mantle.

Olivine is the most abundant and deformable rock-forming mineral in the lithospheric mantle. The olivine crystal displays a marked viscous anisotropy because it has only three independent slip systems to accommodate dislocation creep and because these slip systems have markedly different strengths. At high temperature and moderate pressure, olivine crystals may deform >100 times faster if their orientation allow for deformation by dislocation glide on the easy (010)[100] slip system rather than on the hard (010)[001] slip system (**Durham and Goetze 1977; Bai et al. 1991**). This viscous anisotropy is transferred to the rock-scale through the development of CPO (**Nicolas and Christensen 1987**). However, as the CPO has always some dispersion, the rock-scale anisotropy is significantly weaker than that of a single crystal. Activation of grain-boundary related processes in addition to intracrystalline glide further reduces the magnitude of viscous anisotropy, in particular in fine-grained rocks. For instance, in laboratory experiments under constant strain rate, fine-grained olivine polycrystals deformed in simple shear parallel to a previous shear direction and plane exhibit stresses ~2 times lower than those needed for deforming the polycrystals in extension perpendicular to the previous shear plane (**Hansen et al. 2012**). Polycrystal plasticity simulations carried out under equivalent boundary conditions and using exactly the

same olivine CPOs showed that, if only dislocation creep is considered, the contrast between simple shear and extension yield stresses increases to a factor ~ 6 (Mameri et al. 2019). These studies demonstrated that the viscous anisotropy at the rock-scale depends on the CPO symmetry and intensity, on the imposed boundary conditions, as well as on the relative contributions of dislocation and grain-boundary mechanisms to viscoplastic deformation.

May this CPO-induced viscous anisotropy produce strain localization at the scale of tectonic plates? Based on viscoplastic self-consistent (VPSC) simulations of the viscous anisotropy of olivine polycrystals, Tommasi and Vauchez (2001) concluded that oblique load on a CPO formed in response to a previous strike-slip deformation was likely to produce structural reactivation of collisional belts during plume-triggered rifting and that this reactivation was characterized by deformation in transtension. By coupling VPSC simulations to a finite-element model, Knoll et al. (2009) and Tommasi et al. (2009) proposed that CPO-induced viscous anisotropy in the lithospheric mantle may play an essential role in the deformation patterns at the plate tectonic scale. For instance, when the fossil olivine CPO in the mantle is oriented oblique to the imposed extension, the associated anisotropic viscosity induces strain localization and enhances toroidal flow, leading to transtensional rifting. These fully coupled models provided quantitative estimates of the effects of viscous anisotropy associated with strain-induced CPO in the lithospheric mantle. However, they were very time-consuming.

In the present work, we developed a parameterization of the anisotropic viscosity of olivine based on the prediction of VPSC simulations, which used relative slips system strengths derived from high temperature experiments in olivine single crystals, and implemented it in a 3D finite-element geodynamical code to model the anisotropic deformation of the mantle due to fossil olivine CPO and the mechanical response of the crust to this deformation. We evaluate how the mechanical response of a continental plate is affected by lateral variations in olivine CPO (orientation and intensity), by the boundary conditions, and by the mechanical interplay between crust and mantle deformation related to their strength contrast. The aim is to test whether CPO-induced viscous anisotropy associated with a fossil strike-slip mantle shear zone may trigger strain localization in the entire lithosphere, giving rise for instance to linear arrays of intraplate seismicity, as the New Madrid and South American seismic zones.

5.2.2 Numerical modelling

We use the 3D thermo-mechanical finite-element code Adeli3D (**Hassani 1994**) to model lithospheric-scale deformation. The code is based on a Lagrangian discretization of the *quasi*-static mechanical behavior of the lithosphere, which solves the obtained non-linear equations using a dynamic relaxation method (**Cundall and Board 1988**).

The elasto-viscoplastic deformation is given by:

$$\begin{cases} \boldsymbol{\sigma}^* = 2\mu (\mathbf{D} - \mathbf{D}_v) \\ \dot{p} = 3K \text{tr}(\mathbf{D}) \end{cases} \quad (1)$$

where \mathbf{D} and \mathbf{D}_v are the total and viscoplastic strain rate tensors, $\boldsymbol{\sigma}^*$ is the objective material derivative of the Cauchy stress tensor, p is the mean pressure, μ and K are the shear and bulk moduli, respectively. The equations are solved forward in time $[t^n, t^{n+1}]$ using a Crank-Nicholson scheme that assumes \mathbf{D} constant over the timestep. Further details can be found in **Chéry et al. (2001)**. The crust is elasto-viscoplastic. Frictional (brittle-plastic) behaviour in the upper crust obeys an isotropic Drucker-Prager yield criterion written as:

$$\mathcal{F}(\mathbf{S}) = J_2(\mathbf{S}) + \alpha (p - c / \tan\phi) \leq 0 \quad (2)$$

In this form, the second (2nd) invariant of the deviatoric stress tensor \mathbf{S} corresponds to the Von Mises equivalent stress: $J_2(\mathbf{S}) = \left(\frac{3}{2} \mathbf{S} : \mathbf{S}\right)^{1/2}$, ϕ is the static internal angle of friction, c is the cohesion, and α is a material parameter related to ϕ by $\alpha = 6 \sin\phi / (3 - \sin\phi)$. Frictional weakening may be imposed by decreasing the angle of friction after 1% of plastic strain in the mesh element. Thermally activated viscous creep follows a power law relationship in the form:

$$\mathbf{D}_v = \gamma \exp\left(-\frac{Q}{RT}\right) J_2(\mathbf{S})^{n-1} \mathbf{S} \quad (3)$$

where n , Q , and γ are the experimentally-derived power law exponent, activation energy in kJ mol⁻¹K⁻¹, and fluidity in Pa⁻ⁿ s⁻¹, respectively. R is the gas constant and T is temperature in degrees Kelvin. To simulate viscous anisotropy in the mantle, Eq. (3) was extended as:

$$\mathbf{D}_v = \gamma \exp\left(-\frac{Q}{RT}\right) J_h(\mathbf{S})^{n-1} \mathbf{A}_h : \mathbf{S} \quad (4)$$

where $J_h(\mathbf{S})$ is the Hill equivalent stress (**Hill 1948**) defined as:

$$J_h(\mathbf{S}) = (F(S_{11} - S_{22})^2 + G(S_{22} - S_{33})^2 + H(S_{33} - S_{11})^2 + 2LS_{12}^2 + 2MS_{23}^2 + 2NS_{31}^2)^{1/2} \quad (5)$$

Using the Voigt notation, the components of the stress and strain rate tensors are collected into 6-dimensional vectors. In this notation, \mathbf{A}_h is a rank-4 tensor describing the material anisotropy, which has the following matrix representation:

$$\mathbf{A} = \mathbf{A}_h = \frac{2}{3} \begin{bmatrix} F + H & -F & -H & 0 & 0 & 0 \\ -F & G + F & -G & 0 & 0 & 0 \\ -H & -G & H + G & 0 & 0 & 0 \\ 0 & 0 & 0 & L & 0 & 0 \\ 0 & 0 & 0 & 0 & M & 0 \\ 0 & 0 & 0 & 0 & 0 & N \end{bmatrix} \quad (6)$$

The Hill yield function (Eq. 5) must be defined in the reference frame of the CPO eigenvectors, which has to be orthotropic. The Hill parameters (F, G, H, L, M, N) for a given olivine CPO are evaluated using the second-order viscoplastic self-consistent (SO-VPSC) model as described in the next section. The isotropic case, i.e., $J_h(\mathbf{S}) = J_2(\mathbf{S})$ and $\mathbf{A}_h: \mathbf{S} = \mathbf{S}$, is retrieved by setting $F = G = H = 1/2$ and $L = M = N = 3/2$; this reduces Eq. (4) to Eq. (3).

Parameterizing the CPO-induced viscous anisotropy of olivine polycrystals

The viscoplastic mechanical response of an olivine polycrystal with a given CPO is calculated using the SO-VPSC model (**Ponte Castañeda 2002; Lebensohn et al. 2011**). The response is defined in the stress-space as an equipotential surface for a series of mechanical tests in which we impose the deviatoric stress tensor and determine the associated strain rate tensor. All simulations are run for olivine polycrystals composed by 1000 grains. The slip systems data are derived from experiments at high temperature and moderate pressure conditions (**Table 5.1**). We sample different loading paths (simple shear, pure shear, axial compression or tension) and vary the orientation of the stress tensor relatively to the CPO reference frame by 15° intervals. For defining properly the equipotential surface, the mechanical responses for all evaluated loading paths are normalized by the work rate of a polycrystal that has an isotropic response. A least-square method is used to fit the equipotential surfaces and calibrate the six parameters (F, G, H, L, M, N) that satisfy the anisotropic Hill yield function (Eq. 5).

Table 1: Olivine slip systems parameters used in the SO-VPSC simulations

Slip Systems	Critical Resolved	
	Shear Stress #	Stress Exponent
(010)[100]	1	3
(001)[100]	1	3
(010)[001]	2	3
(100)[001]	3	3
(011)[100]	4	3
(110)[001]	6	3
{111}<110> ^a	50	3
{111}<011> ^a	50	3
{111}<101> ^a	50	3

Adimensional values; normalized by the flow stress of the (010)[100] slip system. ^a Slip systems not active in olivine, used solely for stabilizing the calculations and accommodating << 5% strain in all simulations.

We estimate the viscous anisotropy for olivine polycrystals with an orthorhombic CPO, which is expected to develop by simple shear or combinations of simple and pure shear (Tommasi et al. 1999), and two different CPO intensities. The intensity of the olivine CPO is quantified by the J- or M-indexes calculated based on the orientation distribution function defined using a “*de la Vallée Poussin*” kernel with a halfwidth of 10° (Mainprice et al. 2014). The J-index may range from 1 (random) to infinite (single-crystal orientation) and the M-index from 0 to 1. The two CPO investigated in this study are characterized by a J-index of 2.8 (M-index = 0.12, weak CPO) and of 12.7 (M-index = 0.42, strong CPO). For the sake of comparison, olivine polycrystals deformed in torsion to shear strains between 3 and 19 display J-indexes between 9 and 23, with a median at ~13 and two outliers at 5 and 30 (Hansen et al. 2014). The median of >600 J-index measurements in naturally deformed peridotites is ~4 and the maximum is ~20 (Tommasi and Vauchez 2015).

Two-dimensional projections of the equipotential surfaces used for calculating the Hill parameters for olivine polycrystals with a random and the weak and strong investigated CPO are presented in **Figure 5.1**. The aspect ratio of the projections is proportional to the magnitude of the viscous anisotropy. The isotropic response (random CPO, J-index = 1) is characterized by circular projections (aspect ratio of 1:1). The projections become more elliptical as the strength of the CPO increases. For the olivine CPO used here, the maximum aspect ratio is observed in the S1-S5 projection, where flow stress for a pure-shear test with

traction parallel to the [010]-maximum of the CPO is a factor ~ 6 larger than the flow stress for a simple-shear test with shear parallel to the [100]-maximum on the plane normal to the [010]-maximum. The mathematical formalism and the numerical implementation of the parameterized viscous anisotropy in the code Adeli3D-anis are detailed in a companion article (Signorelli et al. *submitted*).

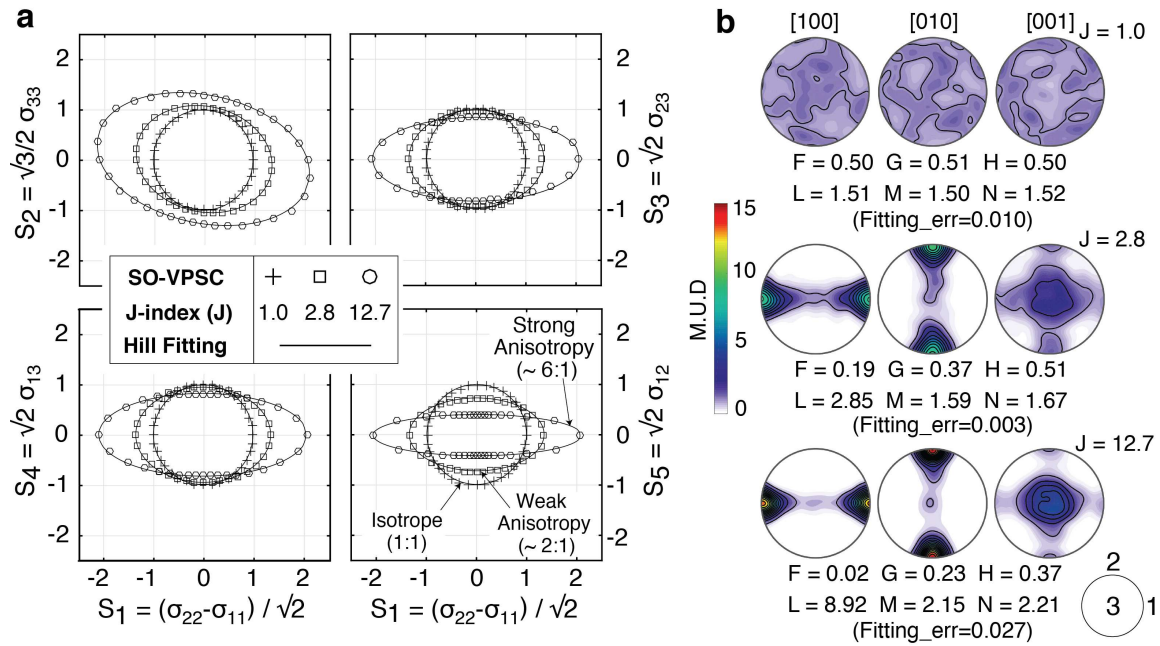


Figure 5.1: **a**) Projections of the equipotential surface predicted by SO-VPSC simulations (black lines) and the least-squares fit (black markers) used for defining the Hill parameters (F, G, H, L, M, and N) for the three olivine CPOs used in the present simulations, which are presented in **(b)**. The aspect ratio of the projections is proportional to the intensity of the viscoplastic anisotropy. The misfit between the SO-VPSC predictions and the Hill fitting is in all cases $\ll 0.1$. Pole figures are contoured at one multiple of uniform distribution intervals. Insert on the bottom right shows the relation between the CPO and the SO-VPSC reference frames.

5.2.3 Geodynamical model setup

Geometry and boundary conditions

The model has a heterogeneous mantle and a homogenous crust (**Figure 5.2**). It simulates a 1100 km long, 500 km wide, and 120 km deep continental plate containing a fossilized mantle shear zone marked solely by a change in the orientation and intensity of the olivine CPO in the lithospheric mantle. The model has therefore three domains: (1) a 40 km-thick crust and (2) an 80 km-thick mantle layer, which is subdivided into (2a) a 50 km-wide vertical fossil mantle shear zone that has an olivine CPO consistent with a previous

strike-slip deformation, and (2b) the surrounding mantle, which in most simulations has a random CPO. Simulations were also performed using a non-random CPO in the surrounding mantle, with a different orientation than in the fossil mantle shear zone. Crustal thickness is based on global models of velocity and density of the lithosphere, which predict crustal thicknesses of ~35-45 km in most continents (**Mooney 2015**). Lithospheric thickness is based on heat flow and seismic measurements, which imply that, outside cratons, the lithosphere in stable continental plates is on average 100-150 kilometres thick (**Steinberger and Becker 2018**). The direction of the fossil mantle shear zone relative to the imposed horizontal shortening in the reference simulation is of 45°; this angle (θ , called here loading-geometry) is varied between 30° and 90° in the different simulations. The dip of the fossil shear zone is vertical in all simulations. To simulate fossil mantle shear zones at $\theta < 30^\circ$ that do not crosscut the boundary on which the shortening is applied the simulation box has to be considerably lengthened. This results in a significant increase of computing time. Thus, the mechanical response at these loading-geometries was inferred based on the prediction for the complementary orientation (e.g., $\theta=30^\circ \approx \theta=60^\circ$), as previous studies show that polycrystals with orthorhombic olivine CPOs, such as those used here, display a *quasi*-symmetric deformation pattern relative to the loading-geometry (**Tommasi and Vauchez 2001**).

A constant compressional velocity of 1.10^{-9} m/s (~3cm/y) imposed normal to the left lateral boundary drives the plate kinematics (**Figure 5.2**). Free-slip conditions are imposed to the right lateral boundary. This results in <10% of bulk shortening along the Y direction after ~2.5 m.y. Gravity-induced body forces are considered. The upper boundary is free and lithostatic pressure conditions (Winkler-like) are imposed to the bottom boundary. In most simulations, lithostatic pressure conditions (P-litho) are imposed to the front and back lateral boundaries, but free-slip conditions were also tested. These two sets of lateral boundary conditions correspond to different strengths of the adjacent lithosphere, free-slip conditions simulating an undeformable domain, such as a cold craton, and lithostatic pressure conditions, a neighbouring domain with similar strength to that of the simulation box. Constant temperatures of 25°C and 1200°C are applied at the top and bottom boundaries of the model, with the Moho discontinuity at 600°C and linear temperature gradients in the crust and mantle. Heat flux is null at all boundaries. The models are discretized in *ca.* 480,000 tetragonal elements, which are on average 5 km wide in the crust and 10 km wide in the mantle. Further increasing the mesh resolution does not significantly change the model predictions at steady-state (Supplementary material **Figure S5.1**).

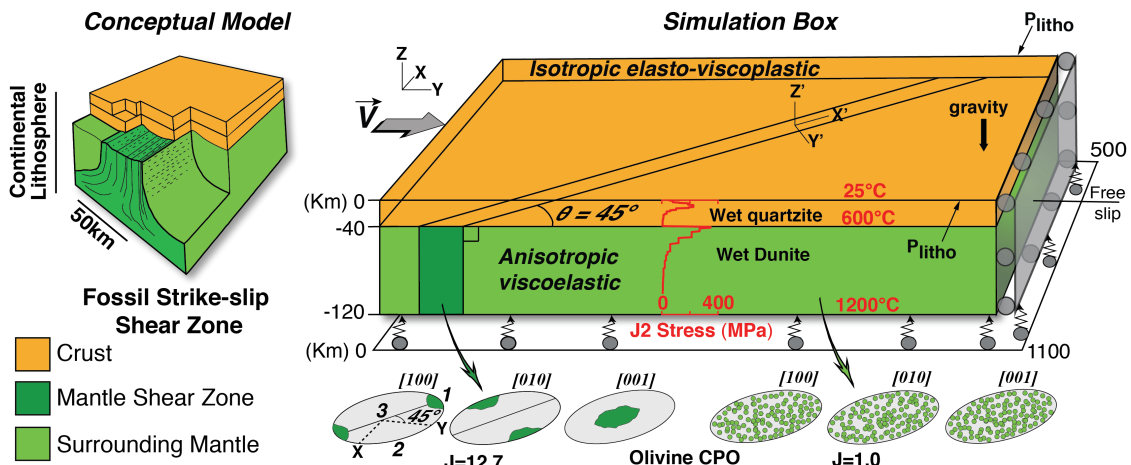


Figure 5.2: Setup for simulating the compressional deformation of a continental plate containing a 50 km wide fossil strike-slip shear zone in the upper mantle, but a homogenous crust. The mantle shear zone displays an olivine CPO consistent with seismic anisotropy measurements in lithospheric-scale strike-slip shear zones, characterized by maximum concentrations of olivine [100]- and [010]-axes horizontal, respectively parallel and normal to the shear zone trend, and a vertical alignment of [001]-axes (Vauchez and Nicolas, 1991). The orientation of the mantle shear zone relatively to the imposed compression axis (θ , loading-geometry) varies between 30° and 90° . In the reference case presented here, the preexisting mantle shear zone is at 45° to the shortening direction ($\theta = 45^\circ$) and has a strong olivine CPO ($J = 12.7$), whereas the surrounding upper mantle has a random CPO ($J=1.0$). The orientation of the mantle shear zone relatively to the imposed compression axis (θ , loading-geometry) varies between 30° and 90° . In the reference case presented here, the preexisting mantle shear zone is at 45° to the shortening direction ($\theta = 45^\circ$) and has a strong olivine CPO ($J = 12.7$), whereas the surrounding upper mantle has a random CPO ($J=1.0$). The external (XYZ) and mantle shear zone (X'Y'Z') reference frames are shown on the top view of the simulation box, and the lithospheric strength profile, the temperature and lateral boundary conditions used in the reference simulation in the lateral view. Average mesh sizes in the crust and mantle are 5 and 10 km, respectively.

Material behaviour and olivine CPO

In most models the crust has a homogeneous composition, but some simulations were run either with a two-layer crust or without the crust. We chose a static internal angle of friction (ϕ) of 30° and low cohesive strength of 10 MPa to simulate the behaviour of the brittle upper crust in a stable continental region containing a large number of faults formed in previous tectonic episodes (Townend and Zoback 2000). In some models, frictional weakening is imposed to the crust faults by reducing ϕ to a final angle of friction ϕ_f ($= 15^\circ, 10^\circ, \text{ or } 5^\circ$) when the plastic strain in the crustal mesh element exceeds 1%. This final angle of friction remains fixed thereafter (i.e., no fault healing). The rheology of the viscous crust in the reference simulation is defined by a ‘wet’ quartzite dislocation creep flow law (Paterson and Luan 1990), but stronger rheologies were also tested, relying on quartz-diorite (Ranalli 1997) and felsic granulite (Wilks and Carter 1990) dislocation creep flow laws (Table 5.2).

For the isotropic part of the mantle rheology, we used a traditional dislocation creep power law because exponential flow laws that better describe the mechanical behaviour of the shallowest lithospheric mantle (**Boioli et al. 2015; Gouriet et al. 2019**) have more complex formulations, which hinder their coupling with our parameterized description of the viscous anisotropy. A ‘wet’ dunite dislocation creep flow law (**Chopra and Paterson 1981**) defines the reference mantle rheology. Although data in natural peridotites indicate that olivine in the shallow lithospheric mantle has low H^+ contents (**Demouchy and Bolfan-Casanova 2016**), this flow law was chosen because it predicts moderate deviatoric stresses in the shallowest mantle (<500 MPa at strain rate of 10^{-15} s^{-1}), which is consistent with low-temperature experimental data on olivine polycrystals (**Demouchy et al. 2014**) and predictions of dislocation dynamics models (**Boioli et al. 2015; Gouriet et al. 2019**). To test the effect of the isotropic part of the mantle rheology on the strain distribution, simulations were also performed for a weaker ‘wet’ (**Hirth and Kohlstedt 2003**) and a stronger ‘dry’ dunite (**Chopra and Paterson 1984**) dislocation creep flow laws. Material parameters for all cases are summarized in **Table 5.2**.

A small finite strain is imposed to test whether the fossil anisotropy in the mantle may produce strain localization in the entire lithospheric column and to quantify the initial stages of this process before it is modified by the evolution of the microstructure. For finite strains $<10\%$, the evolution of the olivine CPO is negligible (**Tommasi et al. 2000; Boneh et al. 2015; Thieme et al. 2018**). The olivine CPO and associated viscous anisotropy (calibrated Hill parameters) in the two mantle domains are therefore maintained constant throughout the simulations. The olivine CPO in the mantle shear zone has maximum concentration of [100]-axes parallel to the fossil shear direction and [010]-axes normal to the fossil shear plane, while [001]-axes lies vertically (**Figure 5.1 and 5.2**). This orthorhombic CPO is representative of ‘wrench-fault type’ mantle fabric, consistent with seismic anisotropy measurements in large-scale strike-slip shear zones (e.g., **Vaucher and Nicolas 1991; Hearn et al. 1996; Tommasi et al. 1999; Baldock and Stern 2005, Vaucher et al. 2012**). The weak ($J=2.8$) and strong ($J=12.7$) CPO used in the present simulations are representative of the range of olivine CPO intensities measured in naturally deformed peridotites (**Tommasi and Vaucher 2015**).

5.3 Results

5.3.1 Impact of the mantle shear zone orientation and CPO intensity

Strain localization in the fossil mantle shear zone, quantified by the contrast in the 2nd invariant of the viscoplastic strain rate $J_2(\mathbf{D}_v) = \left(\frac{3}{2}\mathbf{D}_v:\mathbf{D}_v\right)^{1/2}$ between the fossil mantle shear zone and the surrounding mantle, is only observed between $35^\circ < \theta < 55^\circ$ (**Figure 5.3a**). At these loading-geometries, strain localization in the mantle is transmitted to the crust, as indicated by the contrast in strain rate between the crust directly above the reactivated mantle shear zone and the surrounding crust (**Figure 5.3b**). Strain localization in the mantle and crust varies non-linearly with the orientation of the fossil mantle shear zone. There is a marked reduction in strain localization between $\theta=45^\circ$ and $\theta=40^\circ$ or $\theta=50^\circ$. The mantle within and the crust atop a fossil shear zone trending normal to the imposed shortening ($\theta=90^\circ$) show lower strain rates than the surrounding isotropic mantle and crust, respectively. Finally, fossil shear zones oriented at 30° or between 55° and 75° to the imposed shortening are neutral; they produce neither significant strain localization nor delocalization.

The maximum strain localization occurs for the $\theta=45^\circ$ loading-geometry, because in this configuration the maximum concentrations of both [100]- and [010]-axes of the olivine CPO in the fossil shear zone are at 45° to the imposed horizontal shortening (cf. pole figures in **Figure 5.3**). This leads to high shear stresses resolved on the easy (010)[100] slip system for most olivine crystals within the mantle shear zone. At the $\theta=90^\circ$ loading-geometry, strain rates are low within the mantle shear zone because the maximum concentrations of [100]- and [010]-axes are perpendicular and parallel to the imposed shortening, respectively, resulting in low resolved stresses on the three main slip systems of olivine for most crystals. The reactivation of the fossil mantle shear zone induces the development of faults and shear zones in the crust atop it, but strain localization in the crust is lower than in the mantle (**Figure 5.3a,b**). In simulations for the $\theta=45^\circ$ loading-geometry with the strong olivine CPO, the crust atop the fossil mantle shear zone deforms on average ~ 10 times faster than the surrounding crust, whereas strain rates in the reactivated mantle shear zone are on average ~ 30 times faster than in the surrounding mantle. The contrast in magnitude of strain localization between the mantle and the crust is reduced when the strength of the CPO within the mantle shear zone is weaker. Strain rates are enhanced by a factor ~ 3 in the mantle shear zone and ~ 2 in the crust atop it relative to their surroundings (**Figure 5.3a,b**). The vertical strain distribution in the crust atop the shear zone also differs as a function of the CPO intensity in the fossil mantle shear zone (**Figure 5.3b**). In simulations with a strong CPO, the strain rate in the lower crust atop the mantle shear zone is considerably higher than in the upper crust. In simulations with a weak CPO, the strain rate is more homogeneously distributed with depth.

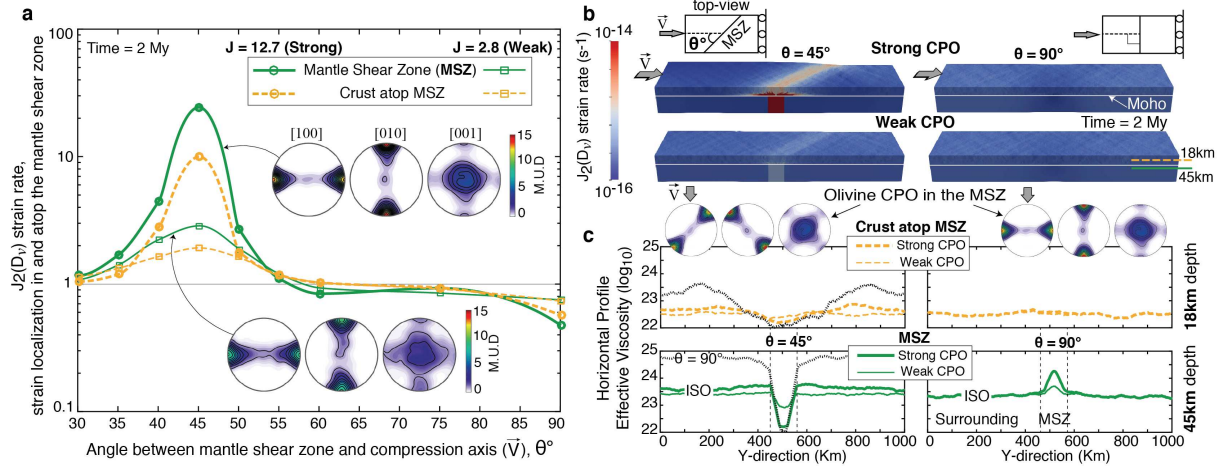


Figure 5.3: **(a)** Strain localization at steady-state ($\sim 2\text{My}$) as a function of the orientation of the fossil mantle shear zone relative to the imposed shortening (θ , loading-geometry). The strain localization is quantified by the ratio between the average of the 2nd invariant of the strain rate $J_2(D_v)$ in the fossil mantle shear zone (MSZ: green full lines) or in the crust right above it (yellow dashed lines) relatively to the surrounding upper mantle or crust, respectively. Simulations were performed for either strong ($J = 12.7$, thick lines) or weak olivine CPO ($J = 2.8$, thin lines) in the fossil mantle shear zone. **(b)** Strain rate field at steady-state in simulations with two different orientations of the fossil strike-slip mantle shear zone relative to the imposed shortening ($\theta = 45^\circ$ or 90°), in which either the strong or the weak olivine CPO was ascribed to the mantle shear zone. Pole figures illustrate the orientation-relation between the olivine CPO in the fossil mantle shear zone and the imposed shortening. **(c)** Horizontal effective viscosity profiles at 18 km (middle crust) and 45 km depth (uppermost mantle) for the four simulations shown in (b). Black thin dashed lines in (c) are the mantle and crust effective viscosity profiles for the relation between CPO in the mantle shear zone and surrounding upper mantle that results in the maximum contrast in mechanical behavior (i.e., [100]-axes at 45° and 90° to the compression direction, respectively). Pole figures are contoured at one multiple of a uniform distribution interval.

The variation in strength between the different domains may be quantified by comparing their effective viscosities, calculated as $\eta = J_2(\mathbf{S})/2J_2(\mathbf{D}_v)$. **Figure 5.3c** shows the effective viscosity along horizontal profiles parallel to the Y-axis (external reference frame XYZ) in the central part of the modelled domain at 18 km depth (ductile crust) and 45 km depth (shallow lithospheric mantle). Deformation of a plate with a fossil mantle shear zone with a strong CPO in the $\theta=45^\circ$ loading-geometry induces effective viscosities within the mantle shear zone ~ 30 times lower than in the surrounding mantle, whereas the middle crust atop the fossil shear zone has an effective viscosity < 5 times lower than the surrounding crust. At the $\theta=90^\circ$ loading-geometry, a mantle shear zone with a strong CPO displays effective viscosities ~ 5 times higher than the surrounding mantle. In this simulation the lateral contrast in effective viscosity in the middle crust is negligible. For cases with a weak CPO in the fossil mantle shear zone and an isotropic surrounding mantle, the effective viscosity

contrast between the mantle shear zone and the surrounding mantle is reduced to <3 times for both $\theta=45^\circ$ and $\theta=90^\circ$ loading-geometries. The contrast is even lower in the crust, being only detectable for the $\theta=45^\circ$ loading-geometry (**Figure 5.3c**).

The contrast in effective viscosity is significantly enhanced if the surrounding upper mantle has a non-random olivine CPO with maximum concentrations of [100]- and [010]-axes oriented perpendicular and parallel to the compression direction, respectively (i.e., equivalent to the CPO in the shear zone at $\theta=90^\circ$). For a strong CPO in both the mantle shear zone at $\theta=45^\circ$ and the surrounding mantle with the orientation described above, the effective viscosity contrast reaches factors ~ 500 in the mantle and ~ 30 in the crust (black dashed lines in **Figure 5.3c**). This is mainly due to the strain rates in the fossil mantle shear zone and in the crust right above, which are a factor ~ 200 and ~ 100 higher than in the surrounding mantle and crust, respectively (Supplementary material **Figure S5.2**).

The mechanical response of the mantle shear zone is not perfectly symmetric regarding complementary loading-geometries, e.g., strain localization is slightly more effective for $\theta=40^\circ$ than for $\theta=50^\circ$ (**Figure 5.3a**). This small asymmetry results from the difference in critical resolved shear stresses (relative strength) between the (001)[100] and (010)[001] slip systems in olivine (**Table 5.1**). For orientations of the fossil mantle shear zone lying at $50^\circ \leq \theta \leq 90^\circ$ to the applied stress, the hard (010)[001] slip system accommodates more deformation than the easy (001)[100] slip system. For a fossil mantle shear zone oriented at $0^\circ \leq \theta \leq 40^\circ$ the easy slip system (001)[100] is more active than (010)[001], which results in slightly more effective strain localization.

5.3.2 Influence of imposing different lateral boundary conditions

In the previous simulations, lithospheric pressure conditions (P-litho) were applied to the lateral boundaries of the model (**Figure 5.2**). In the present section, we investigate the effect of imposing free-slip boundary conditions (F-slip) to these boundaries. In F-slip conditions, the strain localization in the fossil mantle shear zone occurs for a more limited range of loading-geometries and the magnitude of the localization is considerably reduced (**Figure 5.4a**). For a fossil mantle shear zone oriented at 45° to the imposed shortening, the contrast in strain rate relatively to the surrounding mantle is reduced from a factor ~ 30 in P-litho to a factor ~ 2 in F-slip conditions. In the latter, the weaker strain localization in the fossil mantle shear zone does not promote strain localization in the crust atop it. Therefore, the deformation in the crust differs considerably from the one in a simulation with the same

orientation of the fossil shear zone but with P-litho conditions at the lateral boundaries. In F-slip conditions evenly spaced faults oriented normal to the applied shortening develop across the entire crust, regardless the loading-geometry.

Analysis of the different components of the strain rate in the mantle shear zone (D_{ij}) as a function of loading-geometry indicates that the change in the lateral boundary conditions affects essentially shearing parallel to the mantle shear plane - the component parallel to the maximum [100]-axes of the olivine CPO (**Figure 5.4b**). When P-litho conditions are imposed to the lateral boundaries, if the mantle shear zone is oriented at 45° to an imposed horizontal shortening, shearing parallel to the fossil shear plane ($D_{x'y'}$) dominates the deformation. F-slip conditions on the lateral boundaries hinder this shearing component, which is ~ 8 times slower than under the P-litho conditions. The variation of the components $D_{x'x'}$, $D_{y'y'}$ and $D_{z'z'}$ between the two sets of boundary conditions is much smaller. For both P-litho and F-slip lateral boundary conditions, a fossil mantle shear zone is reactivated in transpression when oriented at 40° - 50° to an imposed horizontal shortening. However, the vorticities are markedly different. In F-slip conditions, shortening normal to the fossil shear zone trend is equivalent to along-strike shearing, whereas in P-litho along-strike shearing largely predominates.

For both F-slip and P-litho lateral boundary conditions, the deformation with loading-geometries $\theta < 45^\circ$ are characterized by higher $D_{x'x'}$ than $D_{y'y'}$ strain rates components. The opposite behaviour is observed for loading-geometries $\theta > 45^\circ$. The $D_{z'z'}$ component remains constant and positive (indicating thickening parallel to Z) independent of loading-geometry and boundary conditions. At $\theta > 45^\circ$ loading-geometries, the $D_{y'y'}$ components are negative (indicating shortening parallel to Y') for both sets of lateral boundary conditions, but the $D_{x'x'}$ component are almost null under F-slip conditions and positive under P-litho conditions. At $\theta < 45^\circ$ loading-geometries, $D_{x'x'}$ components are negative, whereas $D_{y'y'}$ components are almost null under F-slip conditions, but positive under P-litho conditions. This implies an unexpected, but small, widening of the mantle shear zone despite the imposed large-scale shortening. This widening does not occur in F-slip conditions, indicating that it is a direct consequence of the full (3D) expression of the olivine viscous anisotropy when the plate is deformed at P-litho conditions.

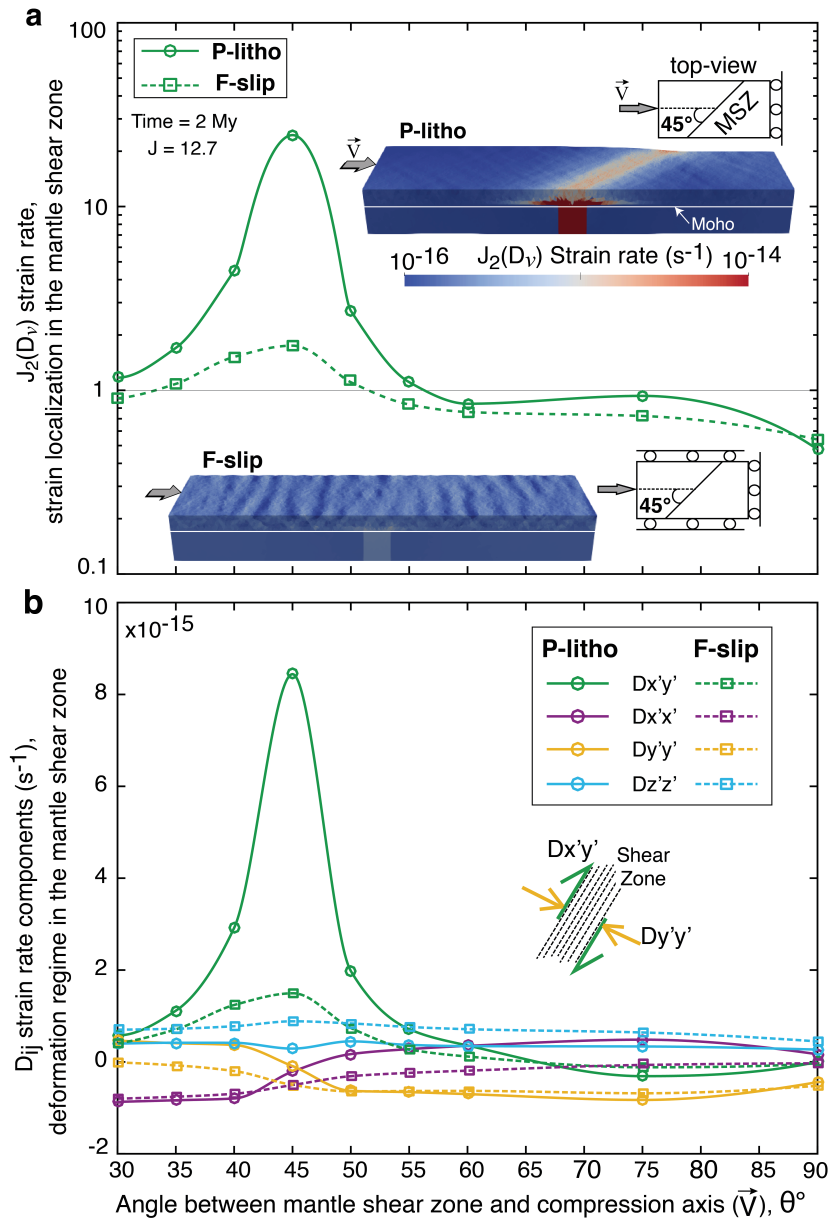


Figure 5.4: Effect of varying the conditions imposed on the lateral boundaries from lithostatic pressure (P-litho, full lines) to free-slip (F-slip, dashed lines) on **(a)** the strain localization, quantified by the ratio between the average of the 2nd invariant of the strain rate $J_2(D_v)$ in the fossil strike-slip mantle shear zone and in the surrounding upper mantle, and on **(b)** deformation regime in the mantle shear zone, characterized by the components of the strain rate (D_{ij}) plotted in the mantle shear zone reference frame ($X'Y'Z'$) as a function of the loading-geometry (θ). Predictions at steady-state conditions ($\sim 2\text{My}$) for simulations with a strong olivine CPO in the mantle shear zone. Inserts in **(a)** show the 2nd invariant of the strain rate field for the reference loading-geometry ($\theta = 45^\circ$) obtained using both boundary conditions.

5.3.3 Anisotropy versus isotropic viscous weakening in the mantle shear zone

Does the effect of heterogeneity in viscous anisotropy (due to a lateral variation in olivine CPO) within the upper mantle differ from the effect of an isotropic rheological

heterogeneity (due to a lateral variation in temperature, composition, grain size...) with the same geometry and orientation relative to the imposed loading? To answer this question, we ran simulations with a fossil strike-slip mantle shear zone with a random olivine CPO, but an *ad-hoc* increase in the fluidity γ (Eq.4; **Table 5.2**) by a factor 10 or 100 relative to the surrounding mantle. At constant stress, an increase in the fluidity results in an increase in strain rate by the same factor.

Table 5.2: Isotropic material parameters used in the geodynamical simulations

	Wet Quartzite ^a	Quartz- Diorite ^b	Felsic Granulite ^c	Dry Dunite ^d	Wet Dunite ^e	Wet Dunite ^f
Density (kg m^{-3}) ρ	2.65e3	2.65e3	2.7e3	3.3e3	3.3e3	3.3e3
Young modulus (GPa)	70	70	70	160	160	160
Poisson ratio	0.25	0.25	0.25	0.28	0.28	0.28
Fluidity ($\text{Pa}^{-n} \text{s}^{-1}$) γ	1.63e-26	1.14e-28	4.e-25	2.42e-16	3.98e-25	3.56e-16
Activation energy ($\text{kJmol}^{-1}\text{K}^{-1}$) Q	135	123	260	545	498	480
Stress exponent n	3.1	3.2	3.4	3.5	4.5	3.5
Angle of friction* ϕ	30	30	30	-	-	-
Cohesion (MPa) c	10	10	10	-	-	-

*In simulations where frictional weakening is imposed, ϕ is reset to 15°, 10°, or 5° once crustal fault plasticity in the mesh element exceeds 1%.

^aPaterson and Luan 1990; ^bRanalli 1997; ^cWilks and Carter 1990; ^dChopra and Paterson 1984; ^eChopra and Paterson 1981; ^fHirth and Kohlstedt 2003

Reactivation of the isotropic rheological heterogeneity within the upper mantle occurs for all loading-geometries (**Figure 5.5a**). The magnitude of strain localization also depends on the orientation of the isotropic heterogeneity relative to the imposed loading, but in a weaker manner than for an anisotropic (olivine CPO-controlled) heterogeneity. Similarly to the anisotropic mantle shear zone, the maximum strain localization occurs when the maximum elongation of the tabular isotropic heterogeneity is at $\theta = 45^\circ$ to the imposed shortening, but strain rates for this orientation are only ~ 10 times higher than for the $\theta = 90^\circ$ loading-geometry. For comparison, the strain rate contrast between the two loading geometries in CPO-induced anisotropic models attains a factor ~ 60 . This may be explained as variations in the mechanical behaviour of the isotropic heterogeneity as a function of its orientation result only from its tabular shape, i.e., from high resolved shear stress projected onto the elongation of the heterogeneity. The anisotropic mantle shear zone presents a more non-linear variation in strain localization as a function of the loading-geometry than the isotropic one (**Figure 5.5a**). At the $\theta = 45^\circ$ loading-geometry, the strain localization in the anisotropic mantle shear zone is similar to the one observed in an isotropic mantle shear zone 100 times weaker than the surrounding mantle (fluidity increased by a factor 100). For $\theta = 40^\circ$ or 50° loading-geometries, an increase in the fluidity of the isotropic fossil shear zone by a factor ~ 10 better approximates the response of the anisotropic fossil mantle shear zone. For loading-geometries between $60^\circ \leq \theta \leq 90^\circ$, strain still weakly localizes in the isotropic fossil

mantle shear zone, whereas the anisotropic one displays a factor <3 lower strain rates than the surrounding mantle.

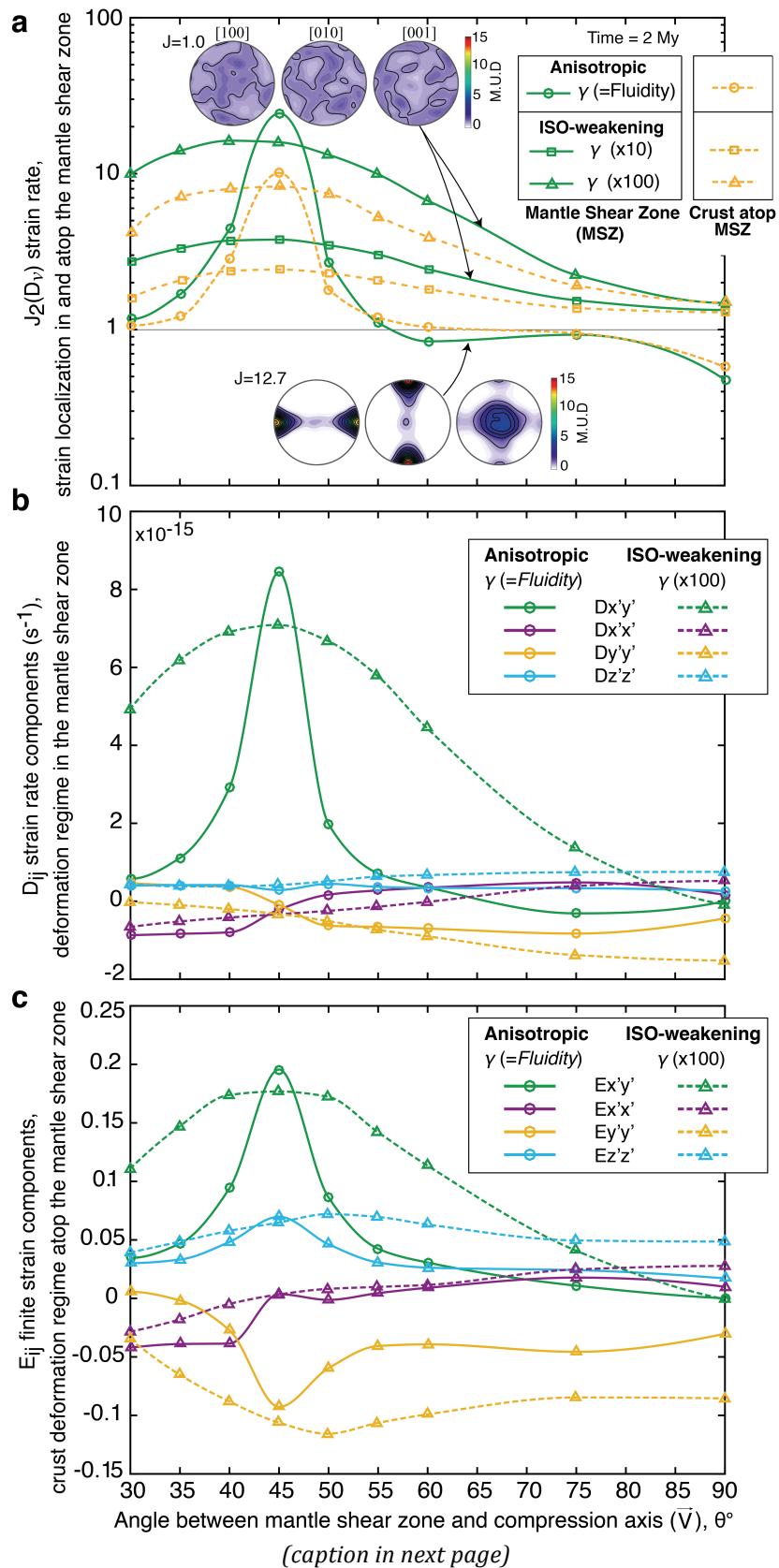


Figure 5.5: (a) Comparison between the strain localization at steady-state ($\sim 2\text{My}$) in a fossil mantle shear zone with either a strong olivine CPO (anisotropic; J-index = 12.7) or a random olivine CPO (isotropic; J-index = 1.0) but a 10- or 100-fold increase in the fluidity (γ in Eq. 3 and 4 and Table 2) for different orientations of the fossil mantle shear zone relative to the imposed shortening direction. Strain localization is quantified by the ratio between the average of the 2nd invariant of the strain rate $J_2(D_v)$ within the mantle shear zone (green full lines) or in the crust right above it (yellow dashed lines) and the same quantity in the surrounding upper mantle or crust, respectively. (b) Deformation regime in the mantle shear zone, characterized by the components of the average strain rate (D_{ij}) in the shear zone reference frame ($X'Y'Z'$) as function of the loading-geometry for both anisotropic and isotropic (100-fold increase in the fluidity) simulations. (c) Deformation regime in the crust just atop the fossil mantle shear zone characterized by the components of the average finite strain (E_{ij}) in the shear zone reference frame ($X'Y'Z'$).

Comparison of the components of the strain rate at steady-state as function of loading-geometry corroborates that in both isotropic and anisotropic cases structural reactivation of a fossil strike-slip mantle shear zone implies strong along-strike shearing ($D_{x'y'}$; **Figure 5.5b**). However, the magnitude of $D_{x'y'}$ component as a function of the loading-geometry differs significantly between the isotropic and anisotropic cases. At the $\theta=45^\circ$ loading-geometry, $D_{x'y'}$ strain rates in the anisotropic fossil mantle shear zone are higher than in the isotropic fossil shear zone with a factor 100 increase in fluidity. For all other oblique loading-geometries, the magnitude of the $D_{x'y'}$ component is significantly higher in the isotropic than in the anisotropic fossil mantle shear zone.

The inversion between the $D_{y'y'}$ and $D_{x'x'}$ components in the mantle shear zone for shortening at angles lower or higher than 45° relative to the fossil shear zone trend also occurs in the isotropic case, indicating that this inversion is due to macroscopic geometrical reasons rather than an effect of the CPO-induced viscous anisotropy. In contrast, widening of the mantle shear zone (positive $D_{y'y'}$) for loading-geometries between $30^\circ \leq \theta \leq 45^\circ$ does not occur in the case with isotropic rheological heterogeneity (**Figure 5.5b**). Therefore, (1) the widening of the fossil strike-slip mantle shear zone despite the imposed shortening, (2) the asymmetry of the mechanical response relative to complementary loading-geometries, and (3) the strong non-linearity of the strain localization pattern as a function of the loading-geometry are direct consequences of the CPO-induced viscous anisotropy within the fossil mantle shear zone.

Analysis of the components of the finite strain (E_{ij}) averaged over depth in the crust atop the fossil mantle shear zone shows that the deformation regime in the crust follows the deformation regime developed in the mantle (**Figure 5.5c**). The $\theta=45^\circ$ loading-geometry is characterized by high transpressional strains in the crust for both isotropic and

anisotropic cases, but vorticity ($E_{x'y'}$) is lower than in the mantle shear zone. In the isotropic case, transpression in the crust is observed for all loading-geometries between $30^\circ \leq \theta \leq 80^\circ$, although strain magnitude decreases with decreasing obliquity of the heterogeneity. In the anisotropic case, the along-strike strain component $E_{x'y'}$ in the crust is only important for loading-geometries $35^\circ \leq \theta \leq 55^\circ$.

5.3.4 Interactions between strain localization in the upper mantle and in the brittle crust

To analyse possible feedbacks between strain localization in the viscous mantle and in the brittle crust, we ran simulations in which frictional weakening is applied by reducing the initial static angle of friction ϕ_0 in the mesh element of the crust fault from 30° to $\phi_f = 15^\circ, 10^\circ$, or 5° after 1% of plastic strain and keeping it thereafter constant. The reduction in the angle of friction lowers locally the resistance of the rocks to further deformation by brittle processes (Eq.2), allowing long-lived faults to form in the upper crust.

The strain localization in the fossil strike-slip mantle shear zone and in the crust in the reference loading-geometry ($\theta = 45^\circ$) increases with increasing frictional weakening, as illustrated by the 2nd invariant of the finite strain field $J_2(\mathbf{E}) = \left(\frac{3}{2} \mathbf{E} : \mathbf{E}\right)^{1/2}$ in **Figure 5.6a**. In absence of frictional weakening ($\phi_0 = \phi_f = 30^\circ$), the upper crust remains homogeneously strong. The evolution of the strain localization with time is similar to that observed in simulations with the same geometry and CPO, but without a crustal layer (black dotted line in **Figure 5.6b**). However, the magnitude of strain localization is significantly reduced. When frictional weakening is active, the crustal faults, once formed, become weaker than the surroundings. This results in long-lived discrete faults forming an anastomosed network in the upper crust right atop the fossil mantle shear zone (**Figure 5.6a**). Strain localization in the upper crust results in further strain localization in the fossil mantle shear zone below, which in turn produces more strain localization in the crust right above it. The vertical distribution of strain in the crust also depends on the frictional weakening. In simulations with no frictional weakening, there is a marked variation of the strain distribution in the crust with depth (**Figure 5.6a**). In such cases, strain localization is weak in the middle and upper crust, and strong in the lowermost crust just atop the limits of the mantle shear zone. Strain in the lower crust is distributed in a diffuse zone with approximately twice the width of the fossil mantle shear zone. Frictional weakening results in a more homogeneous depth distribution of strain

and stronger strain localization in the upper crust. For $\phi_f = 5^\circ$, deformation in the upper crust is focused in a ~ 30 km wide network of crust faults atop the central part of the 50 km wide fossil mantle shear zone.

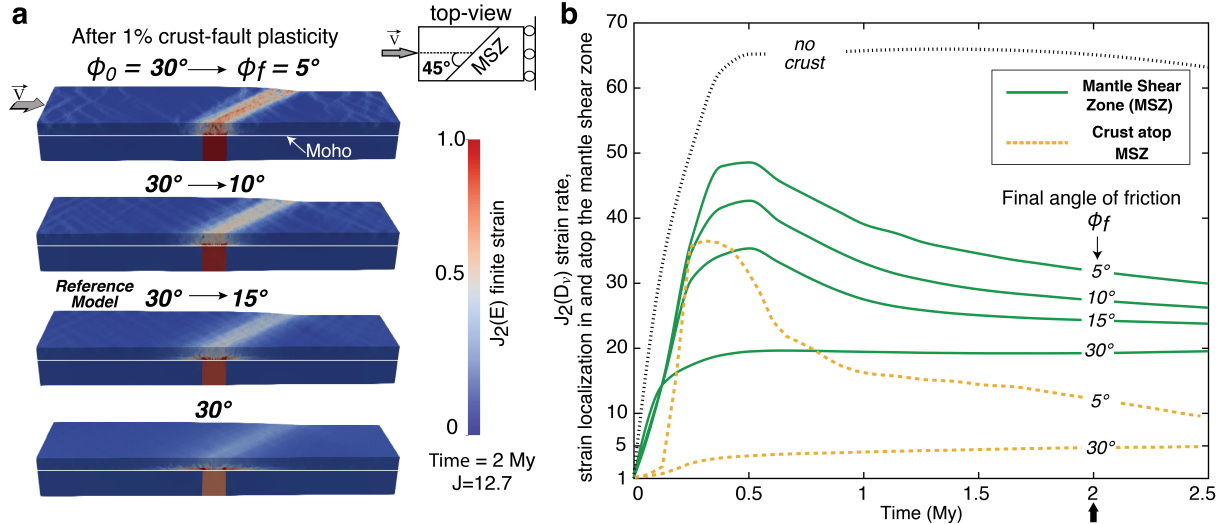


Figure 5.6: Feedbacks between frictional weakening in the brittle crust and strain localization due to viscous anisotropy in the fossil mantle shear zone. **(a)** Finite strain, 2nd invariant $J_2(E)$ field, after 2 My of shortening for simulations with different final (ϕ_f) angles of friction. **(b)** Evolution of the strain localization in the fossil mantle shear zone and in the crust above it, quantified by the ratio between the average of the 2nd invariant of the strain rate $J_2(D_v)$ within the fossil mantle shear zone and at 10 km-depth in the crust above it and the same quantities in the surrounding mantle and crust, as a function of time for the different simulations. All simulations were performed using a fossil shear zone oriented at 45° to the imposed shortening and displaying a strong olivine CPO. The black arrow at 2My in (b) indicates the time at which the finite strain fields presented in (a) are extracted.

Feedbacks between strain localization in the brittle crust and mantle produce a time-dependent behaviour (**Figure 5.6b**). If frictional weakening is not considered, i.e., $\phi_f = 30^\circ$, average strain rates in the mantle shear zone are ~ 20 times faster than in the surrounding mantle and stay stationary over time. In contrast, when frictional weakening is imposed, the strain localization in the fossil mantle shear zone is initially enhanced by a factor proportional to the reduction in the angle of friction and decreases afterwards. Nevertheless, strain localization within the mantle shear zone with a given frictional weakening is at all times more effective than in a simulation with a weaker frictional weakening. The ratio between the average strain rate in the mantle shear zone and in the surrounding mantle is initially ~ 33 and decreases to ~ 25 in the simulation with $\phi_f = 15^\circ$, whereas in a simulation with $\phi_f = 5^\circ$ it is initially ~ 50 and decreases to ~ 32 .

The evolution of strain localization in the crustal shear zone is similar to that in the

fossil shear zone in the mantle (**Figure 5.6b**). For $\phi_f = 5^\circ$, the peak of the average strain rate in the crust atop the fossil mantle shear zone is initially a factor ~ 35 faster than the surrounding crust and decreases to a factor ~ 10 . For the case with $\phi_f = 30^\circ$, the average strain rate in the crust atop the fossil mantle shear zone reaches a factor ~ 5 faster than the surrounding and remains fairly constant, as in the reactivated fossil mantle shear zone. The decrease in strain localization in the fossil mantle shear zone and crust in presence of frictional weakening results from the development, as the shortening proceeds, of faults in the upper crust outside the initial high strain domain right atop the mantle shear zone. Frictional weakening in these faults leads to reduction of the upper crust strength outside the crustal shear zone and to a more distributed deformation in the upper crust, which in turn, leads to less strain localization within the fossil mantle shear zone.

5.3.5 Mechanical coupling between the ductile crust and upper mantle

The results in the previous section highlight strong feedbacks between the mechanical behaviour and strain repartition in the lithosphere. To further investigate the effect of the mechanical coupling between crust and mantle on the strain localization, we varied the composition and hence the ductile strength of the crustal layer for a series of simulations with the fossil mantle shear zone oriented at 45° to the imposed shortening and in which frictional weakening ($\phi_f = 15^\circ$) is imposed in the brittle upper crust.

We found that both the magnitude and the evolution of the strain localization depend on the rheology of the ductile crust (**Figure 5.7a**). Additionally, different behaviours are observed as a function of the strength contrast between the crust and mantle, which may be quantified as the ratio between the average effective viscosities in the two layers (**Figure 5.7b**). When the mantle is significantly stronger than the crust, e.g., dry dunite mantle and wet quartzite crust (red squares), strain localization in the mantle shear zone and in the crust atop it reaches a constant value without subsequent delocalization (similarly to the case with no frictional weakening in **Figure 5.6b**). This evolution, characterized by the absence of time-dependent behaviour, is similar to one displayed by simulations without the crustal layer (dashed line in **Figure 5.7a**), but the presence of a strong crust results in weaker strain localization. A similar evolution, but even weaker strain localization, is predicted in simulations with a dry dunite mantle and two crustal layers, a wet quartzite upper crust and a felsic granulite lower crust (purple/red square), corroborating that increase in the lower crust

strength results in decrease of normalized strain rates in the fossil mantle shear zone with a given (CPO) viscous anisotropy. High strength in the lower crust favours effective crust-mantle coupling and produces localized deformation in the entire crust right above the fossil shear zone. In contrast, simulations with a low strength lower crust display wider shear zones in the lower crust compared to the mantle shear zone, with the highest strain accumulated atop the limits of the mantle shear zone and much less strain localization in the upper crust (compare the inserts displaying the strain field in the coupled and decoupled cases in **Figure 5.7b**).

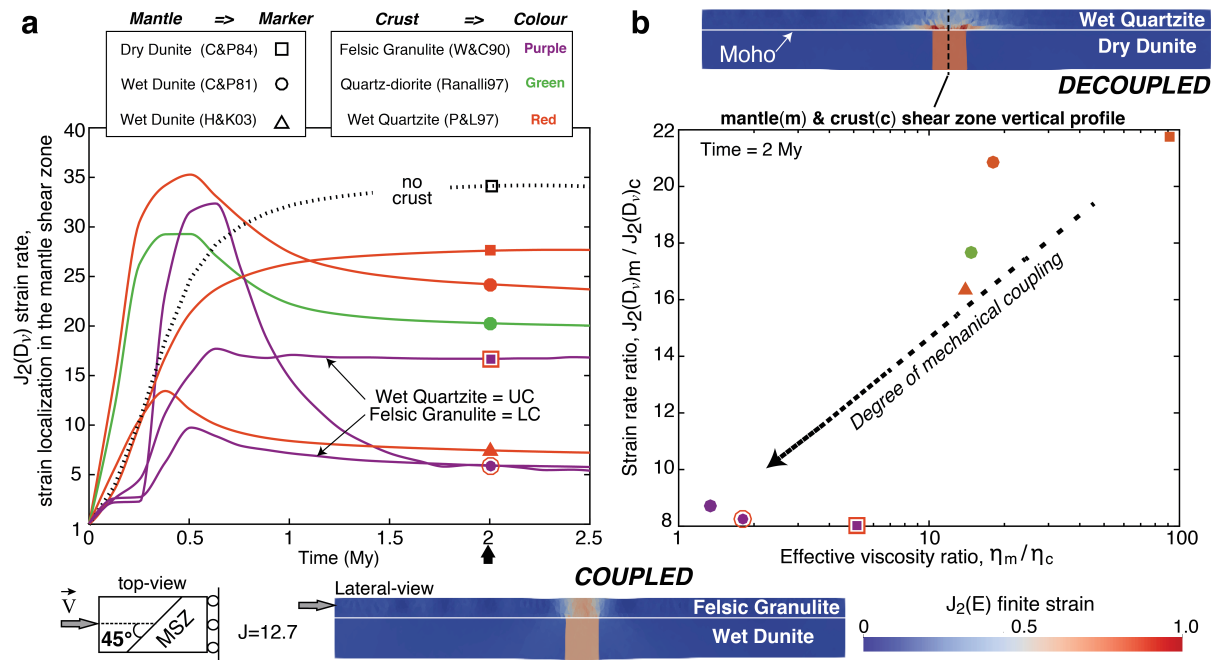


Figure 5.7: (a) Evolution of the strain localization in the anisotropic fossil mantle shear zone as a function of time for simulations with different isotropic part of the mantle and crust rheologies, leading to different degrees of mechanical coupling between these layers. Strain localization is quantified by the ratio between the average of the 2nd invariant of the strain rate $J_2(D_v)$ within the fossil mantle shear zone and in the surrounding upper mantle. The colours indicate the crust rheology and markers the mantle rheology. Most simulations have a crust with a uniform composition, but two have a two-layer crust with a felsic granulite lower crust (LC) and a wet quartzite upper crust (UC). The black arrow indicates the time at which the results plotted in (b) are extracted. (b) Relation between the degree of mechanical coupling and the viscosity contrast between the mantle and the crust. The degree of mechanical coupling is quantified by the ratio between the average strain rate $J_2(D_v)$ vertically integrated in the mantle shear zone and in the crust atop it. The ratio between effective viscosities (η) in both domains is obtained by integrating the effective viscosity from the bottom of the mantle shear zone to the Moho and from the Moho to a depth of 25 km in the crust. The inserts show the strain field (2nd invariant) after steady-state shortening for simulations displaying the highest (bottom) and lowest (above) degree of crust-mantle mechanical coupling. All simulations were performed using a fossil shear zone oriented at 45° and displaying a strong olivine CPO.

When the mantle is weak (wet dunite mantle: red, green and purple circles), strain localization is strongly time-dependent. After a peak at ~ 0.5 My of shortening, strain localization decreases over time and reaches steady-state at ~ 2 My ($\sim 8\%$ of bulk shortening). As in simulations with a strong dry mantle, the highest strain localization at steady-state occurs for the weakest crust (wet quartzite: red circle) and the lowest strain localization at steady-state, for the strongest crust (felsic granulite: purple circle). The highest peak strain localization is also observed for simulations with a weak ductile crust, whereas the lowest occurs when the upper crust is weak and the lower crust is strong (wet quartzite + felsic granulite: purple/red circle). The most vigorous decrease in strain localization as a function of time occurs in the simulation with the strongest ductile crust (felsic granulite: purple circle, from a factor ~ 32 to ~ 7). In this case, strain rates at steady-state are similar to that of the simulations with a two-layer crust where the lower crust have felsic granulite composition, suggesting that the lower crust rheology controls the steady-state deformation. Further reduction in the mantle strength (red triangle) results in less efficient strain localization in the entire lithosphere relative to simulations with a similar crust, but a stronger mantle (red circle) rheology. In summary, for a given isotropic mantle rheology, strain localization in the mantle shear zone (and in the crust) tends to decrease with increasing crustal strength, and for a given lower crust rheology, strain localization tends to increase with increasing mantle strength.

The degree of mechanical coupling between the crust and mantle for the different simulations was estimated using the ratio of the depth-integrated 2nd invariant of the strain rate in the mantle shear zone and in the crust right atop it. Comparison of this coupling measure with the mantle-crust strength contrast, characterized as the ratio of the depth-integrated effective viscosities in both domains (η_m/η_c ; **Figure 5.7b**), confirms that at first order, the higher the strength contrast, the lower the degree of mechanical coupling. Two end-members were recognized in the simulations. The most decoupled case has a weak wet quartzite crust and a strong dry dunite mantle. The most coupled case has a strong felsic granulite crust and a weak wet dunite mantle. When mantle and crust are decoupled, strain localization is highly variable as a function of depth, being strong in the mantle and in the lowermost crust, but weak in the middle and upper crust (cf. upper inset in **Figure 5.7b**). Conversely, when the mantle and crust are coupled, strain localization is more homogeneously distributed as a function of depth and strain localizes in a narrower domain in the crust, which width is equal or lower than the width of the fossil mantle shear zone (cf.

lower inset in **Figure 5.7b**).

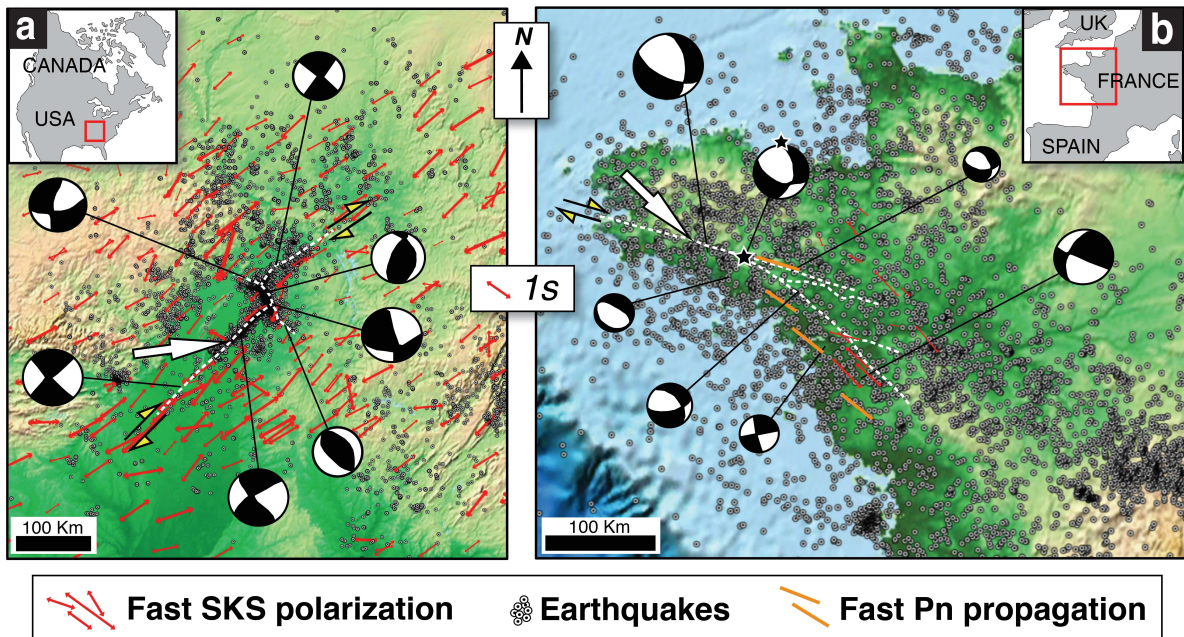


Figure 5.8: Orientation-relation between present-day principal horizontal stresses (large white arrow: compressional) and the horizontal projection of the dominant orientation of olivine [100]-axes (mantle fabric, inferred as parallel to the direction of fast polarization of S-waves or propagation of Pn-waves) in the **(a)** New Madrid (NM) and **(b)** South Armorian (SA) seismic zones. The horizontal stress direction and the focal mechanisms in the NM and SA seismic zones are based on **Johnson et al. (2014)** and **Mazabraud et al. (2004)**. In the NM zone the focal mechanisms are characterized mainly by strike-slip solutions and in the SA mainly by oblique solutions. Seismic anisotropy measurements were derived from the shear-wave splitting database (splitting.gm.univ-montp2.fr/DB/; **Barruol et al. 2009**). Most SKS splitting data in the NM zone are from **Nyamwandha and Powell (2016)**. Pn anisotropy in the SA zone is from **Judenherc (2000)** and SKS splitting data are from **Judenherc (2003)**. Earthquakes locations in the NM and SA seismic zones are derived from the United States Geological Survey (USGS; earthquake.usgs.gov) and from the SHARE European Earthquake Catalogue (SHEEC; **Grünthal et al. 2013; Stucchi et al. 2013**). The black star in *(b)* indicate the location of the Mw=4.3 Lorient event (**Perrot et al. 2005**).

An integrated analysis of the results presented in the **Figure 5.7a,b** indicates that the mechanically coupled and decoupled end-members display the maximum and minimum amount of strain localization at steady-state, respectively. In the coupled case, strain localization in the fossil mantle shear zone is initially high, but decreases significantly over time. In the decoupled case, strain localization is initially lower, but once it attains a maximum value, it remains constant. This difference in the evolution of strain localization over time arises from a higher influence of the strain repartition in the crust when the latter is mechanically strong. Thus, a relatively strong crust has a three-fold effect in the deformation

of the lithosphere: (1) it better transmits stresses from the mantle, resulting in a stronger initial strain localization and a more homogeneous depth distribution of strain in the crust, (2) it increases the resistance to the along-strike shearing during reactivation of the fossil strike-slip mantle shear zone, reducing the strain localization within it, and (3) it better transmits stresses back to the mantle, thus if frictional weakening occurs in the upper crust, deformation in the crust far from the mantle shear zone results in strain delocalization in this latter. The two last effects lead to less efficient long-term strain localization in the entire lithosphere.

5.4 Discussion

Validity and limitations of the model

Comparisons of the present simulations with those from previous studies on CPO-induced viscous anisotropy in the mantle and on the effect of large-scale rheological heterogeneities on lithosphere deformation validate our work. The range of flow stresses in the aggregate-scale due to the presence of olivine CPO is consistent with the maximum viscous anisotropy produced by dislocation creep in upper mantle rocks (**Mameri et al. 2019**). The presence of fossilized olivine CPO in either the mantle shear zone or in its surroundings results in non-parallelism between principal strain and stress components, in agreement with fully-coupled VPSC-finite element models of extension of an isothermal plate with homogenous olivine CPO (**Knoll et al. 2009**). As in the models by **Tommasi et al. (2001) and Tommasi et al. (2009)**, if the fossil mantle shear zone is oblique to the imposed mechanical load, along-strike shearing controls the reactivation of the fossil mantle shear zone. The stronger strain localization predicted in the simulations with a strong olivine CPO relatively to the previous works is consistent with the higher intensity of CPO used here. The present predictions for isotropic rheological heterogeneities agree with previous studies that examined the effects of large-scale isotropic rheological heterogeneities in both extensional and collisional intraplate settings (**Dunbar & Sawyer, 1989; Tommasi et al. 1995; Tommasi & Vauchez, 1997; Brune et al. 2012**). These studies demonstrated that weak heterogeneities always localize strain, with the intensity of the strain localization depending on the strength contrast relatively to the surroundings, but that oblique loading-geometries result in higher shear stress resolved along the maximum elongation of the heterogeneity, hence more effective strain localization.

The lithosphere has certainly large-scale heterogeneous lateral distribution of non-

random olivine CPO. Teleseismic shear-wave splitting data indicate that the lithosphere is characterized by domains with coherent seismic anisotropy patterns (on the scale of hundreds of km) and sharp changes (on the scale of tens of km) of the orientation and intensity of the anisotropy (*cf.* Shear-wave splitting database, <http://splitting.gm.univ-montp2.fr/DB/>). Although the teleseismic shear-wave splitting integrates seismic anisotropy all over the wave path, from the core-mantle boundary to the station, most anisotropy is produced in the upper 250 km of the mantle. Moreover, in continents these data document sharp variations within tens of km in the orientation and intensity of the anisotropy, pointing to a major contribution of the lithospheric mantle to the measured signal (**Alsina and Snieder 1995**). Thus, strain localization (or delocalization) resulting from lateral variations in viscous anisotropy (CPO) in the lithospheric mantle, as documented in the present models, are probably the rule rather than the exception on Earth.

Viscous anisotropy in the present models is parameterized for an olivine polycrystal deforming at high temperature, moderate pressure, and dry conditions, which favour intracrystalline deformation by dislocation glide in the [100] direction (e.g., **Bai et al. 1991**). However, if differential stresses are high or the temperature is low, as expected in the uppermost lithospheric mantle, the critical resolved shear stresses of the different olivine slip systems change and glide in the [001] direction is favoured (e.g., **Durham and Goetze 1977; Demouchy et al. 2014**). Thus, to model olivine deformation under low temperature, high stress conditions, a different parameterization of the viscous anisotropy is required. The transition from dominant [100] to [001] glide occurs at $\sim 1000^{\circ}\text{C}$ under laboratory conditions (**Durham and Goetze 1977; Demouchy et al. 2014**). However, mantle mylonites in peridotite massifs record clear olivine CPO indicative of dominant [100] glide even when deformed at temperatures as low as $\sim 900^{\circ}\text{C}$ (e.g., **Frets et al. 2014**). In peridotite mylonites deformed at lower temperatures (and higher stresses), activation of multiple slip systems, strong grain size reduction by dynamic recrystallization and increasing contribution of grain boundary processes results in weak olivine CPO, but still with a systematic concentration of [100] axes parallel to the stretching lineation (e.g., **Newman et al. 1999; Hidas et al. 2016**). This suggests that in nature the transition from [100] glide to dominant [001] glide occurs at much lower temperatures. In addition, comparison between olivine CPO developed in simple shear experiments on pure olivine synthetic aggregates (**Bystricky et al. 2000; Hansen et al. 2012; Hansen et al. 2014**) with olivine CPO developed in naturally deformed mantle rocks with variable pyroxene contents, as those in the studies cited above, corroborates that the

presence of pyroxenes does not significantly modify the olivine CPO evolution in simple shear. By consequence, the parameterization used in the present simulations is probably valid for most of the lithospheric mantle.

Nevertheless, at low temperature and high stresses, dynamic recrystallization weakens the CPO and produces marked grain size reduction (e.g., **Falus et al. 2011**), allowing for higher contribution of diffusive and grain boundary-related processes. This should in turn result in weaker viscous anisotropy in the shallowest lithospheric mantle (**Mameri et al. 2019**), which would reduce the associated strain localization in the crust. However, inference of large volumes with weak olivine CPO within mantle shear zones in the shallow lithospheric mantle is at odds with the strong Pn-wave anisotropy measured in the vicinity of major strike-slip structures, such as the South Armorican shear zone (**Judenherc et al. 2003**), the San Andreas (**Hearn et al. 1996**) and the Alpine faults (**Scherwath et al. 2002**; **Baldock and Stern 2005**, **Vauchez et al. 2012**), which imply strong olivine CPO consistent with past strike-slip kinematics at sub-Moho depths in the shear zone, producing olivine CPO similar to those used in the modelled fossil shear zone.

The present models consider the crust as isotropic and homogeneous. Field observations show that strike-slip shear zones usually display a strong planar fabric at all depths due to development of both shape- and crystal-preferred orientation, which, in the crust, is often associated with a strong compositional banding. This fabric, in particular the orientation of phyllosilicates, should produce viscous anisotropy characterized by lower viscosity parallel to the shear zone foliation than the viscosity normal to it (**Shea and Kronenberg 1993**). We expect that this crustal anisotropy would enhance along-strike shearing in the lithospheric shear zone and, consequently, the strain localization relative to simulations with a mechanically isotropic crust. However, to confirm this prediction crustal viscous anisotropy would have also to be implemented in 3D geodynamical models. The approach presented in this work could be extended for crustal mechanical anisotropy with the advantage of requiring a simplified parameterization of the viscosity tensor thanks to a higher symmetry (transverse isotropy).

Viscous anisotropy of fossil strike-slip mantle shear zones and the associated crustal response

Until now, numerical models that investigated the role of olivine viscous anisotropy on the intraplate deformation using a 3D finite-element method considered only the

mechanical response of the mantle (**Knoll et al. 2009; Tommasi et al. 2009**). These studies suggested that deformation in the mantle greatly depends on the olivine CPO intensity and orientation relatively to the imposed mechanical load. We have further examined the effect of viscous anisotropy in fossil strike-slip mantle shear zones on the intraplate deformation by analysing the associated crustal response. Our models show that the CPO-produced structural reactivation of mantle structures may produce strain localization in both ductile and brittle crust (**Figure 5.3**). The olivine CPO in the fossil mantle shear zone controls not only the strain localization, but also the strain regime in the entire lithosphere (**Figure 5.5**). The strain regime in the crust follows that in the fossil mantle shear zone. Reactivation of the fossil anisotropic mantle shear zone is systematically associated with shearing parallel to the strike of the fossil shear plane, which leads to transpression in both the crust and mantle when the plate is subjected to compression, or transtension when it is subjected to extension (**Figure 5.5c**). In the present models, vorticity is lower in the crust than in the mantle, but as discussed in the previous section, an anisotropic fabric in the lower crust, for instance due to mica CPO, would probably enhance the strike-slip component in the fossil shear zone.

Not surprisingly, the boundary conditions strongly affect CPO-induced structural reactivation in the lithosphere. The maximum strain localization due to a contrast in viscous anisotropy between a fossil strike-slip mantle shear zone and the surrounding mantle only occurs when the boundary conditions allow for full expression of the intrinsic viscous anisotropy of olivine. If the boundary conditions do not allow the development of shearing parallel to the strike of the fossil shear zone, as it is the case for simulations at oblique loading-geometries in which free-slip boundary conditions are imposed to the lateral boundaries of the model, the strain localization associated with CPO-induced viscous anisotropy is significantly reduced. Thus, CPO-induced structural reactivation will depend on the strength of the neighbouring domains. Presence of a stiff cold craton will tend to hinder reactivation, as this situation will be equivalent to the free-slip lateral conditions tested here. In contrast, weaker or similar strength neighbouring domains will allow for full expression of the CPO-induced viscous anisotropy. Regional seismic tomography models shows thermal (and rheological) heterogeneities at scales of tens to hundreds of km in the continental lithosphere (**Fishwick et al. 2005; Pedersen et al. 2013**), which suggest that in nature the lateral boundary conditions probably vary between the free-slip and P-litho end-members.

Feedbacks between the crust and the mantle affect the strain distribution in the lithosphere and modify the strain localization produced by lateral variations of olivine CPO in

the mantle. If the crust is weak, the stress heterogeneity associated with reactivation of the fossil shear mantle zone, which is higher for a strong isotropic mantle rheology, results in effective strain localization in the crust. However, this strain localization decreases fast with increasing distance from the Moho. This result might nevertheless change if viscous anisotropy in the ductile crust is considered. If the crust is strong, the same stress heterogeneity at Moho levels results in weaker strain localization in the lowermost crust, but in better upward transmission of stresses due to efficient crust-mantle mechanical coupling. Consequently, the most effective strain localization in the entire lithosphere column (crust and mantle) is observed in simulations with a relatively strong crust and mantle. Variations through time in the strain repartition within the crust also affect the strain localization in the mantle. For instance, strain localization due to frictional weakening in the upper crust initially enhances the strain localization triggered by olivine viscous anisotropy in the mantle. However, if continued deformation leads to formation of faults elsewhere in the model, strain also delocalizes in the mantle.

Olivine CPO fossilized in mantle shear zones: a possible trigger for linear arrays of intraplate seismicity

Linear arrays of intraplate seismicity are a direct evidence of strain localization within otherwise stable continental interiors. Many of these enigmatic features are associated with long-lived, lithospheric-scale, strike-slip faults developed in ancient rifts or collisional belts (Sykes 1978; Storti et al. 2003), such as the localized seismicity along New Madrid and East Tennessee shear zones in the eastern North America (e.g., Johnson et al. 2014; Powell and Thomas 2016; Anglin 1984) or along the South Armorican shear zone in Brittany (e.g., Mazabraud et al. 2005; Mazzotti et al. 2020). Despite the different geological evolutions, analysis of seismic anisotropy observations around these intraplate seismically active zones (Judenherc et al. 2003; Long et al. 2016; Nyamwandha and Powell 2016) highlights the parallelism between the orientation of the mantle fabric, materialized by the orientation of the fast polarization direction of the fast split shear-waves, and the trend of the linear seismicity arrays (Figure 5.8). In both the New Madrid and South Armorican seismic zones, the present-day principal horizontal stresses are oblique to the orientation of the mantle fabric deduced from the seismic anisotropy measurements. Analysis of these data on the light of the presented anisotropic models leads us to propose that the development of these intraplate linear seismicity arrays was favoured by the oblique orientation of the fossil strike-slip mantle

fabric relative to present-day stress field (**Figure 5.8a**). The predominance of strike-slip focal mechanisms in the New Madrid seismic zone (**Mazzotti & Townend 2010; Johnson et al. 2014**) is consistent with the model predictions for loading at $\sim 45^\circ$ to a pre-existing strike-slip mantle fabric and lithostatic pressure boundary conditions (transpression with predominance of strike-slip deformation, **Figures 5.4b and 5.5c**). This is in agreement with the interpretation of reactivation of the Proterozoic Reelfoot rift as produced by right-lateral strike-slip motion along a northeast-oriented transform fault that formed the Paleozoic continental margin of southeastern Laurentia (**Thomas 1991**).

The mixed character (strike-slip and normal faulting) of the focal mechanisms in the South Armorican seismic zone (**Mazabraud et al 2005a, Mazabraud et al 2005b**), as observed for instance in the $M_w=4.3$ Lorient earthquake located right atop the major fault trend (black star in **Figure 5.8b; Perrot et al. 2005**), requires a different orientation of the present-day stress field or of the pre-existing olivine CPO, leading to a more equilibrated repartition between shear parallel to the fossil mantle fabric and extension normal to it. The latter hypothesis (different orientation of the CPO) is at odds with the past Hercynian deformation history of the South Armorican shear zone, which had a clear dextral strike-slip kinematics and a vertical trend in the crust. Inversion of earthquakes focal mechanisms in the Armorican massif suggests nevertheless departure of the principal present-day compression axis in the vicinity of the South Armorican shear zone from the horizontal direction (**Mazabraud et al. 2005a,b**). This stress orientation, together with other regional-scale variations in the present-day stress field (**Mazabraud et al. 2005b**), may account for the mixed character of the earthquakes focal mechanisms in the region.

Triggering localized seismicity in the upper crust in response to strain localization due to CPO-induced viscous anisotropy in the mantle requires a moderate to strong mechanical coupling between the mantle and crust. A relatively strong lower crust is required to effectively transfer stress between the mantle and upper crust (clutch tectonics of **Tikoff et al. 2002**). This interpretation is consistent with seismic tomography models that point to a relatively strong crust and a weak upper mantle beneath the New Madrid seismic zone (**Zhan et al. 2016**), and with depth-integrated strength models of Western Europe derived from crustal thickness and heat flow data, which predict relatively high crustal strengths in the Armorican Massif (**Cloetingh et al. 2005**). More effective mantle-crust mechanical coupling results in crustal strain focused in a thinner zone. According to this prediction, the narrower linear array of seismicity associated with the New Madrid shear zone compared to the

relatively wider array in the South Armorican shear zone could reflect, at first order, a higher degree of crust-mantle mechanical coupling in the former (**Figure 5.8**).

Strong mechanical coupling results in a time-dependent behaviour and weaker long-term strain localization. Long-lived intraplate strain localization may, however, be favoured by activation of other strain weakening processes, such as shear heating, microstructural evolution, or focusing of fluids. For instance, seismicity in the New Madrid shear zone has been previously interpreted as due to localized thermal weakening of the lithosphere, based on heat flow data (**Liu and Zoback 1997**) and on low seismic velocities imaged in the mantle beneath it between 80 and 200 km-depth (**Chen et al. 2014**). In the South Armorican shear zone, **Mansard et al. (2018)** proposed that the sheared middle crust has undergone significant weakening by grain size reduction and mica interconnection. These processes may add up to CPO-induced viscous anisotropy, allowing effective strain localization in the fossil strike-slip mantle shear zone for a wider range of loading-geometries (see Supplementary material **Figure S5.3**) and longer times.

5.5 Conclusions

We modelled the mechanical response of a continental plate containing a fossil strike-slip mantle shear zone with a ‘wrench-type’ olivine CPO (i.e. produced by horizontal shear on a vertical plane) using 3D elasto-viscoplastic finite-element models with an anisotropic viscous behaviour in the mantle. The anisotropic rheology produced by the CPO is defined by the Hill (1948) orthotropic yield criteria, with six constant material parameters obtained by fitting second-order viscoplastic self-consistent (SO-VPSC) simulations of deformed olivine polycrystals with relative slips system strengths derived from high temperature experiments in olivine single crystals. Strain localization and deformation regimes in the mantle and crust were examined as a function of the orientation of the mantle shear zone, its CPO intensity, the boundary conditions, and of the different isotropic part of the mantle and crust rheologies. The main conclusions are:

- (1) The parameterized approach we developed effectively simulates the full (3D) anisotropic viscosity tensor associated with the orientation of olivine crystals in the mantle at relatively fast computation times (only a factor ~ 2 longer than equivalent simulations with an isotropic mantle rheology).
- (2) Reactivation of a fossil strike-slip mantle shear zone, when controlled by viscous anisotropy, depends non-linearly on its orientation relative to a new stress

field. Strain localization is most effective at 45° , where it is equivalent (or even stronger if the surrounding mantle is not isotropic) to the one obtained by imposing an isotropic weakening by a factor 100 on a domain with the same geometry and lateral boundary conditions. No reactivation is observed for fossil anisotropic strike-slip mantle shear zones oriented at $<30^\circ$ or $>60^\circ$ to the imposed shortening. This is in marked contrast with the effect of an isotropic rheological heterogeneity, which is reactivated at all orientations, although strain localization is also more effective when the load is oblique to the elongation of the tabular heterogeneity.

- (3) The relation between the orientations of the olivine CPO in the fossil strike-slip mantle shear zone and of the imposed shortening affect the pattern of the strain localization in the entire lithosphere. The strain regime in the crust is controlled by the mantle deformation, with the CPO in the fossil strike-slip mantle shear zone favouring parallel-strike structural reactivation.
- (4) Strain localization affects both the mantle and the isotropic crust atop the fossil mantle shear zone, but it is stronger in the mantle. In the reference simulation, the faults and shear zones that develop in the crust right above the mantle shear zone at 45° deform on average ~ 10 times faster than the surrounding crust, whereas the mantle within the fossil shear zone deforms on average ~ 30 times faster than the surrounding mantle. The contrast between the crust and mantle behaviours is smaller for weaker viscous anisotropies (weaker olivine CPO).
- (5) The strain distribution and the magnitude of strain localization depend mainly on the contrast in mechanical behaviour, which is function of the orientation and intensity of the olivine CPO within the mantle shear zone and in the surroundings. But it also strongly depends on the lateral boundary conditions, which may hinder the expression of the olivine viscous anisotropy within the mantle shear zone.
- (6) Interactions between the mantle and the crust moderate strain localization in the entire lithosphere: (a) high strengths in the crust reduce strain localization in the mantle, but allow for more effective transmission of the deformation to the overlying crust; (b) further strain localization due to frictional weakening in the upper crust does enhance strain localization in the mantle; (c) strong mechanical coupling between the crust and mantle initially increases strain localization, but it produces a time-dependent behaviour with subsequent decrease in the strain

localization; (d) weak (strong) mechanical coupling between the crust and mantle leads to more (less) heterogeneous strain localization across the crust shear zone developed atop the fossil mantle shear zone.

- (7) Spatial variations in CPO-induced viscous anisotropy may contribute to trigger linear seismicity belts in intraplate domains.

Acknowledgments

We are grateful to Ricardo Lebensohn and Carlos Tomé for making the VPSC7c code freely available. We thank Alain Vauchez, Sylvie Demouchy, Catherine Thoraval, Sonia Ouadahi, and Marco Lopez-Sanchez for discussions. The authors thank Alain Vauchez, Sandra Piazzolo, and an anonymous reviewer for insightful comments on the manuscript, and the associate editor for its effective handling. This project received funding from the European Union's Horizon 2020 research and innovation program under the Marie Skłodowska-Curie grant agreement No. 642029 (ITN-CREEP) and from the CNRS (France) and CONICET (Argentina) under the *Projet International de Cooperation Scientifique* MicroTex (No. 067785).

5.6 Supplementary material of the article #3

The supplementary material of this article comprise three figures that presents:

- (1) a comparison of strain localization profiles in the middle crust and in the shallow lithospheric mantle at steady-state for two different mesh resolutions (**Figure S5.1**);

- (2) a simulation in which both the fossil mantle shear zone and the surrounding upper mantle are anisotropic and have olivine CPO-orientations leading to the maximum contrast in (viscous anisotropy) mechanical behaviour (**Figure S5.2**);

(3) a simulation in which a factor 100 isotropic weakening is imposed on a fossil mantle shear zone containing a strong olivine CPO (**Figure S5.3**);

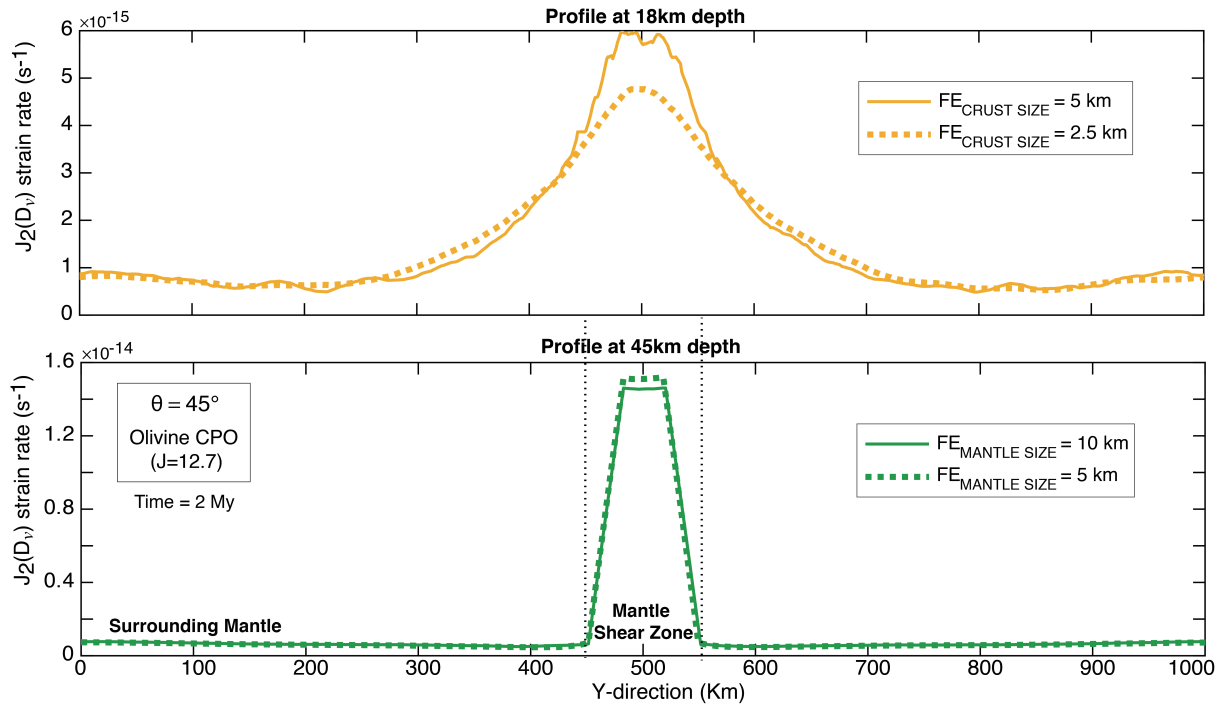


Figure S1: Effect of changing the finite-element (FE) mesh resolution on strain localization (2^{nd} invariant of the strain rate at steady-state) on the middle crust (yellow; profile at 18km depth) and uppermost mantle (green; profile at 45km depth) for the reference model (see Fig. 2 of the article). *Continuous lines*: FE mesh resolution used in the simulations presented in the article. *Dashed lines*: predictions for a two times higher FE mesh resolution.

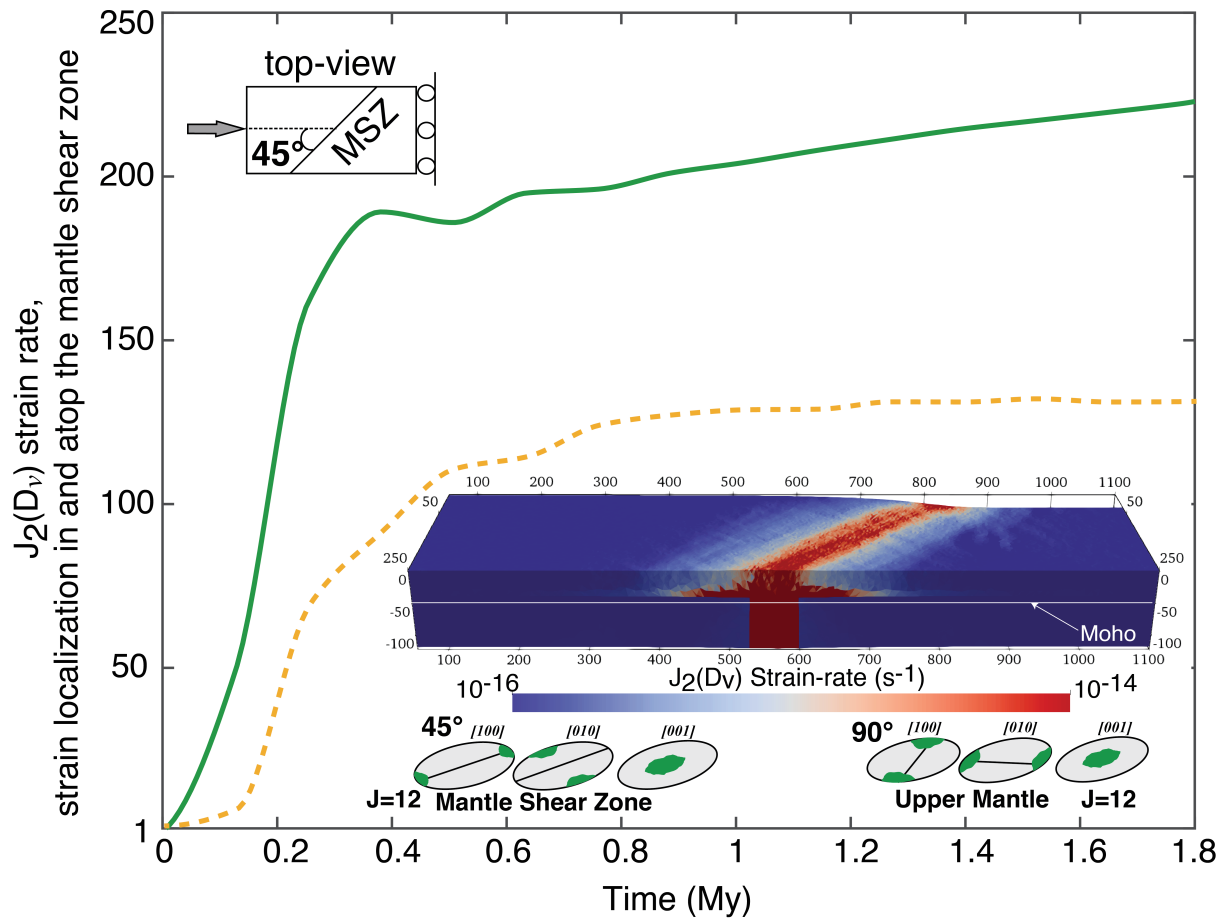


Figure S2: Simulation in which both the fossil mantle shear zone and the surrounding upper mantle are anisotropic and have olivine CPO leading to a maximum contrast in mechanical behaviour. Time evolution of the strain localization in the fossil shear zone, defined by the average of the 2nd invariant of the strain rate $J_2(D_v)$ within the fossil shear zone normalized by the same quantity averaged over the surrounding upper mantle. The fossil mantle shear zone shear plane, and consequently the olivine CPO within it, lies at $\theta = 45^\circ$ to the compression axis, and in the surrounding upper mantle at $\theta = 90^\circ$. Both mantle domains have a strong olivine CPO. P-litho conditions are imposed at the lateral boundaries. The insert displays the strain rate field - $J_2(D_v)$ after 1.8 My of shortening.

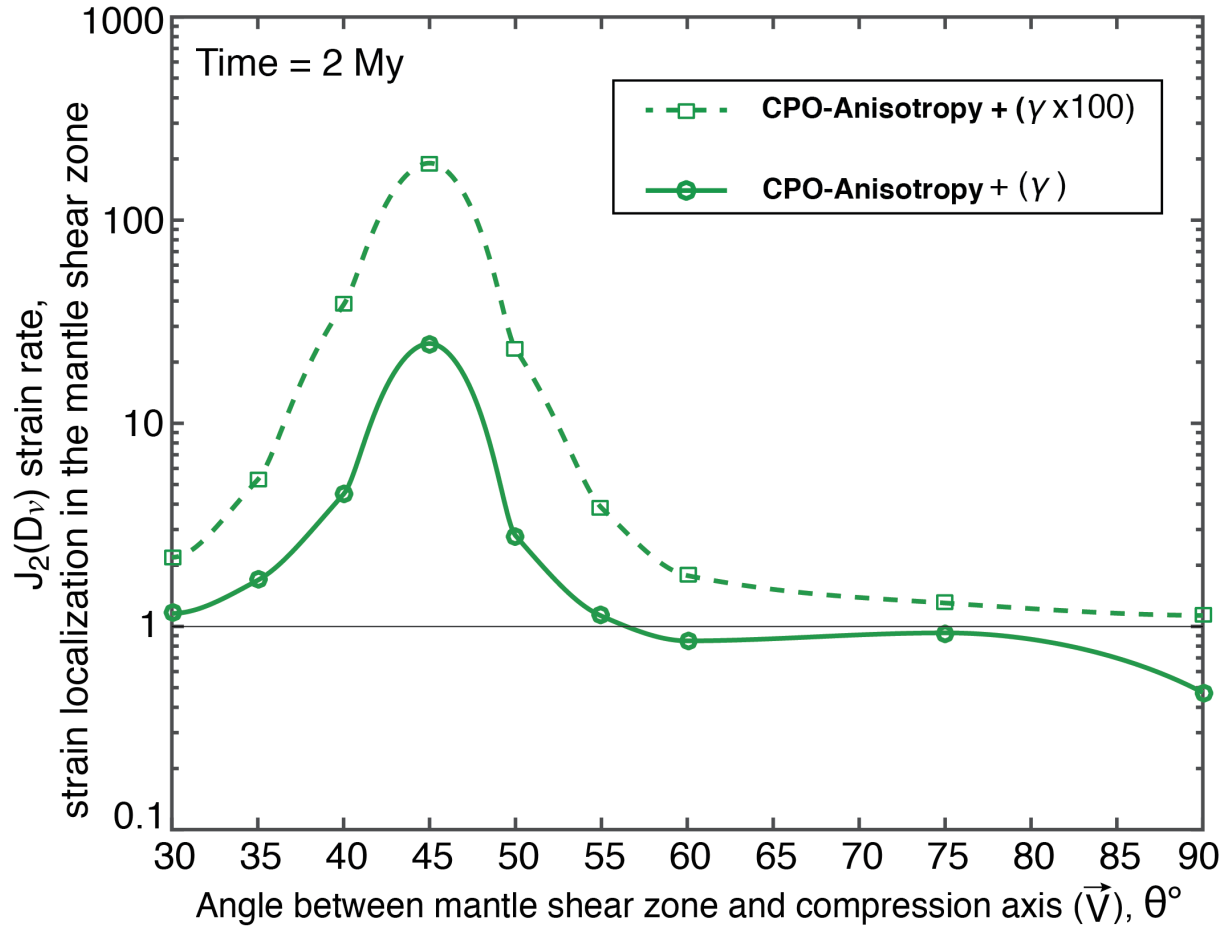


Figure S3: Strain localization at steady-state ($\sim 2\text{My}$) as a function of loading-geometry in a fossil strike-slip mantle shear zone containing a strong olivine CPO (J-index = 12.7) on which is also imposed a factor 100 increase in the fluidity (γ) (dashed line; *squares*) relatively to the strain localization resulting only from the CPO-induced anisotropy (continuous line; *circles*). Strain localization is quantified by the ratio between the average of the second-invariant of the strain rate tensor $J_2(D_v)$ in the fossil mantle shear zone relatively to the surrounding upper mantle.

5.6 Appendix material of the chapter

The material that follows comprise figures not presented in the article. This figures present the:

(1) mechanical response at steady-state of the crust and mantle for the same boundary conditions and olivine CPO in two different mechanical sollicitations: compression and extension.

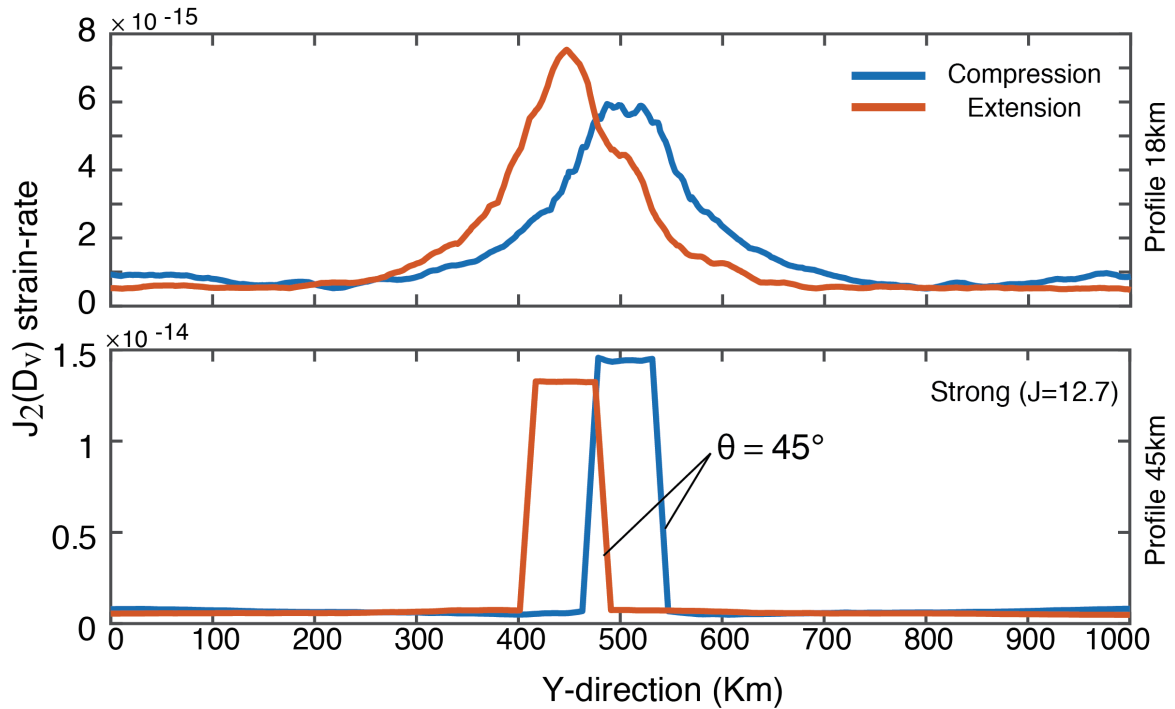


Figure A5.1: Strain rate horizontal profile (2^{nd} -invariant).of the crust (at 18km depth) and mantle (at 45 km depth) at steady-state (≈ 2 My) in both compression and extension deformation for the same model geometry, olivine CPO and thermo-mechanical conditions.

(2) mechanical response for different imposed velocities in a mantle shear zones with the same geometry, CPO intensity and thermomechanical parameters.

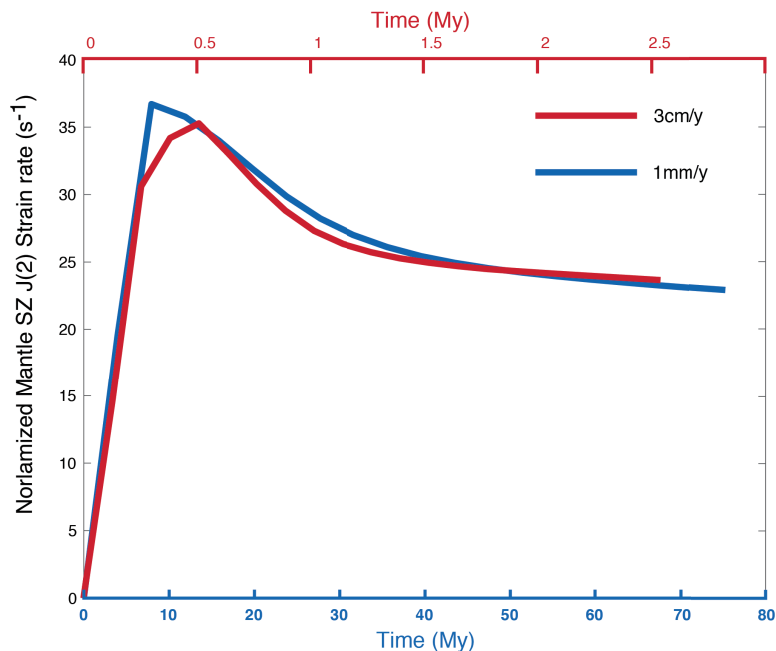


Figure A5.2: Strain localization in the mantle shear zone, calculated as 2^{nd} invariant of the strain rate normalized to the same quantity in the surrounding mantle. Mechanical response for the same CPO and thermo-mechanical conditions, but under different imposed velocities.

(3) Effect of changing the width of the mantle shear zone for models with the same boundary conditions and olivine CPO in the mantle.

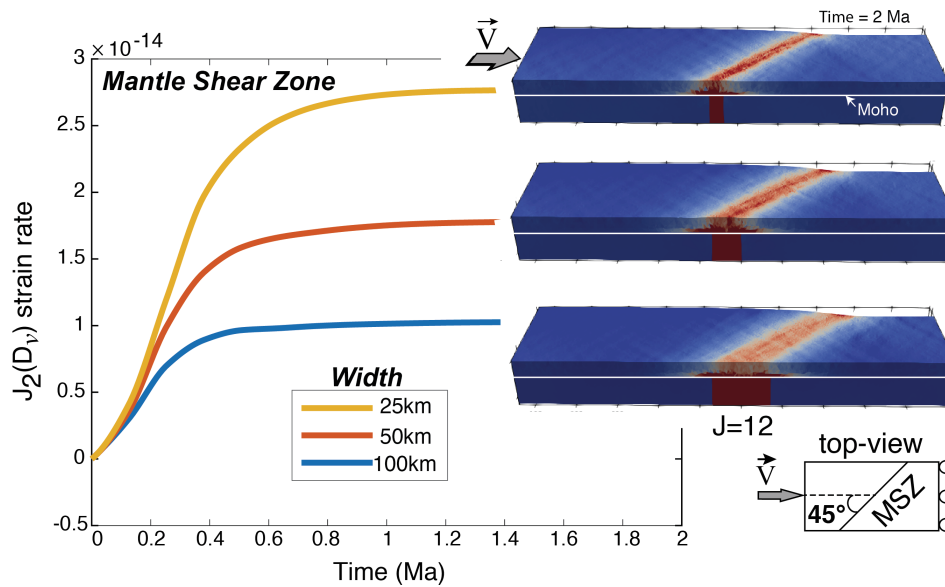


Figure A5.3: Strain rate (2^{nd} invariant) evolution in the mantle shear zone at 45° to the applied loading. At constant imposed velocity, the relation between strain localization and shear zone width is inversely, linearly, proportional - factor of 2 thinner width (or thicker) result in factor 2 faster (or slower) strain rates within the mantle shear zone.

(4) Effect of ascribing a colder Moho temperature in the strain rate within the reactivated mantle shear zone for models under the same boundary conditions.

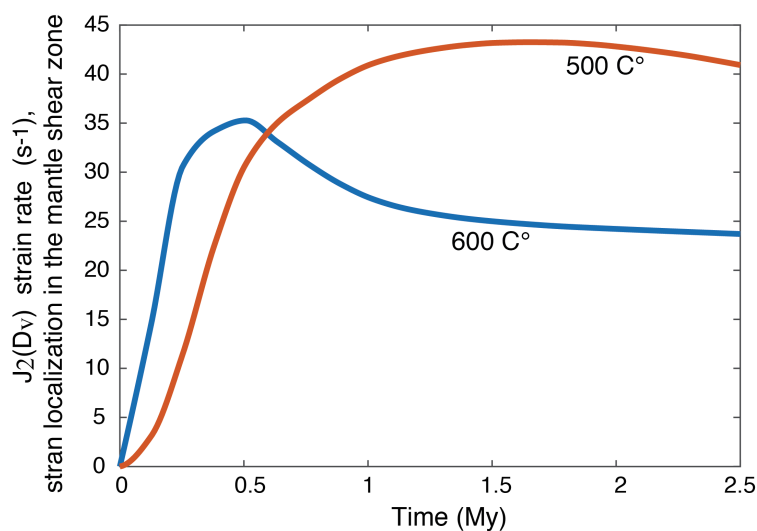
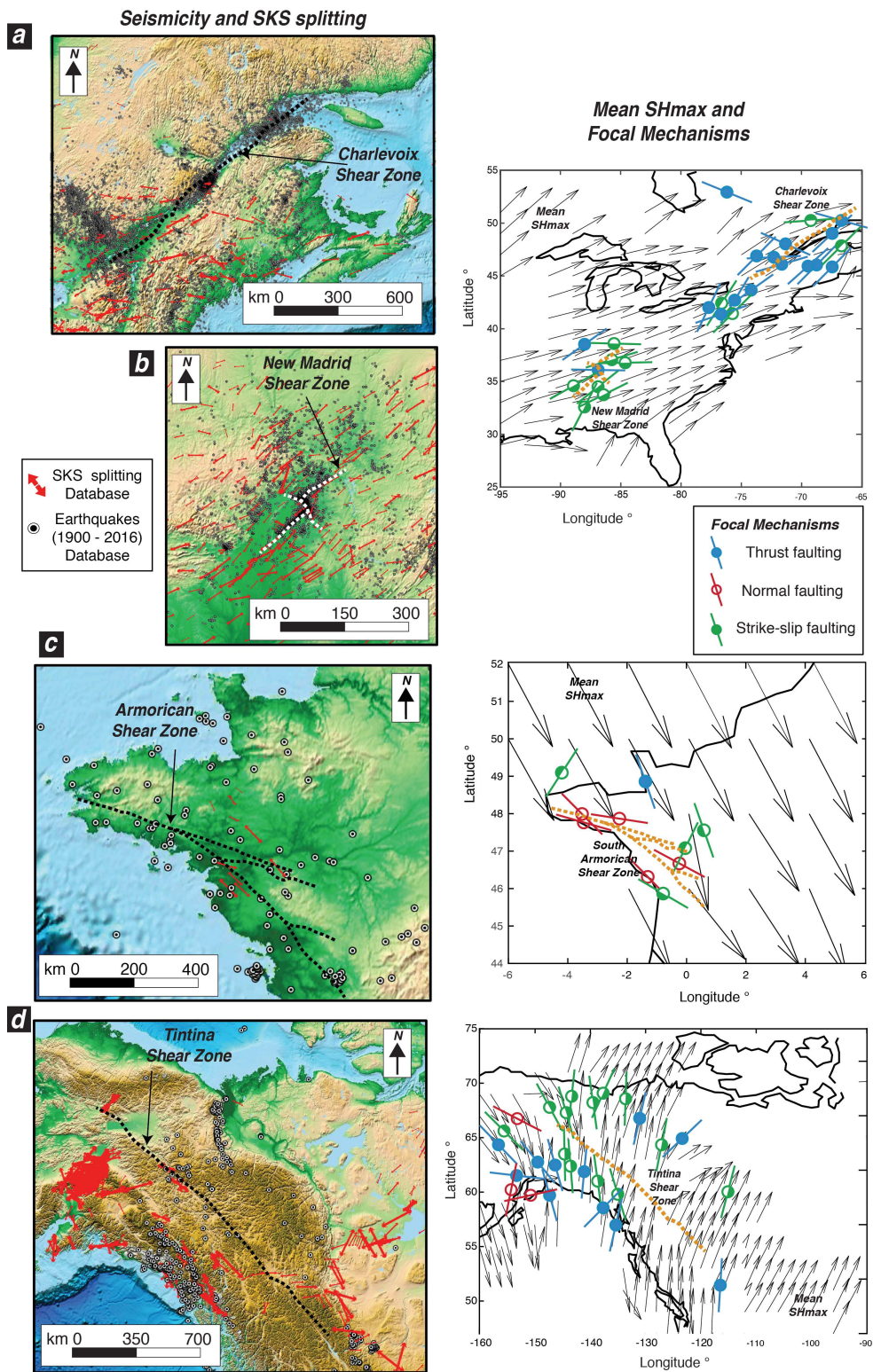


Figure A5.4: Strain rate (2^{nd} invariant) in the mantle shear zone normalized to the same quantity in the surrounding mantle as a function of time for a model with 100°C colder Moho temperature compared to the reference model (with Moho at 600°C). In this case, the mantle rheology is very strong and dominates the deformation of the plate. No strain delocalization is observed.

(5) Other examples of intraplate seismicity and a semi-quantitative estimation of loading geometry.



The relation between the mantle fabric and the present stresses can be estimate by using the Matlab script Stress2Grid to compute the average SHmax orientation from the Word Stress Map database. The script use a given threshold standard deviation (25°) of the mean SHmax to determine the radii of variable search and interpolate the orientation data in a regular grid (here $2^\circ \times 2^\circ$). For further information refer to **Ziegler and Heidbach, 2017**. The approach allow (1) comparing more qualitatively the orientation of maximum horizontal stress (SHmax) in the crust (**Heidbach et al., 2016**; dataservices.gfz-potsdam.de/wsm) to the orientation of the fast-polarization direction of split core shear waves (**Barruol et al., 2009**; splitting.gm.univ-montp2.fr) or to the fast propagation direction of Pn waves, which are both parallel to the preferred orientation of olivine [100] axes in the mantle, and by (2) examining the fault deformation pattern during the earthquakes.

Seismicity in the Charlevoix shear zone does not fully match the present model predictions. The general NE-SW trend of array of linear seismicity is parallel to the ancient rift structure and both structures are oblique to the regional E-W compression direction determined based on focal mechanisms data, but at low angle to the main compressive stresses determined from borehole data, in particular in the southern part of the seismically active zone (Mazzoti and Townend 2010). Moreover, thrust focal mechanisms tend to predominate (Mazzoti and Townend 2010). Therefore, the present-day seismicity in the Charlevoix region cannot be associated to a reactivated strike-slip mantle shear zone. Instead, it could be better explained by the reactivation of a thrust- or normal-type fossil mantle shear zones. However, such structures should produce fast SKS polarization directions normal to their trend. Fast SKS polarization directions oblique to the former continental margin are observed in the southern part of the seismic actively zone (Saint Lawrence Valley), but not in the northern part, where they are at low angle to the fossil margin (Darbyshire et al. 2015).

In the Tintina shear zone, tectonic setting is characterize for a more complicated present structures, i.e., nearby subduction trench and cratons (**Chen et al., 2019**). Despite, based on seismic anisotropy measurements and regional geology arguments, **Audet et al., 2016** suggested that inherited rifted structures deep in the uppermost mantle affect lithospheric strength in northwest Canada and strain localization in the Tintina shear zone, partly controlling the extent of seismic activity in the region.

REFERENCES

- Audet, P., Sole, C., & Schaeffer, A. J. (2016). Control of lithospheric inheritance on neotectonic activity in northwestern Canada?. *Geology*, *44*(10), 807-810.
- Alsina, D. Snieder, R. (1995) Small-scale sublithospheric continental mantle deformation: constraints from SKS splitting observations. *Geophys. J. Intern.*, *123*, 431-448, doi:10.1111/j.1365-246X.1995.tb06864.x
- Anglin, F. M. (1984). Seismicity and faulting in the Charlevoix zone of the St. Lawrence Valley. *Bulletin of the Seismological Society of America*, *74*(2), 595-603.
- Bai, Q., S. J. Mackwell, & D. L. Kohlstedt (1991), High- temperature creep of olivine: 1.Mechanical results for buffered samples, *J. Geophys. Res.*, *96*, 2441-2463, doi:10.1029/90JB01723.
- Baldock, G., & Stern, T. (2005). Width of mantle deformation across a continental transform: Evidence from upper mantle (Pn) seismic anisotropy measurements. *Geology*, *33*(9), 741-744.
- Barruol, G., Wuestefeld, A., & Bokelmann, G. (2009). SKS-Splitting-database. Géosciences Montpellier, Université de Montpellier. https://doi.org/10.18715/sks_splitting_database
- Boioli, F., Tommasi, A., Cordier, P., Demouchy, S., & Mussi, A. (2015). Low steady-state stresses in the cold lithospheric mantle inferred from dislocation dynamics models of dislocation creep in olivine. *Earth and Planetary Science Letters*, *432*, 232-242.
- Boneh, Y., Morales, L. F., Kaminski, E., & Skemer, P. (2015). Modeling olivine CPO evolution with complex deformation histories: Implications for the interpretation of seismic anisotropy in the mantle. *Geochemistry, Geophysics, Geosystems*, *16*(10), 3436-3455.
- Brune, S., Popov, A. A., & Sobolev, S. V. (2012). Modeling suggests that oblique extension facilitates rifting and continental break-up. *Journal of Geophysical Research: Solid Earth*, *117*(B8).
- Bystricky, M., Kunze, K., Burlini, L. & Burg, J.-P. (2000) High shear strain of olivine aggregates: Rheological and seismic consequences. *Science*, *290*, 1564-1567.
- Chen, C., Zhao, D., & Wu, S. (2014). Crust and upper mantle structure of the New Madrid Seismic Zone: Insight into intraplate earthquakes. *Physics of the Earth and Planetary Interiors*, *230*, 1-14.
- Chen, Y., Gu, Y. J., Currie, C. A., Johnston, S. T., Hung, S. H., Schaeffer, A. J., & Audet, P. (2019). Seismic evidence for a mantle suture and implications for the origin of the Canadian Cordillera. *Nature communications*, *10*(1), 1-10.
- Chéry, J., Zoback, M. D., & Hassani, R. (2001). An integrated mechanical model of the San

- Andreas fault in central and northern California. *Journal of Geophysical Research*, 106(B10), 22051–22066.
- Chopra, P.N., & Paterson, M.S., (1981). The experimental deformation of dunite. *Tectonophysics* 78, 453–473.
- Chopra, P.N., & Paterson, M.S., (1984). The role of water in the deformation of dunite. *J. Geophys. Res.* 89, 7861–7876.
- Cloetingh, S. A. P. L., Ziegler, P. A., Beekman, F., Andriessen, P. A. M., Matenco, L., Bada, G., & Sokoutis, D. (2005). Lithospheric memory, state of stress and rheology: neotectonic controls on Europe's intraplate continental topography. *Quaternary Science Reviews*, 24(3-4), 241-304.
- Cundall, P., & Board, M. (1988). A microcomputer program for modeling large-strain plasticity problems. In Swoboda, C. (Ed.), *Numerical methods in geomechanics* (pp. 2102–2108). Rotterdam, the Netherlands: A. A.
- Demouchy, S., & Bolfan-Casanova, N. (2016). Distribution and transport of hydrogen in the lithospheric mantle: A review. *Lithos*, 240, 402-425.
- Demouchy, S., Mussi, A., Barou, F., Tommasi, A., & Cordier, P. (2014). Viscoplasticity of polycrystalline olivine experimentally deformed at high pressure and 900 C. *Tectonophysics*, 623, 123-135.
- Durham, W. B., & Goetze, G (1977). Plastic flow of oriented single crystals of olivine. 1. Mechanical data. *J. Geophys. Res.* 82, 5737–5753.
- Dunbar, J. A., & Sawyer, D. S. (1989). How preexisting weaknesses control the style of continental breakup. *Journal of Geophysical Research: Solid Earth*, 94(B6), 7278-7292.
- Falus, G, Tommasi A. & Soustelle, V. (2011) Effect of dynamic recrystallization on olivine crystal preferred orientations in mantle xenoliths deformed under varied stress conditions. *J. Struct. Geol.*, 33 : 1528-1540, doi : 10.1016/j.jsg.2011.09.010
- Frets, E., Tommasi, A., Garrido, C.J., Vauchez, A., Mainprice, D., Targuisti, K., & Amri, I. (2014). The Beni Bousera peridotite (Morocco): An oblique-slip low-angle shear zone thinning the subcontinental mantle lithosphere. *J. Petrol.* 55, 283-313, doi: 10.1093/petrology/egt067
- Fishwick, S., Kennett, B., Reading, A., 2005. Contrasts in lithospheric structure within the Australian craton—insights from surface wave tomography. *Earth Planet. Sci. Lett.* 231, 163-176.
- Gouriet, K., Cordier, P., Garel, F., Thoraval, C., Demouchy, S., Tommasi, A., & Carrez, P. (2019). Dislocation dynamics modelling of the power-law breakdown in olivine single crystals: Toward a unified creep law for the upper mantle. *Earth and Planetary Science Letters*, 506, 282-291.
- Grünthal, G., Wahlström, R., Stromeyer, D. (2013), The SHARE European Earthquake Catalogue

- (SHEEC) for the time period 1900-2006 and its comparison to EMEC. *Journal of Seismology*, 17, 4, 1339-1344, doi: 10.1007/s10950-013-9379-y.
- Hansen, L. N., Zimmerman, M. E., & Kohlstedt, D. L. (2012). Laboratory measurements of the viscous anisotropy of olivine aggregates. *Nature*, 492(7429), 415.
- Hansen, L.N., Zhao, Y.H., Zimmerman, M.E., & Kohlstedt, D.L., (2014). Protracted fabric evolution in olivine: implications for the relationship among strain, crystallographic fabric, and seismic anisotropy. *Earth Planet. Sci. Lett.* 387, 157–168. <https://doi.org/10.1016/j.epsl.2013.11.009>.
- Hassani, R. (1994). Modélisation numérique de la déformation des systèmes géologiques, Ph.D thesis, Université de Montpellier II, Montpellier, p. 130
- Hearn, T. M. (1996). Anisotropic Pn tomography in the western United States. *Journal of Geophysical Research: Solid Earth*, 101(B4), 8403-84
- Heidbach, O., Tingay, M., Barth, A., Reinecker, J., Kurfeß, D., & Müller, B. (2010). Global crustal stress pattern based on the World Stress Map database release 2008. *Tectonophysics*, 482(1-4), 3-15.
- Heidbach, Oliver; Rajabi, Mojtaba; Reiter, Karsten; Ziegler, Moritz; WSM Team (2016): World Stress Map Database Release 2016. V. 1.1. GFZ Data Services. <http://doi.org/10.5880/WSM.2016.001>
- Hidas, K., Tommasi, A., Garrido, C.J., Padron-Navarta, J.A., Mainprice, D., Vauchez, A. Marchesi, C., & Barou. F. (2016) Fluid-assisted strain localization in the shallow lithospheric mantle. *Lithos*, 636-650. doi:10.1016/j.lithos.2016.07.038
- Hill, R. (1948). A theory of the yielding and plastic flow of anisotropic metals. *Proc. Roy. Soc. London 193A*, 281.
- Hirth, G., & Kohlstedt, D. L. (2003). Inside the subduction factory. Rheology of the Upper Mantle and the Mantle Wedge: A View From the Experimentalists, *Geophys. Monogr. Ser.*, 138, 83-105.
- Johnson, G. A., Horton, S. P., Withers, M., & Cox, R. (2014). Earthquake focal mechanisms in the New Madrid seismic zone. *Seismological Research Letters*, 85(2), 257-267.
- Judenherc, S. (2000). Etude et caractérisation des structures hercyniennes à partir de données sismologiques: le cas du Massif Armoricain (PhD Thesis, Université Louis Pasteur-Strasbourg I).
- Judenherc, S., Granet, M., Brun, J. P., & Poupinet, G. (2003). The Hercynian collision in the Armorican Massif: evidence of different lithospheric domains inferred from seismic tomography and anisotropy. *Bulletin de la Société géologique de France*, 174(1), 45-57.
- Knoll, M., Tommasi, A., Logé, R. E., & Signorelli, J. W. (2009). A multiscale approach to model

- the anisotropic deformation of lithospheric plates. *Geochemistry, Geophysics, Geosystems*, 10(8).
- Lebensohn, R.A., Ponte Castañeda, P., Brenner, R., & Castelnau, O. (2011). Full-field vs. homogenization methods to predict microstructure-property relations for polycrystalline materials. In: *Computational Methods for Microstructure-Property Relationships*. Springer, New York, pp. 393–441.
- Liu, L., & Zoback, M. D. (1997). Lithospheric strength and intraplate seismicity in the New Madrid seismic zone. *Tectonics*, 16(4), 585-595.
- Long, M. D., Jackson, K. G., & McNamara, J. F. (2016). SKS splitting beneath Transportable Array stations in eastern North America and the signature of past lithospheric deformation. *Geochemistry, Geophysics, Geosystems*, 17(1), 2-15.
- Mainprice, D., Bachmann, F., Hielcher, R., & Schaeben, H., (2014). Descriptive tools for the analysis of texture projects with large datasets using MTEX-Strength, symmetry and components. In: Faulkner, D.R., Mariani, E., Mecklenburgh, J. (Eds.), *Rock Deformation from Field, Experiments and Theory: A Volume in Honour of Ernie Rutter*, Spec. Publ. Geol. Soc., London, U. K., pp. 409 [http://dx.doi.org/10.1144/ SP409.8](http://dx.doi.org/10.1144/SP409.8).
- Mameri, L., Tommasi, A., Signorelli, J., & Hansen, L. N. (2019). Predicting viscoplastic anisotropy in the upper mantle: a comparison between experiments and polycrystal plasticity models. *Physics of the Earth and Planetary Interiors*, 286, 69-80.
- Mansard, N., Raimbourg, H., Augier, R., Précigout, J., & Le Breton, N. (2018). Large-scale strain localization induced by phase nucleation in mid-crustal granitoids of the south Armorican massif. *Tectonophysics*, 745, 46-65.
- Mazabraud, Y., Béthoux, N., & Deroussi, S. (2005a). Characterisation of the seismological pattern in a slowly deforming intraplate region: Central and western France. *Tectonophysics*, 409(1-4), 175-192.
- Mazabraud, Y., Béthoux, N., Guilbert, J., & Bellier, O. (2005b). Evidence for short-scale stress field variations within intraplate central-western France. *Geophysical Journal International*, 160(1), 161-178.
- Mazzotti, S., & Townend, J. (2010). State of stress in central and eastern North American seismic zones. *Lithosphere*, 2(2), 76-83.
- Mazzotti, S., Jomard, H., Masson, F. (2020) Processes and deformation rates generating seismicity in metropolitan France and conterminous Western Europe. *BSGF Earth Sciences Bulletin*, DOI:10.1051/bsgf/2020019
- Mooney, W. D. (2015), Crust and lithospheric structure—Global crustal structure, *Treatise of Geophysics*, 2nd ed., vol. 1, pp. 339–390, Elsevier, Amsterdam.

- Newman, J., Lamb, W.M., Drury, M.R., & Vissers, R.L.M. (1999). Deformation processes in a peridotite shear zone: reaction-softening by an H₂O-deficient, continuous net transfer reaction. *Tectonophysics* 303, 193–222.
- Nicolas, A., & Christensen, N. I. (1987). Formation of anisotropy in upper mantle peridotites: A review. *Composition, structure and dynamics of the lithosphere - asthenosphere system*, 16, 111-123.
- Nyamwandha, C. A., & Powell, C. A. (2016). Seismic anisotropy beneath the Mississippi Embayment and the New Madrid Seismic Zone: A study of shear wave splitting. *Journal of Geophysical Research: Solid Earth*, 121(11), 8239-8253.
- Paterson, M.S., & Luan, F.C., (1990). Quartzite rheology under geological conditions. In: Knipe, R.J., Rutter, E.H. (Eds.), *Deformation mechanisms, rheology and tectonics. Geological Society Special Publication*, pp. 299–307.
- Pedersen, H., Debayle, E., Maupin, V., Group, P.L.W., 2013. Strong lateral variations of lithospheric mantle beneath cratons—example from the Baltic Shield. *Earth Planet. Sci. Lett.* 383, 164–172.
- Perrot, J., Arroucau, P., Guilbert, J., Déverchère, J., Mazabraud, Y., Rolet, J., ... & Matias, L. (2005). Analysis of the Mw 4.3 Lorient earthquake sequence: a multidisciplinary approach to the geodynamics of the Armorican Massif, westernmost France. *Geophysical Journal International*, 162(3), 935-950.
- Ponte Castañeda, P., (2002). Second-order homogenization estimates for nonlinear composites incorporating field fluctuations: I—theory. *J. Mech. Phys. Solids* 50, 737–757. [https://doi.org/10.1016/S0022-5096\(01\)00099-0](https://doi.org/10.1016/S0022-5096(01)00099-0).
- Powell, C. A., & Thomas, W. A. (2016). Grenville basement structure associated with the Eastern Tennessee seismic zone, southeastern USA. *Geology*, 44(1), 39-42.
- Ranalli, G., (1997). Rheology of the lithosphere in space and time. In: Burg, J.P., Ford, M. (Eds.), *Orogeny Through Time*, 121. *Geological Society of London Spec. Publ.*, pp. 19–37
- Scherwath, M., Melhuish, A., Stern, T., & Molnar, P. (2002). Pn anisotropy and distributed upper mantle deformation associated with a continental transform fault. *Geophysical research letters*, 29(8), 16-1.
- Shea Jr, W. T., & Kronenberg, A. K. (1993). Strength and anisotropy of foliated rocks with varied mica contents. *Journal of Structural Geology*, 15(9-10), 1097-1121.
- Signorelli, J., Hassani, R., Tommasi, A., Mameri, L (submitted). An effective parameterization of texture-induced viscous anisotropy in orthotropic materials with application for modeling geodynamical flows. (*Modelling and Simulation in Mat. Sc. and Eng*).
- Steinberger, B., & Becker, T. W. (2018). A comparison of lithospheric thickness

- models. *Tectonophysics*, 746, 325-338.
- Storti, F., Holdsworth, R.E., & Salvini, F. (2003). Intraplate strike-slip deformation belts. *Geological Society of London, Special Publication*, 210, pp. 1–14.
- Stucchi, M., Rovida, A., Capera, A. G., Alexandre, P., Camelbeeck, T., Demircioglu, M. B., ... & Sesetyan, K. (2013). The SHARE European earthquake catalogue (SHEEC) 1000–1899. *Journal of Seismology*, 17(2), 523-544. doi: 10.1007/s10950-012-9335-2.
- Sykes, L. R. (1978). Intraplate seismicity, reactivation of preexisting zones of weakness, alkaline magmatism, and other tectonism postdating continental fragmentation, *Rev. Geophys.*, 16(4), 621–688
- Thieme, M., Demouchy, S., Mainprice, D., Barou, F., & Cordier, P. (2018). Stress evolution and associated microstructure during transient creep of olivine at 1000–1200° C. *Physics of the Earth and Planetary Interiors*, 278, 34-46.
- Thomas, W. A. (1991). The Appalachian-Ouachita rifted margin of southeastern North America. *Geological Society of America Bulletin*, 103(3), 415-431.
- Tikoff, B., Teyssier, C., & Waters, C. (2002). Clutch tectonics and the partial attachment of lithospheric layers. *EGU Stephan Mueller Spec Publ Ser*, 1, 57-73.
- Tommasi, A. & Vauchez, A. (1997) Complex tectono-metamorphic patterns in continental collision zones: The role of intraplate rheological heterogeneities. *Tectonophysics*, 279: 327-350.
- Tommasi, A., & Vauchez, A. (2001). Continental rifting parallel to ancient collisional belts: an effect of the mechanical anisotropy of the lithospheric mantle. *Earth and Planetary Science Letters*, 185(1-2), 199-210.
- Tommasi, A., & Vauchez, A. (2015). Heterogeneity and anisotropy in the lithospheric mantle. *Tectonophysics*, 661, 11-37.
- Tommasi, A., Knoll, M., Vauchez, A., Signorelli, J. W., Thoraval, C., & Logé, R. (2009). Structural reactivation in plate tectonics controlled by olivine crystal anisotropy. *Nature Geoscience*, 2(6), 423-427.
- Tommasi, A; Vauchez, A. & Daudré, B. (1995) Initiation and propagation of shear zones in a heterogeneous continental lithosphere. *Journal of Geophysical Research*, 100: 22,083-22,101.
- Tommasi, A., Mainprice, D., Canova, G. & Chastel, Y (2000). Viscoplastic self-consistent and equilibrium-based modelling of olivine lattice preferred orientations. Implications for upper mantle seismic anisotropy. *J. Geophys. Res.* 105, 7893–7908
- Tommasi, A., Tikoff, B., & Vauchez, A. (1999). Upper mantle tectonics: three-dimensional deformation, olivine crystallographic fabrics and seismic properties. *Earth and Planetary Science Letters*, 168, 173-186.

- Townend, J., & Zoback, M. D. (2000). How faulting keeps the crust strong. *Geology*, 28(5), 399-402.
- Tuttle, M. P., Schweig, E. S., Sims, J. D., Lafferty, R. H., Wolf, L. W., & Haynes, M. L. (2002). The earthquake potential of the New Madrid seismic zone. *Bulletin of the Seismological Society of America*, 92, 2080-2089.
- Vauchez, A. & Nicolas, A., 1991. Mountain building: strike-parallel motion and mantle anisotropy. *Tectonophysics*, 185: 183-201.
- Vauchez, A., Barruol, G., & Tommasi, A. (1997). Why do continents break - up parallel to ancient orogenic belts?. *Terra Nova*, 9(2), 62-66.
- Vauchez, A., Tommasi, A., & Barruol, G. (1998). Rheological heterogeneity, mechanical anisotropy and deformation of the continental lithosphere. *Tectonophysics*, 296, 61-86.
- Vauchez, A., Tommasi, A., & Mainprice, D. (2012). Faults (shear zones) in the Earth's mantle. *Tectonophysics*, 558, 1-27.
- Wilks, K. R., & Carter, N. L. (1990). Rheology of some continental lower crustal rocks. *Tectonophysics*, 182(1-2), 57-77.
- Zhan, Y., Hou, G., Kusky, T., & Gregg, P. M. (2016). Stress development in heterogeneous lithosphere: Insights into earthquake processes in the New Madrid Seismic Zone. *Tectonophysics*, 671, 56-62.
- Ziegler, Moritz; Heidbach, Oliver (2017): Matlab script Stress2Grid (Version 1.1). GFZ Data Services. <http://doi.org/10.5880/wsm.2019.002>

CHAPTER VI

CONTRASTING THE EFFECTS OF VISCIOUS ANISOTROPY IN LITHOSPHERIC STRIKE-SLIP & EXTENSIONAL SHEAR ZONES

*All discussion of the ultimate nature of
things must necessarily be barren unless we
have some extraneous standards against
which to compare them.*

Sir James Jeans

6 Comparing CPO-induced viscous anisotropy in fossil lithospheric shear zones with different past kinematics

The research presented in this chapter is in preparation to be submitted in a scientific journal.

6.1 Introduction

Analysis of the deformation of peridotites massifs together with geophysical data suggests the presence of both strike-slip and extensional (or compressional) shear zones in the lithospheric mantle (review in **Vaucher et al., 2012**). Large-scale strike-slip shear zones crosscutting the entire lithospheric plates are inferred from the polarization direction of fast teleseismic S-waves parallel (**Silver et al., 1999; Sénéchal, et al., 1996**), as well as from Moho and LAB offsets beneath major strike-slip shear zones (e.g., **Wittlinger et al. 2004; Ford et al. 2014; Titus et al., 2007**). The measured seismic anisotropy in this shear zones often indicate the presence of a coherent large-scale crystal preferred orientations (CPO) of olivine with maximum concentration of [100] and [010]-axes parallel and normal to the main shear zone foliation, respectively.

Lithospheric extensional (or compressional) mantle shear zones however are not easily detected using seismic anisotropy measurements. The presence of these structures have been inferred mainly based on the analysis of seismic reflectors (**McBride et al., 1995**), field mapped mantle peridotites (**Kaczmarek and Tommasi, 2011; Frets et al. 2013**), such as in active and fossil continental margins and spreading ridges (**Boillot et al. 1987; Sauter et al. 2013**). Lithospheric extension might occur accommodated by a low angle asymmetrical stretching, where the the mantle fabric form as a result of sub-horizontal shear mode deformation (**Wernicke, 1985**). In this model, the maximum concentration of [100] olivine axes is expected to be parallel to the down-dip stretching lineation (**L_x**), while the maximum concentration of [010] olivine axes lies normal to the shear plane (**Figure 6.1**). Similar fabrics might be formed in compressional (thrust) shear zones, though the latter might show some dispersion of the [100] axes within the shear plane due to a transpressional deformation (**Tommasi et al. 1999**). Henceforth, I will refer only to the extensional mantle shear zones.

In this chapter, I run viscoplastic plasticity (SO-VPSC) and 3D finite-element (ADELI-anis) simulations to characterize CPO-produced structural reactivation and

deformation regime in fossil strike-slip and an extensional mantle shear zone. The mechanical responses of these shear zones were compared for using the same olivine CPO (intensity and symmetry), mantle and crust rheologies, and thermomechanical conditions. The orientation of the strike and of the dip of the fossil mantle shear plane relative to the mechanical solicitation was varied from 30° to 90° , as also the intensity of the CPO within the mantle shear zone and imposed boundary conditions. The aim is to establish the first-order features of CPO-induced strain localization in fossil extensional and strike-slip mantle shear zones.

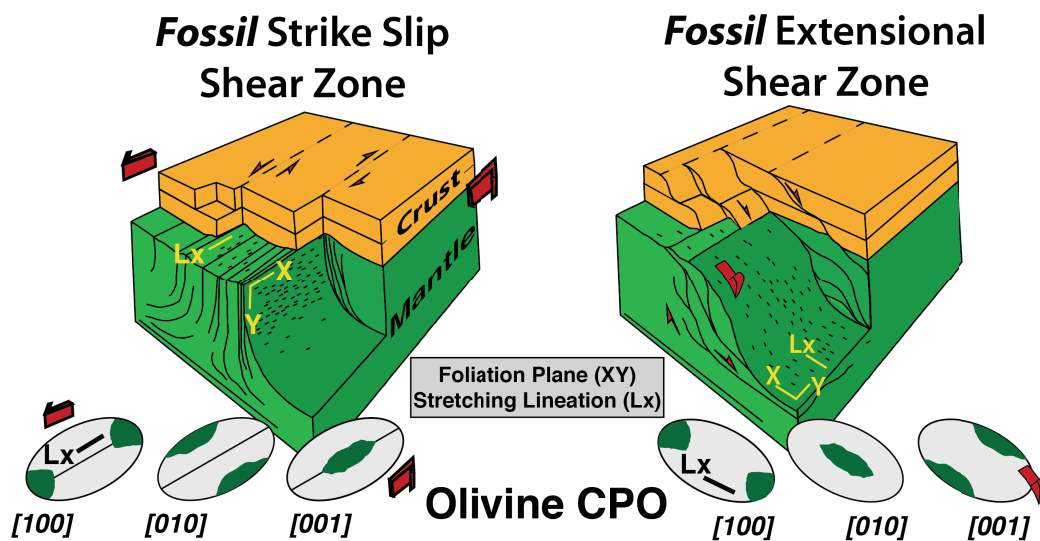


Figure 6.1: Conceptual model of the orientation of the olivine CPO associated with a fossil strike-slip and extensional mantle shear zone. The fossil shear plane XY and stretching lineation Lx are indicated.

6.2 Geodynamical model setup

The code Adeli3D was modified to account for CPO-produced viscous anisotropy in the mantle, produced by olivine intrinsic anisotropy. The upper crust displays an isotropic frictional behaviour, described by a Drucker-Prager rheology. A thermally activated non-Newtonian viscous law describe the mechanical behavior of the lower crust and the upper, which is isotropic in the crust and anisotropic in the mantle. Viscous anisotropy in the mantle is characterized using six Hill coefficients (F , G , H , L , M , N) obtained by fitting SO-VPSC simulations (**Figure 5.1**). Instantaneous viscous yielding was estimated for a random and orthorhombic CPOs. Intracrystalline glide occurs mainly on the $(010)[100]$ and $(001)[100]$ ‘easy’ slip systems and on the $(010)[001]$ ‘hard’ slip system, coherent with most of the lithospheric mantle deforming at high temperature and moderate pressure conditions.

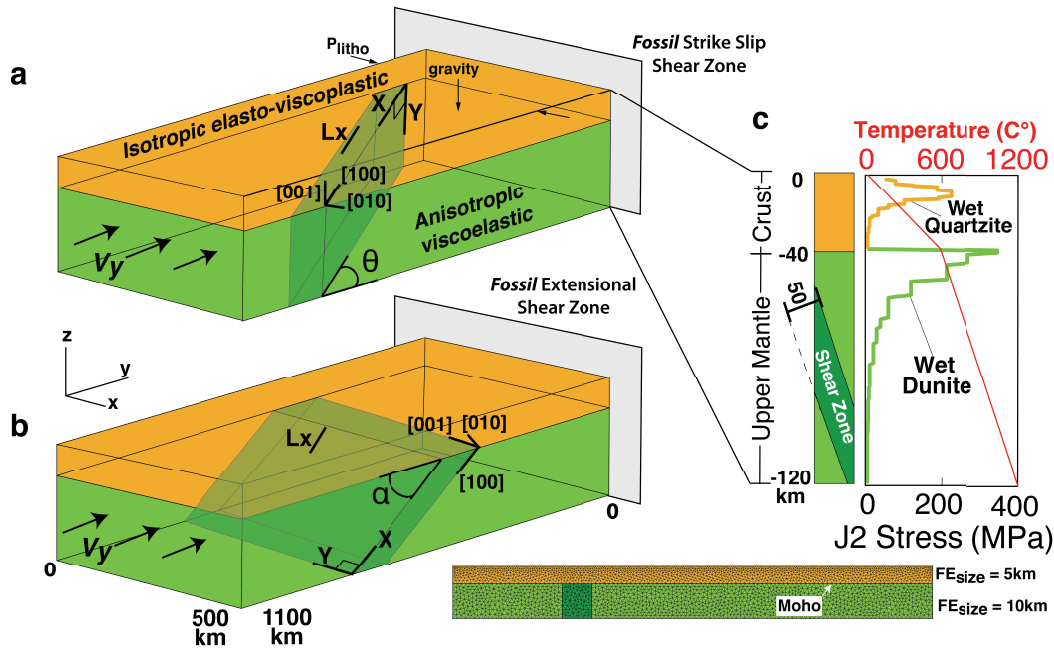


Figure 6.2: Model geometry for simulating a fossil strike-slip (a) or extensional (b) shear zone in the mantle lithosphere. The orientation of the olivine CPO, represented as the orientation of the maximum concentration of the [100], [010], and [001] axes in both shear zones, also the stretching lineation (L_x), the fossil shear plane (XY), as well the rheology and imposed boundary conditions are indicated. The angles α and θ characterize the dip angle and the strike of the fossil mantle shear plane relatively to the imposed shortening or extension. (c) Crust (orange) and isotropic mantle (light green) strength profiles for the chosen compositions and imposed thermal structure.

The boundary conditions and material parameters follows the setup in the chapter 5 (Table 5.2). The anisotropic viscosity (Hill parameters) in the mantle is maintained constant throughout the simulations (i.e. no CPO evolution during simulation). Here, the mantle encloses a 50 km-wide fossil extensional or strike-slip shear zone with either strong or weak olivine CPO; elsewhere (the surrounding mantle) it has a random CPO. In the different simulations, either the dipping angle (α) or the orientation of the strike (θ) of the fossil mantle shear plane is varied from 30° to 90° relative to the imposed compression or extension velocity (Figure 6.2a,b). If α is varied θ is set to 90° (shear plane strike is kept normal to the imposed sollicitation); contrarily, if θ is varied α is set to 90° (shear plane dip is kept vertical). The joint effect of varying simultaneously the strike and the dip of the mantle shear plane on the lithospheric deformation was inferred by performing SO-VPSC simulations.

6.3 Results

Structural reactivation of both fossil extensional or strike-slip mantle shear zone only occurs for imposed shortening between $\approx 30^\circ$ and $\approx 60^\circ$ to the shear plane. In most

cases, for similar angles between the imposed shortening and the trend of the fossil shear zone, strain localization in a fossil extensional mantle shear is higher or similar to the one observed in a strike-slip fossil mantle shear zone (**Figure 6.3**); quantified by the ratio between the average of the second invariant of the strain rate tensor in the fossil shear zone and in the surrounding mantle. The exception occurs when the extensional mantle shear zone dips (α) is close to 45° and the shear zone strike is perpendicular to the imposed shortening ($\theta = 90$). At this loading- the ratio between the average strain rate within and outside the shear zone is a factor of 5 times smaller than in a vertical ($\alpha = 90^\circ$) strike-slip mantle shear zone that is oriented at 45° to the imposed shortening ($\theta = 45^\circ$). At this loading-geometry, strain localization in the crust is less efficient in the extensional mantle shear zone than in the strike-slip shear zone (**Figure 6.3**). More heterogeneously distributed deformation occurs atop the latter than atop the former. The crustal shear zone formed in response to the reactivation of the fossil extensional shear zone develops in the prolongation of the mantle shear plane, whereas in the case of reactivation of the strike-slip mantle shear zone strain localization in the crust occurs right above the fossil shear plane.

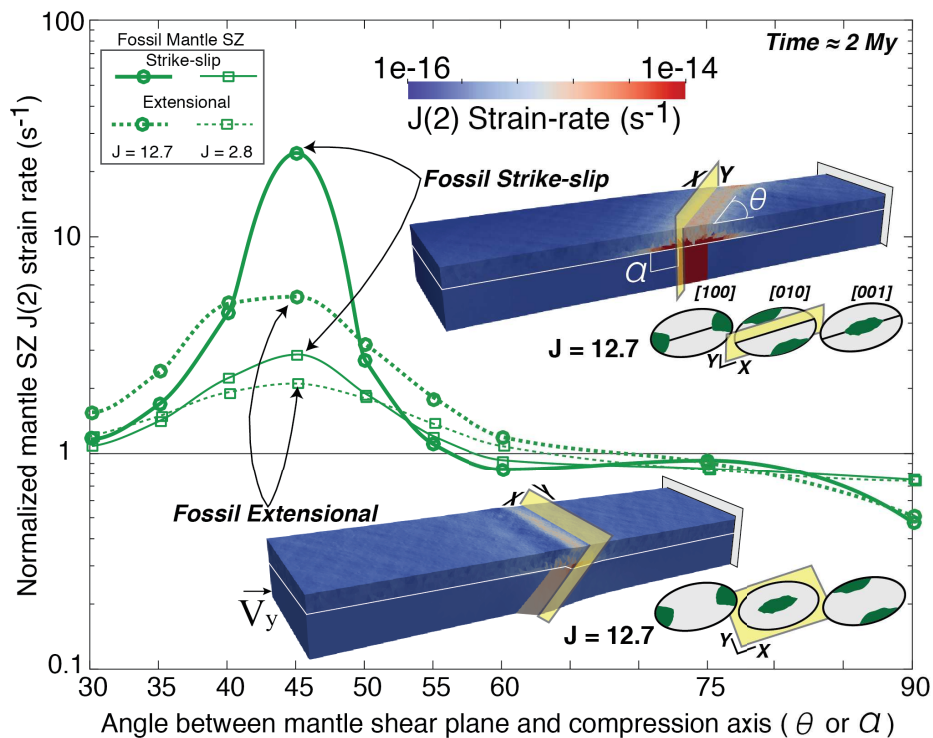
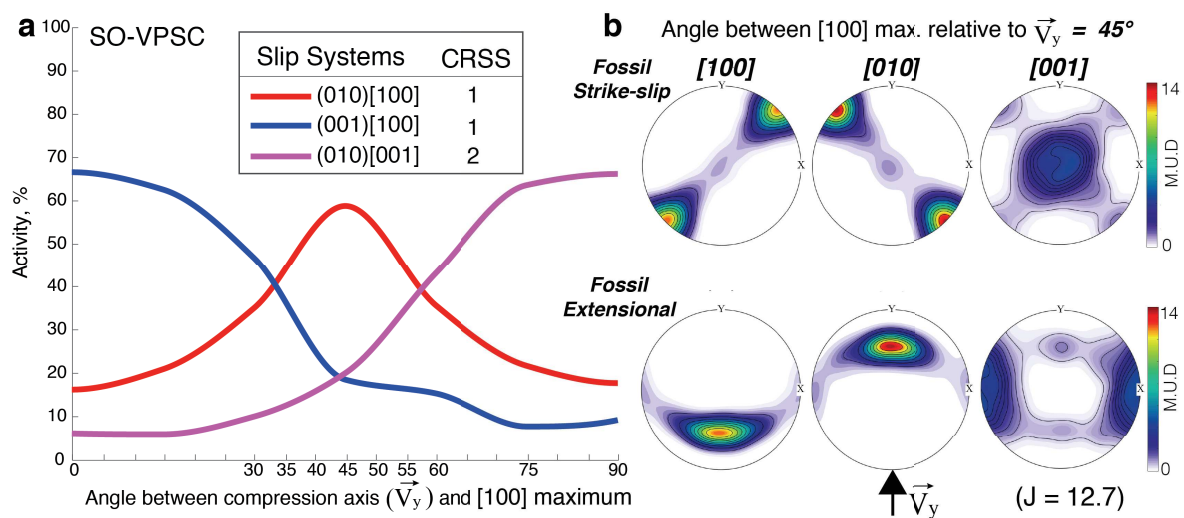


Figure 6.3: Strain localization as a function of the angle between the fossil shear plane and the imposed shortening for strike-slip and extensional fossil mantle shear zones, quantified by the ratio between the average of the second-invariant of the strain rate tensor in the fossil shear zone and in the isotropic surrounding mantle after ≈ 2 m.y of shortening. Simulations were performed for both strong and weak olivine CPO in the fossil mantle shear zone.

Fossil extensional mantle shear zones with steep to moderate dip angle ($90^\circ \leq \alpha \leq 60^\circ$) show average strain rates slightly lower than the isotropic surrounding mantle. For these (hard) loading geometries, the behaviour of a fossil extensional mantle shear zone is comparable to the one of a fossil strike-slip shear zone, regardless the CPO intensity. When the mantle shear zones are well oriented to localize strain ($60^\circ \leq \theta \leq 30^\circ$), the mechanical behavior can varies significantly as a function of CPO intensity.. However, strain localization in a fossil strike-slip mantle shear zone is more sensitivity to a decrease in CPO intensity. A decrease in CPO intensity by a factor ≈ 4 leads to normalized strain rates ≈ 2.5 smaller in the extensional shear zone, and ≈ 10 smaller in the fossil strike slip shear zones.

Polycrystal plasticity (SO-VPSC) simulations indicate that the slip systems' activation as a function of the orientation of the CPO relative to the compression axis is similar for the fossil strike-slip and extensional mantle shear (**Figure 6.4a**). ‘Hard’ behavior for aggregates with non-random olivine CPO occurs when [100] and [010] maxima are either perpendicular or parallel to the compression axis, whereas the ‘soft’ behaviours occur when the [100] and [010] maxima lie at 45° to the compression axis (**Figure 6.4b**). This occurs because at 45° the resolved shear stress (RSS) projected on the easy [100](010) system is high for most crystals in the aggregate, producing $\approx 60\%$ of the deformation accommodated by this easy slip system. Thus, at this loading-geometry the structural reactivation in both mantle shear zones is the most efficient. Once the slip systems are equally activated when the orientation of the mantle shear plane varies, one could argue that both shear zones should equally localize strain; (see **Figure 6.3**). However, the difference in mechanical behavior rises from the distinct boundary conditions setup.



(Figure caption in next page)

Figure 6.4: (a) Slip systems activity in olivine polycrystals predicted by SO-VPSC simulations for the strike-slip and extensional fossil mantle shear zones oriented at 45° to the shortening direction. The critical resolved shear stresses (CRSS) for the three main slip systems of olivine (normalized to the flow stress of the easy (010)[100] slip system) are indicated in the insert. (b) Orientation of the olivine CPO relative to the imposed compressional (V_y). the CPO symmetry and intensity are the same, only the orientation relatively to V_y changes. The pole figures are presented for the same multiple of uniform distribution (M.U.D)

Comparison of strain rate (2nd invariant of the tensor) and effective viscosity profiles at 52km depth (uppermost mantle) for simulations in compression and extensional corroborates this hypothesis (**Figure 6.5**). At the softer loading geometry ($\alpha = 45^\circ$), a fossil extensional mantle shear zone deformed in response to a new extension displays strain rates ≈ 2 times higher than when deformed in response to a new compression. In the former, strain rates are only slightly lower than strain rates within the fossil strike-slip mantle shear reactivated at 45° . The effective viscosity contrast between the mantle shear zone and its surroundings are significantly higher when the fossil extensional shear zone is reactivated in extension (>2 orders of magnitude) than in compression (<1 order of magnitude). Reactivation of an extensional shear zone in response to a new extension produced higher viscosity contrast than the observed during oblique reactivation of a fossil strike-slip shear mantle zone, yet in the latter higher strain rates contrast is observed. This argues in favour of a more complicated role of stress distribution on strain localization in the fossil extensional shear zone.

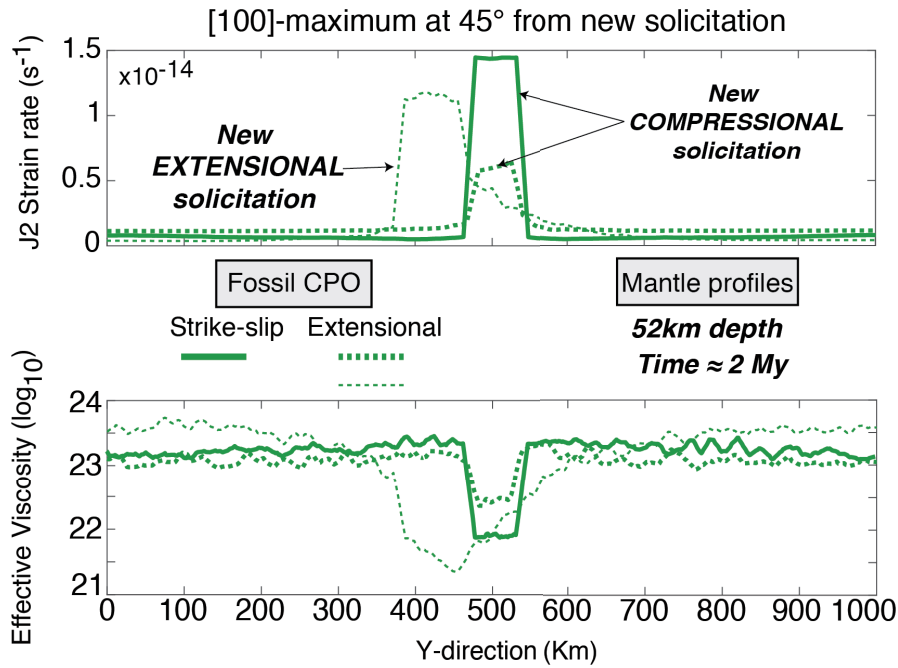


Figure 6.5: Profile of the second-invariant of the strain-rate tensor and of the effective viscosity at 52km depth (uppermost mantle) after ≈ 2 m.y for simulations with strike-slip and extensional fossil shear planes in the softer loading-geometry. Compression or extension is imposed to the fossil extensional mantle shear zone. The fossil strike-slip shear zone deformed in either extensional or compression display negligible variation in the mechanical response. Both fossil shear zones have a strong olivine CPO and are surrounded by a mantle with a random olivine CPO (i.e. isotropic).

During new compression of a fossil dipping extensional mantle shear zone the resistance of the lower boundary of the plate to shear strain parallel to the preexisting shear plane ('up-dip') is higher than the resistance imposed by P-litho lateral boundaries during reactivation of the fossil strike-slip shear zone under oblique compression. This high resistance leads to stress build up. In the case of a new extensional deformation of a fossil extensional mantle shear zone, the gravity applied in upper boundary favours 'down-dip' reactivation, inducing more efficient stress concentration in the lithosphere. Thus, reactivation in extension is favoured relatively to reactivation in compression, due to the interaction between the anisotropy-induced displacement and the boundary conditions, which affect the stress distribution in the lithosphere. These results further emphasize the importance of the boundary conditions for CPO-induced structural reactivation in the lithosphere.

To further test the effect of the orientation of the olivine CPO on the lithospheric response, I performed simulations in which the dip angle (α) of the fossil strike-slip shear zone was varied from 90° to 30° with strike of the shear plane (θ) trending 90° to the imposed shortening. The mechanical behavior of a fossil strike-slip shear zone depends

strongly on its dip angle, as indicated by the ratio between the average second-invariant of strain rate in the shear zone and in the isotropic surrounding mantle (**Figure 6.6a**). A strike-slip mantle shear zone dipping $90^\circ \leq \alpha \leq 60^\circ$ are stronger than the isotropic surrounding mantle (**Figure 6.8b**), whereas when dipping $60^\circ \leq \alpha \leq 30^\circ$ it is slightly weaker. The weakest loading-geometry occurs if the strike-slip mantle shear zone dip at 45° to the imposed shortening. At this loading-geometry, normalized strain rate within the strike-slip mantle shear zone is a factor ~ 20 lower than a vertical strike-slip shear zone in its “softest” loading-geometry ($\theta = 45^\circ, \alpha = 90^\circ$), and it is a factor ~ 10 lower than a 45° dipping fossil extension mantle shear zone (down-dip lineation; **Figure 6.6a**). Analysis of the strain rate field (second-invariant) shows that the strain localized in the fossil strike-slip mantle shear zone does not transmit localized deformation to the crust atop of it.

The deformation regime as a function of the orientation between the reactivated dipping mantle shear zones does not differ significantly (**Figure 6.6b**). The main difference occurs in terms of magnitude of shear components. Reactivation of a fossil dipping strike-slip and extensional mantle shear zone is mainly controlled by down-dip shear (D_{yz} in the shear zone reference frame), with the maximum value occurring at $\alpha = 45^\circ$ dip. However, the shearing component in a strike-slip mantle shear zone is ~ 3 times lower than the one predicted for a extensional shear zone with the same orientation and CPO intensity. This occurs because when the maximum concentration of [100] olivine is at the high angle to the imposed shortening, such as in the dipping strike-slip mantle shear zone, the resolved stresses on the easy (010)[100] and (001)[100] slips system of olivine are almost null. In contrast, in the fossil extensional shear zone dipping by 45° , the [100]- and [010] maxima are at 45° to the imposed shortening and the resolved stresses in these slip systems are maximum.

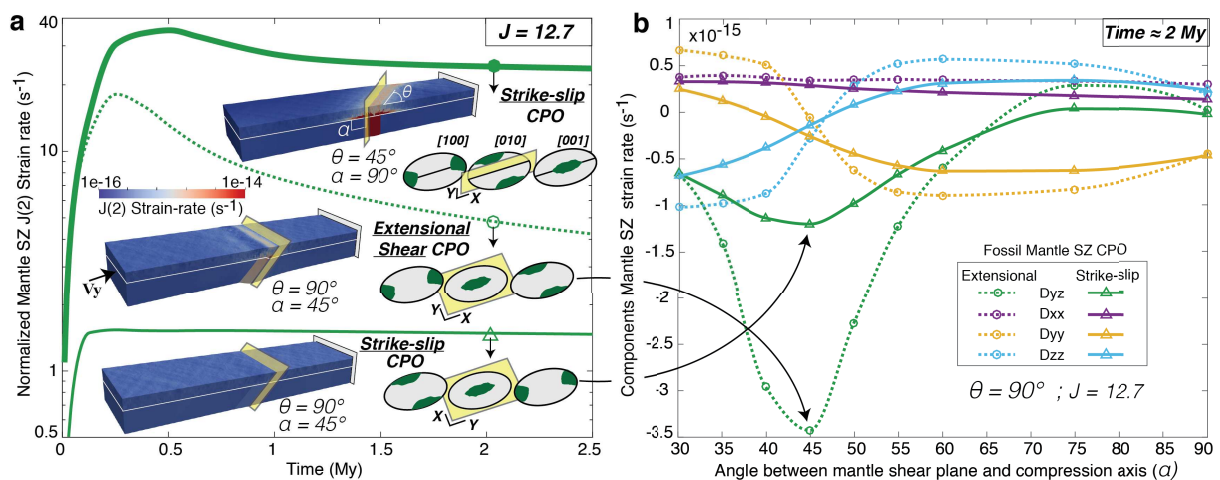


(Figure caption in the page)

Figure 6.6: (a) Time evolution of the strain rate second-invariant (averaged over the entire mantle shear zone) normalized to the same quantity in the surrounding mantle for the fossil mantle shear zones with different orientations of the lineation and foliation. The orientation of the associated olivine CPO relative to the mantle shear plane (XY, in yellow), the dipping angle α and the strike orientation θ , as well as the strain rate field are shown in the inserts. (b) Strain rate components (in the shear zone reference frame) in a 45° dipping fossil extensional and strike-slip shear zones after ≈ 2 m.y of imposed shortening.

In order to maintain the model geometry as in all other simulation (here and chapter 5), the response of the mantle shear zone with oblique dip angle and strike was inferred using from polycrystal plasticity models. Flow stresses were calculated using SO-VPSC for olivine CPO oriented coherent with in a fossil strike-slip shear zone with a constant oblique strike ($\theta = 45^\circ$), but with variable dip angle ($90^\circ \leq \alpha \leq 0^\circ$ at 15° intervals; **Figure 6.7**). The SO-VPSC model predicts lower flow stresses than the isotropic behaviour for all tested orientations. The lowest flow stress occurs for a vertical fossil shear zone oriented at 45° to the imposed shortening (a ‘classical’ strike-slip shear) zone. In this case, the [100] and [010] maximum of the fossil olivine CPO lies in the same plane of the imposed shortening and at 45° of it, which result in maximum resolved shear stresses on the easy (010)[100] slip system.

These predictions suggest that vertical strike-slip shear zones trending at 45° to the imposed shortening (or extension), which is the situation explored in detail in the last chapter, is the most favourable orientation to localize strain in a fossil mantle shear zone. This still needs to be tested for an extensional shear zone, but based on the orientation of the CPO and the resolved stress on the easy slip systems, I infer that a fossil extensional shear zone dipping $\sim 45^\circ$ to the applied stress comprise the most probable loading-geometry for its reactivation.

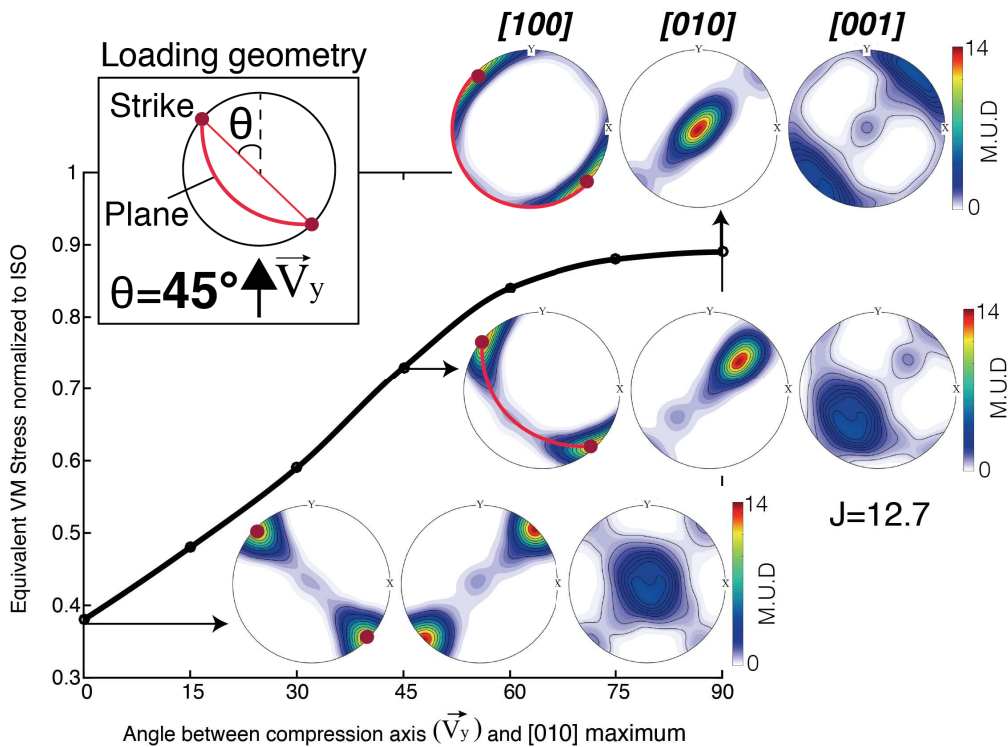


Figure 6.7: Flow stresses predicted by the SO-VPSC model (normalized to the isotropic behavior) for an olivine polycrystal with a strong orthorhombic CPO to which shortening was applied at 45° to the [100] maximum, but at variable angles to the [010] maximum. These models aim to simulate the mechanical response of a fossil strike slip mantle shear zone trending at 45° to the imposed shortening, but with variable dip angles. The pole figures are presented for the same multiple of uniform distribution (M.U.D).

Under compression of the fossil extensional mantle shear zone, lithospheric thickening occurs when the fossil shear plane dips between 55° and 35° to the compression axis. The localized deformation in the fossil extensional shear zone dipping 45° induce 22km thickening of the lithosphere by underplating of the shear zone footwall (**Figure 6.8a**). In contrast, for compression imposed to the dipping strike-slip mantle shear zone significant thickening is not observed (**Figure 6.8b**). Lithospheric thickening comparable to that of a 45° dipping extensional mantle shear zone may occurs for a 45° dipping mantle shear zone with random olivine CPO but with isotropic weakening 2 orders of magnitude higher than produced by anisotropic weakening. For other dipping angles ($\alpha=30^\circ$ - 60°), 1 order of magnitude better approximated the amount of underthrusting produced by CPO.

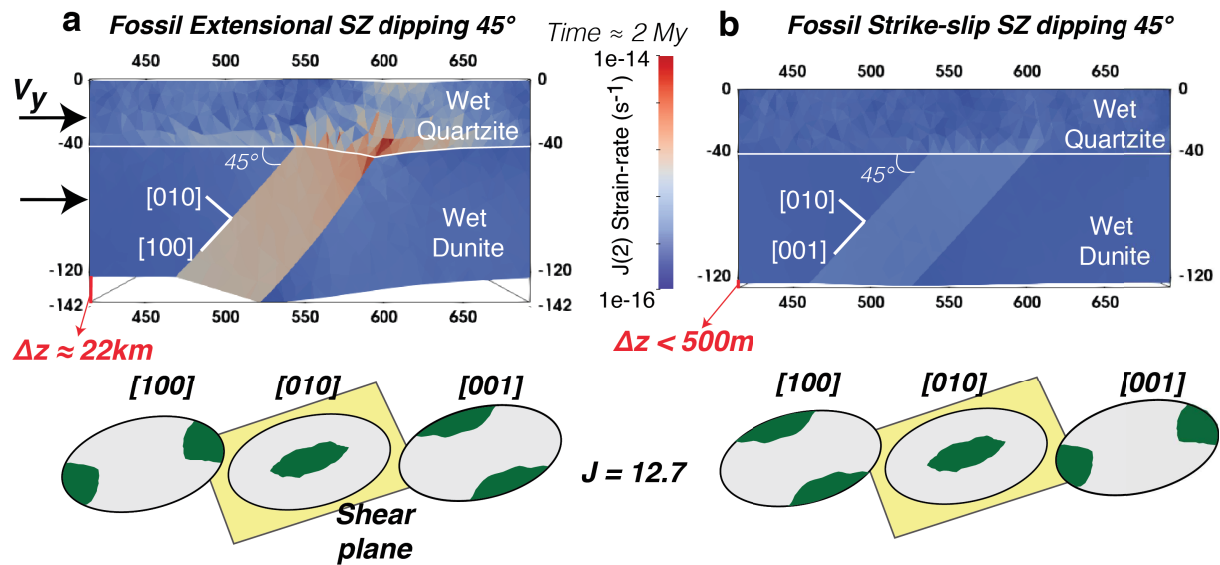


Figure 6.8: Strain rate field after 2 m.y of shortening of the (a) fossil extensional and (b) strike-slip mantle shear zones dipping $\alpha = 45^\circ$. The predicted amount of variation in thickness of the lithosphere (Δz) is show, as well as the orientation of the olivine CPO relative to the fossil shear plane (in yellow).

6.4 Discussion and Conclusions

Significant differences might arise in the mechanical behavior of anisotropic fossil mantle shear zones as a function of the orientation of the fossil shear plane and of the shear direction relative to the new imposed deformation. Thus, together with CPO intensity, boundary conditions, and mantle-crust mechanical coupling, the orientation relations influence considerably the degree and style of strain localization in the lithospheric shear zone. Fossil extensional mantle shear zones have a potential to localize subsequent deformation in a broader range of loading-geometries compared to strike-slip mantle shear zones; yet for the softer loading-geometry (i.e. 45°) the strain localization in the latter is more efficient. Strain localization in fossil extensional mantle shear zone is enhanced when the new deformation is in extension, since in this case gravity-driven forces add up to the tectonic ones. This prediction may shed some light in the scarce evidences of structural reactivation of mantle shear zones by thrusting (**Bastow et al., 2007**) relative to the relatively common evidence of reactivation of extensional or strike-slip mantle shear zones (**Vauchez et al., 1998, 2003, Tommasi and Vauchez, 2001, Storti et al., 2003**).

The reactivation of a fossil strike-slip shear zone is highly sensible to the dip angle of the fossil shear plane, that is, if the dip and strike angles deviate from the optimal loading-geometry (i.e. vertical shear plane and oblique strike relative to mechanical sollicitation) strain

localization is unlikely to occur. Variations in these orientation relations therefore might explain the discontinuous spatial distribution of reactivated strike-slip mantle shear zones. In the eastern United States and Canada, for instance, the linear seismicity is distributed in a series of discrete shear zones, despite the large-scale coherent and continuous fossil olivine CPO in the region. The absence of significant intraplate seismicity associated to the Brevard shear zone in the southeast United States may be justified by the moderate dip angle of the fossil strike-slip shear zone (**Vaucher et al., 1987**) in the mantle.

The orientation relation affects the amount of thickening (or thinning) of the lithosphere. The presence of a moderate dipping fossil mantle shear zone with a down-dip stretching lineation parallel to the [100] of the olivine CPO might promote easier thickening of the lithosphere by underplating (or thinning during stretching). Thus, one could speculate that CPO-induced strain localization in fossil compressional or extensional mantle shear zones might contribute to lithospheric thickening during continental collision and thinning during rifting, as suggested by Moho offsets in active and fossil thickened tectonic environments (**Cook, 1999. Levin and Park, 2000. Kind et al. 2002. Ai et al., 2005, Audet et al., 2019**), and to the inversion of rift basins (**Sibuet et al., 2004**). In addition, it might affect the rate of exhumation of mantle rocks during lithosphere extension (**Kaczmarek and Tommasi, 2011, Frets et al., 2014**).

Our models provide first-order features of the CPO-produced structural reactivation in lithospheric shear zones formed under different past kinematics. To better understand the role of olivine anisotropy mantle shear zones associated to dynamic environments, such as in active orogenic and rifted systems as suggested above. It is necessary to take into account the evolution of the olivine CPO and the specific actual thermomechanical and kinematic conditions of each tectonic setting.

REFERENCES

Ai, Y., Zhao, D., Gao, X., Xu, W., 2005. The crust and upper mantle discontinuity structure beneath Alaska inferred from receiver functions. *Physics of the Earth and Planetary Interiors* 150, 339.

Audet, P., Currie, C. A., Schaeffer, A. J., & Hill, A. M. (2019). Seismic evidence for lithospheric thinning and heat in the Northern Canadian Cordillera. *Geophysical Research Letters*, 46(8), 4249-4257.

Barruol, G., Helffrich, G., Russo, R., Vaucher, A., 1997a. Shear wave splitting around the

northern Atlantic: frozen Pangean lithospheric anisotropy? *Tectonophysics* 279, 135–148.

Barruol, G., Silver, P.G., Vauchez, A., 1997b. Seismic anisotropy in the eastern United States: deep structure of a complex continental plate. *Journal of Geophysical Research* 102, 8329–8348.

Bastow, I.D., Owens, T.J., Helffrich, G., Knapp, J.H., 2007. Spatial and temporal constraints on sources of seismic anisotropy: evidence from the Scottish Highlands. *Geophysical Research Letters* 34, L05305

Boillot, G., Recq, M., Winterer, E. L., Meyer, A. W., Applegate, J., Baltuck, M., ... & Evans, C. A. (1987). Tectonic denudation of the upper mantle along passive margins: a model based on drilling results (ODP leg 103, western Galicia margin, Spain). *Tectonophysics*, 132(4), 335-342.

Cook, F. A., van der Velden, A. J., Hall, K. W., & Roberts, B. J. (1999). Frozen subduction in Canada's Northwest Territories: Lithoprobe deep lithospheric reflection profiling of the western Canadian Shield. *Tectonics*, 18(1), 1-24.

Ford, H. A., Fischer, K. M., & Lekic, V. (2014). Localized shear in the deep lithosphere beneath the San Andreas fault system. *Geology*, 42(4), 295-298.

Frets, E., Tommasi, A., Garrido, C.J., Vauchez, A., Mainprice, D., Targuisti, K., Amri, I. (2014) Petro-structural evolution of the Beni Bousera peridotite massif, Rif, Morocco. *J. Petrol.* ,55 (2): 283-313, doi: 10.1093/petrology/egt067.

Kaczmarek, M.-A., Tommasi, A., 2011. Anatomy of an extensional shear zone in the mantle (Lanzo massif, Italy). *Geochemistry, Geophysics, Geosystems* Q0AG06

Kind, R., Yuan, X., Saul, J., Nelson, D., Sobolev, S.V., Mechie, J., Zhao, W., Kosarev, G., Ni, J., Achauer, U., Jiang, M., 2002. Seismic images of crust and upper mantle beneath Tibet: evidence for Eurasian plate subduction. *Science* 298, 1219–1221

Levin, V., Park, J., 2000. Shear zones in the Proterozoic lithosphere of the Arabian Shield and the nature of the Hales discontinuity. *Tectonophysics* 323, 131–148.

McBride, J.H., Snyder, D.B., Tate, M.P., England, R.W., Hobbs, R.W., 1995. Upper mantle reflector structure and origin beneath the Scottish Caledonides. *Tectonics* 14, 1351–1367

Sauter, D., Cannat, M., Rouméjon, S., Andreani, M., Birot, D., Bronner, A., ... & MacLeod, C. J. (2013). Continuous exhumation of mantle-derived rocks at the Southwest Indian Ridge for 11 million years. *Nature Geoscience*, 6(4), 314

Sénéchal, G., Rondenay, S., Mareschal, M., Guilbert, J., Poupinet, G., 1996. Seismic and electrical anisotropies in the lithosphere across the Grenville Front, Canada. *Geophysical Research Letters* 23, 2255–2258

Sibuet, J. C., Srivastava, S. P., & Spakman, W. (2004). Pyrenean orogeny and plate kinematics. *Journal of Geophysical Research: Solid Earth*, 109(B8).

Silver, P., Mainprice, D., Ismail, W., Tommasi, A., & Barruol, G. (1999). Mantle structural geology from seismic anisotropy.

Storti, F., Holdsworth, R.E., Salvini, F., 2003. Intraplate strike-slip deformation belts. In: Storti, F., Holdsworth, R.E., Salvini, F. (Eds.), *Intraplate strike-slip deformation belts: Geological Society of London, Special Publication*, 210, pp. 1–14.

Titus, S. J., Medaris Jr, L. G., Wang, H. F., & Tikoff, B. (2007). Continuation of the San Andreas fault system into the upper mantle: evidence from spinel peridotite xenoliths in the Coyote Lake basalt, central California. *Tectonophysics*, 429(1-2), 1-20.

Tommasi, A., & Vauchez, A. (2001). Continental rifting parallel to ancient collisional belts: an effect of the mechanical anisotropy of the lithospheric mantle. *Earth and Planetary Science Letters*, 185(1-2), 199-210.

Tommasi, A., Tikoff, B., & Vauchez, A. (1999). Upper mantle tectonics: three-dimensional deformation, olivine crystallographic fabrics and seismic properties. *Earth and Planetary Science Letters*, 168(1-2), 173-186.

Vauchez, A. (1987). Brevard fault zone, southern Appalachians: A medium-angle, dextral, Alleghanian shear zone. *Geology*, 15(7), 669-672.

Vauchez, A., Barruol, G., Tommasi, A., 1997. Why do continents break up parallel to ancient orogenic belts? *Terra Nova* 9, 62–66.

Vauchez, A., Tommasi, A., & Mainprice, D. (2012). Faults (shear zones) in the Earth's mantle. *Tectonophysics*, 558, 1-27.

Vauchez, A., Tommasi, A., 2003. Wrench faults down to the asthenosphere: geological and geophysical evidence and thermo-mechanical effects. In: Storti, F., Holdsworth, R.E., Salvini, F. (Eds.), *Intraplate strike-slip deformation belts. Special Publication*, 210. Geological Society of London, pp. 15–34

Wernicke, B., 1985. Uniform sense normal simple shear of the continental lithosphere. *Can. J. Earth Sci.*, 22: 108-125.

Wittlinger, G., Vergne, J., Tapponnier, P., Farra, V., Poupinet, G., Jiang, M., ... & Paul, A. (2004). Teleseismic imaging of subducting lithosphere and Moho offsets beneath western Tibet. *Earth and Planetary Science Letters*, 221(1-4), 117-130

CHAPTER VII

CONCLUSIONS, LIMITATIONS AND FUTURE PERSPECTIVES

*A journey of a thousand miles begins
with a single step.*

Lao Tzu

7 Conclusions, limitations of the study, and future perspectives

In this chapter, the findings of the present work and the open questions are highlighted. The shortcomings of the study are discussed and future research is proposed. The aim is to contextualise the main outcomes and to propose guidelines for moving forward on the study of viscoplastic anisotropy in mantle rocks and its consequences for geodynamics.

7.1 Overall conclusions

7.1.1 Conclusions 1: Maximum strain-rate contrast induced by olivine viscous anisotropy

Bounds for the contrast of strain rate produced by the viscous anisotropy of olivine in textured mantle peridotites and intraplate mantle shear zones were proposed (**Figure 7.1**). Intrinsic viscous anisotropy due to intracrystalline glide is an invariant property of the material, however, geometrical factors or secondary processes might affect the expression of anisotropy at larger-scales. In the olivine *crystal*, anisotropy result in a factor of >100 times contrast in strain rate (**Bai et al., 1991, Durham & Goetze 1976**). In the olivine-rich *rock*, viscous anisotropy produced by crystallographic preferred orientations (CPO) of olivine is mediated mainly by the intensity of the CPO, by other deformation mechanisms in addition to dislocation creep, and by the imposed boundary conditions, leading to a contrast in strain rate of a factor <10 (**Hansen et al., 2012, 2016**). In the *tectonic plates*, the heterogeneous distribution of olivine CPO in the upper mantle may induce, in most of the cases, to a contrast strain rate in the lithosphere of a factor of <100 times. At this scale, strain localization is also moderated by boundary conditions, crust-mantle mechanical coupling, and also for the activation of other lithospheric weakening mechanisms, which may add to CPO-induced strain localization to produce in even higher contrast in strain rate.

7.1.2 Conclusions 2: Main factors moderating olivine viscous anisotropy and the resulting strain localization

Significant activation of others deformation processes in addition to dislocation creep might reduce in more than 2 times the magnitude of the viscous anisotropy in mantle

peridotites deforming at conditions relevant for most of the lithospheric mantle (i.e. high temperature, moderate pressure and dry conditions). The rock-scale viscous anisotropy at these conditions may be greatly affected by variations in CPO intensity and by the boundary conditions, which control the intensity and mode of the viscous anisotropy expressed, respectively. Only minor changes are observed as a function of common CPO symmetry (orthorhombic and axial-[100] and -[010] CPOs) for polycrystal deformed under high temperature and equivalent boundary conditions. The magnitude of the viscous anisotropy varies proportionally to the intensity of the CPO intensity, but not linearly. If ‘out-of-plane’ strain components develop during oblique deformation cannot fully express due the restrictive boundary conditions, the magnitude of anisotropy as well as its pattern to loading-geometry may be significantly modified.

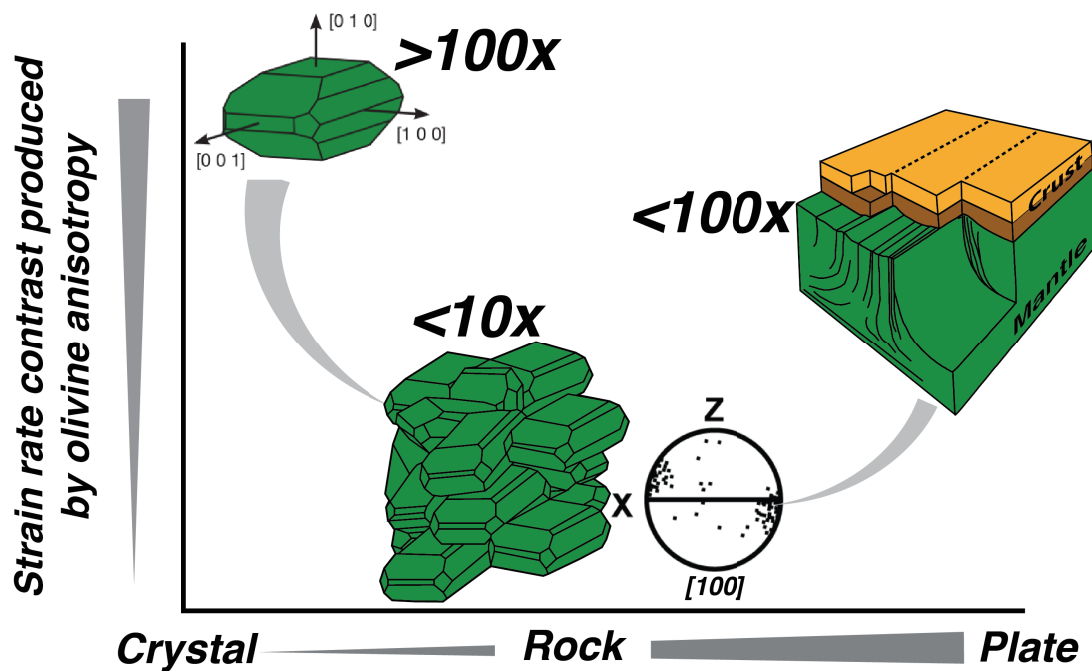


Figure 7.1: Cartoon illustrating the (most-likely) contrast in strain rate that might be induced by olivine viscous anisotropy as a function of the loading-geometry through different spatial scales.

The magnitude and style of strain localization in lithospheric shear zones (mantle and crust) is modulated in time and space by, the heterogeneity in CPO symmetry and intensity in the lithospheric mantle (contrast in viscous anisotropy), by the mechanical interactions between the mantle and the crust, and by the plate boundary conditions. Weaker crustal faults or strong mantle rheology enhance the CPO-induced strain localization in the entire lithospheric shear zone. If mechanical coupling between the mantle and crust is efficient, or if

boundary conditions do not allow the plate accommodate arbitrary deformation, CPO-produced strain components are partially hindered, leading to inefficient strain localization in the lithosphere, if any localization is produced.

7.1.3 Conclusions 3: Structural reactivation due to olivine viscous anisotropy in mantle shear zones

The presence of olivine CPO in mantle shear zone leads to a highly non-linear directional dependence of strain localization in the fossil shear zone. Their reactivation is very unlikely to occur if the fossil shear plane lies either sub-perpendicular or subparallel to the mechanical sollicitation. in contrasts to oblique loading-geometries, notably between 40° - 50° to the mantle foliation. The strong lateral shearing component produced by olivine CPO in oblique reactivated strike-slip mantle shear zone lead to development of crustal shear zone mainly controlled by transpressional or transtensional deformation. Similarly, the strong down-dip shearing produced by olivine CPO in moderate dipping reactivated extensional mantle shear zones also induce the developments of crustal shear zones. In addition, it might contribute to more effective thinning or thickening of the lithosphere.

The CPO intensity and the orientation (strike and dip) of the fossil mantle shear zone can result in heterogeneous distribution of strain localization in continents. This is particularly critical for strike-slip mantle shear zones, since deviation form the softer loading-geometries (between 40° - 50° to the applied stress) can drastically modified the mechanical behavior. For the same viscous anisotropy and thermomechanical conditions, CPO-induced strain localization is more efficient in a fossil strike-slip mantle shear zone than in a fossil extensional (or compression) mantle shear zone, if both oriented at their respective softer loading-geometry. This occurs therefore purely due to geometrical reasons.

7.1.4 Conclusions 4: Structural memory of plate tectonics: the importance of olivine viscous anisotropy fossilized in the mantle

Seismological data available worldwide show that anisotropy in continental lithosphere is the rule rather than the exception. The seismic anisotropy measurements indeed suggest the presence of coherent olivine CPO for tens to hundreds of kilometres in the lithospheric mantle. Thus, for understanding the details of the onset of global tectonics from mantle

convection, anisotropic viscosity resulting from olivine CPO in the lithospheric mantle cannot be neglected. CPO may only be modified by thermo-tectonic events, but not destroyed. Hence, heterogeneous distribution of CPO at large-scale might act at long-term seed for strain localization in the tectonic plates. Moreover, the presence of fossilized olivine CPO greatly influences the deformation regime that develops during the reactivation of lithospheric shear zone, driving the deformation regime that develops during continental break-up and assembly of supercontinents. This has implications therefore for the formation of new plate boundaries from otherwise intraplate stable domains, as suggest by the coherence between mantle fabric and active (**Bosworth and Strecker, 1997**) and fossil (**Geoffroy et al., 1994**) shear zones in continents.

I argue that heterogeneity in viscous anisotropy induced by fossilized olivine CPO, together with variations in thermal structure (**Tommasi and Vauchez, 1997, Jaupart et al., 2007, Neves et al., 2008, Thielmann and Kaus, 2012**) and in grain-size reduction (**Rozel et al., 2011, Précigout and Gueydan, 2009, Bercovici & Ricard, 2012, 2014**), comprise the three main lithospheric weakening mechanisms sustaining large-scale strain localization needed to enable the plate tectonics style of mantle convection (review in **Coltice et al., 2017**) (**Figure 7.2**).

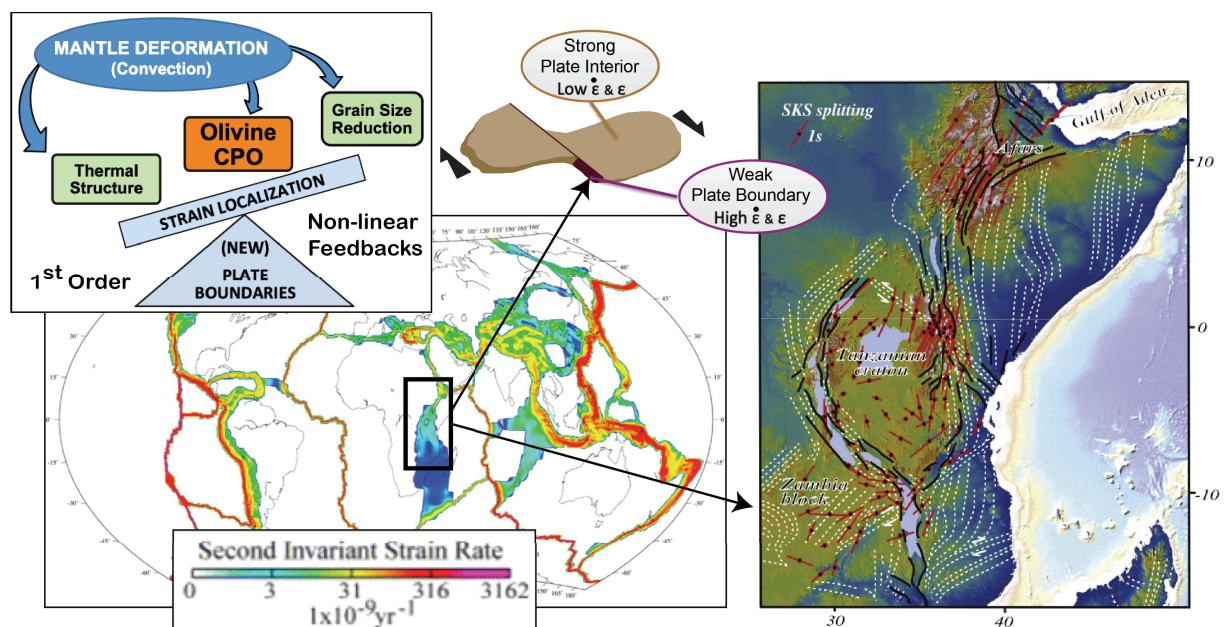


Figure 7.2: First order ‘ingredients’ of strain localization in plate tectonics, characterized by (weak) narrow rapid deforming boundaries surrounding by (strong) undeformed domains. In the East African Rift for example, where a new plate boundary is developing, thermal heterogeneities (stiff cratonic blocks bounded by opening faulting system) and CPO-induced anisotropy controls the rift propagation.

7.2 Main Limitations

The main limitations of this work is that (1) it does not consider evolution of the olivine CPO, (2) it is based on olivine polycrystal deforming at a particular P-T-H₂O conditions, and (3) it does not account for the feedbacks between others lithospheric strain-localization processes.

Details of time-dependent anisotropic viscosity might only be captured if the evolution of the CPO is taken into account. For instance, and **Knoll et al. (2009)** has shown that, for most of the soft orientations, the CPO evolution in the mantle shear zone lead to decrease of the along-strike shearing and of the strain delocalization at high finite strains. Different CPO inside and outside a fossil mantle shear zones evolves in distinct way as a function of the orientation relation (**Skemmer et a., 2015**), this can indeed lead to the inversion of the relative strength between a mantle shear zone and its surroundings. Moreover, further heterogeneity in viscous anisotropy might occur if olivine CPO slightly disperses due to water infiltration (**Wallis et al., 2019**) or presence of secondary-phases (**Raterron, et al., 2014**). CPO evolutions must be notably important for non-steady state orientations of the olivine CPO, where relative high finite strain are required for reaching a stable CPO intensity and symmetry (**Signorelli and Tommasi et al., 2015, Hansen et al., 2016**), such as in corner flows of plate boundaries (**Castelnau et al., 2008**).

The geodynamical model prediction presented rely on rigorous physical models (i.e. SO-VPSC) of olivine polycrystal deforming by easy and hard glides on the [100] and [001] directions, respectively. In the intraplate lithospheric mantle, local variation in the temperature and stresses might favour a different relative strength of the slip directions. Laboratory experiments by **Durham & Goetze 1976** and **Demouchy et al., 2013** indicated that at low temperature and high differential stresses, the relative strength of the slip system shift to dominant sliding in the [001] direction. Thus, the parameterized in this study is not suitable for capturing the viscous anisotropy at these conditions.

In the present thesis only the heterogeneity of the viscous properties originating from olivine CPO is taken into consideration. However, heterogeneity of thermal properties, as well as of rock composition and grain size, interact with CPO-induce viscous anisotropy to regulate strain localization in the lithosphere (review in **Tommasi and Vauchez, 2015**). Indeed, olivine CPO is anisotropic in terms of its thermal properties (**Gilbert et al., 2003**). Once strain localizes in the lithosphere due to thermo-mechanical anisotropy or lateral

variation in geotherm, grain-size reduction and shear heating might further decrease rock-strength and further induced strain localization in the viscous regime (Kaus & Podladchikov, 2006), which in turn can further create or modify olivine CPO. Yet, the (non-linear) feedbacks between these processes are poorly understood.

7.3 Some open questions and future directions

- Shape Preferential Orientation (SPO) can produce anisotropic viscosity (Wheeler, 2010). Sliding velocities in grain boundaries might also be anisotropic. *Are they significant for deformation at upper mantle conditions? How does it scale with CPO-induced anisotropy during grain-size reduction?* A critical issue is how to isolate a single grain boundary interface to study its (anisotropic) mechanical properties (Marquardt and Faul, 2018).
- SPO of melt-lenses (Holtzman et al., 2012) and mica (Shea and Kronenberg, 1993) may produce transverse isotropy viscosity in crustal shear zones. *Does crustal anisotropy modify the mechanical response of the entire lithosphere as mantle anisotropy does? How does crustal and mantle mechanical anisotropy interact?*
- Towards mantle domains where temperature is lower and differential stresses are high, such as towards the uppermost mantle, viscous anisotropy might vary due to changing of dominant slip direction (Durham & Goetze 1976). *What is the effect of this shift in rock- and plate scale viscous anisotropy? Is there a vertical gradient in viscous anisotropy in the lithosphere that can be quantified? Does it affect mantle-crust mechanical coupling?*
- Mechanical coupling is expected to be efficient in intraplate mantle shear zones, allowing transferring deformation between the different rheological layers (Grocott et al., 2004, Tikoff et al., 2004). We showed that mantle-crust coupling regulate CPO-induced strain localization. *What about the opposite way round? Does out-of-plane deformation induced by CPO influence the mechanical coupling in intraplate mantle shear zone?*

- Viscous anisotropy in subduction zones changes the thermal structure of the mantle wedge (**Lev et al., 2011**). *Does viscous anisotropy affect the (3D) mechanical behavior of the down-going slab? What about in even more dynamic scenario, such as slab slab rollback or tearing? High mantle shear viscosity mantle acts as a barrier to fluid flow in the mantle wedge (Cerpa et al., 2017). How viscous anisotropy affect the shear viscosity and consequently the fluid migration in the mantle wedge?*
- CPO-induced viscous anisotropy beneath spreading plates modify the viscous flow at the base of lithosphere (**Blackman et al., 2007**) and can lead to ~15 viscosity contrast in the corner flow (**Castelnau, et al., 2009**). *How viscous anisotropy affect the strain localization in spreading centers? Does it affect the ridge segmentation?*
-

The approach used to parameterized olivine viscous anisotropy at high temperature, moderate pressure and dry conditions (this thesis) can be extended to conditions at which the olivine polycrystal is deformed at lower temperature and high differential stresses in order to consider the viscous anisotropy of olivine raising from dominant deformation by glide in [001] direction. The critical resolved shear stress in VPSC simulations can be modified based on available laboratory experiments data (**Demouchy et al, 2014** and references therein). This can provide insights on the degree of heterogeneity in mechanical behavior in the lithospheric mantle, and on the effect of CPO on degree on mechanical coupling between the mantle and crust, since from the lowermost mantle towards the uppermost mantle, lower temperatures and high differential stresses are expected to modify the dominant slip systems of olivine.

ADELI3D may be modified to consider transverse isotropic plasticity in crustal shear zones (**Backus, 1962**). This can be done based on laboratory experiments of mechanical anisotropy of crustal rocks (**Attewell and Sandford, 1974. Shea and Kronenberg, 1993. Rawling et al., 2002. Collettini et al., 2009. Bonnelye, et al., 2017. Zhang et al., 2019** and references therein). This implementation could allow shedding light on the joint effect of mantle and crustal mechanical anisotropy on the partition between toroidal and poloidal flow, on the magnitude of strain localization in the mantle and crust, and on the evolution of strain components in lithospheric shear zones.

Consider time-evolution anisotropic rheology by means of evolution of CPO in 3D geodynamical simulations can be time consuming. To overcome this issue, the parameterization developed in the present thesis can be combined with the director cosines method to calculate first-order CPO evolution from viscous flow alignment (**Mühlhaus et al., 2003**) and provide the associated viscous anisotropy at large finite strains (**Lev and Hager, 2008**). To simulate olivine CPO evolution during extension followed by torsion at laboratory conditions, and also during shear of peridotites at natural conditions, **Hansen et al. (2016b)** adapted the director method to consider four slip systems in olivine. Another growing possibility is to use a probabilistic approach based on neural network (**Atkins, 2017, Shahnas et al., 2018**). This technique has the advantage of describing the uncertainty of CPO evolution for a given range of the parameter space, for example temperature, stress exponents and finite strain, which can be further used to constrain the different geodynamical scenarios.

For predicting the details of earth-like plate tectonics from convection, the interplay between geothermal gradient, grain size reduction and CPO-induced viscous anisotropy needs to be implemented in global self-consistent plate models (*review in* **Bercovici et al., 2003**). Our prediction can be simplified in these models to account for the bounds of CPO-induced strain localization and for the pattern of the viscous anisotropy as a function of first-order orientation of lithospheric shear zones relative to the far-field driving-force, for example, oblique (45°), parallel (0°) and perpendicular (90°) orientations (**Coltice et al., 2017** and references therein). The amount of shearing produced by CPO in lithospheric strike-slip shear zones in our study could be used for instance to parametrize the rate of along-strike displacement in continental transform boundaries in those models.

REFERENCES

- Atkins, S., 2017. Finding the patterns in mantle convection. PhD Thesis Utrecht University
- Attewell, P. B., & Sandford, M. R. (1974, November). Intrinsic shear strength of a brittle, anisotropic rock—I: experimental and mechanical interpretation. In *International Journal of Rock Mechanics and Mining Sciences & Geomechanics Abstracts*(Vol. 11, No. 11, pp. 423-430). Pergamon.
- Backus, G. E. (1962), Long-Wave Elastic Anisotropy Produced by Horizontal Layering, *J. Geophys. Res.*, 67(11), 4427–4440
- Bercovici, D. (2003). The generation of plate tectonics from mantle convection. *Earth and Planetary Science Letters*, 205(3-4), 107-121.
- Bercovici, D., Ricard, Y., 2012. Mechanisms for the generation of plate tectonics by two-phase grain-damage and pinning. *Phys. Earth Planet. Inter.* 202–203, 27–55.
- Bercovici, D., Ricard, Y., 2014. Plate tectonics, damage and inheritance. *Nature* 508, 513–516
- Blackman, D. K., Boyce, D. E., Castelnau, O., Dawson, P. R., & Laske, G. (2017). Effects of crystal preferred orientation on upper-mantle flow near plate boundaries: rheologic feedbacks and seismic anisotropy. *Geophysical Journal International*, 210(3), 1481-1493.
- Boneh, Y., Morales, L. F., Kaminski, E., & Skemer, P. (2015). Modeling olivine CPO evolution with complex deformation histories: Implications for the interpretation of seismic anisotropy in the mantle. *Geochemistry, Geophysics, Geosystems*, 16(10), 3436-3455.
- Bonnelye, A., Schubnel, A., David, C., Henry, P., Guglielmi, Y., Gout, C., ... & Dick, P. (2017). Strength anisotropy of shales deformed under uppermost crustal conditions. *Journal of Geophysical Research: Solid Earth*, 122(1), 110-129.
- Bosworth, W., Strecker, M.R., 1997. Stress field changes in the Afro-Arabian rift system during the Miocene to Recent period. *Tectonophysics* 278, 47–62.
- Castelnau, O., Blackman, D. K., & Becker, T. W. (2009). Numerical simulations of texture development and associated rheological anisotropy in regions of complex mantle flow. *Geophysical Research Letters*, 36(12).
- Cerpa, N. G., Wada, I., & Wilson, C. R. (2017). Fluid migration in the mantle wedge: Influence of mineral grain size and mantle compaction. *Journal of Geophysical Research: Solid Earth*, 122(8), 6247-6268.

Collettini, C., Niemeijer, A., Viti, C., & Marone, C. (2009). Fault zone fabric and fault weakness. *Nature*, 462(7275), 907.

Coltice, N., G erault, M., & Ulvrova, M. (2017). A mantle convection perspective on global tectonics. *Earth-science reviews*, 165, 120-150.

Demouchy, S., Mussi, A., Barou, F., Tommasi, A., & Cordier, P. (2014). Viscoplasticity of polycrystalline olivine experimentally deformed at high pressure and 900 C. *Tectonophysics*, 623, 123-135.

Demouchy, S., Tommasi, A., Ballaran, T. B., & Cordier, P. (2013). Low strength of Earth's uppermost mantle inferred from tri-axial deformation experiments on dry olivine crystals. *Physics of the Earth and Planetary Interiors*, 220, 37-49.

Durham, W. B., & Goetze, C. (1977). Plastic flow of oriented single crystals of olivine: 1. Mechanical data. *Journal of geophysical Research*, 82(36), 5737-5753.

Geoffroy, L., Bergerat, F., Angelier, J., 1994. Tectonic evolution of the Greenland–Scotland Ridge during the Paleogene. new constraints. *Geology* 22, 653–656.

Gibert, B., Seipold, U., Tommasi, A., Mainprice, D., 2003. Upper mantle thermal diffusivity: pressure- and temperature dependences and anisotropy. *J. Geophys. Res.* 108, 2359. <http://dx.doi.org/10.1029/2002JB002108>.

Grocott, J., McCaffrey, K. J., Taylor, G. K., & Tikoff, B. (2004). Vertical coupling and decoupling in the lithosphere. *Geological Society, London, Special Publications*, 227(1), 1-7.

Hansen, L. N., Conrad, C. P., Boneh, Y., Skemer, P., Warren, J. M., & Kohlstedt, D. L. (2016). Viscous anisotropy of textured olivine aggregates: 2. Micromechanical model. *Journal of Geophysical Research: Solid Earth*, 121(10), 7137-7160.

Hansen, L. N., Warren, J. M., Zimmerman, M. E., & Kohlstedt, D. L. (2016). Viscous anisotropy of textured olivine aggregates, Part 1: Measurement of the magnitude and evolution of anisotropy. *Earth and Planetary Science Letters*, 445, 92-103.

Holtzman, B.K., King, D.S., Kohlstedt, D.L., 2012. Effects of stress-driven melt segregation on the viscosity of rocks. *Earth Planet. Sci. Lett.* 359, 184–193.

Jaupart, C., Mareschal, J. C., & Watts, A. B. (2007). Heat flow and thermal structure of the lithosphere. *Treatise on geophysics*, 6, 217-252.

Kaus, B. J., & Podladchikov, Y. Y. (2006). Initiation of localized shear zones in viscoelastoplastic rocks. *Journal of Geophysical Research: Solid Earth*, 111(B4).

Karato S (1989) Grain growth kinetics in olivine aggregates. *Tectonophysics* 168: 255–273

Lev, E., & Hager, B. H. (2008). Prediction of anisotropy from flow models: A comparison of three methods. *Geochemistry, Geophysics, Geosystems*, 9(7).

Marquardt, K., & Faul, U. H. (2018). The structure and composition of olivine grain boundaries: 40 years of studies, status and current developments. *Physics and Chemistry of Minerals*, 45(2), 139-172.

Molnar, P., Tapponnier, P., 1981. A possible dependence of tectonic strength on the age of the crust in Asia. *Earth Planet. Sci. Lett.* 52, 107–114.

Mühlhaus, H., H. Moresi, and M. Cada (2004), Emergent anisotropy and flow alignment in viscous rock, in *Computational Earthquake Science Part II*, pp. 2451–2463, Springer, Basel, Switzerland.

Précigout, J., & Gueydan, F. (2009). Mantle weakening and strain localization: Implications for the long-term strength of the continental lithosphere. *Geology*, 37(2), 147-150.

Raterron, P., Detrez, F., Castelnau, O., Bollinger, C., Cordier, P., & Merkel, S. (2014). Multiscale modeling of upper mantle plasticity: From single-crystal rheology to multiphase aggregate deformation. *Physics of the Earth and Planetary Interiors*, 228, 232-243.

Rawling, G. C., Baud, P., & Wong, T. F. (2002). Dilatancy, brittle strength, and anisotropy of foliated rocks: Experimental deformation and micromechanical modeling. *Journal of Geophysical Research: Solid Earth*, 107(B10), ETG-8.

Rozel, A., Ricard, Y., Bercovici, D., 2011. A thermodynamically self-consistent damage equation for grain size evolution during dynamic recrystallization. *Geophys. J. Int.* 184, 719–728.

Shahnas, M. H., Yuen, D. A., & Pysklywec, R. N. (2018). Inverse Problems in Geodynamics Using Machine Learning Algorithms. *Journal of Geophysical Research: Solid Earth*, 123(1), 296-310.

Shea Jr, W. T., & Kronenberg, A. K. (1993). Strength and anisotropy of foliated rocks with varied mica contents. *Journal of Structural Geology*, 15(9-10), 1097-1121.

Signorelli, J., & Tommasi, A. (2015). Modeling the effect of subgrain rotation recrystallization on the evolution of olivine crystal preferred orientations in simple shear. *Earth and Planetary Science Letters*, 430, 356-366.

Thielmann, M., & Kaus, B. J. (2012). Shear heating induced lithospheric-scale localization: Does it result in subduction?. *Earth and Planetary Science Letters*, 359, 1-13.

Tikoff, B., Russo, R., Teyssier, C., & Tommasi, A. (2004). Mantle-driven deformation of

orogenic zones and clutch tectonics. Geological Society, London, Special Publications, 227(1), 41-64.

Tommasi, A., & Vauchez, A. (2015). Heterogeneity and anisotropy in the lithospheric mantle. *Tectonophysics*, 661, 11-37.

Tommasi, A., Vauchez, A., Daudré, B., 1995. Initiation and propagation of shear zones in a heterogeneous continental lithosphere. *J. Geophys. Res.* 100, 22,083–22,101

Wallis, D., Hansen, L. N., Tasaka, M., Kumamoto, K. M., Parsons, A. J., Lloyd, G. E., ... & Wilkinson, A. J. (2019). The impact of water on slip system activity in olivine and the formation of bimodal crystallographic preferred orientations. *Earth and Planetary Science Letters*, 508, 51-61.

Zhang, C. L., Armand, G., Conil, N., & Laurich, B. (2019). Investigation on anisotropy of mechanical properties of Callovo-Oxfordian claystone. *Engineering geology*, 251, 128-145.

Zhang, N., Zhong, S., & McNarmara, A. K. (2009). Supercontinent formation from stochastic collision and mantle convection models. *Gondwana Research*, 15(3-4), 267-275.

ABSTRACT

The generation of earth-like plates implies efficient strain localization in the lithosphere for long times-spans. In this thesis, I quantified the contribution of viscous anisotropy due to crystal-preferred orientations (CPO) of olivine in the lithospheric mantle on strain localization at the plate-scale. First, I performed numerical experiments using polycrystal plasticity models (e.g., VPSC) to evaluate the magnitude and controlling parameters of olivine-induced viscous anisotropy at the rock-scale and compared their predictions to experimental data to validate the model results. Then, a parameterization based on these models has been developed and implemented in a 3D finite-element geodynamical code to study structural reactivation and deformation regime associated with fossil lithospheric shear zones. The aim is to investigate the role of intrinsic (olivine CPO) viscous anisotropy on the development old lithospheric shear zones and its possible relation with the onset of linear seismicity in intraplate settings.

The results show that activation of 2nd mechanisms at the rock scale greatly contributes to reducing the magnitude of viscous anisotropy in mantle rocks, resulting in maximum contrast of <6 in stress (for a constant strain rate). Imposed boundary conditions regulate the CPO-induced viscous anisotropy at both rock- and plate scale, mainly due to the 3D (out-of-plane) strain and stress components that develops. The presence of olivine CPO in the lithospheric mantle lead to strong directional dependence of the strain localization within the mantle shear zone, which, if well oriented to be reactivated, induces strain localization in the entire lithosphere. Deformation regime in the crust follows the one in the mantle. The mechanical feedbacks between both rheological layers, which are affect by the isotropic (composition) and anisotropic (CPO) parts, greatly affect strain localization in continental plates.